FACULTY OF SCIENCE
UNIVERSITY OF COPENHAGEN

Interaction-induced Electronic Phases in Twisted Bilayer Graphene

Clara Neerup Breiø

Niels Bohr Institute
University of Copenhagen
Lyngbyvej 2, DK-2100, Copenhagen, Denmark

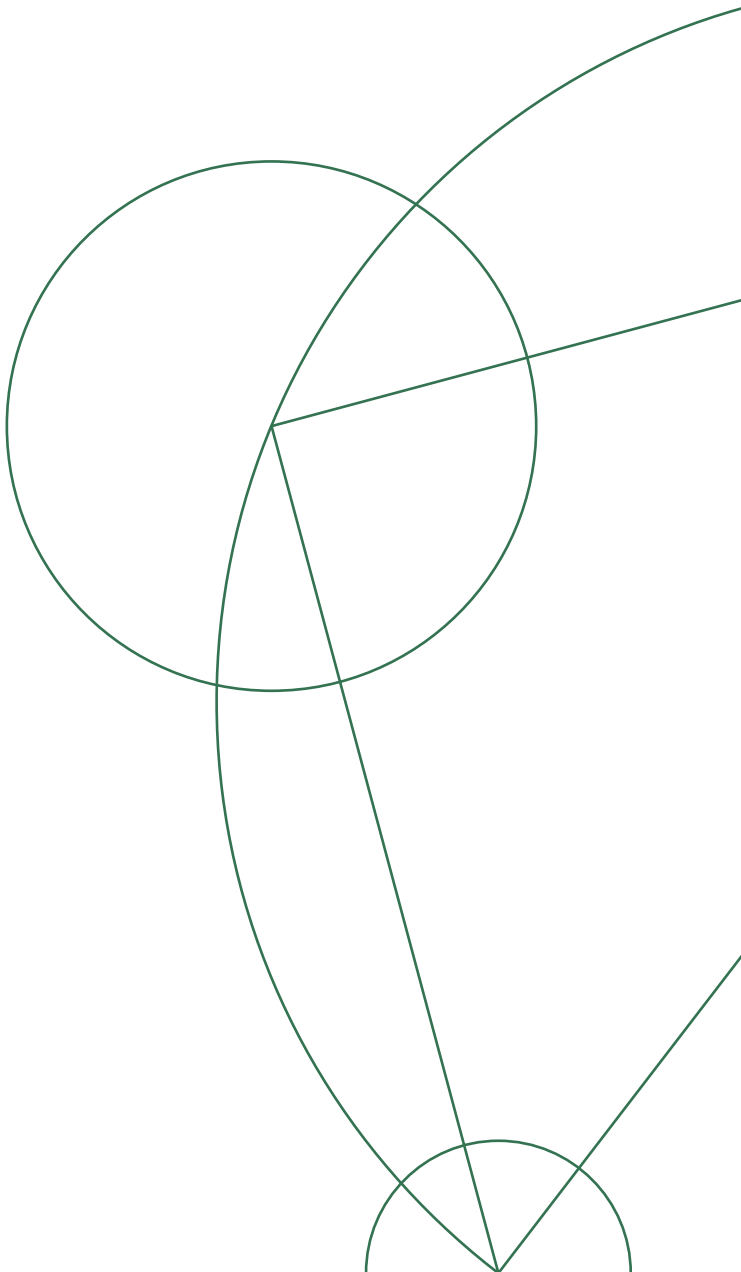

Master's thesis in Physics

Advisor: Brian Møller Andersen

Dated: July 2, 2020

Abstract

Since the discovery of interaction-induced insulating and superconducting states in "magic" angle twisted bilayer graphene in 2018, the scientific interest in this new material has reached incredible heights. While countless theoretical studies have been published, a transparent and completely unbiased search for instabilities in a model mimicking the fundamental features of twisted bilayer graphene is lacking. In this thesis we construct a model based on microscopic symmetry considerations and the extended nature of the Wannier orbitals of the low-energy narrow bands in twisted bilayer graphene. We further perform a Hartree-Fock decoupling and minimize the free energy self-consistently through numerical implementation. We find strong signatures of interaction-induced non-trivial topological insulating states at several commensurate fillings of the low-energy bands. The signatures include emergent edge modes in the insulating gap. Furthermore, we find anisotropic spin density waves in the low-interaction regime at half and three-quarters filling of the valence bands. Both of these findings yield a preliminary agreement with experimental evidence.

Acknowledgements

First and foremost, I would like to express my utmost gratitude to my supervisor, Brian Møller Andersen, for the numerous, long, giving and educational discussions and opportunities as well as, on a personal level, for the bright mood, the encouragement, the jokes and the many laughs. It has been a true pleasure.

I would also like to thank the CMT group for the enjoyable working environment and the relaxed atmosphere. In particular, I would like to thank Hano Sura and Daniel Steffensen for the fruitful discussions needed when my own brain came to a halt.

Finally, I would like to thank my parents for putting up with me these last few months and, last but far from least, I want to thank my August Mutte Mikkelsen in part for the excellent proofreading but most of all for standing by me through thick and thin.

Contents

Chapter 1

Introduction

Electronic correlations in many-body systems have proved to be a tremendous challenge for theoretical physicists ever since the development of quantum theory in the first decades of the 20th century. The lack of a complete description is largely owed to the intrinsic complexity of quantum interactions, where the degrees of freedom increase exponentially with the number of particles. Thus, when the electronic properties of materials are significantly altered by interactions, despite decades of intense scientific research, a full theoretical characterization of the microscopic phases still proves deficient. Such materials often host numerous competing or coexisting phases, e.g. the high-T_c superconductor, anti-ferromagnetic insulator and strange metal all hosted by electron-doped cuprates [1], which further obscures the interpretation of the phase diagram.

The inadequacy of the current understanding of these interaction-induced phases of matter has led to explorations of new and exciting paths in condensed matter physics. If one could somehow enhance interaction effects in relatively simple, well-understood materials and thereby induce new interaction-driven phases, the underlying phenomenons driving these phases might emerge. A way to achieve this enhancement is to reduce the Fermi velocity of bands near the Fermi surface by engineering a slowly varying potential which traps the electrons. In 2007, Neto *et al.* predicted that applying a small relative twist of the two layers in bilayer graphene will generate a moiré superlattice which couples the low-energy Dirac fermions of the graphene monolayers through a slowly varying periodic interlayer hopping and causes a significant reduction of the Fermi velocity [2]. In the first years to follow, additional theoretical studies extended the prediction to not only reduce the Fermi velocity of the low-energy bands but also separate these flattened bands from the remaining bands at the "magic" angle [3–5]. Furthermore, the studies all proposed that the Dirac cones of the monolayer graphene spectrum would persist in twisted bilayer graphene (TBG). Due to the non-trivial topology of the graphene Dirac cones, this finding implied a possibility of topological phases in TBG. However, as the predictions had yet to be confirmed by experimental evidence, the broad scientific interest within the field of condensed matter was limited.

The attention increased dramatically with an experiment performed by Cao *et. al* in 2018 [6]. We present the main result in Fig. 1.1b where the conductance, G, is shown as a function of carrier density, n, of the predicted flat bands near the Fermi energy in "magic" angle TBG. The device is constructed by encapsulating a TBG sample with a relative twist of $\theta = 1.08^\circ$ in a hexagonal boron nitride (hBN) substrate, see Fig. 1.1a. A measurement of the conductance is then performed while varying the carrier density by sweeping the bottom gate potential, V_g. The moiré superlattice density is defined as $n_s = 4/A$, where A is the area of the superlattice unit cell. This definition follows the theoretical predictions of two distinct bands per spin and valley yielding a total capacity of eight electrons per moiré unit cell. The conductance measurement in Fig. 1.1b has several compelling features. First and foremost, it confirmed the prediction of the

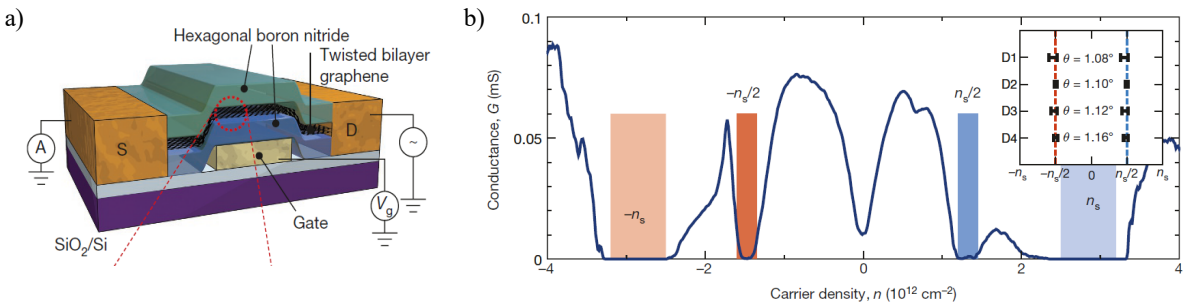

Figure 1.1: **Conductance of low-energy bands in "magic" angle TBG at** $T = 0.3\,\mathrm{K}$. **a)** Schematic of the TBG device. Twist angle is $\theta = 1.08° \pm 0.2°$. **b)** Measured conductance, G, as a function of carrier density, n. The moiré superlattice density, $n_s = 4/A = 2.7 \cdot 10^{12}\,\mathrm{cm}^{-2}$. Light shaded regions at $n = \pm n_s$ are the band separation of the low-energy narrow bands. Darker shaded regions at $n = \pm n_s/2$ are the suggested interaction-induced insulating states. Inset show the density locations of these insulating states in four different "magic" angle TBG devices. The figure is adopted from [6].

separation of narrow, low-energy bands through significant insulating gaps at $n = \pm n_s$ which can be directly related to the band gaps found in Refs. [4, 5]. It further yielded the anticipated semi-metallic behaviour at charge neutrality. More strikingly, the result suggested interaction-induced insulating behaviour at $n = \pm n_s/2$ which was *not* entailed in the single-particle band structure calculations. The result amazed the entire condensed matter community and sparked an intense exploration of the intriguing prospects of "magic" angle TBG.

In 2019, only a year after the publication of Ref. [6], new astonishing experiments were published. In Fig. 1.2 we present results from Ref. [7]. These measurements are also performed on a "magic" angle TBG sample encapsulated in a hBN substrate placed on a layer of graphite used as a bottom gate, see Fig. 1.2a,b. The present device differs from the previous device in two manners: The homogeneity of the twist angle across the sample is improved by a factor of ten and alignment with the hBN subtrate was carefully avioded. Such alignment is known to explicitly break spatial symmetries of the combined system which could possibly induce otherwise symmetry-forbidden phases in the TBG phase diagram [7, 8]. Due to these two sample improvements, the measurements presented in Ref. [7] are believed to exhibit more of the intrinsic "magic" angle TBG properties. Fig. 1.2c presents the longitudinal resistance as a function of carrier density and perpendicular magnetic field at temperature $T = 16$ mK. While the result is reminiscent of the result in Fig. 1.1b, several additional features have emerged. Resistance peaks are now evident at all commensurate fillings of the low-energy bands, that is at all fillings, ν, corresponding to an integer number of electrons in the moiré unit cell. In particular, we note the strong insulating behaviour at charge neutrality. Furthermore, superconducting characteristics in the form of field-dependent resistance dips are visible at four distinct fillings intervals between the peaks. This conjecture is verified by the temperature dependent phase diagram in Fig. 1.2d, where four superconducting domes are marked by yellow, dashed lines. The phase diagram displays a multitude of phase transitions across the low-energy bands all abscent in the single-particle band structure calculations and underline the strong influence of interactions in "magic" angle TBG.

The experiment performed in Ref. [7] was followed by a related investigation performed by the same group disclosed only eight months later in Ref. [9]. In this new experiment, Stepanov *et al.* investigated the screening effects of the phase diagram. This was done by varying the hBN thickness thereby controlling the screening from the image charges in the lower lying graphite

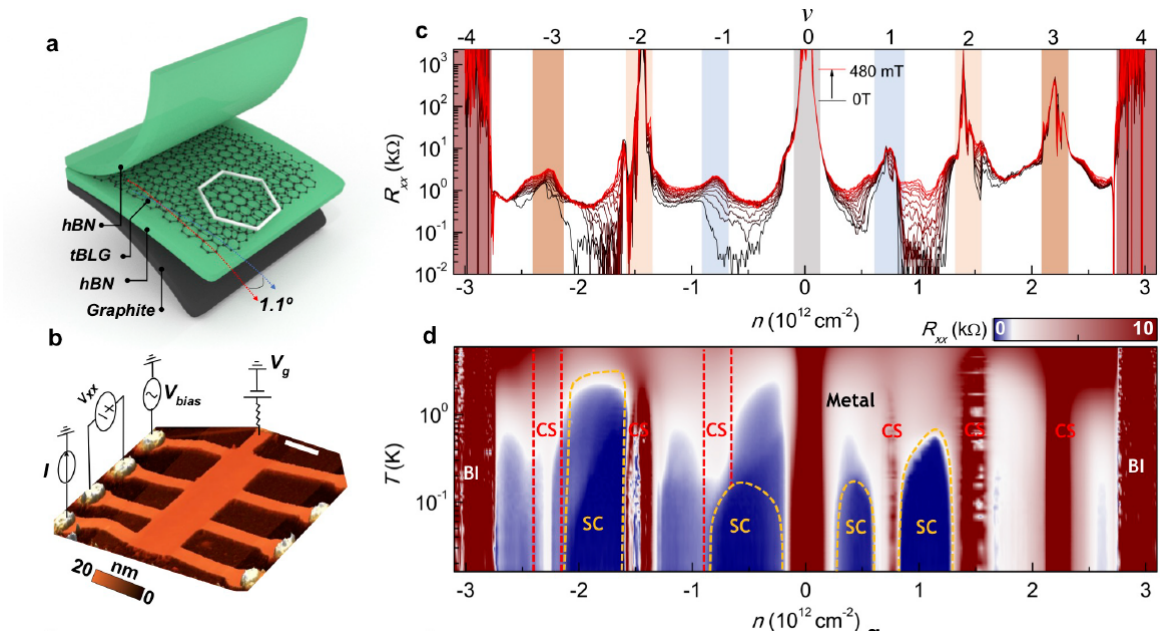

Figure 1.2: **Phase diagram of low-energy bands in "magic" angle TBG**. **a)** Schematic of the TBG device. Twist angle is $\theta = 1.10° \pm 0.02°$. **b)** Atomic force microscopy image and measurement schematic. **c)** Four-terminal longitudinal resistance as a function of carrier density at $T = 16$ mK. Line colors indicate perpendicular magnetic field strength spanning from 0 T (black line) to 480 mT (red line). Filling factor, ν, is the number of electrons per moiré unit cell relative to charge neutrality. **d)** Colour plot of longitudinal resistance, R_{xx}, as a function of temperature T, and carrier density, n. The phase diagram shows a multitude of different phases including metal, band insulator (BI), suggested interaction-induced insulating phases (CS) and superconducting domes (SC). Boundaries of the superconducting domes are defined as 50% of the normal state resistance value. The figure is adopted from [7].

layer, see Fig. 1.3a. The investigation revealed significant screening dependence as seen in Fig. 1.3b. While the result further stresses that the phases are deeply rooted in interaction effects it also provides a highly advantageous tunability of the interaction strength thereby expanding the experimental platform of TBG investigations.

The intriguing phase diagram in Fig. 1.2d and the theoretical predictions of non-trivial topology also motivated detailed investigations of "magic" angle TBG at specific commensurate fillings. In Fig. 1.4 we show captivating results from the very recent Hall experiment presented in Ref. [10]. The device was constructed similar to the previous devices with a "magic" angle TBG sample encapsulated by hBN and with a graphite bottom gate. The device is connected to four contacts enabling both longitudinal and transverse (Hall) resistance measurements. The experiment was performed at fillings close to the commensurate filling of seven electrons per moiré unit cell. Fig. 1.4B shows the longitudinal resistance, R_{xx}, and Hall resistance, R_{xy}, as a function of perdendicular magnetic field at $n = 2.37 \cdot 10^{12}\,\mathrm{cm}^{-2}$. The Hall resistance shows clear hysteresis with well-quantized magnitudes. Alongside a longitudinal resistance of $R_{xy} \sim 0$ at $B = 0$, the result suggests a quantized anomalous Hall (QAH) effect arising from a spontanous breaking of time-reversal symmetry and quantized edge states. Fig. 1.4C shows the Hall resistance as a function of magnetic field and carrier density. While a small hysteresis persists across a relative large span of carrier densities, the region of a seemingly quantized Hall resistance is very narrow. This result ties well into the phase diagrams in Figs. 1.2 and 1.3 where the multitude of phases causes very narrow filling ranges beween transitions. The result in Fig. 1.4 quickly placed TBG as one of the most promising candidates in the state-of-the-art

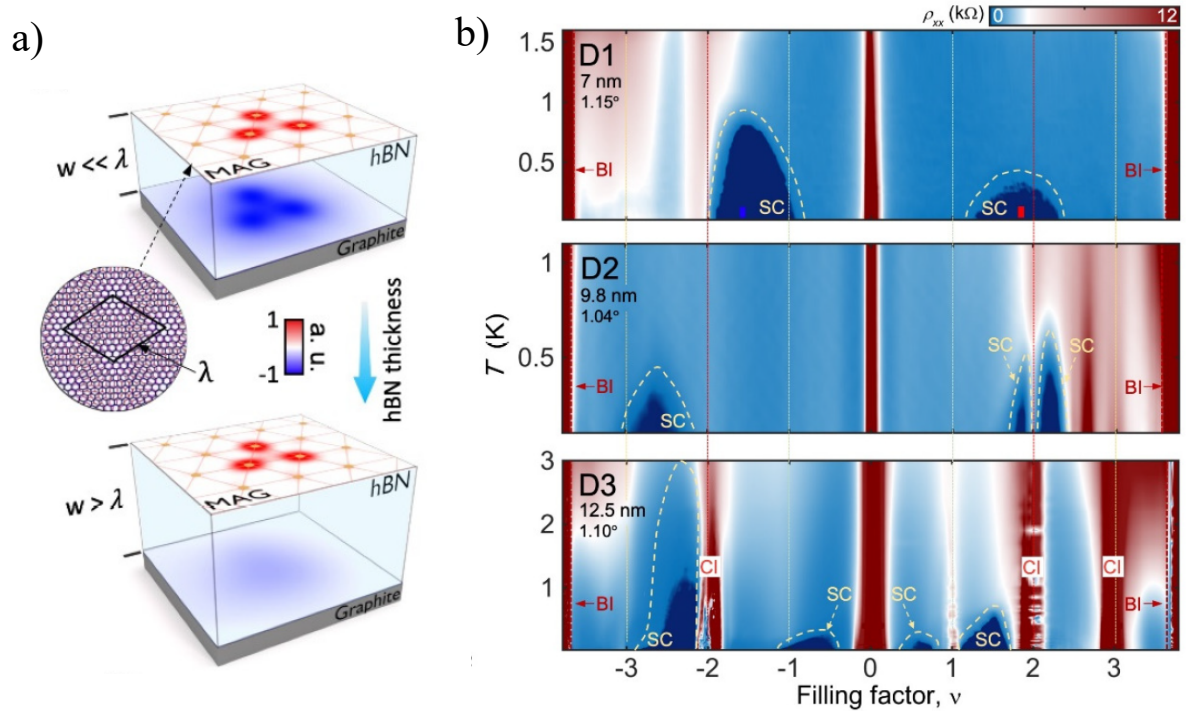

Figure 1.3: **Effect of screening in "magic" angle TBG**. **a)** Schematic of the electronic screening by graphite image charges in a TBG device as a function hBN thickness, w. λ refers to the moiré modulation length as indicated in the inset. **b)** Colour plot of the longitudinal resistivity, ρ_{xx}, as a function of temperature, T, and filling factor, ν. The measurements has been performed on three different TBG devices with hBN thickness spanning from 7 nm to 12.5 nm and twist angles from $1.04° \pm 0.02°$ to $1.15° \pm 0.02°$. The phase diagrams are highly screening dependent at all fillings away from charge neutrality. The figure is adopted from [9].

scientific search for interaction-induced topological phases.

The exciting development of "magic" angle TBG investigations on the experimental side has naturally generated an immense attention on the theoretical side and a baffling amount of publications have been released the past few years with methods spanning from renormalization group analysis to self-consistent solutions of on-site Hubbard models [11,12]. However, the theoretical investigations are complicated by two fundamental features of TBG, namely the multiple degrees of freedom (spin, valley and sublattice) alongside an extended shape of the low-energy moiré Wannier states. These two features combined opens for countless ordering possibilities where long-range effects cannot be neglected. In this thesis, we will perform a completely unbiased Hartree-Fock study of an effective model reflecting the dominating long-range interactions in TBG. The model will be solved self-consistently in a manner which allows for all possible orders and configurations that will minimize the free energy. Such unconditional solutions is, to our knowledge, unprecedented in TBG investigations. The Hartree-Fock method is, by definition, a weak-coupling approach and its applicability in the narrow band regime of "magic" angle TBG can be questioned. However, with the persistence of interaction-induced phases despite the reduction of interaction strength in Fig. 1.3, it is not unlikely that the approach can capture the mechanisms driving these phases. Furthermore, we will show that our method has a striking agreement with quantum Monte Carlo (QMC) simulations even in the intermediate-high interaction regime. This agreement serves not only as a strong justification of the Hartree-Fock

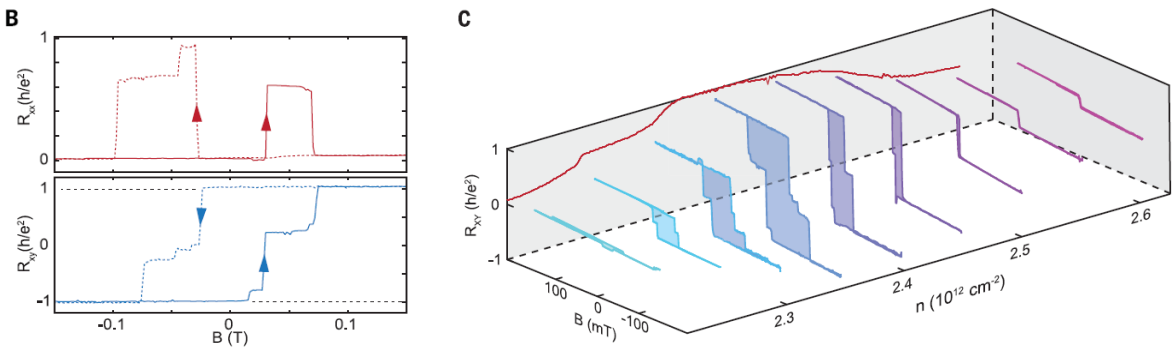

Figure 1.4: **Quantum anomalous Hall effect in TBG with $\theta = 1.15° \pm 0.01°$ at $T = 1.6\,\mathrm{K}$. B)** Longitudinal resistance, R_{xx}, and Hall resistance, R_{xy}, as a function of perpendicular magnetic field, B, at carrier density $n = 2.37 \cdot 10^{12}\,\mathrm{cm}^{-2}$. Sweep directions are indicated by arrows. Hall resistance has well-quantized magnitudes and show clear hysteresis around $B = 0$ while $R_{xx}(B = 0) \approx 0$. **C)** Hall resistance as a function of magnetic field and carrier density, n. Hysterises loops are shaded for clarity. Rear wall show the Hall resistance at $B = 0$. Hysteresis loops are evident across a broad filling region while Hall resistance is only quantized in a narrow filling region around $n = 2.37 \cdot 10^{12}\,\mathrm{cm}^{-2}$. The figure is adopted from [10].

approach but also highlight its many advantages. While the QMC simultations are indeed valid in the high interaction regime, they are inevitably limited to investigations at charge neutrality due to sign-problems. The Hartree-Fock method, on the other hand, can go beyond this filling and - in principle - allows for a full mapping of the phase diagram. The many fascinating experiments published during the recent years offer a unique opportunity of direct comparison between theoretical results and experimental evidence across the entire narrow band region. If general agreement is found, the results obtained by our transparent approach could prove to be a valuable asset in the on-going exploration of the intriguing new scientific platform of "magic" angle TBG.

The thesis in structured as follows: In Chapter 2 we remind the reader of the fundamental properties of graphene. In Chapter 3 we give a phenomenological description of the emergent moiré pattern in twisted bilayer graphene and the separation of the eight low-energy, narrow bands at the "magic" angle. In Chapter 4 we deduce an effective lattice of the moiré superstructure through symmetry analysis. We then proceed to set up a minimal tight-binding and interaction model of the effective lattice. In Chapter 5 we combine the two models and perform an unbiased Hartree-Fock decoupling of the interactions. We further perform a Fourier transformation of the model followed by a Hartree-Fock decoupling in reciprocal space. In Chapter 6 we describe the numerical set up and self-consistent solution of the decoupled model. Finally, in Chapter 7 we present and analyze the electronic phases of the effective twisted bilayer graphene model at various fillings and interaction strengths. We find signatures of non-trivial topological insulating phases at commensurate fillings corresponding to two, three and four electrons per moiré unit cell. The topological insulator at charge neutrality, that is with four electrons per moiré unit cell, is stable across all interaction strengths in the low-intermediate regime, while the insulating phases at two and three electrons per moiré unit cell are destroyed in the low interaction regime. Below these critical interaction strengths, we find multiple phases with three general features in common: They are metallic, magnetic and break one or more spatial symmetries.

Chapter 2

Graphene

In this chapter we remind the reader of some fundamental properties of monolayer graphene. We will set up a tight-binding model, present the band structure and discuss the emerging Dirac cones at high-symmetry points $\mathbf{K}$ and $\mathbf{K}'$.
Graphene is a 2D sheet of carbon atoms arranged in a honeycomb lattice, see Fig. 2.1. The in-plane $2p_x, 2p_y$ and $2s$ orbitals hybridize to form strongly bound sp^2 orbitals, which constitute the so-called σ-band. The $2p_z$ orbital alone forms the π-band. As the sp^2 orbitals are strongly bound, the σ-band has energies far from the Fermi energy. Thus, when discussing all low-energy properties of the system, it is sufficient to consider the π-band and we drop all band (orbital) indices in the proceeding calculations.

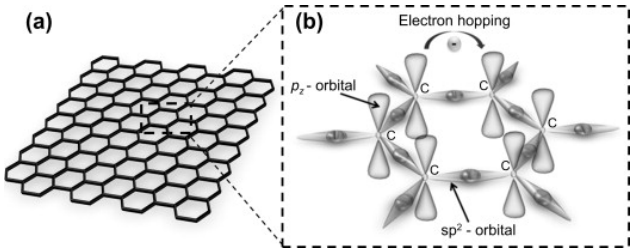

Figure 2.1: **Illustration of graphene structure. (a)** 2D graphene sheet. **(b)** Zoom-in of a single honeycomb with illustration of strongly bound sp^2 orbitals and loosely bound $2p_z$ orbitals with electron hopping indicated at the top. The figure is adopted from [13].

The honeycomb lattice consists of two identical triangular lattices with a relative shift of a lattice spacing (a_0), see Fig. 2.2. We label these two triangular sublattices as A and B. The unit cell of the honeycomb lattice thus contains two atoms, one from each triangular sublattice. The lattice vectors are denoted $\mathbf{a}_{1,2}$ and can be determined through straightforward trigonometrics to be,

$$\mathbf{a}_1 = \frac{1}{2}\begin{pmatrix}\sqrt{3}\\ 3\end{pmatrix} a_0, \qquad \mathbf{a}_2 = \frac{1}{2}\begin{pmatrix}-\sqrt{3}\\ 3\end{pmatrix} a_0. \tag{2.1}$$

We identify the corresponding reciprocal lattice vectors using that $\mathbf{K}_i \cdot \mathbf{a}_j = 2\pi\delta_{ij}$, and find

$$\mathbf{K}_1 = \frac{2\pi}{a_0}\begin{pmatrix}\frac{1}{\sqrt{3}}\\ \frac{1}{3}\end{pmatrix}, \qquad \mathbf{K}_2 = \frac{2\pi}{a_0}\begin{pmatrix}-\frac{1}{\sqrt{3}}\\ \frac{1}{3}\end{pmatrix}. \tag{2.2}$$

We set $a_0 = 1$ from now on. The first Brillouin zone (BZ) is found by connecting perpendicular bisectors of the reciprocal vectors as usual. It is depicted in Fig. 2.2.

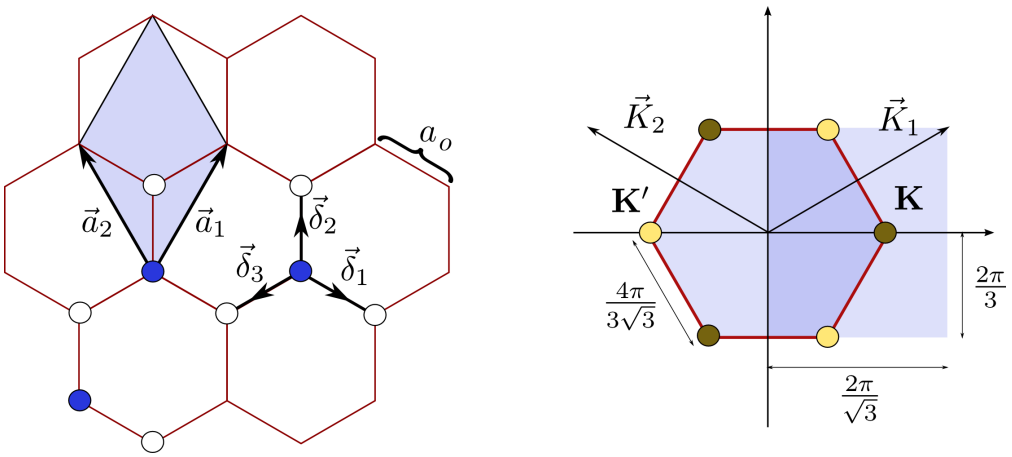

Figure 2.2: **Honeycomb lattice and Brillouin zone of graphene.** *Left:* Graphene lattice with unit vectors denoted by $\mathbf{a}_{1,2}$. Blue dots indicate A sites and white dots indicate B sites. The NN hopping vectors are denoted $\boldsymbol{\delta}_n$ with $n = 1, 2, 3$. *Right:* Brillouin zone of graphene with reciprocal vectors $\mathbf{K}_{1,2}$. Brown and yellow dots ($\mathbf{K}$ and $\mathbf{K}'$ respectively) are the Dirac points. The figure is adopted from [14].

2.1 Tight-binding model of graphene

Since we know that the electronic properties of graphene is well described by site-localized p_z orbitals, we set up a tight-binding Hamiltonian of the system,

$$H_0 = \sum_{ij} t_{ij} c_i^\dagger c_j, \tag{2.3}$$

where $c_{i\sigma}^\dagger$ ($c_{i\sigma}$) creates (annihilates) an electron at site i. t_{ij} is the hopping matrix-element connecting sites i and j. We have set $\mu = \epsilon_{p_z}$ shifting the zero-point energy to coincide with the on-site energy without loss of generality. The localization of the operators in a tight-binding model is in strong contrast to the well-known Bloch states commonly used to describe free electrons in a crystal. Bloch states are delocalized throughout the entire crystal with a periodicity reflecting the periodic potential of the underlying crystal. By setting up a tight-binding model we move away from the picture of delocalized Bloch wave functions and construct a basis of atomic orbitals. The atomic orbitals are a specific example of a localized basis set. A localized basis set can often be constructed as a superposition of Bloch states in many-body systems and the wave functions may or may not refer to the usual atomic orbitals [15]. Generally, the localized states forming a complete basis set are known as Wannier states. The Wannier states of twisted bilayer graphene will prove to be of great importance in the following chapters.

We proceed from Eq. (2.3) by restricting the model to nearest-neighbour (NN) hopping and letting $\sum_i \to \sum_{\mathbf{R}_i}$, where $\mathbf{R}_i$ is the position of the unit cell (i.e. $\mathbf{R}_i = l\mathbf{a}_1 + m\mathbf{a}_2$ for l, m integers), and get

$$H_0 = -t \sum_{\mathbf{R}_i=1}^{N} \sum_{n=1}^{3} (a_i^\dagger b_{i+\boldsymbol{\delta}_n} + b_{i+\boldsymbol{\delta}_n}^\dagger a_i), \tag{2.4}$$

where we have let $\boldsymbol{\delta}_n$ denote the NN hopping vectors and set $t_{i,i+\boldsymbol{\delta}_n} = -t$. $a^\dagger$ and $b^\dagger$ denote electron creation on A- and B-sites, respectively. The three hopping vectors are,

$$\boldsymbol{\delta}_1 = \frac{1}{2}\begin{pmatrix}\sqrt{3}\\-1\end{pmatrix}, \qquad \boldsymbol{\delta}_2 = \begin{pmatrix}0\\1\end{pmatrix}, \qquad \boldsymbol{\delta}_3 = -\frac{1}{2}\begin{pmatrix}\sqrt{3}\\1\end{pmatrix}. \tag{2.5}$$

Fourier tranformation of Eq. (2.3) yields,

$$\begin{aligned} H_0 &= -\frac{t}{N}\sum_{\mathbf{R}_i=1}^{N}\sum_{n=1}^{3}\sum_{\mathbf{k},\mathbf{k}'\in BZ}(e^{-i\mathbf{k}\mathbf{R}_i}e^{i\mathbf{k}'(\mathbf{R}_i+\boldsymbol{\delta}_n)}a_{\mathbf{k}}^{\dagger}b_{\mathbf{k}'}+e^{-i\mathbf{k}(\mathbf{R}_i+\boldsymbol{\delta}_n)}e^{i\mathbf{k}'\mathbf{R}_i}b_{\mathbf{k}}^{\dagger}a_{\mathbf{k}'}) \\ &= -t\sum_{n=1}^{3}\sum_{\mathbf{k}\in BZ}(e^{i\mathbf{k}\boldsymbol{\delta}_n}a_{\mathbf{k}}^{\dagger}b_{\mathbf{k}}+h.c.) \\ &= -t\sum_{\mathbf{k}\in BZ}\begin{pmatrix}a_{\mathbf{k}}^{\dagger} & b_{\mathbf{k}}^{\dagger}\end{pmatrix}\begin{pmatrix}0 & e^{i\mathbf{k}\boldsymbol{\delta}_1}+e^{i\mathbf{k}\boldsymbol{\delta}_2}+e^{i\mathbf{k}\boldsymbol{\delta}_3}\\ e^{-i\mathbf{k}\boldsymbol{\delta}_1}+e^{-i\mathbf{k}\boldsymbol{\delta}_2}+e^{-i\mathbf{k}\boldsymbol{\delta}_3} & 0\end{pmatrix}\begin{pmatrix}a_{\mathbf{k}}\\ b_{\mathbf{k}}\end{pmatrix} \end{aligned} \tag{2.6}$$

Letting $b_{\mathbf{k}} \to e^{i\mathbf{k}\delta_2}b_{\mathbf{k}}$, using that $\delta_2-\delta_1=\mathbf{a}_2$ and $\delta_2-\delta_3=\mathbf{a}_1$ and defining $f(\mathbf{k})=e^{-i\mathbf{k}\mathbf{a}_1}+e^{-i\mathbf{k}\mathbf{a}_2}+1$ we get,

$$H_0=\sum_{\mathbf{k}\in BZ}\begin{pmatrix}a_{\mathbf{k}}^{\dagger} & b_{\mathbf{k}}^{\dagger}\end{pmatrix}\begin{pmatrix}0 & -tf(\mathbf{k})\\ -tf^*(\mathbf{k}) & 0\end{pmatrix}\begin{pmatrix}a_{\mathbf{k}}\\ b_{\mathbf{k}}\end{pmatrix}, \tag{2.7}$$

(2.8)

with excitation energies and diagonalizing transformation,

$$E_{\mathbf{k}}=\pm t|f(\mathbf{k})|, \qquad U=\frac{1}{\sqrt{2}}\begin{pmatrix}\sqrt{\frac{f(\mathbf{k})}{f^*(\mathbf{k})}} & -\sqrt{\frac{f(\mathbf{k})}{f^*(\mathbf{k})}}\\ 1 & 1\end{pmatrix}. \tag{2.9}$$

The energy bands can be seen in Fig. 2.3. The energy landscape is strongly suppressed at six points commonly refered to as valleys. As the six points correspond to three $\mathbf{K}$ points and three $\mathbf{K}'$ points in the BZ (see Fig. 2.2), there are two inequivalent valleys. The two valleys are degenerate and graphene is said to exhibit valley degeneracy.

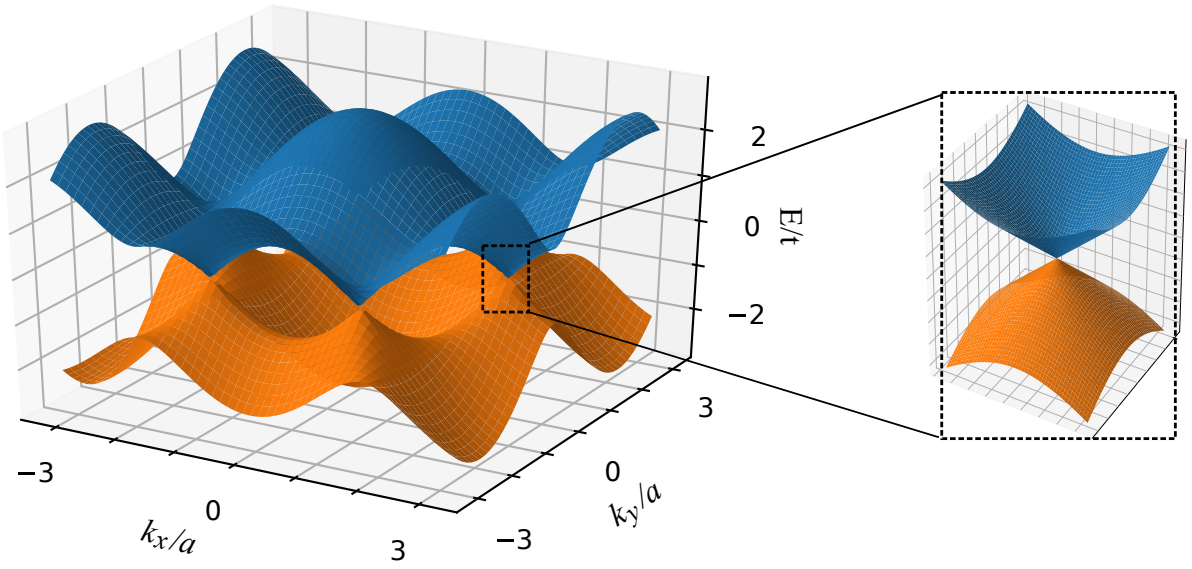

Figure 2.3: **Energy bands of monolayer graphene.** The energy landscape dips in areas surrounding high-symmetry points $\mathbf{K}$ and $\mathbf{K}'$ commonly refered to as valleys. The zoom-in displays the Dirac cone at $\mathbf{K}$.

2.2 Dirac cones and chirality

To investigate the features of the graphene valleys in the very-low-energy regime, we first identify the band touching points where $E_{\mathbf{k}}=\pm t|f(\mathbf{k})|=0$ as shown in the zoom-in in Fig. 2.3.

It can easily be verified, that these points coincide exactly with the high-symmetry points $\mathbf{K} = (4\pi/(3\sqrt{3}), 0)$ and $\mathbf{K}' = (-4\pi/(3\sqrt{3}), 0)$ marked by yellow and brown dots, respectively, in Fig. 2.2.
Expanding $f(\mathbf{k})$ to linear order in small deviations, $\mathbf{q}$, around $\mathbf{K}$, we get

$$\begin{aligned} f(\mathbf{K}+\mathbf{q}) &= e^{-i(\mathbf{K}+\mathbf{q})\mathbf{a}_1} + e^{-i(\mathbf{K}+\mathbf{q})\mathbf{a}_2} + 1 \\ &\approx e^{-i2\pi/3}[1 - i\mathbf{q}\mathbf{a}_1] + e^{i2\pi/3}[1 - i\mathbf{q}\mathbf{a}_2] + 1 \\ &= -ie^{-i2\pi/3}\frac{\sqrt{3}q_x + 3q_y}{2} + ie^{i2\pi/3}\frac{\sqrt{3}q_x - 3q_y}{2} \\ &= -\frac{3}{2}(q_x - iq_y), \end{aligned} \tag{2.10}$$

leading to,

$$\begin{aligned} H_0 &= \frac{3}{2}t\sum_{\mathbf{q}} \begin{pmatrix} a^\dagger_{\mathbf{K}+\mathbf{q}} & b^\dagger_{\mathbf{K}+\mathbf{q}} \end{pmatrix} \begin{pmatrix} 0 & q_x + iq_y \\ q_x - iq_y & 0 \end{pmatrix} \begin{pmatrix} a_{\mathbf{K}+\mathbf{q}} \\ b_{\mathbf{K}+\mathbf{q}} \end{pmatrix}, \\ &= \sum_{\mathbf{q}} \begin{pmatrix} a^\dagger_{\mathbf{K}+\mathbf{q}} & b^\dagger_{\mathbf{K}+\mathbf{q}} \end{pmatrix} \mathcal{H}_{\mathbf{K}}(\mathbf{q}) \begin{pmatrix} a_{\mathbf{K}+\mathbf{q}} \\ b_{\mathbf{K}+\mathbf{q},} \end{pmatrix} \end{aligned} \tag{2.11}$$

where $\mathcal{H}_{\mathbf{K}}(\mathbf{q}) = v_F\, \mathbf{q}\cdot\vec{s}$. $\vec{s}$ are the Pauli matrices in two dimensions, i.e. s_x and s_y, and $v_F = 3t/2$ is the Fermi velocity. Performing a similar expansion around $\mathbf{K}'$ yields $\mathcal{H}_{\mathbf{K}'}(\mathbf{q}) = -v_F\mathbf{q}\cdot\vec{s}^*$. Several important points should be noted. Firstly, from Eq. (2.11) we see the infamous linear graphene dispersion $E_{\mathbf{q}} = \pm v_F q$ which yields an effectively massless behavior of the fermions. Since massless fermions are usually described by the relativistic Dirac equation, the cone evident in the zoom-in of Fig. 2.3 is dubbed a Dirac cone and the zero-dimensional avioded crossing at each valley is known as a Dirac point. Secondly, it is evident that the sublattice degree of freedom acts as a pseudospin moving in a field of size $v_F q$ pointing along $\mathbf{q}$. For positive energies, we see that pseudospins at $\mathbf{K}$ must point along $\mathbf{q}$ (positive chirality) while pseudospins at $\mathbf{K}'$ point opposite to $\mathbf{q}$ (negative chirality). The opposite chirality of the two valleys emphasizes their distinction. To underline this feature many authors refer to them as valley $\mathbf{K}^+$ and valley $\mathbf{K}^-$. Finally, we note that the two valleys are related by time-reversal and inversion symmetries.

The very low-energy regime of graphene, i.e. the two Dirac cones, is the only relevant regime when characterizing the electronic properties of twisted bilayer graphene. To summarize, in this regime we can describe the electronic states by two two-dimensional degrees of freedom: valley (or chirality) and sublattice. That should of course be put on top of the usual spin, which has been omitted this entire chapter. In the next chapter we will give a phenomenological explanation as to why this picture is sufficient to describe all relevant features of twisted bilayer graphene.

Chapter 3

Adding a Twist

In this chapter we aim to give the reader a phenomenological understanding of the underlying mechanisms leading to separated, low-energy, narrow bands. The separation of said bands opens the possiblity of a relatively simple effective lattice model describing the emergent superstructure.

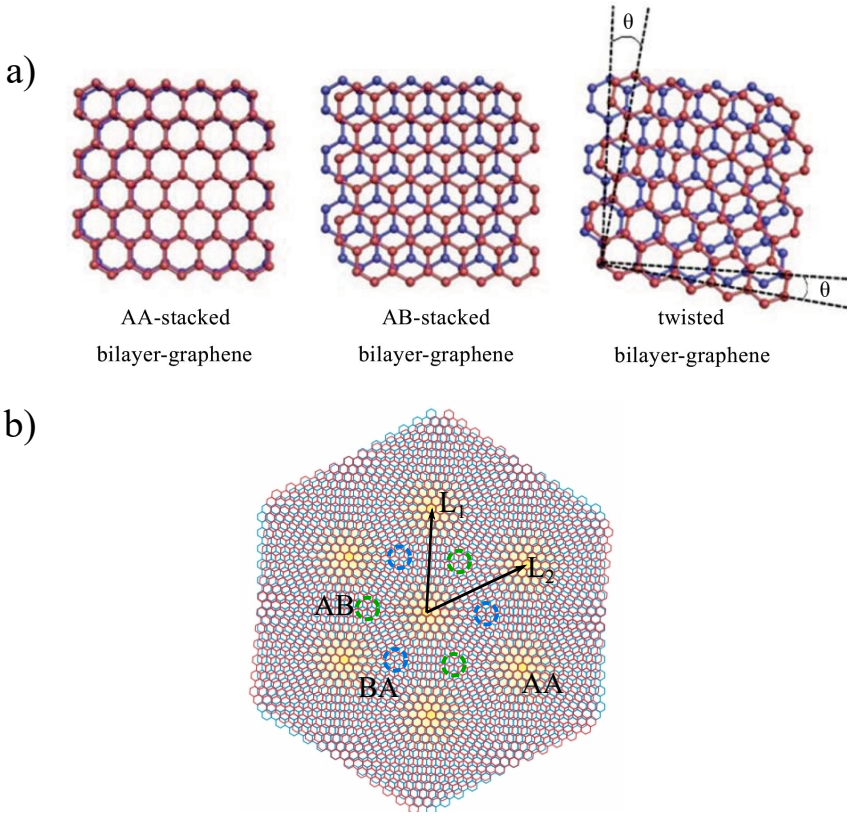

Figure 3.1: **Schematics of atomic alignment in twisted bilayer graphene. a)** Different types of bilayer stacking. Coincidence of all sites are known as AA-stacking and coincidence of A (B) sites of the top layer with B (A) sites of the bottom layers is known as AB-stacking (BA-stacking). Starting from AA-stacked bilayer graphene and applying a relative twist results in a continuous variation of the atomic alignment. The figure is adopted from [16]. **b)** Illustration of the AA-stacked regions highlighted in yellow and the AB- and BA-stacked regions marked in green and blue circles, respectively. The emering periodic pattern is known as a moiré pattern.

As discussed in the previous chapter, monolayer graphene has two distinct types of sites dubbed A- and B-sites. When stacking two layers of graphene, one option is to completely align the two honeycomb lattices, meaning that A-sites (B-sites) from one layer coincide with A-sites (B-sites) from the other layer. This stacking is known as AA-stacking, see Fig. 3.1a. Another option is to create a perfect misalignment such that A-sites (B-sites) from the top layer coincides with B-sites (A-sites) from the bottom layer resulting in so-called AB-stacking (BA-stacking). Twisted bilayer graphene (TBG) is, as the name suggests, a system in which to layers of graphene are stacked on top of each other and a relative twist angle, θ, is applied. We will assume AA-stacked bilayer graphene where the top layer is rotated by θ while the bottom layer is fixed as indicated in Fig. 3.1a. The rotation of the top layer causes a continuous varition in the atomic alignment, where regions of both stackings will appear. To visualize this more clearly, we consider the much larger system depicted in Fig. 3.1b. The AA-stacked regions are highlighted in yellow and the AB-stacked (BA-stacked) regions are marked in dashed, green (blue) circles. The emerging periodic pattern, a so-called moiré pattern, reveals a superstructure with length scales extending over several unit cells of the individual graphene layers. The moiré pattern can be divided into two superlattices: AA-regions form a triangular superlattice and AB-/BA-regions form a honeycomb superlattice similar to that of monolayer graphene. An obvious question to pose is: Which of these two lattices is the relevant effective lattice describing the low-energy electronic properties of TBG? This question will be addressed in great detail the next chapter. For the purposes of this chapter, it is sufficient to realize that both lattices have lattice vectors $\mathbf{L}_{1,2}$ as indicated in Fig. 3.1b, hence the BZs will also be identical.

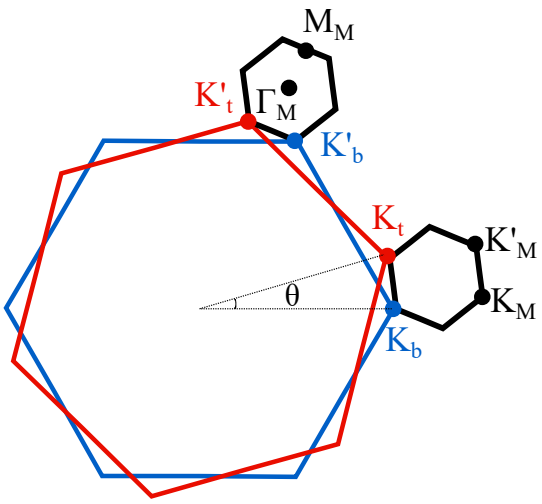

Figure 3.2: **Monolayer BZs and MBZ of twisted bilayer graphene.** Red (blue) hexagon is the monolayer BZ of top (bottom) monolayer graphene. Applying a rotation of θ to the top layer results in a moiré pattern with corresponding MBZ (black hexagons) with high-symmetry points as marked. $\mathbf{K}'_t$ and $\mathbf{K}_b$ and folded into $\mathbf{K}_M$ while $\mathbf{K}_t$ and $\mathbf{K}'_b$ are folded to $\mathbf{K}'_M$. This folding ensures TRS preservation.

The twist angle in Fig. 3.1 is relatively large for clarity, however, in usual TBG samples $\theta \sim 1^\circ$ (for reasons which will become clear shortly). Such small twist angles give rise to an extremely large modulation wave length of the moiré pattern spanning up to hundreds of carbon atoms. Generally, $\mathbf{L}_{1,2} \sim \mathcal{O}(a/\theta)$, where a is the length of the monolayer lattice vectors [6,17]. As a consequence, the BZs of monolayer graphene are folded numerous times to obtain the moiré BZ which is thus refered to as the mini BZ (MBZ). An intructive way to visualize the MBZ and directly determine the folding of the original monolayer high-symmetry points can be seen in Fig. 3.2, where red (blue) indicates the top (bottom) graphene monolayer. Two MBZs are shown in black with high-symmetry points as marked. From Fig. 3.2 it is clear that $\mathbf{K}_b$ and $\mathbf{K}'_t$ fold into $\mathbf{K}_M$ while $\mathbf{K}_t$ and $\mathbf{K}'_b$ fold into $\mathbf{K}'_M$. This folding of the Dirac points can also be understood by considering time-reversal symmetry (TRS). Since $\mathcal{T}\mathbf{K}_{t,b} = \mathbf{K}'_{t,b}$, the two Dirac points of the monolayers cannot fold to the same Dirac point in the MBZ while preserving $\mathcal{T}\mathbf{K}_M = -\mathbf{K}_M = \mathbf{K}'_M$.

Additionally, when $\theta \sim 1^\circ$ we have that $|\mathbf{K}_t - \mathbf{K}_b| << |\mathbf{K}'_t - \mathbf{K}_b|$. Since the moiré potential in this case is slowly varying, the low-energy Bloch states will have equally long wave length periodicity making small momentum scattering processes dominating. This effect ensures that

although $\mathbf{K}_t'$ and $\mathbf{K}_b$ are folded to the same Dirac point, the direct coupling of the two is highly suppressed [17]. The two decoupled Dirac cones at $\mathbf{K}_M$ act as an additional degree of freedom effectively doubling the number of bands. The decoupling results in an internal charge conservation within each valley which is represented by an overall $U_v(1)$ symmetry.

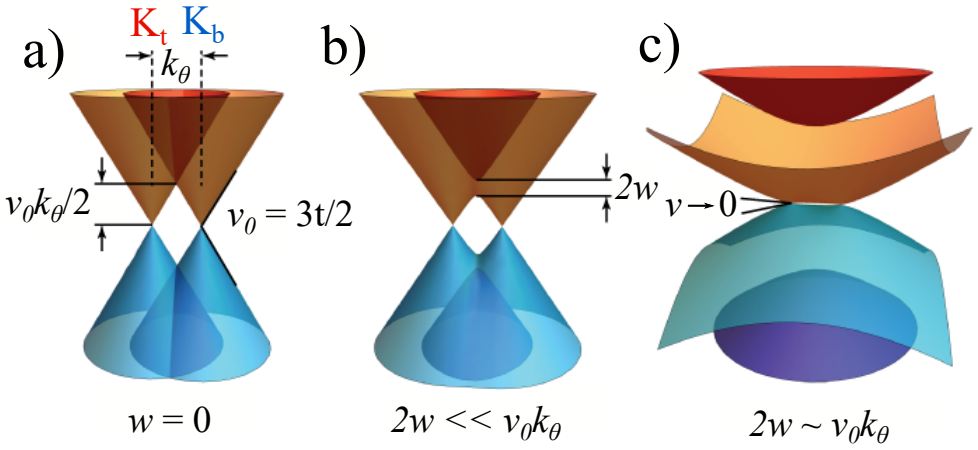

Figure 3.3: **Schematic of intersecting Dirac cones.** The two Dirac cones at $\mathbf{K}_t$ and $\mathbf{K}_b$ in the top and bottom monolayers, respectively. **a)** Interlayer tunneling $w = 0$. The slope of the cones are given by v_F of monolayer graphene derived in Chapter 2. Momentum separation of the two cones are given by k_θ and easily tuned by adjusting the twist angle. Energy at intersection is given by $v_0 k_\theta/2$ due to the linearity of the dispersion. **b)** Hybridization and resulting band separation ($\Delta = 2w$) at large twist angles when $2w << v_0 k_\theta$. **c)** Band separation for $\theta \sim 1°$ where $2w \sim v_0 k_\theta$. In this limit the band width $W = v_0 k_\theta - 2w \to 0$ and Δ/W increases.

Having established the emergent moiré pattern and corresponding MBZ, we now move on to describe the separation of the low-energy bands. To understand how this separation comes about, we focus on the two monolayer Dirac cones $\mathbf{K}_t$ and $\mathbf{K}_b$ in the small θ limit and consider the interlayer tunneling, w. Fig. 3.3a depicts the two intersecting Dirac cones from the top and bottom monolayer without interlayer tunneling. The electron velocity is given by the Fermi velocity derived in Chapter 2, $v_0 = v_F = 3t/2$, and the momentum separation of the cones due to the rotation of the top layer is given by k_θ. As the dispersion is linear, the energy at the point of intersection is given by $v_0 k_\theta/2$. In Fig. 3.3b we tune k_θ such that $2w << v_0 k_\theta$. The two cones hybridize to form low-energy bands connecting $\mathbf{K}_t$ and $\mathbf{K}_b$ separated by $\Delta = 2w$ from higher lying bands. Finally in Fig. 3.3c we illustrate the case for $\theta \sim 1°$ where $2w \sim v_0 k_\theta$. Here the band width of the low-energy bands $W = v_0 k_\theta - 2w \to 0$ (i.e. $v \to 0$) and Δ/W increases correspondingly. TBG with a twist angle in this regime in dubbed "magic" angle TBG, due to the astonishing phase diagrams discussed in Chapter 1. While the relatively simple idea shown in Fig. 3.3 is sufficient to understand the prominent mechanisms behind the separation of narrow bands, it does not clarify the "magic" entailed in "magic" angle TBG. As with most other "magical" phenomena, there is - unfortunately - nothing magical about it.

To conclude this chapter, we present the TBG band structure at various twist angles obtained by Nam & Kosino in Ref. [18], see Fig. 3.4. The results are computed by allowing for **r**-dependent, relative atomic shifts between the two monolayers. They optimize the microscopic atomic structure by minimizing the total energy of the combined system and find significant atomic shifts surrounding the AA-regions for twist angles $< 1.5°$. The relaxation of the microscopic lattices has the overall impact of enhancing the AB-/BA-regions at the expense of the AA-regions in the moiré structure. Applying a combined inter- and intralayer tight-binding model to the relaxed

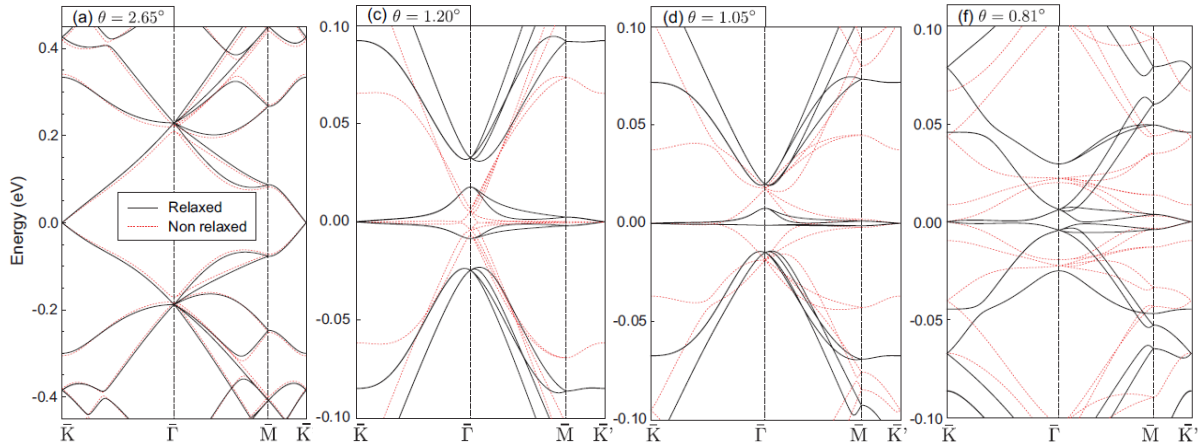

Figure 3.4: **Band structure of TBG at various twist angles.** Solid, black lines are band structures of microscopically relaxed atomic structures and dotted, red lines are the non-relaxed band structures. The structures in (c) and (d) have clearly separated narrow bands while the stuctures in (a) and (f) do not. This figure has been adopted from [18].

microscopic structure yields the results in Fig. 3.4. For $\theta = 2.65°$, Fig. 3.4a, it is evident that relaxation effects are insignificant and neither the relaxed nor the non-relaxed band struture have separated, low-energy bands. By decreasing θ the relaxation effects increase and band gaps develop while the Fermi velocity of the low-energy bands is reduced, Fig. 3.4(c,d). These twist angles ($\theta \sim 1.0° - 1.5°$) defines the regime of "magic" angle TBG. Interestingly, while relaxation effects proceed to be significant with a further decrease of θ, the band gaps close and the low-energy bands can no longer be described separately. We have thus moved away from the "magic" angle regime.
Before we proceed to set up an effective low-energy model of the separated bands in the "magic" angle regime depicted in Fig. 3.4(c,d), several important features of the bands should be noted. First and foremost, Dirac points at $\mathbf{K}$ and $\mathbf{K}'$ are evident. Secondly, the bands split along $\mathbf{\Gamma} - \mathbf{M}$. From this we deduce, that the bands must be doubly degenerate along the other symmetry paths, including a two-fold degeneracy of the energies at both $\mathbf{\Gamma}$ and $\mathbf{M}$. Finally, the particle-hole symmetry is broken. We also note that all band structures of Fig. 3.4 are spin degenerate protected by an internal $SU(2)$ symmetry in each decoupled valley. Including spin, we thus have a total of eight bands reflecting the layer, valley and spin degrees of freedom.

In the remainder of this thesis, we will develop and solve an effective model of the separated, low-energy, narrow bands. We thus focus at the "magic" angle regime, and omit this (somewhat bewildering) term in all subsequent chapters.

Chapter 4

Symmetries and Effective Model

In this chapter we will dive into the symmetry considerations of TBG and construct an effective model of the moiré superlattice. In the first section we will give an introduction to point group protected degeneracies from a quantum mechanical perspective. In Section 4.2 we will perform a symmetry analysis of the high-symmetry points of TBG and use this to deduce the effective Wannier orbitals. In Section 4.3 we discuss the peculiar, extended shape of the Wannier orbitals leading to significant long-range effects. Finally we use this property to set up a tight-binding model describing the separated, low-energy, narrow bands of TBG (Section 4.4) and an effective interaction model including on-site as well as dominating long-range interactions (Section 4.5). Since we already know from the previous chapter that the bare bands are spin degenerate, we only include spin when including interactions.

4.1 Introduction to point group protected degeneracies

We will begin this chapter with an introduction of the general idea behind a symmetry analysis. Consider a system described by a Hamiltonian, H, which exhibits a number of rotational and reflection symmetries. Together these symmetries constitute the elements of a point group, G.[1] All elements in G will leave the Hamiltonian invariant, hence if $S \in G$ we have $[\hat{S}, H] = 0$, where $\hat{S}$ is an operator representing the symmetry S. From this it directly follows that

$$H\hat{S}\left|\psi_n\right\rangle = \hat{S}H\left|\psi_n\right\rangle = \hat{S}E_n\left|\psi_n\right\rangle = E_n(\hat{S}\left|\psi_n\right\rangle), \tag{4.1}$$

where we have assumed $|\psi_n\rangle$ to be an eigenfunction of H with eigenvalue E_n. Thus $\hat{S}|\psi_n\rangle$ is also an eigenfunction of H with eigenvalue E_n, which leaves us with two options. The first option is that $\hat{S}|\psi_n\rangle \to |\psi_n\rangle$ (up to a phase), and we say that $|\psi_n\rangle$ transforms as a singlet under S. The other option is that $\hat{S}|\psi_n\rangle \to |\psi_m\rangle \neq |\psi_n\rangle$ and we must have that $|\psi_n\rangle$ and $|\psi_m\rangle$ are degenerate under S. Similarly, for a different symmetry operation $P \in G$ we have that $\hat{P}\hat{S}|\psi_n\rangle$ is also an eigenfunction of H with energy E_n, where $\hat{P}(\hat{S}|\psi_n\rangle) \to |\psi_k\rangle$ and either $|\psi_n\rangle = |\psi_k\rangle$ or $|\psi_n\rangle \neq |\psi_k\rangle$. Thus we can establish the symmetry protected degeneracies of the eigenfunctions by determining their transformations under all symmetry operations in G. To do so we must determine how the set of operators in G can be represented. Representation theory itself is an entire branch of mathematics and we will by no means dive into the details of this. For the purposes of this thesis, it is sufficient to use the common matrix representation within quantum mechanics, namely $\langle\psi_i|\hat{S}|\psi_j\rangle = \mathcal{D}(S)_{ij}$, where $\mathcal{D}(S)_{ij}$ is the entry on the i'th row and j'th coloumn. Computing entries for the complete set of eigenfunctions, $\{|\psi_l\rangle\}$, we obtain an $l \times l$ dimensional matrix representation of the symmetry S.

[1] The term point group very neatly refers to the fact that all symmetries keep at least one point fixed.

To recognize the potential of this type of representation, we will consider a specific example with a system described by a 4×4 dimensional Hamiltonian, where we only know that H obeys the symmetries represented by $\hat{S}$ and $\hat{P}$, i.e. $[H, \hat{S}] = [H, \hat{P}] = 0$. Since H has dimension 4, we must have four eigenstates. We now pick a set of four states, e.g. four orbitals localized at four different lattice sites, and investigate their transformation under S, that is compute $\mathcal{D}(S)$. We get,

$$\mathcal{D}(S) = \begin{pmatrix} \boldsymbol{\alpha} & 0 & 0 & 0 \\ 0 & \beta & 0 & 0 \\ 0 & 0 & 0 & \gamma \\ 0 & 0 & \delta & 0 \end{pmatrix},$$

where $|\boldsymbol{\alpha}|, |\beta|, |\gamma|, |\delta| = 1$. From Eq. (4.1) we then naively assume that $|\psi_1\rangle, |\psi_2\rangle$ are singlets and $(|\psi_3\rangle, |\psi_4\rangle)$ form a doublet (i.e. a two-fold degenerate set). We proceed to compute $\mathcal{D}(P)$ and consider two different scenarios. In the first scenario,

$$\mathcal{D}(P) = \begin{pmatrix} \boldsymbol{\alpha}' & 0 & 0 & 0 \\ 0 & \beta' & 0 & 0 \\ 0 & 0 & 0 & \gamma' \\ 0 & 0 & \delta' & 0 \end{pmatrix},$$

where again $|\boldsymbol{\alpha}'|, |\beta'|, |\gamma'|, |\delta'| = 1$. In this scenario, the four states transform as two singlets and a doublet under both S and P. However, we note that $\mathcal{D}(S)$ and $\mathcal{D}(P)$ can be simultaneously diagonalized by the same unitary transformation, U, where $\mathcal{D}'(P) = U\mathcal{D}(P)U^{-1}$ and $\mathcal{D}'(S) = U\mathcal{D}(S)U^{-1}$ are now diagonal[2]. As unitary transformations cannot alter the system properties, $\mathcal{D}'(S)$ and $\mathcal{D}'(P)$ must be equally valid representations expressed in a new basis $(|\psi_1\rangle, |\psi_2\rangle, |\psi_3'\rangle, |\psi_4'\rangle)$, where $|\psi_{3,4}'\rangle$ are linear superpositions of $|\psi_{3,4}\rangle$. In this basis, all four states will transform as singlets and we can have four distinct eigenenergies of $H' = UHU^{-1}$. From the symmetry analysis we thus conclude that, neglecting the possibility of accidental degeneracies, the original set of states cannot be the eigenstates of the system.

In the second scenario, we find that

$$\mathcal{D}(P) = \begin{pmatrix} \boldsymbol{\alpha}' & 0 & 0 & 0 \\ 0 & \beta' & 0 & 0 \\ 0 & 0 & \gamma' & 0 \\ 0 & 0 & 0 & \delta' \end{pmatrix}.$$

In this case, we cannot apply a unitary transformation that diagonalizes both $\mathcal{D}(P)$ and $\mathcal{D}(S)$, hence $|\psi_{3,4}\rangle$ must be degenerate and transform as a doublet. We conclude that H can at most have three eigenvalues corresponding to two singlet states $|\psi_{1,2}\rangle$ and a doublet $(|\psi_3\rangle, |\psi_4\rangle)$ and $\{|\psi_l\rangle\}$ (l = 1,2,3,4) are really the eigenstates of the system exihibiting the symmetry protected degeneracies.

In physical systems we will often encounter much larger dimensionality as well as numerous elements in the point groups. If one were to perform all the steps of the analysis above for every system, the method quickly loses its appeal. However, if we rewind slightly and consider at a very general level what was used to perform the analysis, one finds a very powerful tool hiding between the lines. Our naive assumption from only considering $\mathcal{D}(S)$ was discarded in the first scenario solely due to the fact that we could *simultaneously* diagonalize $\mathcal{D}(S)$ and $\mathcal{D}(P)$. Having done so, we found two new representations, $\mathcal{D}'(S)$ and $\mathcal{D}'(P)$ only consisting of

[2]For the sake of argument, we ignore the fact that PS must also be an element in the point group and since $\mathcal{D}(PS)$ is already diagonal, it will not be diagonalized by the same transformation.

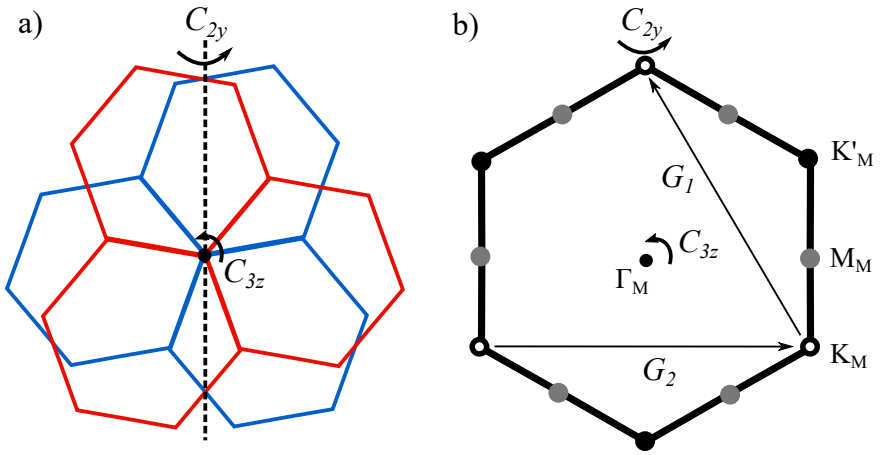

Figure 4.1: **Rotation of bilayer graphene lattices and MBZ of TBG. a)** The microscopic graphene monolayers with $\theta = 40°$. Top (bottom) monolayer is red (blue). Lattice sites are located at each hexagon corner but removed here for clarity. When the rotation center coincides with the lattice sites of the two graphene layers, the resulting rotation symmetries of the system are C_{2y} and C_{3z} as indicated. Together these symmetries places TBG in point group D_3. **b)** MBZ of TBG with reciprocal lattice vectors $\mathbf{G}_{1,2}$ and high-symmtry points as indicated.

four one-dimensional blocks along the diagonal. Each block then corresponded to a singlet. In the second scenario we could *not* simultaneously diagonalize $\mathcal{D}(S)$ and $\mathcal{D}(P)$, thus the entire set of representations can only be described by two one-dimensional blocks (two singlets) and a two-dimensional block (a doublet). The blocks on the diagonal are exactly what is known as the *irreducible* representations of a point group, which is defined as a representation of the group where no unitary transformation can simultaneously diagonalize all elements. Each irreducible representation thus corresponds to a set of degenerate eigenstates and the degeneracy level is defined alone from the dimensionalty of the irreducible representation. This dimensionality is linked to the underlying physics of a given point group and is thus uniquely defined. Consequently, by determining the point group of a given system, we can immediately deduce the degeneracy of the energy levels without knowing the energies, the Hamiltonian or the wave functions. This is one of the very powerful tools of group theory.

4.2 Point group symmetry and effective lattice of twisted bilayer graphene

In this section the aim is to set up an effective moiré lattice with localized Wannier orbitals that reproduces the symmetry transformations of the low-energy Bloch states forming the bare bands of TBG. To do so, we first determine the transformations at high-symmetry points of the MBZ either directly from the relaxed band structure in Fig. 3.4 or through symmetry analysis of the low-energy monolayer states constituting the separated narrow bands. We then search for Wannier orbitals with symmetries and centers (i.e. lattice sites) which reflect these transformations in a faithful manner. Once these two features of the Wannier orbitals have been established, we can directly set up an effective tight-binding model of TBG, which will be presented in Section 4.4. The findings presented in this section follow the work performed in Ref. [19].

First and foremost, we must determine the point group of TBG. To do so, we consider two graphene layers with a relative rotation. The rotation center is chosen to be an AA-stacked

site, see Fig. 4.1a. Two rotational symmetries are present: a two-fold rotation about the y-axis, C_{2y}, and a three-fold rotation about the z-axis, C_{3z}. Importantly, C_{2y} is not equivalent to a mirror symmetry along $\hat{y}$, since it also exchanges the two layers. Together these two symmetries constitute the D_3 point group. The irreducible representations of D_3 are two one-dimensional represention (A_1, A_2) and a two-dimensional representation (E).[3] From the previous section we thus know that $[H, \hat{O}] = 0$, where $\hat{O}$ represents the elements of D_3. We can write the kinetic Hamiltonian of the system, H, as a sum of single-particle Hamiltonians, $\mathcal{H}_{\mathbf{k}}$, for all $\mathbf{k} \in MBZ$. While H must commute with all elements of D_3, this is rarely the case for the individual $\mathcal{H}_{\mathbf{k}}$ since a rotation of a point $\mathbf{k}$ will usually take it to distinct point $\mathbf{k}'$ in the MBZ. However, if we focus our attention on the high-symmetry points, where a subgroup $S \in D_3$ will take $\mathbf{k}$ into itself, the states can be classified by the irreducible representations of S. As previously mentioned, we have four distinct high-symmetry points in the MBZ of TBG: $\mathbf{\Gamma}_M$, $\mathbf{K}_M$, $\mathbf{K}'_M$ and $\mathbf{M}_M$. The $\mathbf{\Gamma}_M$-point will naturally fall into the full group D_3. From inspection of Fig. 4.1b, we see both rotations of D_3 will take $\mathbf{K}_M$ and $\mathbf{K}'_M$ to identical points related to the original ones by a reciprocal vector, thus these points also fall into the full group D_3. Finally we note that only C_{2y} will take $\mathbf{M}_M$ to an identical point, hence $\mathbf{M}_M$ falls into the subgroup (or little group) $C_2 \in D_3$.

4.2.1 $\mathbf{\Gamma}_M$-point

As we have two graphene layers and an additional valley degree of freedom in TBG, we must have at least four distinct states at $\mathbf{\Gamma}_M$. Furthermore, since $\mathbf{\Gamma}_M$ falls into the D_3 group, we know that the (point group symmetry protected) degeneracy of each energy can at most be two-fold, meaning that we have at least two different energies. This is in good agreement with the band structure results presented in Fig. 3.4, where we have two separate energies at $\mathbf{\Gamma}_M$. Both energies are two-fold degenerate and the degeneracy is split along the $\mathbf{\Gamma}_M\mathbf{M}_M$-line. We thus look for states at $\mathbf{\Gamma}_M$ transforming as doublets under D_3.

The transformation of a Bloch state under D_3 can be directly classified from the eigenvalue under C_{3z}, i.e. $(1, \omega, \omega^2)$ where $\omega = e^{-2i\pi/3}$. From a completely group theoretical approach this can be seen by computing the basis functions (or wave functions) corresponding to the D_3 point group, where one finds that states with C_{3z} eigenvalue 1 transforms as singlets and states with ω, ω^2 transform as a doublet (see e.g. Chapter 4 of Ref. [20]). The eigenvalues have a direct correspondence to angular momentum $L_z = 0, \pm 1$, where $C_{3z} |\psi_n\rangle = e^{-2i\pi L_z/3} |\psi_n\rangle$. Thus, from a physical perspective, the states with $L_z = \pm 1$ should indeed form a doublet to preserve time-reversal symmetry. Furthermore, we can safely restrict our effective Wannier orbitals to s- or p-orbitals, since the angular momentum is defined modulo 3, thus all higher order orbitals will transform as either s or p (take e.g. a d-orbital with $L_z = 2$, then $e^{-2i\pi L_z/3} = e^{-4i\pi/3} = e^{2i\pi/3}$, which is identical to a transformation of a p-orbital with $L_z = +1$). We write a general Bloch state as,

$$c_{\mathbf{k},\tau} = \sum_i e^{i\mathbf{k}\mathbf{R}_i} c_{i,\tau}, \tag{4.2}$$

where $c_{i,\tau}$ is the (yet to be determined) Wannier orbital at site i with orbital angular momentum $L_z^{orb} = -\tau$. The reason for this rather counter-intuitive notation will become clear in the

[3] In the case of D_3 this a quite trivially seen from the theorem $\sum_i l_i^2 = h$, where h is the order of D_3 (that is the number of elements in D_3) and l_i is the dimension of the i'th irreducible representation. We have 6 elements in D_3: indentity, three two-fold rotations (along $\hat{y}$ and the two axes related to y by three-fold rotation) and two three-fold rotations (clockwise and counter-clockwise rotation). Thus $h = 6$. Furthermore the number of irreducible representations are equal to the number of classes: identity, C_2 and C_3 rotations. Combining this we get $l_1^2 + l_2^2 + l_3^2 = 6$, which can only be true if we have two one-dimensional representations and one two-dimensional.

subsequent sections. We have dropped the overall normalization, as it will not affect the transformation of the states. From Eq. (4.2) we see that the transformation of $c_{\mathbf{k},\tau}$ under C_3 will depend on the orbital angular momentum defined by τ, as well as the Bloch wave phase factor, $e^{i\mathbf{k}\mathbf{R}_i}$, thus $L_z = L_z^{B.w.} + L_z^{orb}$. In the present case $e^{i\mathbf{\Gamma}_M\mathbf{R}_i} = 1$ for all $\mathbf{R}_i$, hence $L_z^{B.w.} = 0$. It directly follows, that we must have $L_z^{orb} = \pm 1$ to form doublets at $\mathbf{\Gamma}_M$ and reproduce the band structure in Fig. 3.4. As we only consider s- and p-orbitals, this leads us to effective Wannier orbitals of type $p_x \pm ip_y$. C_{2y} will take $p_x \pm ip_y \to -(p_x \mp ip_y)$ and we have that

$$C_{2y}C_{3z}c_{\mathbf{\Gamma}_M,\tau} = \sum_i C_{2y}C_{3z}c_{i,\tau} = \sum_{i'} C_{2y}e^{2i\pi\tau/3}c_{i',\tau} = \sum_{i''} -e^{2i\pi(-\tau)/3}c_{i'',-\tau} = -e^{-2i\pi\tau/3}c_{\mathbf{\Gamma}_M,-\tau},$$

where $C_{3z}\mathbf{R}_i = \mathbf{R}_{i'}$, $C_{2y}\mathbf{R}_{i'} = \mathbf{R}_{i''}$ and we recall that $L_z^{orb} = -\tau$. We see that Bloch states labelled by $\tau = \pm 1$ do indeed transform as a doublet under D_3. While this result is sufficient to establish the overall transformation of the Bloch states at $\mathbf{\Gamma}_M$, we have yet to determine some addtional degree of freedom resulting in two separate doublets as seen in Fig. 3.4.

4.2.2 $\mathbf{K}_M$-point

Having established the orbital angular momentum of the Wannier orbitals, $L_z^{orb} = \pm 1$, we will now perform a symmetry analysis at $\mathbf{K}_M$ to establish the centers of the Wannier orbitals through $L_z^{B.w.}(\mathbf{K}_M)$. Before doing so, we identify the Bloch state transformations at $\mathbf{K}_M$ which must be obeyed by the effective model.

The group of the $\mathbf{K}_M$-point and $\mathbf{K}'_M$-point is D_3. Since the two points are related through time-reversal, it is sufficient to consider one, here we focus on $\mathbf{K}_M$. From the results in Fig. 3.4 we can identify four degenerate zero-energy states at $\mathbf{K}_M$. However, we know that the D_3 group can not protect four-fold degeneracy, thus we determine the transformation of the states through microscopic considerations. As previously mentioned, two Dirac points of the graphene monolayers fold onto $\mathbf{K}_M$ and we write $\mathbf{K}_M = \mathbf{K}'_t + \mathbf{K}_b$. From the analysis of monolayer graphene in Chapter 2, we know that the Bloch states at $\mathbf{K}_{t,b}$ and $\mathbf{K}'_{t,b}$ are zero-energy states with off-diagional elements $f(\mathbf{k}) = e^{-i\mathbf{k}\mathbf{a}_1} + e^{-i\mathbf{k}\mathbf{a}_2} + 1 = 0$, thus at these points there will be no sublattice mixing. Consequently, we have two zero-energy eigenstates at each Dirac point of monolayer graphene, where each state only has weight on one sublattice. As $\mathbf{K}_M = \mathbf{K}'_t + \mathbf{K}_b$ we will have four states at $\mathbf{K}_M$ which we label as a^t, b^t, a^b, b^b, where a (b) lives on sublattice A (B) and superscript indicates the layer. The transformation of the Bloch states at $\mathbf{K}_M$ must be preserved in the effective model. Thus by determining the transformation of the four monolayer states, we also determine the transformation of the effective Wannier orbitals. Since the monolayer Bloch states are constructed from p_z orbitals, the total angular momentum is given solely by the Bloch wave contribution. The Bloch wave contribution depends on the position of the A- and B-sites with respect to the rotation center. As the rotation center coincides with an AA-stacked site, we can use the analysis of monolayer graphene from Chapter 2, where the positions of the A-sites are given by $\mathbf{r}_a = (n\mathbf{a}_1 + m\mathbf{a}_2)$ with $\mathbf{a}_{1,2} = (\pm\sqrt{3}/2, 3/2)$ and the postions of the B-sites are given by $\mathbf{r}_b = (n\mathbf{a}_1 + m\mathbf{a}_2 + \boldsymbol{\delta}_2)$ with $\boldsymbol{\delta}_2 = (0,1)^T$. We can neglect the relative rotation of the two layers, since it merely acts as a rotation of the entire system in the monolayered subsystems. From Chapter 2 we also have that $\mathbf{K} = (4\pi/(3\sqrt{3}), 0)$ and $\mathbf{K}' = -\mathbf{K} = (-4\pi/(3\sqrt{3}), 0)$. The Bloch wave phase factors are $e^{\pm i\mathbf{K}\mathbf{r}_{a,b}}$, and the total anglular momentum of the state is given by the additional phase arising from a three-fold rotation of $\mathbf{r}_{a,b}$. Here we have immediately infered that $\pm\mathbf{K} \to \pm\mathbf{K}$ under C_{3z}. Inserting values, we find that

$$\pm\mathbf{K}\mathbf{r}_a = \pm\frac{2\pi(n-m)}{3} \xrightarrow{C_{3z}} \pm\mathbf{K}(nC_{3z}\mathbf{a}_1 + mC_{3z}\mathbf{a}_2) = \pm\mathbf{K}[n(-\sqrt{3},0)^T + m(-\sqrt{3}/2, -3/2)^T]$$

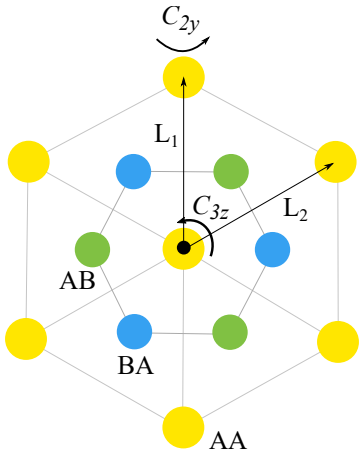

Figure 4.2: **Effective lattice candidates of TBG.** Triangular lattice (yellow dots) coincides with AA-regions of the moiré structure. Honeycomb lattice (gree/blue dots) coincides with AB/BA-regions of the moiré structure. Both lattices have lattice vectors $\mathbf{L}_{1,2}$ spanning the unit cell. The triangular lattice has a single site in each unit cell (AA) and the honeycomb lattice has two sites (AB/BA) in each unit cell.

$$= \mp\Big(\frac{4\pi n}{3} + \frac{2\pi m}{3}\Big) \xrightarrow{\text{mod } 3} \pm\frac{2\pi(n-m)}{3}, \tag{4.3}$$

thus the two monolayer Bloch states living at the A-sublattices, $a^{t,b}$, both have $L_z = 0$. This result is very reasonable from a physical perspective, since any state with finite angular momentum must vanish at the rotation center and $a^{t,b}$ both have weight at the AA-site coinciding with the rotation center. However, $b^{t,b}$ will not have weight at the rotation center, and the states can carry finite angular momentum. Since we have already established that a C_{3z} rotation of $\mathbf{a}_{1,2}$ will not add any additional phase, we can limit the analysis of $b^{t,b}$ to the effect of C_{3z} on $\boldsymbol{\delta}_2$. Here we find,

$$\pm\mathbf{K}\boldsymbol{\delta}_2 = 0 \xrightarrow{C_{3z}} \pm\mathbf{K}C_{3z}\boldsymbol{\delta}_2 = \pm\mathbf{K}(-\sqrt{3}/2, -1/2)^T = \mp\frac{2\pi}{3}. \tag{4.4}$$

Recall that $\mathbf{K}_M = \mathbf{K}'_t + \mathbf{K}_b$, meaning that the Bloch states b^t lives at $\mathbf{K}'_t = -\mathbf{K}_t$ and has $L_z = -1$ while b^b lives at $\mathbf{K}_b$ and has $L_z = +1$. C_{2y} takes $\mathbf{K}'_t \to \mathbf{K}_b$ and the two states form the doublet representation, (E) ,of the D_3 group of $\mathbf{K}_M$. The singlet representations, (A_1, A_2), furnished by $a^{t,b}$ must have C_{2y} eigenvalues ± 1 corresponding to symmetric and anti-symmetric combinations $(a^t \pm a^b)$, respectively. Thus the single energy at $\mathbf{K}_M$ has two one-dimensional irreducible representations, $A_{1,2}$, furnished by $a^t \pm a^b$ and a two-dimensional irreducible representation, E, furnished by the doublet (b^t, b^b). The result is identical to the transformations obtained in Ref. [19].

Recall that the aim of this section is to determine the centers of the Wannier orbtial, i.e. the effective lattice, which reproduces the transformation of the Bloch states in $\mathbf{K}_M$ expressed in terms of the Wannier orbitals. Having established the required transformations of the Bloch states, we now consider the possible lattices. The point group of the lattice must be D_3, thus C_{2y} and C_{3z} must both take any given lattice site to another lattice site. The two sites can either belong to the same or inequivalent sublattices. This leaves us with four options: *i*) Both rotations will take all sites to an inequivalent site, *ii*) C_{2y} will transform all sites to equivalent sites and C_{3z} will transform all sites to inequivalent sites, *iii*) C_{3z} will transform all sites to equivalent sites and C_{2y} will transform all sites to inequivalent sites and *iv*) both rotations will transform all sites to equivalent sites. C_{2y} relates two lattice sites, where each of the two sites is part of a set of three C_{3z} related sites. Thus, for the case *i*) we must have six inequivalent

sublattices, i.e. six inequivalent sites in each unit cell. In that case, we have a six-dimensional degree of freedom and the number of bands in the band structure must be multiples of 6. Since the band structure in Fig. 3.4 has a total of four bands (neglecting spin), we can rule out option *i*). Similarly, for case *ii*) we must have three sites in each unit cell, and the number of bands should be multiples of three, which we can also rule out. On the contrary, for case *iii*) we only have two sites in each unit cell, and the number of bands in the band structure of Fig. 3.4 is indeed a multiple of two. Finally, for case *iv*) we have a single site in each unit cell, which trivially also agrees with the band structure. The two possible lattices are depicted in Fig. 4.2. Comparing to Fig. 3.1, it is evident that case *iii*) corresponds to a honeycomb lattice with sites coinciding with AB/BA regions and case *iv*) corresponds to a triangular lattice with sites at the AA-regions. To reproduce the irreducible representations (A_1, A_2, E) of $\mathbf{K}_M$, we search for Wannier orbitals where two transform as singlets ($L_z = 0$) and the remaining two transforms as a doublet ($L_z = \pm 1$). We already have $L_z^{orb} = \pm 1$ and have yet to determine the $L_z^{B.w.}(\mathbf{K}_M)$ for the two lattice types. Beginning with the triangular lattice, we note that the only differences between the AA-sites of the moiré lattice and the A-sites of the monolayer graphene in Fig. 2.2 is an overall rotation as well as much larger length scales in the moiré case. None of these discrepancies will have an effect on the Bloch wave phase factor, and we can use the transformation of Eq. (4.3) to directly conclude, that the phase factor will not contribute to the total angular momentum of the Bloch wave. Thus for a triangular lattice, we have

$$\begin{aligned} C_{2y}C_{3z}c_{\mathbf{K}_M,\tau} &= \sum_i C_{2y}C_{3z}e^{i\mathbf{K}_M\mathbf{R}_i}c_{i,\tau} = \sum_{i'} C_{2y}e^{i\mathbf{K}_M\mathbf{R}_{i'}}e^{2i\pi\tau/3}c_{i',\tau} \\ &= \sum_{i''} -e^{i\mathbf{K}_M\mathbf{R}_{i''}}e^{2i\pi(-\tau)/3}c_{i'',-\tau} = -e^{-2i\pi\tau/3}c_{\mathbf{K}_M,-\tau}, \end{aligned}$$

where again $C_{3z}\mathbf{R}_i = \mathbf{R}_{i'}$ and $C_{2y}\mathbf{R}_{i'} = \mathbf{R}_{i''}$ and we recall that $L_z^{orb} = -\tau$. Thus, for the triangular lattice we have a single doublet at $\mathbf{K}_M$ furnished by $(c_{\mathbf{K}_M,+}, c_{\mathbf{K}_M,-})$. This is not consistent with the irreducible representations found from microscopic considerations.

In the case of a honeycomb lattice, we can again rely on the monolayer result since, apart from an overall rotation and a change of length scales, the Bloch wave phase factor of the BA-sites is identical to the phase factor of the B-sites. Thus from Eq. (4.4) we directly have that the Bloch state in $\mathbf{K}_M$ living at the BA-sublattice has $L_z^{B.w.} = +1$. Letting $\boldsymbol{\delta}_2 \to 2\boldsymbol{\delta}_2$ in Eq. (4.4) we find that the state living at the AB-sublattice will have $L_z^{B.w} = -1$. Denoting the sublattice degree of freedom by $s = 1, 2$ corresponding to states living at AB- and BA-sublattice, respectively, we find the total transformation of a Bloch state at $\mathbf{K}_M$ to be,

$$\begin{aligned} C_{2y}C_{3z}c_{\mathbf{K}_M,\tau,s} &= \sum_{i\in s} C_{2y}C_{3z}e^{i\mathbf{K}_M\mathbf{R}_i}c_{i,\tau,s} = \sum_{i'\in s} C_{2y}e^{i\mathbf{K}_M\mathbf{R}_{i'}-2i\pi(-1)^s/3}e^{2i\pi\tau/3}c_{i,\tau,s} \\ &= \sum_{i''\in\bar{s}} -e^{i\mathbf{K}_M\mathbf{R}_{i''}-2i\pi(-1)^{\bar{s}}/3}e^{2i\pi(-\tau)/3}c_{i'',-\tau,\bar{s}} = -e^{-2i\pi(\tau+(-1)^{\bar{s}})/3}c_{\mathbf{K}_M,-\tau,\bar{s}}, \quad (4.5) \end{aligned}$$

where $\bar{s}$ denotes the opposite sublattice of s. From this we gather that Bloch states $c_{\mathbf{K}_M,+,1}, c_{\mathbf{K}_M,-,2}$ both have $L_z = L_z^{B.w.} + L_z^{orb} = 0$ since $\tau + (-1)^s = 1 - 1 = -1 + 1 = 0$. Additionally, C_{2y} takes $c_{\mathbf{K}_M,+,1} \to -c_{\mathbf{K}_M,-,2}$ and we have two singlet representations furnished by $c_{\mathbf{K}_M,+,1} \mp c_{\mathbf{K}_M,-,2}$ with C_{2y} eigenvalue ± 1, respectively. The Bloch states $(c_{\mathbf{K}_M,+,2}, c_{\mathbf{K}_M,-,1})$ have total angular momentum $L_z = \mp 1$, respectively. These two states furnish the doublet representation at $\mathbf{K}_M$. Thus the honeycomb lattice reproduces the required representations at $\mathbf{K}_M$.

4.2.3 $\mathbf{M}_M$-point

The analysis performed at $\mathbf{K}_M$ and $\boldsymbol{\Gamma}_M$ is sufficient to determine the Wannier orbitals required to reproduce the band structure of TBG. In this section we merely ensure that a

honeycomb lattice with $p_x \pm ip_y$ orbitals obeys the little group C_2 of $\mathbf{M}_M$ which can only host two one-dimensional representations A and B with eigenvalues ± 1, respectively [19]. C_{2y} takes $c_{\mathbf{M}_M,\tau,s} \to -c_{\mathbf{M}_M,-\tau,-s}$, thus $c_{\mathbf{M}_M,\pm,+} - c_{\mathbf{M}_M,\mp,-}$ belongs to the A representation and $c_{\mathbf{M}_M,\pm,+} + c_{\mathbf{M}_M,\mp,-}$ belongs to the B representation. The band structure in Fig. 3.4 has two separate energies at $\mathbf{M}_M$. The little group C_2 allows for an $\{A, B\}$ set at each energy, which is consistent with our findings.

Finally, we briefly return to $\mathbf{\Gamma}_M$, where the additional sublattice degree of freedom from the honeycomb lattice yields two doublets $((c_{\mathbf{\Gamma}_M,+,1}, c_{\mathbf{\Gamma}_M,-,2})$ and $(c_{\mathbf{\Gamma}_M,-,1}, c_{\mathbf{\Gamma}_M,+,2}))$ as required. We conclude that the only Wannier orbitals reproducing the band structure and microscopic symmetries of TBG are $p_x \pm ip_y$ orbitals with centers forming a honeycomb lattice. We have summarized the analysis of the Wannier orbitals in Table 4.1.

	$\mathbf{\Gamma}_M$	$\mathbf{K}_M$	$\mathbf{M}_M$
Group	D_3	D_3	C_2
Reps	$\{E; E\}$	$\{A_1, A_2, E\}$	$\{A, B; A, B\}$
Bloch states	$(c_{\mathbf{\Gamma}_M,+,1}, c_{\mathbf{\Gamma}_M,-,2})$;	$(c_{\mathbf{K}_M,+,2} - c_{\mathbf{K}_M,-,1})$,	$(c_{\mathbf{M}_M,+,1} - c_{\mathbf{M}_M,-,2}), (c_{\mathbf{M}_M,+,1} + c_{\mathbf{M}_M,-,2})$;
$c_{\mathbf{k},\tau,s}$	$(c_{\mathbf{\Gamma}_M,-,1}, c_{\mathbf{\Gamma}_M,+,2})$	$(c_{\mathbf{K}_M,+,2} + c_{\mathbf{K}_M,-,1})$, $(c_{\mathbf{K}_M,+,1}, c_{\mathbf{K}_M,-,2})$	$(c_{\mathbf{M}_M,-,1} - c_{\mathbf{M}_M,+,2}), (c_{\mathbf{M}_M,-,1} + c_{\mathbf{M}_M,+,2})$

Table 4.1: **Symmetries, irreducible representations and Bloch states at high-symmetry points.** First line denotes the symmetry group of each high-symmetry point. Second line denotes the irreducible representations, where A_1, A_2, A and B are one-dimensional representations and E is two-dimensional. Third line display the Bloch states furnishing the representations. The Bloch states are ordered according to the ordering of representations in the second line. Semicolon indicates symmetry required energy separations.

4.3 Extended Wannier orbitals

We have now established that the only Wannier orbitals reproducing the symmetries of the band structure will be centered at a honeycomb lattice. Since Wannier orbitals are localized by definition, we expect the electron densities to peak in a honeycomb pattern, where the peaks coincide with the centers of the Wannier orbitals at AB-/BA-sites. However, this is certainly not what experimental data show. In Fig. 4.3 a scanning tunneling microscope (STM) measurement performed in Ref. [21] is displayed. For the readers not familiar with STM, this is an experimental technique used to image materials at the atomic level. The technique is based on quantum tunneling, where a conducting tip is brought close to the surface of the material. By applying a bias voltage to the tip, a tunneling current will flow between the tip and the substrate. The present example of an STM measurement uses a constant-current scheme, where the perpendicular distance from the tip to the material is varied across the surface to reach the same tunneling current at all points. If the tip must be brought very close to the sample at a given point, we can directly deduce, that the electron density at this point must be low. On the contrary, if the tip can be far away from a point in the sample while supporting the same current flow, the electron density at the given point must be high. In Fig. 4.3 the colorbar displays the perpendicular height from the tip to the TBG sample. Clearly, the electron densities are not arranged in a honeycomb lattice but rather in a triangular lattice resembling the AA-stacked structure, which we already ruled out as an effective lattice in the previous section. If we trust our symmetry analysis to be correct, the only reasonable explanation for this discrepancy must be, that the Wannier orbitals are not localized at their respective centers. The only way to verify this assumption is to construct the Wannier orbitals.

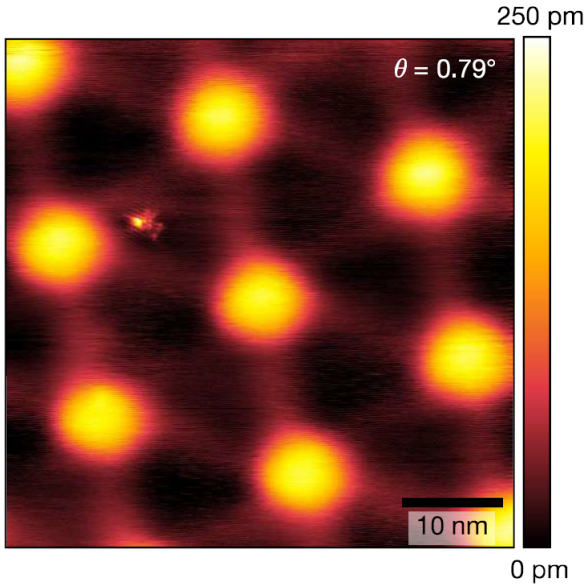

Figure 4.3: **STM topography of TBG at** $\theta = 0.79°$. Topography was taken at a constant current of 50 pA and a bias voltage of 1 V. Colorbar indicates perpendicular distance from tip to substrate. The electron densities are arranged in a triangular pattern corresponding to the AA-regions of the moiré pattern. This figure is adopted from [21].

They must be constructed as a superposition of the monolayer Bloch states which on one hand maximizes the localization and on the other hand obeys the symmetry findings of the previous section. Fortunately, this construction has been carried out in Refs. [22] and [23]. The two studies are in very good agreement and we choose to present the results obtained by Koshino *et al.* (Ref. [22]) in Fig. 4.4. The maximally localized Wannier orbitals presented here have $\tau = +1$. Before discussing the unusual shape Wannier functions, let us first sort out a possible confusion for the reader, namely the τ degree of freedom. In Chapter 3 we discussed the $U_v(1)$ symmetry arising from the decoupled valleys at $\mathbf{K}_{t,b}$ and $\mathbf{K}'_{t,b}$. This symmetry yielded an overall doubling of the number of bands reaching a total number of four (neglecting spin) from layer and valley degrees of freedom. In the symmetry analysis performed in the previous section, we also reached a total of four bands. However, these were expressed in terms of a sublattice and orbital degree of freedom. The sublattice degree of freedom quite naturally relates to the layer degree of freedom, as the sites are defined as AB/BA directly expressing the site and order of the two monolayers. In Ref. [22] they find that the valley degree of freedom expresses itself in our effective model as the orbital degree of freedom, τ, where there is

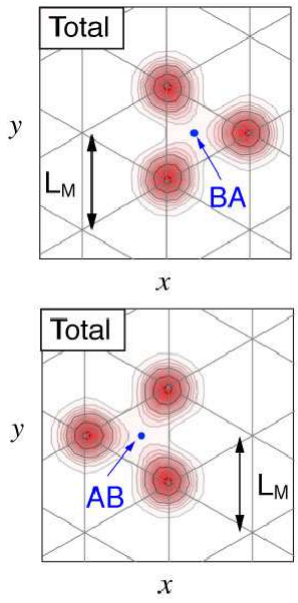

Figure 4.4: **Maximally localized Wannier orbitals of valley** $\tau = +1$**.** The orbitals have centers but no weight at AB-/BA-sites. Approximately all weight of the orbitals is localized at the three adjacent hexagon centers corresponding to AA-regions of the moiré pattern. The Wannier orbitals individually obey the C_{3z} symmetry while a C_{2y} rotation will transfrom them into each other. The extended shape is expected to cause significant long-range effects. This figure is adopted from [22].

one-to-one correspondence between chirality of the valley and the orbital angular momentum given by, $L_z^{orb} = -\tau$, where τ denotes the valley. This relation is the reason for choosing the rather counter-intuitive labelling of L_z^{orb} in the previous section. We conclude that one can use sublattice/layer and orbital/valley interchangably to denote the degrees of freedom in the system and the reader is encouraged to make a note of this equivalence.

Having sorted out the nomenclature, let us return to the intriguing result presented in Fig. 4.4. In agreement with our symmetry considerations, we have two Wannier orbitals of valley $+1$ centered at inequivalent sublattices. The orbitals locally obey C_{3z} and C_{2y}, where, to verify the latter, we recall that C_{2y} exchanges the two layers, thus $AB \leftrightarrow BA$. More importantly, we note the peculiar extended nature of the orbitals. They are by no means localized at their center. On the contrary, they exhibit three clearly distinguishable peaks at the neighboring hexagon centers. By inspection of Figs. 4.2 and 3.1 the hexagon centers exactly constitute the AA-regions arranged in a triangular lattice. Although the general shape of the Wannier functions is curious, it does indeed merge the symmetry analysis from the previous section with the experimental data of Fig. 4.3.

The extended nature of the Wannier functions has the direct consequence that orbitals centered at different sites will have a significant overlap, and all models restricted to on-site or nearest-neighbor hopping/interaction must be immediatly abandoned. The electrons in the narrow bands are fundamentally linked to substantial long-range effects. These effects must be taken into account in any physically reasonable search for the plethora of phases discussed in Chapter 1. Obviously, long-range interactions will immensely complicate any model. We will devote the remainder of this chapter to set up a model of TBG which incorporates the extended nature of the Wannier orbitals in a manner simple enough to enable solutions within reasonable computing times.

4.4 Tight-binding model

In this section we set up a tight-binding model of the TBG honeycomb lattice. In agreement with the findings from the previous sections, the orbitals exhibit on-site (p_x, p_y) symmetry. The aim of the tight-binding model is to reproduce the important features of the relaxed band structure discussed in Chapter 3, namely Dirac cones at $\mathbf{K}_M(\mathbf{K}'_M)$, two-fold degeneracies at $\mathbf{\Gamma}_M$ splitting along $\mathbf{\Gamma}_M\mathbf{M}_M$ and broken particle-hole symmetry. Due to the extended shape of the Wannier orbitals, we expect that long-range hoppings will have significant magnitudes and play an important role in the tight-binding model. In Ref. [22] they explicitly calculate the hopping integrals between the Wannier functions and find that all hoppings with a radius $r < 9|\mathbf{L}_1|$ are necessary to exactly reproduce the band structure obtained from a continuum model. A tight-binding model including all of these hoppings is a lot more complex than what we hoped for. Fortunately, it is possible to set up a minimal model, which, while not reproducing the exact shape of the bands, *does* reproduce the important features of the bands [19, 22]. This model reads,

$$\begin{aligned} H_{tb} = &- \mu \sum_i \mathbf{c}_i^\dagger \cdot \mathbf{c}_i + t_1 \sum_{\langle ij \rangle} [\mathbf{c}_i^\dagger \cdot \mathbf{c}_j + h.c.] \\ &+ t_2 \sum_{\langle ij \rangle'} [\mathbf{c}_i^\dagger \cdot \mathbf{c}_j + h.c.] + t_2' \sum_{\langle ij \rangle'} [(\mathbf{c}_i^\dagger \times \mathbf{c}_j)_z + h.c.], \end{aligned} \tag{4.6}$$

where $\mathbf{c}_i^\dagger = (c_{i,x}^\dagger, c_{i,y}^\dagger)$ with $c_{i\nu}^\dagger$ creating an electron at site i in orbital p_ν. μ is the chemical potential, t_1 is the real nearest-neighbor (NN) hopping amplitude and t_2 (t_2') is the real (imaginary) part of the hopping amplitude between fifth NNs. Inspecting Fig. 4.5 we note that t_1 is

intersublattice hoppings whereas t_2 and t_2' are intrasublattice hoppings.

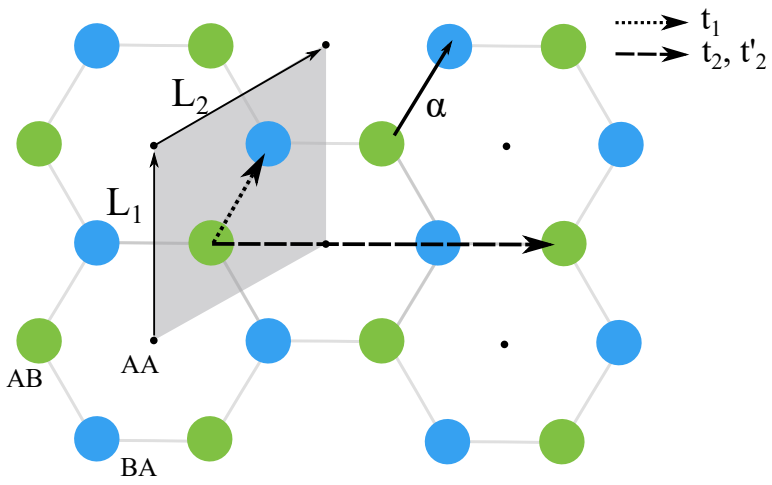

Figure 4.5: **Unit cell and relevant hoppings.** Illustration of the effective honeycomb lattice of TBG. Green (blue) sites are AB (BA) sites. AA-stacked sites at the hexagon center are marked by black dots. Filled, grey area is the unit cell defined by vectors $\mathbf{L}_{1,2}$. The position of the AB-site (BA-site) within the unit cell is defined by $\boldsymbol{\alpha}$ ($2\boldsymbol{\alpha}$). Dotted line indicates NN hopping, t_1, and dashed line indicates fifth NN hopping, t_2, t_2'.

The second term containing the NN hoppings is by far the largest, which should be of no surprise as two out of the three peaks of NN Wannier orbitals will overlap. However, the fact that the fifth NN is the second most important coupling is not what one would expect intuitively. In Ref. [22] they find that the fifth NN hopping is the third largest coupling only exceeded by first and fourth NN by a factor of 3.4 and 1.2, respectively. Surprisingly, the fifth NN hopping amplitude is larger than the second NN hopping by approximately a factor of 6. Hence the consideration of this long-range coupling is fully justified.
However, neglecting the fourth NN hopping cannot be justified through this line of thought. Hence we must return to the aim of this model, i.e. setting up the simplest tight-binding model reproducing important features of the band structure *qualitatively*. Returning to Ref. [22] they find, when including the fourth NN hopping, only a quantitative difference in the bands and we must conclude that, for the particular scope in question, these terms can be neglected.

To express the sublattice degree of freedom explicitly in our model, we rewrite it in the Bravais lattice picture with a two-point basis (AB-/BA-sites). We denote the lattice vectors as $\mathbf{L}_{1,2}$ and the vector between AB- and BA-sites as $\boldsymbol{\alpha}$, see Fig. 4.5. $\mathbf{a}_{i+\boldsymbol{\alpha}}$ ($\mathbf{a}^\dagger_{i+\boldsymbol{\alpha}}$) annihilates (creates) electrons at the AB-site in the unit cell positioned at $\mathbf{R}_i = n\mathbf{L}_1 + m\mathbf{L}_2$, $n, m \in \mathbb{Z}$. Likewise $\mathbf{b}_{i+2\boldsymbol{\alpha}}$ ($\mathbf{b}^\dagger_{i+2\boldsymbol{\alpha}}$) annihilates (creates) electrons at the BA-site in the same cell. As before $\mathbf{f}_i^\dagger = (f^\dagger_{i,x}, f^\dagger_{i,y})$ for $\mathbf{f}_i^\dagger \in \{\mathbf{a}^\dagger_{i+\boldsymbol{\alpha}}, \mathbf{b}^\dagger_{i+2\boldsymbol{\alpha}}\}$. Using this separately on the four terms in Eq. (4.6), we find

$$H_0 = -\mu \sum_i \mathbf{c}_i^\dagger \cdot \mathbf{c}_i = -\mu \sum_{\mathbf{R}_i} [\mathbf{a}^\dagger_{i+\boldsymbol{\alpha}} \cdot \mathbf{a}_{i+\boldsymbol{\alpha}} + \mathbf{b}^\dagger_{i+2\boldsymbol{\alpha}} \cdot \mathbf{b}_{i+2\boldsymbol{\alpha}}], \tag{4.7}$$

Likewise,

$$\begin{aligned} H_1 &= t_1 \sum_{\langle ij \rangle} [\mathbf{c}_i^\dagger \cdot \mathbf{c}_j + h.c.] \\ &= t_1 \sum_{\mathbf{R}_i} [\mathbf{a}^\dagger_{i+\boldsymbol{\alpha}} \cdot (\mathbf{b}_{i+2\boldsymbol{\alpha}} + \mathbf{b}_{i+2\boldsymbol{\alpha}-\mathbf{L}_1} + \mathbf{b}_{i+2\boldsymbol{\alpha}-\mathbf{L}_2}) + h.c.]. \end{aligned} \tag{4.8}$$

The remaining two terms require a bit more consideration as they are intrasublattice couplings and including all six couplings will double count each term. Double counting is usually dealt with by a simple factor of 1/2. However, since $[(\mathbf{c}_i^\dagger \times \mathbf{c}_j)_z + h.c.] = c_{i,x}^\dagger c_{j,y} - c_{i,y}^\dagger c_{j,x} - c_{j,x}^\dagger c_{i,y} + c_{j,y}^\dagger c_{i,x}$, the terms will cancel and not double, if we include all six couplings and let i run over all sites. Instead, we choose the same convention as in [19], where the i'th site couples to the site indicated in Fig. 4.5 and its two C_{3z} related partners. Thus,

$$\begin{aligned} H_2 &= t_2 \sum_{\langle ij \rangle'} [\mathbf{c}_i^\dagger \cdot \mathbf{c}_j + h.c.] \\ &= t_2 \sum_{\mathbf{R}_i} \big[\mathbf{a}_{i+\boldsymbol{\alpha}}^\dagger \cdot (\mathbf{a}_{i+\boldsymbol{\alpha}-\mathbf{L}_1+2\mathbf{L}_2} + \mathbf{a}_{i+\boldsymbol{\alpha}-\mathbf{L}_1-\mathbf{L}_2} + \mathbf{a}_{i+\boldsymbol{\alpha}+2\mathbf{L}_1-\mathbf{L}_2}) \\ &\quad + \mathbf{b}_{i+2\boldsymbol{\alpha}}^\dagger \cdot (\mathbf{b}_{i+2\boldsymbol{\alpha}-\mathbf{L}_1+2\mathbf{L}_2} + \mathbf{b}_{i+2\boldsymbol{\alpha}-\mathbf{L}_1-\mathbf{L}_2} + \mathbf{b}_{i+2\boldsymbol{\alpha}+2\mathbf{L}_1+\mathbf{L}_2}) + h.c. \big] \end{aligned} \tag{4.9}$$

and

$$\begin{aligned} H_{2'} &= t_2' \sum_{\langle ij \rangle'} [(\mathbf{c}_i^\dagger \times \mathbf{c}_j)_z + h.c.] \\ &= t_2' \sum_{\mathbf{R}_i} \Big[\big[\mathbf{a}_{i+\boldsymbol{\alpha}}^\dagger \times (\mathbf{a}_{i+\boldsymbol{\alpha}-\mathbf{L}_1+2\mathbf{L}_2} + \mathbf{a}_{i+\boldsymbol{\alpha}-\mathbf{L}_1-\mathbf{L}_2} + \mathbf{a}_{i+\boldsymbol{\alpha}-2\mathbf{L}_1+\mathbf{L}_2}) \big]_z \\ &\quad + \big[\mathbf{b}_{i+2\boldsymbol{\alpha}}^\dagger \times (\mathbf{b}_{i+2\boldsymbol{\alpha}-\mathbf{L}_1+2\mathbf{L}_2} + \mathbf{b}_{i+2\boldsymbol{\alpha}-\mathbf{L}_1-\mathbf{L}_2} + \mathbf{b}_{i+2\boldsymbol{\alpha}-2\mathbf{L}_1+\mathbf{L}_2}) \big]_z + h.c. \Big]. \end{aligned} \tag{4.10}$$

Having represented our Hamiltonian in the desired basis, we can now proceed to perform Fourier transformations (FTs) of all four terms, diagonalize $H_{tb} = H_0 + H_1 + H_2 + H_{2'}$ and present the resulting bands.

4.4.1 Narrow bands

We define the FTs as follows,

$$\begin{aligned} \mathbf{a}_{i+\boldsymbol{\alpha}} &= \frac{1}{\sqrt{\tilde{N}}} \sum_{\mathbf{k} \in BZ} e^{i\mathbf{k}(\mathbf{R}_i + \boldsymbol{\alpha})} \mathbf{a}_\mathbf{k}, \\ \mathbf{a}_{i+\boldsymbol{\alpha}}^\dagger &= \frac{1}{\sqrt{\tilde{N}}} \sum_{\mathbf{k} \in BZ} e^{-i\mathbf{k}(\mathbf{R}_i + \boldsymbol{\alpha})} \mathbf{a}_\mathbf{k}^\dagger, \\ \mathbf{b}_{i+2\boldsymbol{\alpha}} &= \frac{1}{\sqrt{\tilde{N}}} \sum_{\mathbf{k} \in BZ} e^{i\mathbf{k}(\mathbf{R}_i + 2\boldsymbol{\alpha})} \mathbf{b}_\mathbf{k}, \\ \mathbf{b}_{i+2\boldsymbol{\alpha}}^\dagger &= \frac{1}{\sqrt{\tilde{N}}} \sum_{\mathbf{k} \in BZ} e^{-i\mathbf{k}(\mathbf{R}_i + 2\boldsymbol{\alpha})} \mathbf{b}_\mathbf{k}^\dagger, \end{aligned} \tag{4.11}$$

where $\tilde{N}$ is the number of unit cells in the system. Performing the FT of all terms we get

$$\begin{aligned} H_{tb} = \sum_{\mathbf{k} \in BZ} \Bigg(& -\mu [\mathbf{a}_\mathbf{k}^\dagger \cdot \mathbf{a}_\mathbf{k} + \mathbf{b}_\mathbf{k}^\dagger \cdot \mathbf{b}_\mathbf{k}] + t_1 \big[e^{i\mathbf{k}\boldsymbol{\alpha}} (1 + e^{-i\mathbf{k}\mathbf{L}_1} + e^{-i\mathbf{k}\mathbf{L}_2}) \mathbf{a}_\mathbf{k}^\dagger \cdot \mathbf{b}_\mathbf{k} + h.c. \big] \\ & + 2t_2 \big[\cos\big(\mathbf{k} \cdot (-\mathbf{L}_1 + 2\mathbf{L}_2)\big) + \cos\big(\mathbf{k} \cdot (-\mathbf{L}_1 - \mathbf{L}_2)\big) + \cos\big(\mathbf{k} \cdot (2\mathbf{L}_1 - \mathbf{L}_2)\big) \big] (\mathbf{a}_\mathbf{k}^\dagger \cdot \mathbf{a}_\mathbf{k} + \mathbf{b}_\mathbf{k}^\dagger \cdot \mathbf{b}_\mathbf{k}) \\ & + 2it_2' \big[\sin\big(\mathbf{k} \cdot (-\mathbf{L}_1 + 2\mathbf{L}_2)\big) + \sin\big(\mathbf{k} \cdot (-\mathbf{L}_1 - \mathbf{L}_2)\big) + \sin\big(\mathbf{k} \cdot (2\mathbf{L}_1 - \mathbf{L}_2)\big) \big] \cdot \big(\big[\mathbf{a}_\mathbf{k}^\dagger \times \mathbf{a}_\mathbf{k} \big]_z + \big[\mathbf{b}_\mathbf{k}^\dagger \times \mathbf{b}_\mathbf{k} \big]_z \big) \Bigg). \end{aligned} \tag{4.12}$$

The full derivation can be seen in Appendix A.
Writing this in terms of the basis $\mathbf{f}_{\mathbf{k}}^{\dagger} = \begin{pmatrix} a_{\mathbf{k},x}^{\dagger} & a_{\mathbf{k},y}^{\dagger} & b_{\mathbf{k},x}^{\dagger} & b_{\mathbf{k},y}^{\dagger} \end{pmatrix}$, we have

$$H_{tb} = \sum_{\mathbf{k}\in BZ} \mathbf{f}_{\mathbf{k}}^{\dagger} \begin{pmatrix} -\mu + \tilde{t_2}(\mathbf{k}) & \tilde{t_2'}(\mathbf{k}) & \tilde{t_1}(\mathbf{k}) & 0 \\ -\tilde{t_2'}(\mathbf{k}) & -\mu + \tilde{t_2}(\mathbf{k}) & 0 & \tilde{t_1}(\mathbf{k}) \\ \tilde{t_1^*}(\mathbf{k}) & 0 & -\mu + \tilde{t_2}(\mathbf{k}) & \tilde{t_2'}(\mathbf{k}) \\ 0 & \tilde{t_1^*}(\mathbf{k}) & -\tilde{t_2'}(\mathbf{k}) & -\mu + \tilde{t_2}(\mathbf{k}) \end{pmatrix} \mathbf{f}_{\mathbf{k}}, \tag{4.13}$$

where,

$$\begin{aligned} \tilde{t_1}(\mathbf{k}) &= t_1\big[e^{i\mathbf{k}\boldsymbol{\alpha}}(1 + e^{-i\mathbf{k}\mathbf{L}_1} + e^{-i\mathbf{k}\mathbf{L}_2})\big], \\ \tilde{t_2}(\mathbf{k}) &= 2t_2\big[\cos\big(\mathbf{k}\cdot(-\mathbf{L}_1 + 2\mathbf{L}_2)\big) + \cos\big(\mathbf{k}\cdot(-\mathbf{L}_1 - \mathbf{L}_2)\big) + \cos\big(\mathbf{k}\cdot(2\mathbf{L}_1 - \mathbf{L}_2)\big)\big], \\ \tilde{t_2'}(\mathbf{k}) &= 2it_2'\big[\sin\big(\mathbf{k}\cdot(-\mathbf{L}_1 + 2\mathbf{L}_2)\big) + \sin\big(\mathbf{k}\cdot(-\mathbf{L}_1 - \mathbf{L}_2)\big) + \sin\big(\mathbf{k}\cdot(2\mathbf{L}_1 - \mathbf{L}_2)\big)\big]. \end{aligned} \tag{4.14}$$

Note that $\tilde{t_2}(\mathbf{k})$ is real while $\tilde{t_2'}(\mathbf{k})$ is purely imaginary in agreement with the real space model in Eq. (4.6).

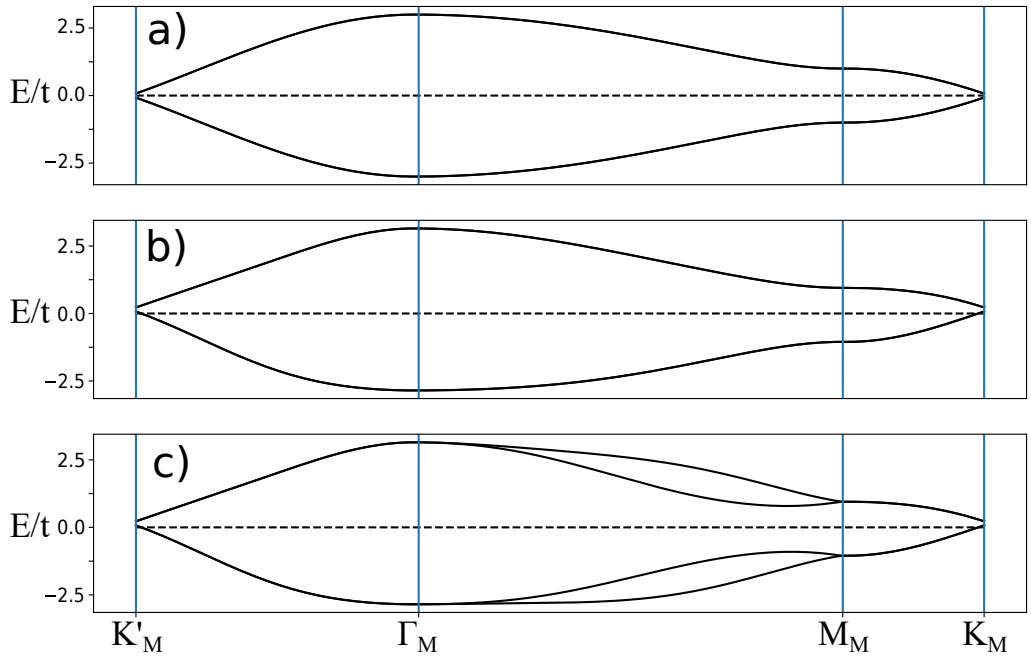

Figure 4.6: **Energy bands of the tight-binding model.** Parameters are **a)** $t_1 = 1$, $t_2 = t_2' = 0$, **b)** $t_1 = 1$, $t_2 = 0.025$, $t_2' = 0$ and **c)** $t_1 = 1$, $t_2 = 0.025$, $t_2' = 0.1$. All three structures has $\mu = 0$ indicated by dashed lines. In **b)** particle-hole symmetry is broken and in **c)** both particle-hole and orbital symmetry is broken. All three band structures are spin degenerate.

Diagonalizing Eq. (4.13) yields the energy bands seen in Fig. 4.6. In Fig. 4.6a parameters are $t_1 = 1$, $t_2 = t_2' = 0$ and $\mu = 0$. This band structure exhibits particle-hole symmetry. Furthermore, the two valleys/orbitals are degenerate yielding an emergent $SU(2)$ valley symmetry. In

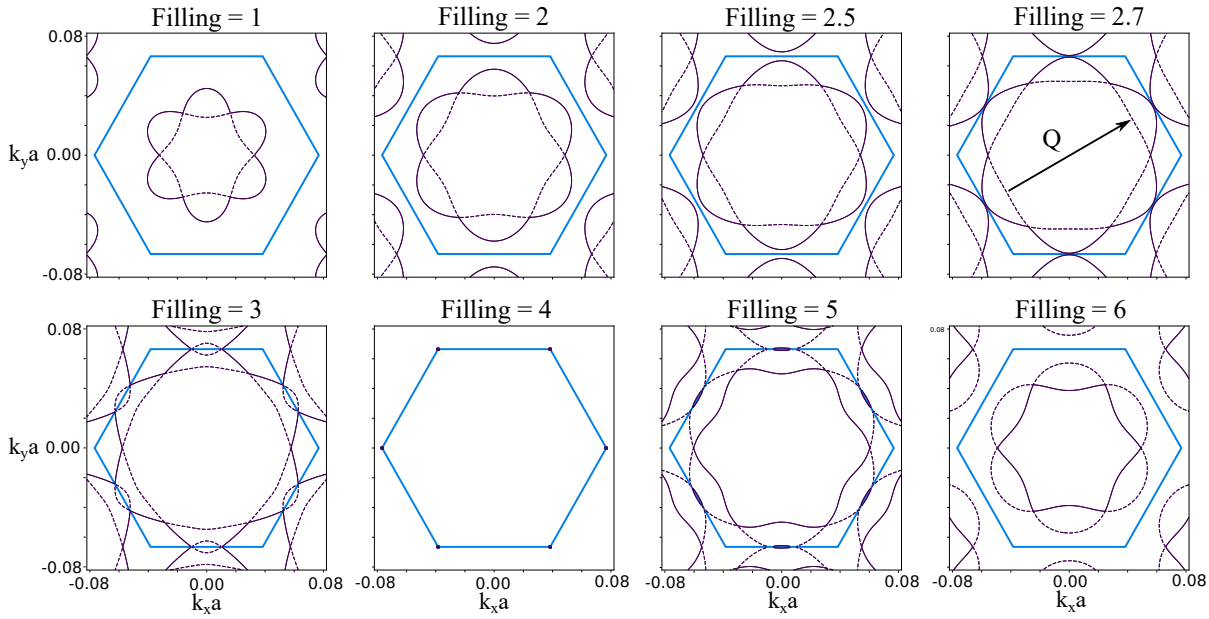

Figure 4.7: **Fermi surfaces of TBG at various fillings.** Parameters are $t_1 = 1, t_2 = 0.025$ and $t_2' = 0.1$. Momentum are in units of $1/a$, where a is the length of the monolayer graphene unit vector. Fillings are labelled according to the number of electrons in the unit cell running from zero to eight. Dashed and solid lines are the two distinct electron (hole) bands for fillings above (below) four. Blue hexagons are the TBG MBZ and is inserted as a guide to the eye. **Q** in top right figure indicates a possible nesting at filling 2.7.

Fig. 4.6b we set $t_2 = 0.025$, which breaks the particle-hole symmetry. This is evident from Eq. (4.13), since this term adds the same amount of (**k**-dependent) energy to particle and hole bands, i.e. $E_p(\mathbf{k}) + \tilde{t_2}(\mathbf{k}) = -E_h(\mathbf{k}) + \tilde{t_2}(\mathbf{k})$. Hence t_2 also gives rise to an overall upwards shift of the bands, meaning that $\mu = 0$ no longer coincides with the Dirac points at $\mathbf{K}_M$ and $\mathbf{K}'_M$. Finally, we set $t_2' = 0.1$ in Fig. 4.6c, which breaks orbital symmetry along $\mathbf{\Gamma}_M$-$\mathbf{M}_M$ thus the emergent $SU(2)$ valley symmetry of Fig. 4.6 is broken down to the minimal $U_v(1)$ valley symmetry. The band structure in Fig. 4.6c exhibits the same features as the relaxed band structure discussed in Chapter 3. We have thus accomplished what we set out to do, and are now ready to consider interactions in the system.

4.4.2 Fermi surfaces

When searching for possible interaction-driven instabilities in a system, it is always instructive to investigate the Fermi surfaces of the non-interacting system. This investigation will reveal predominant scatterings such as nesting vectors or van Hove singularities, which can be relevant when looking for susceptibility divergences, i.e. instabilities. It thus provides a guidance towards the areas of parameter space most likely to exihibit spontaneous symmetry breaking.

In Fig. 4.7 the Fermi surfaces at various fillings are displayed. There is no general agreement on the definition of the fillings in the litterature. To avoid any confusion, this thesis will label all fillings according to the number of electrons in each unit cell. As each unit cell contains two sites, each with two orbitals and two spins, the maximal number of electrons in each unit cell is eight. Dashed and solid lines in Fig. 4.7 are the two distinct electron (hole) bands for fillings above (below) four. Blue hexagons are the TBG MBZ. Note the small scale on the momentum

axis reflecting the immense amount of folding when going from the original, monolayer graphene lattice to the extended moiré pattern in TBG. It is evident that the bands are degenerate along $\mathbf{K}'_M$-$\mathbf{\Gamma}_M$ and $\mathbf{M}_M$-$\mathbf{K}_M$ but split along $\mathbf{\Gamma}_M$-$\mathbf{M}_M$ in good agreement with the band structure in Fig. 4.6c.
Regarding the Fermi surfaces themselves, we first verify that at filling 4, i.e. charge neutrality, the Fermi surface is identical to the monolayer graphene at half filling with Dirac point at all $\mathbf{K}_M$ and $\mathbf{K}'_M$ points. Hence quasiparticles with momenta in the vicinity of these high-symmetry points perserve the pseudo-relativistic behavior of monolayer graphene. We further note the broken particle-hole symmetry especially evident at fillings 3 and 5. This is again in good agreement with the band structure in Fig. 4.6b,c. The Fermi surface at filling 2.7 in top right corner exihibits several interesting features. For one, it reveals a van Hove point at $\mathbf{M}_M$ leading to a peak in the density of states enabling a large amount of small $\mathbf{q}$-scattering. When scattering with $\mathbf{q} \approx 0$ dominates, the system is expected to be unstable towards homogeneous phases, e.g. ferromagnetism. Another prominent feature is the apparent nesting vector, $\mathbf{Q}$, connecting parallel sections of the Fermi surface, which can make the system instable towards $2\pi/\mathbf{Q}$ modulated phases, e.g. charge density wave. Thus from inspecting the Fermi surface one would expect a competition between a homogeneous and a $2\pi/\mathbf{Q}$ modulated phase. While these expectations all appear intriguing, the experimental data does not exhibit any striking features in this filling region (see Fig. 1.2 at $\nu \sim -1.5$). This should be of no surprise, as we expect interactions to significantly modify the bands in TBG due to the very low Fermi velocity and the considerable orbital overlap enhancing interaction effect. Thus we will not rely notably on the considerations presented in this section. Instead we focus on deriving an interaction model which directly incorporates the shape of the Wannier functions without bias towards certain phases. By solving an unbiased model including both interaction and kinetic terms, we avoid exaggeration of the bare band influence.

4.5 Interaction model

In this section our goal is to obtain an interaction model of TBG. We will follow the line of argument in Ref. [24] to set up the effective model of the Coulomb interaction and describe all approximations made along the way.

The effective interaction model is based on the general Coulomb interaction,

$$U = \frac{1}{2}\sum_{\mathbf{r},\mathbf{r}'}\sum_{\sigma,\sigma'} c^\dagger_\sigma(\mathbf{r})c_\sigma(\mathbf{r})V(\mathbf{r}-\mathbf{r}')c^\dagger_{\sigma'}(\mathbf{r}')c_{\sigma'}(\mathbf{r}'), \tag{4.15}$$

where $c^\dagger_\sigma(\mathbf{r})$ ($c_\sigma(\mathbf{r})$) creates (annihilates) an electron with spin σ at $\mathbf{r}$ and $V(\mathbf{r}-\mathbf{r}')$ is the Coulomb interaction. The operators are expanded in terms of the maximally localized Wannier states (WSs). We have argued that these states are centered at honeycomb sites (AB-/BA-stacking) with peaks at neighboring hexagon centers (AA-stacking). The expansion is defined as,

$$c_\sigma(\mathbf{r}) = \frac{1}{3}\sum_{\mathbf{R}}\sum_{p=1}^{6}\sum_{\tau=\pm1} w_{\mathbf{R}+\boldsymbol{\delta}_p,\tau}(\mathbf{r})d_{\tau,\sigma}(\mathbf{R}+\boldsymbol{\delta}_p), \tag{4.16}$$

where $\mathbf{R} = m\mathbf{L}_1 + n\mathbf{L}_2$ defines the hexagon and p defines the 6 sites related to each hexagon, see Fig. 4.8. $c_\sigma(\mathbf{r})$ is also expanded in terms of the valley degree of freedom, τ.
Before expanding Eq. (4.15) three approximations are made. *i*) $V(\mathbf{r}-\mathbf{r}')$ is set to V_0 for all $\mathbf{r}$ and $\mathbf{r}'$ residing in the same hexagon *ii*) and 0 otherwise. *iii*) All valley mixing terms are neglected. *i*) Is justified by numerical calculations performed in [23], *ii*) is justified due to the presence of metallic gates causing significant screening and *iii*) is justified by the emergent $U_v(1)$ valley

symmetry.

With these three approximations implemented we reach

$$U \approx \frac{V_0}{2}\sum_{\mathbf{R}}\sum_{\mathbf{r},\mathbf{r}'\in\hexagon}\sum_{\sigma,\sigma'} c^\dagger_\sigma(\mathbf{R}+\mathbf{r})c_\sigma(\mathbf{R}+\mathbf{r})c^\dagger_{\sigma'}(\mathbf{R}+\mathbf{r}')c_{\sigma'}(\mathbf{R}+\mathbf{r}')$$
$$= \frac{V_0}{2}\sum_{\mathbf{R}}\sum_{\tau,\tau'=\pm1}\sum_{\sigma,\sigma'}\sum_{\mathbf{r},\mathbf{r}'\in\hexagon} n_{\tau,\sigma}(\mathbf{R}+\mathbf{r})n_{\tau',\sigma'}(\mathbf{R}+\mathbf{r}'), \qquad \text{with} \tag{4.17}$$

$$n_{\tau,\sigma}(\mathbf{R}+\mathbf{r}) = \frac{1}{3^2}\sum_{\bar{\mathbf{R}},\bar{\mathbf{R}}'}\sum_{p,p'=1}^{6} w^*_{\bar{\mathbf{R}}-\mathbf{R}+\boldsymbol{\delta}_p,\tau}(\mathbf{r})w_{\bar{\mathbf{R}}'-\mathbf{R}+\boldsymbol{\delta}_{p'},\tau}(\mathbf{r})d^\dagger_{\tau,\sigma}(\bar{\mathbf{R}}+\boldsymbol{\delta}_p)d_{\tau,\sigma}(\bar{\mathbf{R}}'+\boldsymbol{\delta}_{p'})$$
$$\approx \sum_{p,p'=1}^{6} w^*_{\boldsymbol{\delta}_p,\tau}(\mathbf{r})w_{\boldsymbol{\delta}_{p'},\tau}(\mathbf{r})d^\dagger_{\tau,\sigma}(\mathbf{R}+\boldsymbol{\delta}_p)d_{\tau,\sigma}(\mathbf{R}+\boldsymbol{\delta}_{p'}). \tag{4.18}$$

In the last line we have used that a particle density in a given hexagon (defined by $\mathbf{R}$) only has non-zero projections onto the six corresponding hexagon sites. Thus $\sum_{\bar{\mathbf{R}}} \to 3\boldsymbol{\delta}_{\bar{\mathbf{R}},\mathbf{R}}$. The factor of three makes up for the fact that we no longer triple-count the hexagon sites. Eq. (4.18) is divided into two dominating contributions. The usual density interaction with $p = p'$ and a rather peculiar hopping-like contribution with $|p - p'| = 1$. We only include NN hopping-like terms and all terms with $|p - p'| > 1$ are set to 0. We thus get,

$$\sum_{\mathbf{r}\in\hexagon} n_{\tau,\sigma}(\mathbf{R}+\mathbf{r}) = \sum_{p=1}^{6}\sum_{\mathbf{r}\in\hexagon}|w_{\boldsymbol{\delta}_p,\tau}(\mathbf{r})|^2 d^\dagger_{\tau,\sigma}(\mathbf{R}+\boldsymbol{\delta}_p)d_{\tau,\sigma}(\mathbf{R}+\boldsymbol{\delta}_p)$$
$$+\sum_{p=1}^{6}\Big(\sum_{\mathbf{r}\in\hexagon} w^*_{\boldsymbol{\delta}_p,\tau}(\mathbf{r})w_{\boldsymbol{\delta}_{p+1},j}(\mathbf{r})d^\dagger_{\tau,\sigma}(\mathbf{R}+\boldsymbol{\delta}_p)d_{\tau,\sigma}(\mathbf{R}+\boldsymbol{\delta}_{p+1}) + h.c.\Big), \tag{4.19}$$

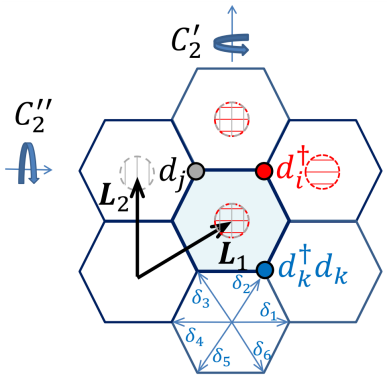

Figure 4.8: **Real space schematic of TBG.** Lattice vectors $\mathbf{L}_{1,2}$ span the unit cell and define the position of the hexagon, $\mathbf{R} = n\mathbf{L}_1 + m\mathbf{L}_2$. $d_i^\dagger$ creates a maximally localized WS at honeycomb lattice site i with maxima at the three neighboring hexagon centers marked by areas with horizontal, red lines. The WSs of two neighbouring honeycomb sites overlap at two hexagon centers as illustrated by the areas marked by horisontal red lines and vertical grey lines. The position of honeycomb site i is defined by $\mathbf{R} + \boldsymbol{\delta}_i$, where $i = 1, ..., 6$. This figure is adopted from [24].

where we impose periodic boundary conditions such that $\boldsymbol{\delta}_7 = \boldsymbol{\delta}_1$.

To a good approximation the WSs are normalized and completely C_{3z}-symmetric with equal weights in the three neighboring hexagon centers and no weight elsewhere. Using this we identify

$$\sum_{r\in\hexagon}|w_{\boldsymbol{\delta}_p,j}(\mathbf{r})|^2 = \frac{1}{3}. \tag{4.20}$$

The hopping-like contributions are less straight forward. For $p \neq p'$ orthogonality requires,

$$0 = \sum_{all\,\mathbf{r}} w^*_{\boldsymbol{\delta}_p}(\mathbf{r})w_{\boldsymbol{\delta}_{p'}}(\mathbf{r})$$
$$= \sum_{\bar{\mathbf{R}}}\sum_{\mathbf{r}\in\hexagon} w^*_{\bar{\mathbf{R}}+\boldsymbol{\delta}_p}(\mathbf{r})w_{\bar{\mathbf{R}}+\boldsymbol{\delta}_{p'}}(\mathbf{r}),$$

where we have suppressed the valley subscript for simplicity. As we only include NN couplings, each coupling will have contributions from two hexagon centers, $\bar{\mathbf{R}} = \mathbf{R} \vee \mathbf{R}'$, when

performing the sum. Take e.g. $p = 2$ and $p' = 3$ with $\mathbf{R}$ defining the hexagon illustrating the $\boldsymbol{\delta}$-vectors in Fig. 4.8. This coupling is also represented for $\mathbf{R}'$ defining the centered, light blue hexagon with $p = 6$ and $p' = 5$. We thus get,

$$\sum_{\mathbf{r}\in\hexagon} w^*_{\mathbf{R}+\boldsymbol{\delta}_2}(\mathbf{r}) w_{\mathbf{R}+\boldsymbol{\delta}_3}(\mathbf{r}) + \sum_{\mathbf{r}\in\hexagon} w^*_{\mathbf{R}'+\boldsymbol{\delta}_6}(\mathbf{r}) w_{\mathbf{R}'+\boldsymbol{\delta}_5}(\mathbf{r}) = 0$$

$$\Rightarrow -\sum_{\mathbf{r}\in\hexagon} w^*_{\mathbf{R}+\boldsymbol{\delta}_2}(\mathbf{r}) w_{\mathbf{R}+\boldsymbol{\delta}_3}(\mathbf{r}) = \sum_{\mathbf{r}\in\hexagon} w^*_{\mathbf{R}'+\boldsymbol{\delta}_6}(\mathbf{r}) w_{\mathbf{R}'+\boldsymbol{\delta}_5}(\mathbf{r}) \tag{4.21}$$

As the model must obey discrete translational symmetry, this relation must hold for $\mathbf{R} = \mathbf{R}'$. Imposing this condition on the expression in the second line of Eq. (4.19) yields

$$\begin{aligned}\sum_{p=1,3,5} \Big(\sum_{r\in\hexagon} & w^*_{\boldsymbol{\delta}_p,\tau}(\mathbf{r}) w_{\boldsymbol{\delta}_{p+1},\tau}(\mathbf{r}) d^\dagger_{\tau,\sigma}(\mathbf{R}+\boldsymbol{\delta}_p) d_{\tau,\sigma}(\mathbf{R}+\boldsymbol{\delta}_{p+1}) \\ & - \sum_{r\in\hexagon} w^*_{\boldsymbol{\delta}_{p+1},\tau}(\mathbf{r}) w_{\boldsymbol{\delta}_{p+2},\tau}(\mathbf{r}) d^\dagger_{\tau,\sigma}(\mathbf{R}+\boldsymbol{\delta}_{p+1}) d_{\tau,\sigma}(\mathbf{R}+\boldsymbol{\delta}_{p+2}) \\ & + \sum_{r\in\hexagon} w^*_{\boldsymbol{\delta}_{p+1},\tau}(\mathbf{r}) w_{\boldsymbol{\delta}_{p},\tau}(\mathbf{r}) d^\dagger_{\tau,\sigma}(\mathbf{R}+\boldsymbol{\delta}_{p+1}) d_{\tau,\sigma}(\mathbf{R}+\boldsymbol{\delta}_{p}) \\ & - \sum_{r\in\hexagon} w^*_{\boldsymbol{\delta}_{p+2},\tau}(\mathbf{r}) w_{\boldsymbol{\delta}_{p+1},\tau}(\mathbf{r}) d^\dagger_{\tau,\sigma}(\mathbf{R}+\boldsymbol{\delta}_{p+2}) d_{\tau,\sigma}(\mathbf{R}+\boldsymbol{\delta}_{p+1}) \Big)\end{aligned} \tag{4.22}$$

We have written out the hermitian conjugated terms to explicitly see that the condition in Eq. (4.21) is fulfilled by combining the second term for $p = 1$ and the third term for $p = 5$. The expression indeed fulfills the orthogonality condition for all couplings, which can easily be verified.

In addition to the orthogonality requirement, the couplings are related through the symmetries exhibited by the system, i.e. C_{2y}, C_{3z} and time-reversal. Thus they should only vary up to a phase. In general these terms can be written as,

$$\sum_{r\in\hexagon} w^*_{\boldsymbol{\delta}_p,\tau}(\mathbf{r}) w_{\boldsymbol{\delta}_{p+1},\tau}(\mathbf{r}) = \alpha_1 e^{i\phi_{p,\sigma,\tau}}, \tag{4.23}$$

where α_1 is a constant valid for all NN couplings. The phase dependencies can be further reduced. The entire system exhibits $SU(2)$ spin symmetry, thus the phase cannot differ due to change in spin. Furthermore the site dependence, i.e. p-dependence, is fully restricted by orthogonality and point group symmetries. This dependence can be determined from Eq. (4.21), where we have

$$\begin{aligned}-\sum_{\mathbf{r}\in\hexagon} w^*_{\mathbf{R}+\boldsymbol{\delta}_2,\tau}(\mathbf{r}) w_{\mathbf{R}+\boldsymbol{\delta}_3,\tau}(\mathbf{r}) = -\alpha_1 e^{i\phi_{2,\tau}} &= \sum_{\mathbf{r}\in\hexagon} w^*_{\mathbf{R}'+\boldsymbol{\delta}_6,\tau}(\mathbf{r}) w_{\mathbf{R}'+\boldsymbol{\delta}_5,\tau}(\mathbf{r}) \\ &= \Big(\sum_{\mathbf{r}\in\hexagon} w^*_{\mathbf{R}'+\boldsymbol{\delta}_5,\tau}(\mathbf{r}) w_{\mathbf{R}'+\boldsymbol{\delta}_6,\tau}(\mathbf{r}) \Big)^* = \alpha_1 e^{-i\phi_{5,\tau}}.\end{aligned}$$

As the overall sign is already incorporated in Eq. (4.22), we can directly identify $-\phi_{2,\tau} = \phi_{5,\tau}$. Since the summation is only performed for $p = 1, 3, 5$, this leads to $-\phi_{p+1,\tau} = \phi_{p,\tau}$. Finally we note that the two valley are related by time-reversal, thus $\phi_+ = -\phi_- = \tau\phi$. Imposing these findings in Eq. (4.22) yields

$$\alpha_1 \sum_{p=1,3,5} \Big(e^{i\tau\phi} d^\dagger_{\tau,\sigma}(\mathbf{R}+\boldsymbol{\delta}_p) d_{\tau,\sigma}(\mathbf{R}+\boldsymbol{\delta}_{p+1})$$

$$
\begin{aligned}
&- e^{-i\tau\phi} d^\dagger_{\tau,\sigma}(\mathbf{R}+\boldsymbol{\delta}_{p+1}) d_{\tau,\sigma}(\mathbf{R}+\boldsymbol{\delta}_{p+2}) \\
&+ e^{-i\tau\phi} d^\dagger_{\tau,\sigma}(\mathbf{R}+\boldsymbol{\delta}_{p+1}) d_{\tau,\sigma}(\mathbf{R}+\boldsymbol{\delta}_{p}) \\
&- e^{i\tau\phi}(\mathbf{r}) d^\dagger_{\tau,\sigma}(\mathbf{R}+\boldsymbol{\delta}_{p+2}) d_{\tau,\sigma}(\mathbf{R}+\boldsymbol{\delta}_{p+1})\Big).
\end{aligned}
$$

We note that the expression is still hermitian, as required. It is now clear that the phases can be absorbed through a gauge transformation as follows,

$$
\begin{aligned}
d_{\tau,\sigma}(\mathbf{R}+\boldsymbol{\delta}_p) &\longrightarrow e^{i\tau\phi/2} d_{\tau,\sigma}(\mathbf{R}+\boldsymbol{\delta}_p), \qquad p\,\text{odd} \\
d_{\tau,\sigma}(\mathbf{R}+\boldsymbol{\delta}_p) &\longrightarrow e^{-i\tau\phi/2} d_{\tau,\sigma}(\mathbf{R}+\boldsymbol{\delta}_p), \qquad p\,\text{even}
\end{aligned}
\tag{4.24}
$$

Performing the transformation and letting the sum run over all p's, we get

$$
\alpha_1 \sum_{p=1}^{6} (-1)^{p-1} \Big(d^\dagger_{\tau,\sigma}(\mathbf{R}+\boldsymbol{\delta}_p) d_{\tau,\sigma}(\mathbf{R}+\boldsymbol{\delta}_{p+1}) + d^\dagger_{\tau,\sigma}(\mathbf{R}+\boldsymbol{\delta}_{p+1}) d_{\tau,\sigma}(\mathbf{R}+\boldsymbol{\delta}_p) \Big) \tag{4.25}
$$

Inserting this and Eq. (4.20) into Eq. (4.19) we get the much simpler expression,

$$
\begin{aligned}
\sum_{r\in\hexagon} n_{\tau,\sigma}(\mathbf{R}+\mathbf{r}) = \frac{1}{3}\sum_{p=1}^{6} & d^\dagger_{\tau,\sigma}(\mathbf{R}+\boldsymbol{\delta}_p) d_{\tau,\sigma}(\mathbf{R}+\boldsymbol{\delta}_p) \\
&+ \alpha_1 \sum_{p=1}^{6} (-1)^{p-1} \Big(d^\dagger_{\tau,\sigma}(\mathbf{R}+\boldsymbol{\delta}_p) d_{\tau,\sigma}(\mathbf{R}+\boldsymbol{\delta}_{p+1}) + h.c. \Big),
\end{aligned}
\tag{4.26}
$$

yielding the final interaction model to be,

$$
U = \frac{V_0}{2} \sum_{\mathbf{R}} \sum_{\tau,\tau'} \sum_{\sigma,\sigma'} \Big(Q_{\tau,\sigma}(\mathbf{R}) + T_{\tau,\sigma}(\mathbf{R}) \Big) \Big(Q_{\tau',\sigma'}(\mathbf{R}) + T_{\tau',\sigma'}(\mathbf{R}) \Big), \text{ where} \tag{4.27}
$$

$$
Q_{\tau,\sigma}(\mathbf{R}) = \frac{1}{3}\sum_{p=1}^{6} d^\dagger_{\tau,\sigma}(\mathbf{R}+\boldsymbol{\delta}_p) d_{\tau,\sigma}(\mathbf{R}+\boldsymbol{\delta}_p), \qquad \text{and}
$$

$$
T_{\tau,\sigma}(\mathbf{R}) = \alpha_1 \sum_{p=1}^{6} (-1)^{p-1} \Big(d^\dagger_{\tau,\sigma}(\mathbf{R}+\boldsymbol{\delta}_p) d_{\tau,\sigma}(\mathbf{R}+\boldsymbol{\delta}_{p+1}) + h.c. \Big).
$$

$Q_{\tau,\sigma}(\mathbf{R})$ only contains usual density-density interactions and the terms are dubbed the cluster charge interaction terms. Due to the curious hopping-like appearance of $T_{\tau,\sigma}(\mathbf{R})$, these terms are dubbed assisted hopping interaction terms.
All statements used to simplify the interaction are verified through numerical calculations presented in Supplementary Material of [24].

4.5.1 Topology and assisted hopping terms

With the tight-binding and interaction model in place, we are ready to combine the two, decouple the interactions and search for the ground states preferred at various commensurate fillings. Before doing so, we dedicate this short section to discuss the origins of our interaction terms. The cluster charge terms, $Q_{\tau,\sigma}(\mathbf{R})$, is the TBG analogue to the common on-site Hubbard repulsion terms. Usually, the on-site repulsion expresses the overlap of two site-localized Wannier orbitals. Due to the extended shape of the Wannier functions in TBG, the usual on-site terms must be expressed as "on-hexagon", or similarly "on-peak", where the atypical TBG wavefunctions overlap. Thus the origin of $Q_{\tau,\sigma}(\mathbf{R})$ is nothing but an on-site repulsion of a triangular

lattice projected onto the honeycomb lattice.

On the contrary, the origin of the assisted hopping terms, $T_{j,\sigma}(\mathbf{R})$, is rooted deeply in the underlying topology. To recognize this, we take several steps back and begin with the microscopic picture of two graphene layers with a relative twist angle. As mentioned previously, this system can be represented microscopically by a continuum model describing the Dirac cones of each layer with interlayer tunneling. The continuum model exhibits full C_{6z} symmetry [17, 25, 26]. If the rotation of the two layers is performed about coinciding hexagon centers of the monolayers rather than at an AA-stacked site, the point group of TBG will be D_6, which extends the symmetries of the continuum model to the lattice model. However, if one performs a symmetry analysis similar to the one performed in Section 4.2, one finds that this point group *cannot* reproduce realistic band symmetries [22]. Specifically, it is not possible to generate four zero-energy states at $\mathbf{K}_M$ and the Dirac points are destroyed. This might seem alarming to the reader, as we have apparently ignored the symmetries of the microscopic model. Fortunately, this is not exactly true.

The additional symmetry required on top of C_{3z} and C_{2y} to generate point group D_6 is a two-fold C_{2x} symmmetry. This is the symmetry labelled C_2'' in Fig. 4.8. The C_{2x} symmetry is not locally implemented. The easiest way to see this, is to consider an AB-site. C_{2x} will, as C_{2y}, flip the two layers, thus $AB \to BA$. However, from inspection of Fig. 4.5, we will need an additional lattice translation to get back to the original lattice. Furthermore, if we consider the Wannier states themselves, a C_{2x} transformation of the orbitals $p_x \pm ip_y \to p_x \mp ip_y$. Comparing this to a C_{2x} transformation of the valleys in Fig. 3.2 it is clear, that the orbitals transform into each other while the valleys transform into themselves. As we have argued that these two degrees of freedom are equivalent, the C_{2x} symmetry is evidently not respected by the effective orbitals. However, since the valleys are decoupled, flipping all valley indices will not affect the system globally. Thus we say that C_{2x} is implemented albeit only non-locally.
To figure out the effect of the non-local implementation of C_{2x} we consider the case, where the symmetry *is* locally implemented. We then have a C_{2y} symmetry flipping the valley index and a C_{2x} symmetry preserving the valley index. To represent the valley degree of freedom as an orbital degree of freedom, one should consider general effective orbitals respecting these transformation. As the two valleys are decoupled and related by time-reversal, we must have that the orbital basis is complex conjugated under C_{2y}. We write this generally as $o_1 \pm io_2$, where $o_{1,2}$ can be any atomic orbital, and we demand that the two orbitals have opposite parity under C_{2y}. In a similar manner, since C_{2x} does not flip the valley index, the two orbitals must have the same parity under C_{2x}. Now if all orbitals have the same parity under C_{2x} it directly follows that the overlap of two orbitals must have even parity under C_{2x}. From inspection of Fig. 4.8 we must then have that,

$$\sum_{\mathbf{r}\in\hexagon} w^*_{\mathbf{R}+\boldsymbol{\delta}_2}(\mathbf{r}) w_{\mathbf{R}+\boldsymbol{\delta}_3}(\mathbf{r}) = \sum_{\mathbf{r}\in\hexagon} w^*_{\mathbf{R}'+\boldsymbol{\delta}_6}(\mathbf{r}) w_{\mathbf{R}'+\boldsymbol{\delta}_5}(\mathbf{r}).$$

Recalling the orthogonality requirement of the Wannier states,

$$-\sum_{\mathbf{r}\in\hexagon} w^*_{\mathbf{R}+\boldsymbol{\delta}_2}(\mathbf{r}) w_{\mathbf{R}+\boldsymbol{\delta}_3}(\mathbf{r}) = \sum_{\mathbf{r}\in\hexagon} w^*_{\mathbf{R}'+\boldsymbol{\delta}_6}(\mathbf{r}) w_{\mathbf{R}'+\boldsymbol{\delta}_5}(\mathbf{r}),$$

we see that these two conditions combined directly leads to $\alpha_1 = 0$, i.e. all assisted hopping terms must vanish.
As previously mentioned, the reason for not implementing C_{2x} locally, is to preserve the Dirac points of the band structure. Since Dirac points have non-zero Chern numbers, reproducing these points is equivalent to a preservation of the topology. We conclude that the origin of $T_{j,\sigma}(\mathbf{R})$ is topological and reflects the presence of Dirac points. We will later see that the assisted hopping terms have significant impact on the preferred ground states.

Chapter 5

Full Model and Hartree-Fock Decoupling

In this chapter the goal is, first and foremost, to combine the tight-binding and interaction model. Once this is accomplished, we will perform a Hartree-Fock decoupling of the interaction terms enabling a concurrent, self-consistent solution of the TBG model. These two tasks will be performed in the first two sections. We will then proceed to consider the full model of TBG in reciprocal space and present the the Hartree-Fock decoupled Hamiltonian in the $\mathbf{q} = 0$, i.e. homogeneous, case. Solving the model in reciprocal space will provide direct access to the interaction-induced band structure modulations, thus adding additional insight to the results presented in the subsequent chapter.

5.1 Full model in real space

To obtain a model describing the bare, kinetic, bands as well as the interactions, the first step is to combine the two models in a common basis. The basis of our real space tight-binding model is simply $\mathbf{c}_i^\dagger = (c_{i,x}^\dagger, c_{i,y}^\dagger)$ (recall Eq. (4.6)), whereas the operators in the interaction model as described in Eq. (4.27) are labeled by valley and spin indices. As the tight-binding model is fully spin degenerate, we can directly expand Eq. (4.6) to include spin as follows,

$$H_{tb} = \sum_\sigma \Big[-\mu \sum_i \mathbf{c}_{i\sigma}^\dagger \cdot \mathbf{c}_{i\sigma} + t_1 \sum_{\langle ij \rangle} [\mathbf{c}_{i\sigma}^\dagger \cdot \mathbf{c}_{j\sigma} + h.c.] + t_2 \sum_{\langle ij \rangle'} [\mathbf{c}_{i\sigma}^\dagger \cdot \mathbf{c}_{j\sigma} + h.c.] + t_2' \sum_{\langle ij \rangle'} [(\mathbf{c}_{i\sigma}^\dagger \times \mathbf{c}_{j\sigma})_z + h.c.] \Big]. \tag{5.1}$$

This expression clearly preserves the four narrow bands of Fig. 4.6 but explicitly includes the spin degeneracy of each band. Next we consider the correspondence between orbital index and valley index. Thus far we have expressed the tight-binding model in terms of orbitals (p_x, p_y). To establish the one-to-one correspondence, we rotate $(p_x, p_y) \to (p_x \pm i p_y)$ and introduce $c_{i,\tau,\sigma}^\dagger = \frac{1}{\sqrt{2}}(c_{i,\tau,\sigma} + \tau i c_{i,\tau,\sigma})^\dagger$. We note again the highly counter-intuitive definition, that the orbitals $p_x \pm i p_y$ have $L_z^{orb} = \mp 1$ underlining the fact that this is merely an effective decription of the symmetries. The Wannier orbitals do not resemble the usual atomic $p_x \pm i p_y$ orbitals, which the reader is hopefully fully aware of by now. It can be easily verified that the rotation will only affect the last term of Eq. (5.1), and we get

$$\begin{aligned} H_{tb} = \sum_{j\sigma} \Big[& -\mu \sum_i c_{i,\tau,\sigma}^\dagger c_{i,\tau,\sigma} + t_1 \sum_{\langle ij \rangle} [c_{i,\tau,\sigma}^\dagger c_{j,\tau,\sigma} + h.c.] \\ & + t_2 \sum_{\langle ij \rangle'} [c_{i,\tau,\sigma}^\dagger c_{j,\tau,\sigma} + h.c.] \Big] + t_2' \sum_{\langle ij \rangle'} \sum_\sigma [-i(c_{i,+,\sigma}^\dagger c_{j,+,\sigma} - c_{i,-,\sigma}^\dagger c_{j,-,\sigma}) + h.c.], \end{aligned} \tag{5.2}$$

where τ indicates valley index. In the fifth NN terms, we only include the couplings depicted in Fig. 5.1, since (as discussed in Section 4.4) a double counting will cancel the last term. We

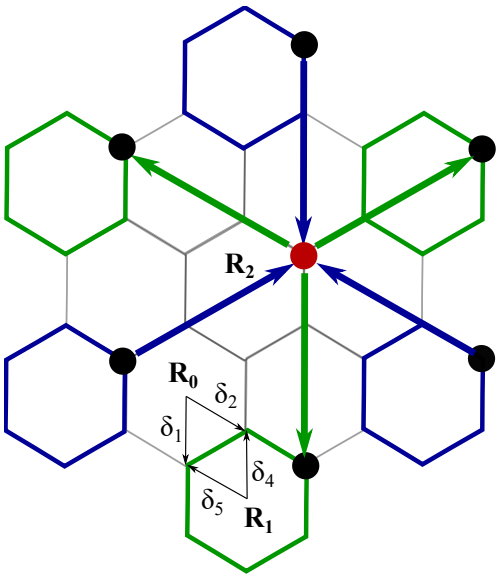

Figure 5.1: **Illustration of NN and fifth NN hoppings**. $\mathbf{R}_0 + \boldsymbol{\delta}_{1,2}$ and $\mathbf{R}_1 + \boldsymbol{\delta}_{4,5}$ illustrate NN hoppings. It is evident that $\left(c^\dagger_{\tau,\sigma}(\mathbf{R}_0 + \boldsymbol{\delta}_1)c_{\tau,\sigma}(\mathbf{R}_0 + \boldsymbol{\delta}_2)\right)^\dagger = c^\dagger_{\tau\sigma}(\mathbf{R}_1 + \boldsymbol{\delta}_4)c_{\tau\sigma}(\mathbf{R}_1 + \boldsymbol{\delta}_5)$. Green/blue arrows and hexagons illustrate the fifth NN hoppings. For fixed $\mathbf{R} = \mathbf{R}_2$, the red site corresponds to $p = 3$. By letting the $\mathbf{R}'$ summation in Eq. (5.3) run over the three NNN hexagons marked in green, we will couple to the correct sites if $p = 3$. The remaning three fifth NN couplings will be accounted for when $\mathbf{R}$ runs over the hexagons marked in blue, still fixing $p = 3$.

also note that this rotated tight-binding model manifests the time-reversal relation between the two valleys.

As a final step, we wish to label our sites by the hexagon, denoted by $\mathbf{R}$, and the site's postion within that hexagon, i.e. $n \to \mathbf{R} + \boldsymbol{\delta}_p$ for $p = 1, .., 6$, as in Eq. (4.27). The on-site terms are trivial, and we simply let $\sum_n \to \frac{1}{3}\sum_{\mathbf{R}}\sum_p$. The factor of one third accounts for the triple counting arising as each lattice site is associated with three hexagons. In the NN terms we use that e.g. $\left(c^\dagger_{\tau,\sigma}(\mathbf{R}_0+\boldsymbol{\delta}_1)c_{\tau,\sigma}(\mathbf{R}_0+\boldsymbol{\delta}_2)\right)^\dagger = c^\dagger_{\tau,\sigma}(\mathbf{R}_0+\boldsymbol{\delta}_2)c_{\tau,\sigma}(\mathbf{R}_0+\boldsymbol{\delta}_1) = c^\dagger_{\tau\sigma}(\mathbf{R}_1+\boldsymbol{\delta}_4)c_{\tau\sigma}(\mathbf{R}_1+\boldsymbol{\delta}_5)$, see Fig. 5.1. Thus we have that $\sum_{\langle ij\rangle}[c^\dagger_{i,\tau,\sigma}c_{j,\tau,\sigma} + h.c.] \to \sum_{\mathbf{R}}\sum_p d^\dagger_{\tau,\sigma}(\mathbf{R} + \boldsymbol{\delta}_p)d_{\tau,\sigma}(\mathbf{R} + \boldsymbol{\delta}_{p+1})$ will directly include the hermitian conjugation when performing the sum over $\mathbf{R}$. We have also renamed our operators to match the interaction model.

Next we consider the fifth NN hoppings illustrated in Fig. 5.1. As these are interhexagon couplings, we must introduce a sum over $\mathbf{R}'$, where $\mathbf{R}'$ are the three NNN hexagons marked in green in Fig. 5.1. We further note that all th NNs are positioned at the same site with respects to the hexagon center, i.e. $p' = p$ for all six interhexagon couplings. Finally we note that these terms, like the on-site terms, will all be accounted for three times when summing over all hexagons. Implementing all of these considerations in Eq. (5.2), we get

$$H_{tb} = \sum_{\mathbf{R}}\sum_{p,\tau,\sigma}\Big[-\frac{\mu}{3}d^\dagger_{\tau,\sigma}(\mathbf{R}+\boldsymbol{\delta}_p)d_{\tau,\sigma}(\mathbf{R}+\boldsymbol{\delta}_p) + t_1 d^\dagger_{\tau,\sigma}(\mathbf{R}+\boldsymbol{\delta}_p)d_{\tau,\sigma}(\mathbf{R}+\boldsymbol{\delta}_{p+1}) \\ + \frac{1}{3}\sum_{\mathbf{R}'}[(t_2 + (-\tau)it_2')d^\dagger_{\tau,\sigma}(\mathbf{R}+\boldsymbol{\delta}_p)d_{\tau,\sigma}(\mathbf{R}'+\boldsymbol{\delta}_p) + h.c.]\Big]. \tag{5.3}$$

This adaptation of the tight-binding model seemingly shares a common basis with the interaction model in Eq. (4.27). However, we remind the reader of the gauge transformation performed in

Section 4.5 to reach Eq. (4.27),

$$d_{\tau,\sigma}(\mathbf{R}+\boldsymbol{\delta}_p) \longrightarrow e^{i\tau\phi/2} d_{\tau,\sigma}(\mathbf{R}+\boldsymbol{\delta}_p), \qquad p\,\text{odd}$$
$$d_{\tau,\sigma}(\mathbf{R}+\boldsymbol{\delta}_p) \longrightarrow e^{-i\tau\phi/2} d_{\tau,\sigma}(\mathbf{R}+\boldsymbol{\delta}_p), \qquad p\,\text{even}.$$

To solve the combined model in a concurrent manner, we must of course implement this transformation in Eq. (5.3). First and foremost, it is easily verified that the phases will cancel for on-site and fifth NN terms. Thus we only need to consider additional phases in the NN hoppings, where we have for p odd

$$t_1 d^\dagger_{\tau,\sigma}(\mathbf{R}+\boldsymbol{\delta}_p) d_{\tau,\sigma}(\mathbf{R}+\boldsymbol{\delta}_{p+1}) \to t_1 e^{-i\tau\phi/2} d^\dagger_{\tau,\sigma}(\mathbf{R}+\boldsymbol{\delta}_p) e^{-i\tau\phi/2} d_{\tau,\sigma}(\mathbf{R}+\boldsymbol{\delta}_{p+1}),$$

and for p even,

$$t_1 d^\dagger_{\tau,\sigma}(\mathbf{R}+\boldsymbol{\delta}_p) d_{\tau,\sigma}(\mathbf{R}+\boldsymbol{\delta}_{p+1}) \to t_1 e^{i\tau\phi/2} d^\dagger_{\tau,\sigma}(\mathbf{R}+\boldsymbol{\delta}_p) e^{i\tau\phi/2} d_{\tau,\sigma}(\mathbf{R}+\boldsymbol{\delta}_{p+1}).$$

Combining these two expression yields

$$\begin{aligned} H_{tb} = \sum_{\mathbf{R}} \sum_{p,\tau,\sigma} \Big[&- \frac{\mu}{3} d^\dagger_{\tau,\sigma}(\mathbf{R}+\boldsymbol{\delta}_p) d_{\tau,\sigma}(\mathbf{R}+\boldsymbol{\delta}_p) + t_1 e^{(-1)^p i\tau\phi} d^\dagger_{\tau,\sigma}(\mathbf{R}+\boldsymbol{\delta}_p) d_{\tau,\sigma}(\mathbf{R}+\boldsymbol{\delta}_{p+1}) \\ &+ \frac{1}{3} \sum_{\mathbf{R}'} [(t_2 + (-\tau) i t_2') d^\dagger_{\tau,\sigma}(\mathbf{R}+\boldsymbol{\delta}_p) d_{\tau,\sigma}(\mathbf{R}'+\boldsymbol{\delta}_p) + h.c.] \Big]. \end{aligned} \tag{5.4}$$

It is now clear, that our interaction model in Eq. (4.27) and Eq. (5.4) share a common basis and the full model reads $H = H_{tb} + U$, where

$$\begin{aligned} U &= \frac{V_0}{2} \sum_{\mathbf{R}} (Q+T)(Q'+T'), \qquad \text{where} \\ Q &= \frac{1}{3} \sum_{j\sigma} \sum_{p=1}^{6} d^\dagger_{j\sigma}(\mathbf{R}+\boldsymbol{\delta}_p) d_{j\sigma}(\mathbf{R}+\boldsymbol{\delta}_p), \qquad \text{and} \\ T &= \alpha_1 \sum_{j\sigma} \sum_{p=1}^{6} (-1)^{p-1} \Big(d^\dagger_{j\sigma}(\mathbf{R}+\boldsymbol{\delta}_p) d_{j\sigma}(\mathbf{R}+\boldsymbol{\delta}_{p+1}) + h.c. \Big). \end{aligned} \tag{5.5}$$

We have shortened the notation slightly for readability. Primes on Q and T indicate primes on j, σ and p. We will now proceed to decouple the interaction terms to reach a final expression which can be solved self-consistently.

5.1.1 Hartree-Fock decoupling

A Hartree-Fock (HF) decoupling relies on the assumption that particles can be treated independently (i.e. one assumes the existence of an uncorrelated ground state) and that the density operators only deviate slightly from the average value. By considering a system of two distinguishable particles (a, b), we can then approximate their interaction as

$$\gamma\, a^\dagger a\, b^\dagger b \approx \gamma(\langle a^\dagger a\rangle + \delta_{aa})(\langle b^\dagger b\rangle + \delta_{bb}),$$

where γ sets the interaction strength and $\delta_{ff} = f^\dagger f - \langle f^\dagger f\rangle$ $(f = a, b)$ are the density operator's deviation from the average value. As we assume the deviations to be small, we drop the second order term in deviations and get

$$\gamma\, a^\dagger a\, b^\dagger b \approx \gamma(\langle a^\dagger a\rangle\langle b^\dagger b\rangle + \langle a^\dagger a\rangle b^\dagger b - \langle a^\dagger a\rangle\langle b^\dagger b\rangle + a^\dagger a\langle b^\dagger b\rangle - \langle a^\dagger a\rangle\langle b^\dagger b\rangle)$$

$$= \gamma(a^\dagger a\langle b^\dagger b\rangle + \langle a^\dagger a\rangle b^\dagger b - \langle a^\dagger a\rangle\langle b^\dagger b\rangle).$$

The last term ensures that $\gamma\langle a^\dagger a\, b^\dagger\rangle$ is unchanged by preserving the original energy reference. Within this approximation, we see that the average values of the density operators effectively act as a field coupling to the density operators of the opposite particle type. We thus refer to the average values as mean fields and the approximation is also known as a mean field approximation. The mean field approximation very effectively deals with the consistently recurring issue of four-operator interaction terms in many-body physics. However, a minor issue must be dealt with before decoupling our interaction: the particles of our system are fermions and *indistingushable* by definition. Fortunatly, we can rely on Wick's theorem, which states that any n-particle correlation function is given by the determinant of a matrix containing all of the single-particle Green's functions [27]. Using this on a general (same-time) two particle correlation function yields,

$$\langle c_\nu^\dagger c_\mu^\dagger c_{\mu'} c_{\nu'}\rangle = \begin{vmatrix} \langle c_\nu^\dagger c_{\nu'}\rangle & \langle c_\nu^\dagger c_{\mu'}\rangle \\ \langle c_\mu^\dagger c_{\nu'}\rangle & \langle c_\mu^\dagger c_{\mu'}\rangle \end{vmatrix} = \langle c_\nu^\dagger c_{\nu'}\rangle\langle c_\mu^\dagger c_{\mu'}\rangle - \langle c_\nu^\dagger c_{\mu'}\rangle\langle c_\mu^\dagger c_{\nu'}\rangle,$$

where ν, μ can be any quantum number labelling the states. The indistingushability of the particles is expressed by including the last term, since an operator combination with exchange in quantum numbers is treated on equal footing as the first, non-exchanged operator combinations, i.e. we cannot by measurement tell whether the particle is of type ν or μ. As Wick's theorem must hold before and after a decoupling, we include these new exchange terms when dealing with indistingushable particles. A general HF decoupling of a fermionic interaction term thus reads

$$c_\nu^\dagger c_\mu^\dagger c_{\mu'} c_{\nu'} \approx c_\nu^\dagger c_{\nu'}\langle c_\mu^\dagger c_{\mu'}\rangle + c_\mu^\dagger c_{\mu'}\langle c_\nu^\dagger c_{\nu'}\rangle - c_\mu^\dagger c_{\nu'}\langle c_\nu^\dagger c_{\mu'}\rangle - c_\nu^\dagger c_{\mu'}\langle c_\mu^\dagger c_{\nu'}\rangle + \langle c_\nu^\dagger c_{\nu'}\rangle\langle c_\mu^\dagger c_{\mu'}\rangle - \langle c_\nu^\dagger c_{\mu'}\rangle\langle c_\mu^\dagger c_{\nu'}\rangle.$$

This decoupling can be directly applied to the TBG interaction model. A short comment should be made about the ordering of our operators. The application of Wick's theorem, hence the HF decoupling itself, relies on normal ordering of the operators. At first glance, our interaction contains terms as $d_{p+1}^\dagger d_p d_{p'+1}^\dagger d_{p'} = \delta_{p,p'+1} d_{p+1}^\dagger d_{p'} + d_p^\dagger d_{p'+1}^\dagger d_{p'} d_p$, where we suppressed the $\mathbf{R}$-dependence as well as spin and valley indices. Evidently, normal ordering will introduce NNN hoppings in the kinetic Hamiltonian. From physical considerations, this seems highly illegitimate. The underlying reason for normal ordering in second quantization is to avoid divergencies of the vacuum energy, which should never affect the shape of the bands. It should most definitely not introduce new hoppings in a tight-binding model. Furthermore, our interaction model is derived from a Coulomb interaction, which does not affect the kinetics of a model through normal ordering. We must conclude, that these terms are an unphysical artefact of the projection and assume $U =: U :$ enabling the decoupling directly. We will drop the energy offset of the latter two terms in the decoupling which simply amounts to setting an arbitrary zero-energy reference.

The Hartree terms are all direct terms, i.e. terms *not* mixing primed and unprimed indices. We can thus separate all primed and unprimed summations yielding

$$\begin{aligned} U^H &= \frac{V_0}{2}\sum_{\mathbf{R}} \langle Q+T\rangle(Q'+T') + (Q+T)\langle Q'+T'\rangle \\ &= V_0 \sum_{\mathbf{R}} \bar{n}(\mathbf{R})(Q+T), \quad \text{where} \\ \bar{n}(\mathbf{R}) &= \langle Q'+T'\rangle \\ &= \sum_{\tau'\sigma'p'} \Big(\frac{1}{3}\langle d_{\tau',\sigma',p'}^\dagger d_{\tau',\sigma',p'}\rangle + \alpha_1(-1)^{p'-1}[\langle d_{\tau',\sigma',p'}^\dagger d_{\tau',\sigma',p'+1}\rangle + \langle d_{\tau',\sigma',p'+1}^\dagger d_{\tau',\sigma',p'}\rangle]\Big). \end{aligned}$$

In the first equality we use that primed and unprimed indices are dummy indices and can be exchanged. In the last expression we introduce p as subscript, making the $\mathbf{R}$-dependence implicit. Often when performing a HF decoupling, the Hartree terms will simply represent the individual particle's interaction with the average electron charge. This interaction usually enters as an overall shift of the chemical potential and effectively cancel the charge of ionic crystal background. When this is the case, the Hartree terms can be neglected in computations. In our model, due to the topological assisted hopping terms, some Hartree terms will be off-diagonal elements in the Hamiltonian. The off-diagonal terms will effectively shift the NN hopping, which will affect the actual shape of the bands. Allowing for inhomogeneous solutions, these terms alone could break the one or more spatial symmetries giving rise to e.g. density waves. With this in mind, the importance of including the Hartree terms in our computations is clear.

In the exchange terms (i.e. Fock terms) of the decoupling we can no longer separate our sums and we must progress more carefully. We will separate our considerations into three types, namely $Q \times Q'$, $Q \times T'$, and $T \times T'$ terms.
Starting with the $Q \times Q'$ terms, we get

$$\begin{aligned} U^F_{QQ} &\propto -\frac{1}{9}\sum_{\tau,\tau'}\sum_{\sigma,\sigma'}\sum_{p,p'}\left[\langle d^\dagger_{\tau,\sigma,p} d_{\tau',\sigma',p'}\rangle d^\dagger_{\tau',\sigma',p'} d_{\tau,\sigma,p} + \langle d^\dagger_{\tau',\sigma',p'} d_{\tau,\sigma,p}\rangle d^\dagger_{\tau,\sigma,p} d_{\tau',\sigma',p'}\right] \\ &= -\frac{2}{9}\sum_{\tau,\tau'}\sum_{\sigma,\sigma'}\sum_{p,p'}\langle d^\dagger_{\tau',\sigma',p'} d_{\tau,\sigma,p}\rangle d^\dagger_{\tau,\sigma,p} d_{\tau',\sigma',p'}. \end{aligned} \tag{5.6}$$

We drop the overall $\frac{V_0}{2}\sum_{\mathbf{R}}$ for now.
For the $Q \times T'$ terms we first note that $U^F_{QT'} = U^F_{TQ'}$. We thus get,

$$\begin{aligned} U^F_{QT} &= U^F_{QT'} + U^F_{TQ'} \\ &\propto -\frac{2\alpha_1}{3}\sum_{\tau\tau'}\sum_{\sigma\sigma'}\sum_{pp'}(-1)^{p'-1}\left[\langle d^\dagger_{\tau\sigma p} d_{\tau'\sigma'p'}\rangle d^\dagger_{\tau'\sigma'p'+1} d_{\tau\sigma p} + \langle d^\dagger_{\tau'\sigma'p'+1} d_{\tau\sigma p}\rangle d^\dagger_{\tau\sigma p} d_{\tau'\sigma'p'}\right. \\ &\quad \left. + \langle d^\dagger_{\tau\sigma p} d_{\tau'\sigma'p'+1}\rangle d^\dagger_{\tau'\sigma'p'} d_{\tau\sigma p} + \langle d^\dagger_{\tau'\sigma'p'} d_{\tau\sigma p}\rangle d^\dagger_{\tau\sigma p} d_{\tau'\sigma'p'+1}\right] \end{aligned}$$

In the final U^F expression we wish to combine all the terms into one prefactor containing the mean field parameters and just a single operator term. To get all operators in U^F_{QT} on the same form as the ones in U^F_{QQ}, we first exhange primed and unprimed indices in the first and third term. Second we need consider the p subscripts, where two facts are relevant: *i)* The p- and p'-summations run completely independent, *ii)* the p subscripts have periodic boundary conditions. These two facts allow us to shift the p' sum on all terms in U^F_{QT} independently. Doing so we get

$$\begin{aligned} U^F_{QT} \propto -\frac{2\alpha_1}{3}\sum_{\tau\tau'}\sum_{\sigma\sigma'}\sum_{pp'}&\left[(-1)^p\langle d^\dagger_{\tau'\sigma'p'} d_{\tau\sigma p-1}\rangle + (-1)^{p'-1}\langle d^\dagger_{\tau'\sigma'p'+1} d_{\tau\sigma p}\rangle\right. \\ &\left. + (-1)^{p-1}\langle d^\dagger_{\tau'\sigma'p'} d_{\tau\sigma p+1}\rangle + (-1)^{p'}\langle d^\dagger_{\tau'\sigma'p'-1} d_{\tau\sigma p}\rangle\right] d^\dagger_{\tau\sigma p} d_{\tau'\sigma'p'} \end{aligned} \tag{5.7}$$

where we have also used that $(-1)^{p'\pm 2} = (-1)^{p'}$. Moving on to U^F_{TT} we will have - as for U^F_{QQ} - all combinations twice with primed and unprimed indices exchanged. We account for this by a factor of two, and get

$$\begin{aligned} U^F_{TT} \propto -2\alpha_1^2\sum_{\tau,\tau'}\sum_{\sigma,\sigma'}\sum_{p,p'}(-1)^{p+p'}&\left[\langle d^\dagger_{\tau'\sigma'p'+1} d_{\tau\sigma p}\rangle d^\dagger_{\tau\sigma p+1} d_{\tau'\sigma'p'} + \langle d^\dagger_{\tau'\sigma'p'} d_{\tau\sigma p+1}\rangle d^\dagger_{\tau\sigma p} d_{\tau'\sigma'p'+1}\right. \\ &\left. + \langle d^\dagger_{\tau'\sigma'p'+1} d_{\tau\sigma p+1}\rangle d^\dagger_{\tau\sigma p} d_{\tau'\sigma'p'} + \langle d^\dagger_{\tau'\sigma'p'} d_{\tau\sigma p}\rangle d^\dagger_{\tau\sigma p+1} d_{\tau'\sigma'p'+1}\right] \end{aligned}$$

$$= -2\alpha_1^2 \sum_{\tau\tau'}\sum_{\sigma\sigma'}\sum_{pp'}\big[(-1)^{p-1+p'}\langle d^\dagger_{\tau'\sigma'p'+1}d_{\tau\sigma p-1}\rangle + (-1)^{p+p'-1}\langle d^\dagger_{\tau'\sigma'p'-1}d_{\tau\sigma p+1}\rangle$$
$$+ (-1)^{p+p'}\langle d^\dagger_{\tau'\sigma'p'+1}d_{\tau\sigma p+1}\rangle + (-1)^{p+p'}\langle d^\dagger_{\tau'\sigma'p'-1}d_{\tau\sigma p-1}\rangle\big]d^\dagger_{\tau\sigma p}d_{\tau'\sigma'p'} \tag{5.8}$$

where we have performed the same manipultations as in U^F_{QT}. Combining the three terms we get

$$\begin{aligned}
U^F &= U^F_{QQ} + U^F_{QT} + U^F_{TT} \\
&= -V_0\sum_{\mathbf{R}}\sum_{\tau\tau'}\sum_{\sigma\sigma'}\sum_{pp'}\Big[\frac{1}{9}\langle d^\dagger_{\tau'\sigma'p'}d_{\tau\sigma p}\rangle + \frac{\alpha_1}{3}\big[(-1)^p\langle d^\dagger_{\tau'\sigma'p'}d_{\tau\sigma p-1}\rangle + (-1)^{p'-1}\langle d^\dagger_{\tau'\sigma'p'+1}d_{\tau\sigma p}\rangle \\
&\quad + (-1)^{p-1}\langle d^\dagger_{\tau'\sigma'p'}d_{\tau\sigma p+1}\rangle + (-1)^{p'}\langle d^\dagger_{\tau'\sigma'p'-1}d_{\tau\sigma p}\rangle\big] \\
&\quad + \alpha_1^2\big[(-1)^{p-1+p'}\langle d^\dagger_{\tau'\sigma'p'+1}d_{\tau\sigma p-1}\rangle + (-1)^{p+p'-1}\langle d^\dagger_{\tau'\sigma'p'-1}d_{\tau\sigma p+1}\rangle \\
&\quad + (-1)^{p+p'}\langle d^\dagger_{\tau'\sigma'p'+1}d_{\tau\sigma p+1}\rangle + (-1)^{p+p'}\langle d^\dagger_{\tau'\sigma'p'-1}d_{\tau\sigma p-1}\rangle\big]\Big]d^\dagger_{\tau\sigma p}d_{\tau'\sigma'p'} \\
&= -V_0\sum_{\mathbf{R}}\sum_{\text{all}}\Big[\sum_{n,m}\alpha_n(p')\alpha_m(p)\langle d^\dagger_{\tau'\sigma'p'+n}d_{\tau\sigma p+m}\rangle\Big]d^\dagger_{\tau\sigma p}d_{\tau'\sigma'p'},
\end{aligned} \tag{5.9}$$

where $\sum_{\text{all}} = \Big(\sum_{\tau\tau'}\sum_{\sigma\sigma'}\sum_{pp'}\Big)$, $n,m = \{-1,0,1\}$ and we have defined,

$$\bar{\alpha}(p) = \begin{pmatrix}\alpha_{-1}\\ \alpha_0\\ \alpha_1\end{pmatrix} = \begin{pmatrix}\alpha_1(-1)^p\\ 1/3\\ \alpha_1(-1)^{p-1}\end{pmatrix}. \tag{5.10}$$

We have thus accomplished everything we set out to do in these first sections. The full Hamiltonian reads,

$$H = H_{tb} + U^{HF} \tag{5.11}$$

where

$$H_{tb} = \sum_{\mathbf{R}}\sum_{p,\tau,\sigma}\Big[-\frac{\mu}{3}d^\dagger_{\tau,\sigma}(\mathbf{R}+\delta_p)d_{\tau,\sigma}(\mathbf{R}+\delta_p) + t_1 e^{(-1)^p i\tau\phi}d^\dagger_{\tau,\sigma}(\mathbf{R}+\delta_p)d_{\tau,\sigma}(\mathbf{R}+\delta_{p+1}) \tag{5.12}$$
$$+ \frac{1}{3}\sum_{\mathbf{R}'}[(t_2 + (-\tau)it_2')d^\dagger_{\tau\sigma}(\mathbf{R}+\delta_p)d_{\tau\sigma}(\mathbf{R}'+\delta_p) + h.c.]\Big]$$

and

$$U^{HF} = V_0\sum_{\mathbf{R}}\Big[\bar{n}(\mathbf{R})(Q+T) - \sum_{\text{all}}\Big[\sum_{n,m}\alpha_n(p')\alpha_m(p)\langle d^\dagger_{\tau'\sigma'p'+n}d_{\tau\sigma p+m}\rangle\Big]d^\dagger_{\tau\sigma p}d_{\tau'\sigma'p'}\Big]. \tag{5.13}$$

5.2 Full model in reciprocal space

As mentioned in the short introduction to this chapter, we can gain direct access to interaction-induced modifications of the kinetic bands by performing a Fourier transformation (FT) and subsequent decoupling of the interaction model and combining it with the Fourier transformed tight-binding model. To maintain the sublattice degree of freedom in reciprocal space we will rewrite the interaction model in the Bravais lattice picture. However, as the model is already rather tedious, we will begin this section with a discussion of intricate details in the HF decoupling before transforming to the Bravais lattice picture.
We wish to perform FT of Eq. (5.5) and define the transformations as,

$$d_{\tau,\sigma}(\mathbf{R}+\boldsymbol{\delta}_p) = \frac{1}{\sqrt{N}}\sum_{\mathbf{k}\in BZ}e^{i\mathbf{k}(\mathbf{R}+\delta_p)}c_{\tau,\sigma,\mathbf{k}}\,,$$

$$d^\dagger_{\tau,\sigma}(\mathbf{R}+\delta_p) = \frac{1}{\sqrt{N}} \sum_{\mathbf{k}\in BZ} e^{-i\mathbf{k}(\mathbf{R}+\delta_p)} c^\dagger_{\tau,\sigma,\mathbf{k}} \tag{5.14}$$

where N is the number of sites and $\mathbf{k} = (k_x, k_y)$ are points within the first Brillouin zone. This definition leads to

$$Q_{\tau,\sigma}(\mathbf{R}) = \frac{1}{N}\sum_{p=1}^{6}\sum_{\mathbf{k},\mathbf{q}} e^{i\mathbf{q}(\mathbf{R}+\boldsymbol{\delta}_p)} c^\dagger_{\tau,\sigma,\mathbf{k}} c_{\tau,\sigma,\mathbf{k}+\mathbf{q}},$$

and

$$T_{\tau,\sigma}(\mathbf{R}) = \frac{1}{N}\sum_{p=1}^{6}(-1)^{p-1}\sum_{\mathbf{k},\mathbf{q}}\left(e^{i\mathbf{q}\cdot(\mathbf{R}+\delta_{p+1})}e^{i\mathbf{k}\cdot(\delta_{p+1}-\delta_p)}c^\dagger_{\tau,\sigma,\mathbf{k}}c_{\tau,\sigma,\mathbf{k}+\mathbf{q}} + e^{-i\mathbf{q}(\mathbf{R}+\delta_{p+1})}e^{-i\mathbf{k}\cdot(\delta_{p+1}-\delta_p)}c^\dagger_{\tau,\sigma,\mathbf{k}+\mathbf{q}}c_{\tau,\sigma,\mathbf{k}}\right)$$

where $\mathbf{q} = \mathbf{k}' - \mathbf{k}$. We have suppressed the restriction on the $\mathbf{k}$-,$\mathbf{q}$-summations.
Inserting in Eq. (5.5) and simplifying, one finds

$$\begin{aligned}
U \quad = \frac{V_0}{2N}\sum_{\tau,\tau'}\sum_{\sigma,\sigma'}\sum_{\mathbf{k},\mathbf{k}',\mathbf{q}}\sum_{p,p'}\Bigg(&\Big(\frac{1}{3}e^{i\mathbf{q}\cdot\boldsymbol{\delta}_p} + \alpha_1(-1)^{p-1}e^{i\mathbf{q}\cdot\delta_{p+1}}e^{i\mathbf{k}\cdot(\delta_{p+1}-\delta_p)}\Big)\\
&\times\Big(\frac{1}{3}e^{-i\mathbf{q}\cdot\delta_{p'}} + \alpha_1(-1)^{p'-1}e^{-i\mathbf{q}\cdot\delta_{p'+1}}e^{i\mathbf{k}'\cdot(\delta_{p'+1}-\delta_{p'})}\Big)c^\dagger_{\tau,\sigma,\mathbf{k}}c_{\tau,\sigma,\mathbf{k}+\mathbf{q}}c^\dagger_{\tau',\sigma',\mathbf{k}'}c_{\tau',\sigma',\mathbf{k}'-\mathbf{q}}\\
&+\Big(\alpha_1(-1)^{p-1}e^{-i\mathbf{q}\cdot\delta_{p+1}}e^{-i\mathbf{k}\cdot(\delta_{p+1}-\delta_p)}\Big)\\
&\times\Big(\frac{1}{3}e^{i\mathbf{q}\cdot\delta_{p'}} + \alpha_1(-1)^{p'-1}e^{i\mathbf{q}\cdot\delta_{p'+1}}e^{i\mathbf{k}'\cdot(\delta_{p'+1}-\delta_{p'})}\Big)c^\dagger_{\tau,\sigma,\mathbf{k}+\mathbf{q}}c_{\tau,\sigma,\mathbf{k}}c^\dagger_{\tau',\sigma',\mathbf{k}'}c_{\tau',\sigma',\mathbf{k}'+\mathbf{q}}\\
&+\Big(\frac{1}{3}e^{i\mathbf{q}\cdot\delta_p} + \alpha_1(-1)^{p-1}e^{i\mathbf{q}\cdot\delta_{p+1}}e^{i\mathbf{k}\cdot(\delta_{p+1}-\delta_p)}\Big)\\
&\times\Big(\alpha_1(-1)^{p'-1}e^{-i\mathbf{q}\cdot\delta_{p'+1}}e^{-i\mathbf{k}'\cdot(\delta_{p'+1}-\delta_{p'})}\Big)c^\dagger_{\tau,\sigma,\mathbf{k}}c_{\tau,\sigma,\mathbf{k}+\mathbf{q}}c^\dagger_{\tau',\sigma',\mathbf{k}'+\mathbf{q}}c_{\tau',\sigma',\mathbf{k}'}\\
&+\Big(\alpha_1(-1)^{p-1}e^{-i\mathbf{q}\cdot\delta_{p+1}}e^{-i\mathbf{k}\cdot(\delta_{p+1}-\delta_p)}\Big)\\
&\times\Big(\alpha_1(-1)^{p'-1}e^{i\mathbf{q}\cdot\delta_{p'+1}}e^{-i\mathbf{k}'\cdot(\delta_{p'+1}-\delta_{p'})}\Big)c^\dagger_{\tau,\sigma,\mathbf{k}+\mathbf{q}}c_{\tau,\sigma,\mathbf{k}}c^\dagger_{\tau',\sigma',\mathbf{k}'-\mathbf{q}}c_{\tau',\sigma',\mathbf{k}'}\Bigg).
\end{aligned}\tag{5.15}$$

The full derivation can be seen in Appendix B. Due to the rather complicated form factors it is unclear whether the operators can be collected to a single term. We thus proceed be considering separate decouplings of each term.
Decoupling the operators of the first term in Eq. (5.15) yields,

$$\begin{aligned}
c^\dagger_{\tau,\sigma,\mathbf{k}}c^\dagger_{\tau',\sigma',\mathbf{k}'}c_{\tau',\sigma',\mathbf{k}'-\mathbf{q}}c_{\tau,\sigma,\mathbf{k}+\mathbf{q}} \approx{}& \langle c^\dagger_{\tau',\sigma',\mathbf{k}'}c_{\tau',\sigma',\mathbf{k}'-\mathbf{q}}\rangle c^\dagger_{\tau,\sigma,\mathbf{k}}c_{\tau,\sigma,\mathbf{k}+\mathbf{q}} + \langle c^\dagger_{\tau,\sigma,\mathbf{k}}c_{\tau,\sigma,\mathbf{k}+\mathbf{q}}\rangle c^\dagger_{\tau',\sigma',\mathbf{k}'}c_{\tau',\sigma',\mathbf{k}'-\mathbf{q}}\\
&- \langle c^\dagger_{\tau',\sigma',\mathbf{k}'}c_{\tau,\sigma,\mathbf{k}+\mathbf{q}}\rangle c^\dagger_{\tau,\sigma,\mathbf{k}}c_{\tau',\sigma',\mathbf{k}'-\mathbf{q}} - \langle c^\dagger_{\tau,\sigma,\mathbf{k}}c_{\tau',\sigma',\mathbf{k}'-\mathbf{q}}\rangle c^\dagger_{\tau',\sigma',\mathbf{k}'}c_{\tau,\sigma,\mathbf{k}+\mathbf{q}},
\end{aligned}$$

where we have dropped the energy offset. Clearly, if we impose no further restrictions, we are left with an overwhelming amount of terms. As we have no general knowledge of specific $\mathbf{q}$-modulated phases, we choose to study all homogeneous instabilities, i.e. set $\langle c^\dagger_{j,\sigma,\mathbf{k}}c_{j',\sigma',\mathbf{k}'}\rangle = \delta_{\mathbf{k},\mathbf{k}'}\langle c^\dagger_{j,\sigma,\mathbf{k}}c_{j',\sigma',\mathbf{k}'}\rangle$. When including the $\mathbf{k}$-,$\mathbf{k}'$- and $\mathbf{q}$-summation, this yields

$$\begin{aligned}
\sum_{\mathbf{k},\mathbf{k}',\mathbf{q}} c^\dagger_{\tau,\sigma,\mathbf{k}}c^\dagger_{\tau',\sigma',\mathbf{k}'}c_{\tau',\sigma',\mathbf{k}'-\mathbf{q}}c_{\tau,\sigma,\mathbf{k}+\mathbf{q}} \approx \sum_{\mathbf{k},\mathbf{k}',\mathbf{q}}\Big(&\delta_{\mathbf{q},0}\big[\langle c^\dagger_{\tau',\sigma',\mathbf{k}'}c_{\tau',\sigma',\mathbf{k}'-\mathbf{q}}\rangle c^\dagger_{\tau,\sigma,\mathbf{k}}c_{\tau,\sigma,\mathbf{k}+\mathbf{q}} + \langle c^\dagger_{\tau,\sigma,\mathbf{k}}c_{\tau,\sigma,\mathbf{k}+\mathbf{q}}\rangle c^\dagger_{\tau',\sigma',\mathbf{k}'}c_{\tau',\sigma',\mathbf{k}'-\mathbf{q}}\big]\\
&- \delta_{\mathbf{k}',\mathbf{k}+\mathbf{q}}\big[\langle c^\dagger_{\tau',\sigma',\mathbf{k}'}c_{\tau,\sigma,\mathbf{k}+\mathbf{q}}\rangle c^\dagger_{\tau,\sigma,\mathbf{k}}c_{\tau',\sigma',\mathbf{k}'-\mathbf{q}} - \langle c^\dagger_{\tau,\sigma,\mathbf{k}}c_{\tau',\sigma',\mathbf{k}'-\mathbf{q}}\rangle c^\dagger_{\tau',\sigma',\mathbf{k}'}c_{\tau,\sigma,\mathbf{k}+\mathbf{q}}\big]\Big)
\end{aligned}$$

$$= \sum_{\mathbf{k},\mathbf{k}'} \Big(\big[\langle c^\dagger_{\tau',\sigma',\mathbf{k}'} c_{\tau',\sigma',\mathbf{k}'} \rangle c^\dagger_{\tau,\sigma,\mathbf{k}} c_{\tau,\sigma,\mathbf{k}} + \langle c^\dagger_{\tau,\sigma,\mathbf{k}} c_{\tau,\sigma,\mathbf{k}} \rangle c^\dagger_{\tau',\sigma',\mathbf{k}'} c_{\tau',\sigma',\mathbf{k}'} \big] \\ - \big[\langle c^\dagger_{\tau',\sigma',\mathbf{k}'} c_{\tau,\sigma,\mathbf{k}'} \rangle c^\dagger_{\tau,\sigma,\mathbf{k}} c_{\tau',\sigma',\mathbf{k}} + \langle c^\dagger_{\tau,\sigma,\mathbf{k}} c_{\tau',\sigma',\mathbf{k}} \rangle c^\dagger_{\tau',\sigma',\mathbf{k}'} c_{\tau,\sigma,\mathbf{k}'} \big] \Big)$$

Inspecting Eq. (5.15) one finds that the form factors in this first term is equal in unprimed and primed indices. We can thus exchange the two and find

$$\sum_{\mathbf{k},\mathbf{k}',\mathbf{q}} c^\dagger_{\tau,\sigma,\mathbf{k}} c^\dagger_{\tau',\sigma',\mathbf{k}'} c_{\tau',\sigma',\mathbf{k}'-\mathbf{q}} c_{\tau,\sigma,\mathbf{k}+\mathbf{q}} \approx 2 \sum_{\mathbf{k}} \big[\bar{n}^{\sigma'\sigma'}_{\tau'\tau'} c^\dagger_{\tau,\sigma,\mathbf{k}} c_{\tau,\sigma,\mathbf{k}} - \bar{n}^{\sigma'\sigma}_{\tau'\tau} c^\dagger_{\tau,\sigma,\mathbf{k}} c_{\tau',\sigma',\mathbf{k}} \big],$$

where $\bar{n}^{\sigma\sigma'}_{\tau\tau'} = \sum_{\mathbf{k}'} \langle c^\dagger_{\tau,\sigma,\mathbf{k}'} c_{\tau',\sigma',\mathbf{k}'} \rangle$. From this we gather, that by decoupling the first term in Eq. (5.15), $U^{(1)}$, we can write $U^{(1)} = \sum_{\mathbf{k}} \mathbf{c}^\dagger_{\mathbf{k}} \mathcal{U}_{\mathbf{k}} \mathbf{c}_{\mathbf{k}}$, where the $\mathbf{k}'$-sum is contained in $\mathcal{U}_{\mathbf{k}}$ and completely separated from the $\mathbf{k}$-dependence. This result is well-known from e.g. the Stoner model and yields no complications when setting up the self-consistent solution. However, when applying the homogeneity condition to the second term, we get

$$\begin{aligned} c^\dagger_{\tau,\sigma,\mathbf{k}+\mathbf{q}} c^\dagger_{\tau',\sigma',\mathbf{k}'} c_{\tau',\sigma',\mathbf{k}'+\mathbf{q}} c_{\tau,\sigma,\mathbf{k}} \approx{}& \langle c^\dagger_{\tau',\sigma',\mathbf{k}'} c_{\tau',\sigma',\mathbf{k}'+\mathbf{q}} \rangle c^\dagger_{\tau,\sigma,\mathbf{k}+\mathbf{q}} c_{\tau,\sigma,\mathbf{k}} + \langle c^\dagger_{\tau,\sigma,\mathbf{k}+\mathbf{q}} c_{\tau,\sigma,\mathbf{k}} \rangle c^\dagger_{\tau',\sigma',\mathbf{k}'} c_{\tau',\sigma',\mathbf{k}'+\mathbf{q}} \\ &- \langle c^\dagger_{\tau',\sigma',\mathbf{k}'} c_{\tau,\sigma,\mathbf{k}} \rangle c^\dagger_{\tau,\sigma,\mathbf{k}+\mathbf{q}} c_{\tau',\sigma',\mathbf{k}'+\mathbf{q}} - \langle c^\dagger_{\tau,\sigma,\mathbf{k}+\mathbf{q}} c_{\tau',\sigma',\mathbf{k}'+\mathbf{q}} \rangle c^\dagger_{\tau',\sigma',\mathbf{k}'} c_{\tau,\sigma,\mathbf{k}} \\ ={}& \delta_{\mathbf{q},0} \big[\langle c^\dagger_{\tau',\sigma',\mathbf{k}'} c_{\tau',\sigma',\mathbf{k}'+\mathbf{q}} \rangle c^\dagger_{\tau,\sigma,\mathbf{k}+\mathbf{q}} c_{\tau,\sigma,\mathbf{k}} + \langle c^\dagger_{\tau,\sigma,\mathbf{k}+\mathbf{q}} c_{\tau,\sigma,\mathbf{k}} \rangle c^\dagger_{\tau',\sigma',\mathbf{k}'} c_{\tau',\sigma',\mathbf{k}'+\mathbf{q}} \big] \\ &- \delta_{\mathbf{k}',\mathbf{k}} \big[\langle c^\dagger_{\tau',\sigma',\mathbf{k}'} c_{\tau,\sigma,\mathbf{k}} \rangle c^\dagger_{\tau,\sigma,\mathbf{k}+\mathbf{q}} c_{\tau',\sigma',\mathbf{k}'+\mathbf{q}} - \langle c^\dagger_{\tau,\sigma,\mathbf{k}+\mathbf{q}} c_{\tau',\sigma',\mathbf{k}'+\mathbf{q}} \rangle c^\dagger_{\tau',\sigma',\mathbf{k}'} c_{\tau,\sigma,\mathbf{k}} \big], \end{aligned}$$

leaving no restriction on $\mathbf{q}$ in the exchange terms. To obtain a solution where we can write $U^{(2)}$ in terms of a $\mathbf{q}$-independent spinor (as was the case for $U^{(1)} = \sum_{\mathbf{k}} \mathbf{c}^\dagger_{\mathbf{k}} \mathcal{U}_{\mathbf{k}} \mathbf{c}_{\mathbf{k}}$) we must perform a shift in momenta such that e.g. $c^\dagger_{\tau,\sigma,\mathbf{k}+\mathbf{q}} c^\dagger_{\tau',\sigma',\mathbf{k}'} c_{\tau',\sigma',\mathbf{k}'+\mathbf{q}} c_{\tau,\sigma,\mathbf{k}} \to c^\dagger_{\tau,\sigma,\mathbf{k}+\mathbf{q}} c^\dagger_{\tau',\sigma',\mathbf{k}'-\mathbf{q}} c_{\tau',\sigma',\mathbf{k}'} c_{\tau,\sigma,\mathbf{k}}$, i.e. $\mathbf{k}' \to \mathbf{k}' - \mathbf{q}$. In a simpler model such shifts can be performed with no further considerations as the $\mathbf{k}'$-sum runs independently over the entire first BZ. Even if $\mathbf{k}' - \mathbf{q}$ resides outside the first BZ, it is related to a point within the first BZ through a reciprocal vector, and thus will be included in the sum. The complicated form factors of our model makes the validity of any such shift less straightforward. A detailed discussion of said shift is presented in Appendix C. Here we merely state that we can indeed shift the momentum dependence independently in each term. Applying this to the second term now yields,

$$\begin{aligned} \sum_{\mathbf{k},\mathbf{k}',\mathbf{q}} c^\dagger_{\tau,\sigma,\mathbf{k}+\mathbf{q}} c^\dagger_{\tau',\sigma',\mathbf{k}'-\mathbf{q}} c_{\tau',\sigma',\mathbf{k}'} c_{\tau,\sigma,\mathbf{k}} \approx{}& \sum_{\mathbf{k},\mathbf{k}',\mathbf{q}} \Big(\delta_{\mathbf{q},0} \big[\langle c^\dagger_{\tau',\sigma',\mathbf{k}'-\mathbf{q}} c_{\tau',\sigma',\mathbf{k}'} \rangle c^\dagger_{\tau,\sigma,\mathbf{k}+\mathbf{q}} c_{\tau,\sigma,\mathbf{k}} + \langle c^\dagger_{\tau,\sigma,\mathbf{k}+\mathbf{q}} c_{\tau,\sigma,\mathbf{k}} \rangle c^\dagger_{\tau',\sigma',\mathbf{k}'-\mathbf{q}} c_{\tau',\sigma',\mathbf{k}'} \big] \\ &- \delta_{\mathbf{k}',\mathbf{k}+\mathbf{q}} \big[\langle c^\dagger_{\tau',\sigma',\mathbf{k}'-\mathbf{q}} c_{\tau,\sigma,\mathbf{k}} \rangle c^\dagger_{\tau,\sigma,\mathbf{k}+\mathbf{q}} c_{\tau',\sigma',\mathbf{k}'} - \langle c^\dagger_{\tau,\sigma,\mathbf{k}+\mathbf{q}} c_{\tau',\sigma',\mathbf{k}'} \rangle c^\dagger_{\tau',\sigma',\mathbf{k}'-\mathbf{q}} c_{\tau,\sigma,\mathbf{k}} \big] \Big) \\ ={}& \sum_{\mathbf{k},\mathbf{k}'} \Big(\big[\langle c^\dagger_{\tau',\sigma',\mathbf{k}'} c_{\tau',\sigma',\mathbf{k}'} \rangle c^\dagger_{\tau,\sigma,\mathbf{k}} c_{\tau,\sigma,\mathbf{k}} + \langle c^\dagger_{\tau,\sigma,\mathbf{k}} c_{\tau,\sigma,\mathbf{k}} \rangle c^\dagger_{\tau',\sigma',\mathbf{k}'} c_{\tau',\sigma',\mathbf{k}'} \big] \\ &- \big[\langle c^\dagger_{\tau',\sigma',\mathbf{k}} c_{\tau,\sigma,\mathbf{k}} \rangle c^\dagger_{\tau,\sigma,\mathbf{k}'} c_{\tau',\sigma',\mathbf{k}'} - \langle c^\dagger_{\tau,\sigma,\mathbf{k}'} c_{\tau',\sigma',\mathbf{k}'} \rangle c^\dagger_{\tau',\sigma',\mathbf{k}} c_{\tau,\sigma,\mathbf{k}} \big] \Big). \end{aligned}$$

We can now write $U^{(2)} = \sum_{\mathbf{k}} \mathbf{c}^\dagger_{\mathbf{k}} \mathcal{U}_{\mathbf{k}} \mathbf{c}_{\mathbf{k}}$ by performing similar manipulations as for $U^{(1)}$. The considerations and final structure of the homogeneous, HF decoupled interaction model in reciprocal space presented in this section is equally valid in the Bravais lattice picture.

5.2.1 Interaction model in the Bravais lattice picture

Before expanding the interaction model to the Bravais lattice picture, we briefly mention the manipulations of the tight-binding model required to obtain a common basis of the two models. As in the real space case, we can easily expand the model to include spin due to the $SU(2)$ symmetry. Furthermore we rotate the basis $\begin{pmatrix} a^\dagger_{x,\sigma,\mathbf{k}} & a^\dagger_{y,\sigma,\mathbf{k}} & b^\dagger_{x,\sigma,\mathbf{k}} & b^\dagger_{y,\sigma,\mathbf{k}} \end{pmatrix} \rightarrow \begin{pmatrix} a^\dagger_{+,\sigma,\mathbf{k}} & a^\dagger_{-,\sigma,\mathbf{k}} & b^\dagger_{+,\sigma,\mathbf{k}} & b^\dagger_{-,\sigma,\mathbf{k}} \end{pmatrix}$, where $c^\dagger_{\tau,\sigma,\mathbf{k}} = (c_{x,\sigma,\mathbf{k}} + \tau i c_{y,\sigma,\mathbf{k}})^\dagger/\sqrt{2}$ with $c = a, b$ and $L_z^{orb} = -\tau$. Applying the expansion and rotation to Eq. (4.13) yields,

$$H_{tb} = \sum_{\mathbf{k}\in BZ} \mathbf{f}^\dagger_{\mathbf{k}} \begin{pmatrix} \tilde{t_-}(\mathbf{k}) & 0 & 0 & 0 & \tilde{t_1}(\mathbf{k}) & 0 & 0 & 0 \\ 0 & \tilde{t_+}(\mathbf{k}) & 0 & 0 & 0 & \tilde{t_1}(\mathbf{k}) & 0 & 0 \\ 0 & 0 & \tilde{t_-}(\mathbf{k}) & 0 & 0 & 0 & \tilde{t_1}(\mathbf{k}) & 0 \\ 0 & 0 & 0 & \tilde{t_+}(\mathbf{k}) & 0 & 0 & 0 & \tilde{t_1}(\mathbf{k}) \\ \tilde{t_1}^*(\mathbf{k}) & 0 & 0 & 0 & \tilde{t_-}(\mathbf{k}) & 0 & 0 & 0 \\ 0 & \tilde{t_1}^*(\mathbf{k}) & 0 & 0 & 0 & \tilde{t_+}(\mathbf{k})) & 0 & 0 \\ 0 & 0 & \tilde{t_1}^*(\mathbf{k}) & 0 & 0 & 0 & \tilde{t_-}(\mathbf{k}) & 0 \\ 0 & 0 & 0 & \tilde{t_1}^*(\mathbf{k}) & 0 & 0 & 0 & \tilde{t_+}(\mathbf{k}) \end{pmatrix} \mathbf{f}_{\mathbf{k}}, \quad (5.16)$$

where $\mathbf{f}^\dagger_{\mathbf{k}} = \begin{pmatrix} a^\dagger_{+\uparrow\mathbf{k}} & a^\dagger_{-\uparrow\mathbf{k}} & a^\dagger_{+\downarrow\mathbf{k}} & a^\dagger_{-\downarrow\mathbf{k}} & b^\dagger_{+\uparrow\mathbf{k}} & b^\dagger_{-\uparrow\mathbf{k}} & b^\dagger_{+\downarrow\mathbf{k}} & b^\dagger_{-\downarrow\mathbf{k}} \end{pmatrix}$ and $\tilde{t_\pm}(\mathbf{k}) = -\mu + \tilde{t_2}(\mathbf{k}) \pm i\tilde{t_2'}(\mathbf{k})$. Recall that $\tilde{t_2'}(\mathbf{k})$ is purely imaginary. We write this as

$$H_{tb} = \sum_{\mathbf{k}\in BZ} \mathbf{f}^\dagger_{\mathbf{k}}[-\mu + \tilde{t_2}(\mathbf{k})]s_0\sigma_0\tau_0 - i\tilde{t_2'}(\mathbf{k})s_0\sigma_0\tau_z + Re[\tilde{t_1}(\mathbf{k})]s_x\sigma_0\tau_0 + Im[\tilde{t_1}(\mathbf{k})]s_y\sigma_0\tau_0, \quad (5.17)$$

where s_i, σ_i, τ_i $(i = 0, 1, 2, 3)$ are the Pauli matrices in sublattice, spin and valley space, respectively. Finally, we incorporate the gauge transformation. Recall that $t_1 \rightarrow t_1 e^{(-1)^p i\tau\phi}$ in real space. This phase can be pulled straight through the FT, and we incorporate it by simply letting $\tilde{t_1}(\mathbf{k}) \rightarrow \tilde{t_1}(\mathbf{k})e^{i\tau\phi}$. Here we have used that AB-sites (a operators) corresponds to p even and BA-sites (b operators) corresponds to p odd. This is easily verified by inspection of Figs. 4.5 and 4.8. Thus the site-dependent sign is already incorporated through complex conjugation in Eq. (5.16) and we can now focus our attention on the interaction model.

To represent U in the Bravais lattice picture, we return to the original real space representation. The real space interactions reads

$$U = \frac{V_0}{2} \sum_{\mathbf{R}} \sum_{\tau,\tau'} \sum_{\sigma,\sigma'} \left(\frac{1}{3} Q_{\tau,\sigma}(\mathbf{R}) + \alpha_1 T_{\tau,\sigma}(\mathbf{R}) \right) \left(\frac{1}{3} Q_{\tau',\sigma'}(\mathbf{R}) + \alpha_1 T_{\tau',\sigma'}(\mathbf{R}) \right), \quad \text{where} \quad (5.18)$$

$$Q_{\tau,\sigma}(\mathbf{R}) = \sum_{p=1}^{6} d^\dagger_{\tau,\sigma}(\mathbf{R} + \boldsymbol{\delta}_p) d_{\tau,\sigma}(\mathbf{R} + \boldsymbol{\delta}_p), \qquad \text{and}$$

$$T_{\tau,\sigma}(\mathbf{R}) = \sum_{p=1}^{6} (-1)^{p-1} \Big(d^\dagger_{\tau,\sigma}(\mathbf{R} + \boldsymbol{\delta}_p) d_{\tau,\sigma}(\mathbf{R} + \boldsymbol{\delta}_{p+1}) + h.c. \Big).$$

This can be written as,

$$\begin{aligned} Q_{\tau,\sigma}(\mathbf{R}) &= \sum_{p\,\text{even}} a^\dagger_{\tau,\sigma}(\mathbf{R}+\boldsymbol{\delta}_p)a_{\tau,\sigma}(\mathbf{R}+\boldsymbol{\delta}_p) + \sum_{p\,\text{odd}} b^\dagger_{\tau,\sigma}(\mathbf{R}+\boldsymbol{\delta}_p)b_{\tau,\sigma}(\mathbf{R}+\boldsymbol{\delta}_p) \\ &= \sum_{p=2,4,6} (a^\dagger_{\tau,\sigma}(\mathbf{R}+\boldsymbol{\delta}_p)a_{\tau,\sigma}(\mathbf{R}+\boldsymbol{\delta}_p) + b^\dagger_{\tau,\sigma}(\mathbf{R}+\boldsymbol{\delta}_{p+1})b_{\tau,\sigma}(\mathbf{R}+\boldsymbol{\delta}_{p+1})), \end{aligned} \tag{5.19}$$

where a (b) operators correspond to AB-sites (BA-sites) as usual. The assisted hopping terms are

$$\begin{aligned} T_{\tau,\sigma}(\mathbf{R}) &= -\sum_{p\,\text{even}} \Big(a^\dagger_{\tau,\sigma}(\mathbf{R}+\boldsymbol{\delta}_p)b_{\tau,\sigma}(\mathbf{R}+\boldsymbol{\delta}_{p+1}) + h.c.\Big) + \sum_{p\,\text{odd}} \Big(b^\dagger_{\tau,\sigma}(\mathbf{R}+\boldsymbol{\delta}_p)a_{\tau,\sigma}(\mathbf{R}+\boldsymbol{\delta}_{p+1}) + h.c.\Big) \\ &= \sum_{p=2,4,6} \Big[- a^\dagger_{\tau,\sigma}(\mathbf{R}+\boldsymbol{\delta}_p)b_{\tau,\sigma}(\mathbf{R}+\boldsymbol{\delta}_{p+1}) + b^\dagger_{\tau,\sigma}(\mathbf{R}+\boldsymbol{\delta}_{p+1})a_{\tau,\sigma}(\mathbf{R}+\boldsymbol{\delta}_{p+2}) + h.c.\Big]. \end{aligned} \tag{5.20}$$

Note the periodic boundary conditions. The Fourier transformations reads,

$$\begin{aligned} a_{\tau,\sigma}(\mathbf{R}+\boldsymbol{\delta}_p) &= \frac{1}{\sqrt{\tilde{N}}}\sum_{\mathbf{k}\in BZ} e^{i\mathbf{k}(\mathbf{R}+\boldsymbol{\delta}_p)}a_{\tau,\sigma,\mathbf{k}}, \\ a^\dagger_{\tau,\sigma}(\mathbf{R}+\boldsymbol{\delta}_p) &= \frac{1}{\sqrt{\tilde{N}}}\sum_{\mathbf{k}\in BZ} e^{-i\mathbf{k}(\mathbf{R}+\boldsymbol{\delta}_p)}a^\dagger_{\tau,\sigma,\mathbf{k}}, \\ b_{\tau,\sigma}(\mathbf{R}+\boldsymbol{\delta}_p) &= \frac{1}{\sqrt{\tilde{N}}}\sum_{\mathbf{k}\in BZ} e^{i\mathbf{k}(\mathbf{R}+\boldsymbol{\delta}_p)}b_{\tau,\sigma,\mathbf{k}}, \\ b^\dagger_{\tau,\sigma}(\mathbf{R}+\boldsymbol{\delta}_p) &= \frac{1}{\sqrt{\tilde{N}}}\sum_{\mathbf{k}\in BZ} e^{-i\mathbf{k}(\mathbf{R}+\boldsymbol{\delta}_p)}b^\dagger_{\tau,\sigma,\mathbf{k}}, \end{aligned} \tag{5.21}$$

where $\tilde{N}$ is now the number of unit cells. Performing the transformations, we get

$$\begin{aligned} Q_{\tau,\sigma}(\mathbf{R}) &= \frac{1}{\tilde{N}}\sum_{\mathbf{k},\mathbf{q}}\sum_{p=2,4,6}\big(e^{i\mathbf{q}(\mathbf{R}+\boldsymbol{\delta}_p)}a^\dagger_{\tau\sigma\mathbf{k}}a_{\tau\sigma\mathbf{k}+\mathbf{q}} + e^{i\mathbf{q}(\mathbf{R}+\boldsymbol{\delta}_{p+1})}b^\dagger_{\tau\sigma\mathbf{k}}b_{\tau\sigma\mathbf{k}+\mathbf{q}}\big), \\ T_{\tau,\sigma}(\mathbf{R}) &= \frac{1}{\tilde{N}}\sum_{\mathbf{k},\mathbf{q}}\sum_{p=2,4,6}\Big[e^{i\mathbf{q}\mathbf{R}}e^{i\mathbf{q}\boldsymbol{\delta}_{p+1}}(e^{i\mathbf{k}\boldsymbol{\delta}_p} - e^{i\mathbf{k}\boldsymbol{\delta}_{p+2}})a^\dagger_{\tau\sigma\mathbf{k}}b_{\tau\sigma\mathbf{k}+\mathbf{q}} \\ &\quad + e^{-i\mathbf{q}\mathbf{R}}e^{-i\mathbf{q}\boldsymbol{\delta}_{p+1}}(e^{-i\mathbf{k}\boldsymbol{\delta}_p} - e^{-i\mathbf{k}\boldsymbol{\delta}_{p+2}})b^\dagger_{\tau\sigma\mathbf{k}+\mathbf{q}}a_{\tau\sigma\mathbf{k}}\Big], \end{aligned} \tag{5.22}$$

where $\mathbf{q} = \mathbf{k}' - \mathbf{k}$. We have used that $\boldsymbol{\delta}_{p+1} - \boldsymbol{\delta}_p = \boldsymbol{\delta}_{p+2}$. With these expressions one can obtain the following rather tedious interaction model (see Appendix D)

$$U = U_{Q\times Q'} + U_{Q\times T'} + U_{T\times Q'} + U_{T\times T'} \tag{5.23}$$

with

$$\begin{aligned} U_{Q\times Q'} = \frac{V_0}{2\tilde{N}}\sum_{\tau,\tau'}\sum_{\sigma,\sigma'}\sum_{\mathbf{k},\mathbf{k}',\mathbf{q}}\sum_{p,p'=2,4,6}\frac{1}{9}\Big(&e^{i\mathbf{q}(\boldsymbol{\delta}_p-\boldsymbol{\delta}_{p'})}a^\dagger_{\tau\sigma\mathbf{k}}a_{\tau\sigma\mathbf{k}+\mathbf{q}}a^\dagger_{\tau'\sigma'\mathbf{k}'}a_{\tau'\sigma'\mathbf{k}'-\mathbf{q}} \\ &+ e^{i\mathbf{q}(\boldsymbol{\delta}_{p+1}-\boldsymbol{\delta}_{p'+1})}b^\dagger_{\tau\sigma\mathbf{k}}b_{\tau\sigma\mathbf{k}+\mathbf{q}}b^\dagger_{\tau'\sigma'\mathbf{k}'}b_{\tau'\sigma'\mathbf{k}'-\mathbf{q}} \\ &+ e^{i\mathbf{q}(\boldsymbol{\delta}_p-\boldsymbol{\delta}_{p'+1})}a^\dagger_{\tau\sigma\mathbf{k}}a_{\tau\sigma\mathbf{k}+\mathbf{q}}b^\dagger_{\tau'\sigma'\mathbf{k}'}b_{\tau'\sigma'\mathbf{k}'-\mathbf{q}} \\ &+ e^{i\mathbf{q}(\boldsymbol{\delta}_{p+1}-\boldsymbol{\delta}_{p'})}b^\dagger_{\tau\sigma\mathbf{k}}b_{\tau\sigma\mathbf{k}+\mathbf{q}}a^\dagger_{\tau'\sigma'\mathbf{k}'}a_{\tau'\sigma'\mathbf{k}'-\mathbf{q}}\Big). \end{aligned} \tag{5.24}$$

$$
\begin{aligned}
U_{Q\times T'} = \frac{V_0}{2\tilde{N}} \sum_{\tau,\tau'} \sum_{\sigma,\sigma'} \sum_{\mathbf{k},\mathbf{k}',\mathbf{q}} \sum_{p,p'=2,4,6} \frac{\alpha_1}{3} \Big(& e^{i\mathbf{q}(\boldsymbol{\delta}_p - \boldsymbol{\delta}_{p'+1})} (e^{i\mathbf{k}'\boldsymbol{\delta}_{p'}} - e^{i\mathbf{k}'\boldsymbol{\delta}_{p'+2}}) a^\dagger_{\tau\sigma\mathbf{k}} a_{\tau\sigma\mathbf{k}+\mathbf{q}} a^\dagger_{\tau'\sigma'\mathbf{k}'} b_{\tau'\sigma'\mathbf{k}'-\mathbf{q}} \\
& + e^{i\mathbf{q}(\boldsymbol{\delta}_{p+1} - \boldsymbol{\delta}_{p'+1})} (e^{i\mathbf{k}'\boldsymbol{\delta}_{p'}} - e^{i\mathbf{k}'\boldsymbol{\delta}_{p'+2}}) b^\dagger_{\tau\sigma\mathbf{k}} b_{\tau\sigma\mathbf{k}+\mathbf{q}} a^\dagger_{\tau'\sigma'\mathbf{k}'} b_{\tau'\sigma'\mathbf{k}'-\mathbf{q}} \\
& + e^{i\mathbf{q}(\boldsymbol{\delta}_p - \boldsymbol{\delta}_{p'+1})} (e^{-i(\mathbf{k}'-\mathbf{q})\boldsymbol{\delta}_{p'}} - e^{-i(\mathbf{k}'-\mathbf{q})\boldsymbol{\delta}_{p'+2}}) a^\dagger_{\tau\sigma\mathbf{k}} a_{\tau\sigma\mathbf{k}+\mathbf{q}} b^\dagger_{\tau'\sigma'\mathbf{k}'} a_{\tau'\sigma'\mathbf{k}'-\mathbf{q}} \\
& + e^{i\mathbf{q}(\boldsymbol{\delta}_{p+1} - \boldsymbol{\delta}_{p'+1})} (e^{-i(\mathbf{k}'-\mathbf{q})\boldsymbol{\delta}_{p'}} - e^{-i(\mathbf{k}'-\mathbf{q})\boldsymbol{\delta}_{p'+2}}) b^\dagger_{\tau\sigma\mathbf{k}} b_{\tau\sigma\mathbf{k}+\mathbf{q}} b^\dagger_{\tau'\sigma'\mathbf{k}'} a_{\tau'\sigma'\mathbf{k}'-\mathbf{q}} \Big).
\end{aligned} \tag{5.25}
$$

$$
\begin{aligned}
U_{T\times Q'} = \frac{V_0}{2\tilde{N}} \sum_{\tau,\tau'} \sum_{\sigma,\sigma'} \sum_{\mathbf{k},\mathbf{k}',\mathbf{q}} \sum_{p,p'=2,4,6} \frac{\alpha_1}{3} \Big(& e^{-i\mathbf{q}(\boldsymbol{\delta}_{p'} - \boldsymbol{\delta}_{p+1})} (e^{i\mathbf{k}\boldsymbol{\delta}_p} - e^{i\mathbf{k}\boldsymbol{\delta}_{p+2}}) a^\dagger_{\tau\sigma\mathbf{k}} b_{\tau\sigma\mathbf{k}+\mathbf{q}} a^\dagger_{\tau'\sigma'\mathbf{k}'} a_{\tau'\sigma'\mathbf{k}'-\mathbf{q}} \\
& + e^{-i\mathbf{q}(\boldsymbol{\delta}_{p'+1} - \boldsymbol{\delta}_{p+1})} (e^{i\mathbf{k}\boldsymbol{\delta}_p} - e^{i\mathbf{k}\boldsymbol{\delta}_{p+2}}) a^\dagger_{\tau\sigma\mathbf{k}} b_{\tau\sigma\mathbf{k}+\mathbf{q}} b^\dagger_{\tau'\sigma'\mathbf{k}'} b_{\tau'\sigma'\mathbf{k}'-\mathbf{q}} \\
& + e^{i\mathbf{q}(\boldsymbol{\delta}_{p'} - \boldsymbol{\delta}_{p+1})} (e^{-i\mathbf{k}\boldsymbol{\delta}_p} - e^{-i\mathbf{k}\boldsymbol{\delta}_{p+2}}) b^\dagger_{\tau\sigma\mathbf{k}+\mathbf{q}} a_{\tau\sigma\mathbf{k}} a^\dagger_{\tau'\sigma'\mathbf{k}'-\mathbf{q}} a_{\tau'\sigma'\mathbf{k}'} \\
& + e^{i\mathbf{q}(\boldsymbol{\delta}_{p'+1} - \boldsymbol{\delta}_{p+1})} (e^{-i\mathbf{k}\boldsymbol{\delta}_p} - e^{-i\mathbf{k}\boldsymbol{\delta}_{p+2}}) b^\dagger_{\tau\sigma\mathbf{k}+\mathbf{q}} a_{\tau\sigma\mathbf{k}} b^\dagger_{\tau'\sigma'\mathbf{k}'-\mathbf{q}} b_{\tau'\sigma'\mathbf{k}'} \Big).
\end{aligned} \tag{5.26}
$$

$$
\begin{aligned}
U_{T\times T'} = \frac{V_0}{2\tilde{N}} \sum_{\tau,\tau'} \sum_{\sigma,\sigma'} \sum_{\mathbf{k},\mathbf{k}',\mathbf{q}} \sum_{p,p'=2,4,6} \alpha_1^2 \Big[& e^{i\mathbf{q}(\boldsymbol{\delta}_{p+1} - \boldsymbol{\delta}_{p'+1})} (e^{i\mathbf{k}\boldsymbol{\delta}_p} - e^{i\mathbf{k}\boldsymbol{\delta}_{p+2}}) (e^{i\mathbf{k}'\boldsymbol{\delta}_{p'}} - e^{i\mathbf{k}'\boldsymbol{\delta}_{p'+2}}) a^\dagger_{\tau\sigma\mathbf{k}} b_{\tau\sigma\mathbf{k}+\mathbf{q}} a^\dagger_{\tau'\sigma'\mathbf{k}'} b_{\tau'\sigma'\mathbf{k}'-\mathbf{q}} \\
& + e^{i\mathbf{q}(\boldsymbol{\delta}_{p+1} - \boldsymbol{\delta}_{p'+1})} (e^{i\mathbf{k}\boldsymbol{\delta}_p} - e^{i\mathbf{k}\boldsymbol{\delta}_{p+2}}) (e^{-i(\mathbf{k}'-\mathbf{q})\boldsymbol{\delta}_{p'}} - e^{-i(\mathbf{k}'-\mathbf{q})\boldsymbol{\delta}_{p'+2}}) a^\dagger_{\tau\sigma\mathbf{k}} b_{\tau\sigma\mathbf{k}+\mathbf{q}} b^\dagger_{\tau'\sigma'\mathbf{k}'} a_{\tau'\sigma'\mathbf{k}'-\mathbf{q}} \\
& + e^{-i\mathbf{q}(\boldsymbol{\delta}_{p+1} - \boldsymbol{\delta}_{p'+1})} (e^{-i\mathbf{k}\boldsymbol{\delta}_p} - e^{-i\mathbf{k}\boldsymbol{\delta}_{p+2}}) (e^{i(\mathbf{k}'-\mathbf{q})\boldsymbol{\delta}_{p'}} - e^{i(\mathbf{k}'-\mathbf{q})\boldsymbol{\delta}_{p'+2}}) b^\dagger_{\tau\sigma\mathbf{k}+\mathbf{q}} a_{\tau\sigma\mathbf{k}} a^\dagger_{\tau'\sigma'\mathbf{k}'-\mathbf{q}} b_{\tau'\sigma'\mathbf{k}'} \\
& + e^{-i\mathbf{q}(\boldsymbol{\delta}_{p+1} - \boldsymbol{\delta}_{p'+1})} (e^{-i\mathbf{k}\boldsymbol{\delta}_p} - e^{-i\mathbf{k}\boldsymbol{\delta}_{p+2}}) (e^{-i\mathbf{k}'\boldsymbol{\delta}_{p'}} - e^{-i\mathbf{k}'\boldsymbol{\delta}_{p'+2}}) b^\dagger_{\tau\sigma\mathbf{k}+\mathbf{q}} a_{\tau\sigma\mathbf{k}} b^\dagger_{\tau'\sigma'\mathbf{k}'-\mathbf{q}} a_{\tau'\sigma'\mathbf{k}'} \Big].
\end{aligned} \tag{5.27}
$$

We devote the next section to consider the Hartree terms followed by a section on the Fock terms.

Hartree terms

In principle one should of course perform 16 independent HF decouplings however, as we are only interested in the homogeneous Hartree terms for now, we recall that these require $\mathbf{q} = 0$. Applying this restriction, one can easily show that $\sum_{p=2,4,6}(e^{(-)i\mathbf{k}\boldsymbol{\delta}_p} - e^{(-)i\mathbf{k}\boldsymbol{\delta}_{p+2}}) = 0$, which leads to $U^H_{Q\times T'} = U^H_{T\times Q'} = U^H_{T\times T'} = 0$. Thus we return to Eq. (5.24) and insert the direct terms of the decoupling,

$$
\begin{aligned}
U^H = \frac{V_0}{2\tilde{N}} \sum_{\tau,\tau'} \sum_{\sigma,\sigma'} \sum_{\mathbf{k},\mathbf{k}',\mathbf{q}} \sum_{p,p'=2,4,6} \frac{1}{9} \boldsymbol{\delta}_{\mathbf{q},0} \Big(& e^{i\mathbf{q}(\boldsymbol{\delta}_p - \boldsymbol{\delta}_{p'})} (\langle a^\dagger_{\tau\sigma\mathbf{k}} a_{\tau\sigma\mathbf{k}+\mathbf{q}} \rangle a^\dagger_{\tau'\sigma'\mathbf{k}'} a_{\tau'\sigma'\mathbf{k}'-\mathbf{q}} + a^\dagger_{\tau\sigma\mathbf{k}} a_{\tau\sigma\mathbf{k}+\mathbf{q}} \langle a^\dagger_{\tau'\sigma'\mathbf{k}'} a_{\tau'\sigma'\mathbf{k}'-\mathbf{q}} \rangle) \\
& + e^{i\mathbf{q}(\boldsymbol{\delta}_{p+1} - \boldsymbol{\delta}_{p'+1})} (\langle b^\dagger_{\tau\sigma\mathbf{k}} b_{\tau\sigma\mathbf{k}+\mathbf{q}} \rangle b^\dagger_{\tau'\sigma'\mathbf{k}'} b_{\tau'\sigma'\mathbf{k}'-\mathbf{q}} + b^\dagger_{\tau\sigma\mathbf{k}} b_{\tau\sigma\mathbf{k}+\mathbf{q}} \langle b^\dagger_{\tau'\sigma'\mathbf{k}'} b_{\tau'\sigma'\mathbf{k}'-\mathbf{q}} \rangle) \\
& + e^{i\mathbf{q}(\boldsymbol{\delta}_p - \boldsymbol{\delta}p'+1)} (\langle a^\dagger_{\tau\sigma\mathbf{k}} a_{\tau\sigma\mathbf{k}+\mathbf{q}} \rangle b^\dagger_{\tau'\sigma'\mathbf{k}'} b_{\tau'\sigma'\mathbf{k}'-\mathbf{q}} + a^\dagger_{\tau\sigma\mathbf{k}} a_{\tau\sigma\mathbf{k}+\mathbf{q}} \langle b^\dagger_{\tau'\sigma'\mathbf{k}'} b_{\tau'\sigma'\mathbf{k}'-\mathbf{q}} \rangle) \\
& + e^{i\mathbf{q}(\boldsymbol{\delta}_{p+1} - \boldsymbol{\delta}_{p'})} (\langle b^\dagger_{\tau\sigma\mathbf{k}} b_{\tau\sigma\mathbf{k}+\mathbf{q}} \rangle a^\dagger_{\tau'\sigma'\mathbf{k}'} a_{\tau'\sigma'\mathbf{k}'-\mathbf{q}} + b^\dagger_{\tau\sigma\mathbf{k}} b_{\tau\sigma\mathbf{k}+\mathbf{q}} \langle a^\dagger_{\tau'\sigma'\mathbf{k}'} a_{\tau'\sigma'\mathbf{k}'-\mathbf{q}} \rangle) \Big) \\
= \frac{V_0}{2\tilde{N}} \sum_{\tau,\tau'} \sum_{\sigma,\sigma'} \sum_{\mathbf{k},\mathbf{k}'} \sum_{p,p'=2,4,6} \frac{1}{9} \Big(& \langle a^\dagger_{\tau\sigma\mathbf{k}} a_{\tau\sigma\mathbf{k}} \rangle a^\dagger_{\tau'\sigma'\mathbf{k}'} a_{\tau'\sigma'\mathbf{k}'} + a^\dagger_{\tau\sigma\mathbf{k}} a_{\tau\sigma\mathbf{k}} \langle a^\dagger_{\tau'\sigma'\mathbf{k}'} a_{\tau'\sigma'\mathbf{k}'} \rangle \\
& + \langle b^\dagger_{\tau\sigma\mathbf{k}} b_{\tau\sigma\mathbf{k}} \rangle b^\dagger_{\tau'\sigma'\mathbf{k}'} b_{\tau'\sigma'\mathbf{k}'} + b^\dagger_{\tau\sigma\mathbf{k}} b_{\tau\sigma\mathbf{k}} \langle b^\dagger_{\tau'\sigma'\mathbf{k}'} b_{\tau'\sigma'\mathbf{k}'} \rangle \\
& + \langle a^\dagger_{\tau\sigma\mathbf{k}} a_{\tau\sigma\mathbf{k}} \rangle b^\dagger_{\tau'\sigma'\mathbf{k}'} b_{\tau'\sigma'\mathbf{k}'} + a^\dagger_{\tau\sigma\mathbf{k}} a_{\tau\sigma\mathbf{k}} \langle b^\dagger_{\tau'\sigma'\mathbf{k}'} b_{\tau'\sigma'\mathbf{k}'} \rangle \\
& + \langle b^\dagger_{\tau\sigma\mathbf{k}} b_{\tau\sigma\mathbf{k}} \rangle a^\dagger_{\tau'\sigma'\mathbf{k}'} a_{\tau'\sigma'\mathbf{k}'} + b^\dagger_{\tau\sigma\mathbf{k}} b_{\tau\sigma\mathbf{k}} \langle a^\dagger_{\tau'\sigma'\mathbf{k}'} a_{\tau'\sigma'\mathbf{k}'} \rangle \Big)
\end{aligned}
$$

$$
\begin{aligned}
&= \frac{V_0}{2\tilde{N}} \sum_{\tau,\tau'} \sum_{\sigma,\sigma'} \sum_{\mathbf{k},\mathbf{k}'} \Big(2a^\dagger_{\tau\sigma\mathbf{k}} a_{\tau\sigma\mathbf{k}} \langle a^\dagger_{\tau'\sigma'\mathbf{k}'} a_{\tau'\sigma'\mathbf{k}'} \rangle + 2b^\dagger_{\tau\sigma\mathbf{k}} b_{\tau\sigma\mathbf{k}} \langle b^\dagger_{\tau'\sigma'\mathbf{k}'} b_{\tau'\sigma'\mathbf{k}'} \rangle \\
&\qquad + 2a^\dagger_{\tau\sigma\mathbf{k}} a_{\tau\sigma\mathbf{k}} \langle b^\dagger_{\tau'\sigma'\mathbf{k}'} b_{\tau'\sigma'\mathbf{k}'} \rangle + 2b^\dagger_{\tau\sigma\mathbf{k}} b_{\tau\sigma\mathbf{k}} \langle a^\dagger_{\tau'\sigma'\mathbf{k}'} a_{\tau'\sigma'\mathbf{k}'} \rangle \Big) \\
&= V_0 \sum_{\tau\sigma\mathbf{k}} (a^\dagger_{\tau\sigma\mathbf{k}} \bar{n} a_{\tau\sigma\mathbf{k}} + b^\dagger_{\tau\sigma\mathbf{k}} \bar{n} b_{\tau\sigma\mathbf{k}}) \\
&= V_0 \sum_{\mathbf{k}} \mathbf{f}^\dagger_{\mathbf{k}} [\bar{n} \otimes \mathbb{1}_{8\times 8}] \mathbf{f}_{\mathbf{k}} \\
&\equiv V_0 \sum_{\mathbf{k}} \mathbf{f}^\dagger_{\mathbf{k}} M^H \mathbf{f}_{\mathbf{k}}
\end{aligned} \tag{5.28}
$$

where,

$$
\bar{n} = \frac{1}{\tilde{N}} \sum_{\tau'\sigma'\mathbf{k}'} (\langle a^\dagger_{\tau'\sigma'\mathbf{k}'} a_{\tau'\sigma'\mathbf{k}'} \rangle + \langle b^\dagger_{\tau'\sigma'\mathbf{k}'} b_{\tau'\sigma'\mathbf{k}'} \rangle), \tag{5.29}
$$

and $\mathbf{f}^\dagger_{\mathbf{k}} = \begin{pmatrix} a^\dagger_{+\uparrow\mathbf{k}} & a^\dagger_{-\uparrow\mathbf{k}} & a^\dagger_{+\downarrow\mathbf{k}} & a^\dagger_{-\downarrow\mathbf{k}} & b^\dagger_{+\uparrow\mathbf{k}} & b^\dagger_{-\uparrow\mathbf{k}} & b^\dagger_{+\downarrow\mathbf{k}} & b^\dagger_{-\downarrow\mathbf{k}} \end{pmatrix}$ as in Eq. (5.17).

Fock terms

The exchange terms will contain contributions from all four combinations in Eqs. (5.24)-(5.27). A detailed derivation of U^F can be seen in Appendix E. Here we simply list the findings after applying the homogenuity condition and performing the required shifts in momentum space as discussed previously.

$$
\begin{aligned}
U^F_{Q\times Q'} = -\frac{V_0}{2\tilde{N}} \sum_{\tau,\tau'} \sum_{\sigma,\sigma'} \sum_{\mathbf{k},\mathbf{k}'} \sum_{p,p'} \frac{1}{9} \Big(&(e^{i(\mathbf{k}'-\mathbf{k})(\boldsymbol{\delta}_p - \boldsymbol{\delta}_{p'})} + e^{-i(\mathbf{k}'-\mathbf{k})(\boldsymbol{\delta}_p - \boldsymbol{\delta}_{p'})}) \langle a^\dagger_{\tau'\sigma'\mathbf{k}'} a_{\tau\sigma\mathbf{k}'} \rangle a^\dagger_{\tau\sigma\mathbf{k}} a_{\tau'\sigma'\mathbf{k}} \\
&+ (e^{i(\mathbf{k}'-\mathbf{k})(\boldsymbol{\delta}_{p+1} - \boldsymbol{\delta}_{p'+1})} + e^{-i(\mathbf{k}'-\mathbf{k})(\boldsymbol{\delta}_{p+1} - \boldsymbol{\delta}_{p'+1})}) \langle b^\dagger_{\tau'\sigma'\mathbf{k}'} b_{\tau\sigma\mathbf{k}'} \rangle b^\dagger_{\tau\sigma\mathbf{k}} b_{\tau'\sigma'\mathbf{k}} \\
&+ (e^{i(\mathbf{k}'-\mathbf{k})(\boldsymbol{\delta}_p - \boldsymbol{\delta}_{p'+1})} + e^{-i(\mathbf{k}'-\mathbf{k})(\boldsymbol{\delta}_{p+1} - \boldsymbol{\delta}_{p'})}) \langle b^\dagger_{\tau'\sigma'\mathbf{k}'} a_{\tau\sigma\mathbf{k}'} \rangle a^\dagger_{\tau\sigma\mathbf{k}} b_{\tau'\sigma'\mathbf{k}} \\
&+ (e^{i(\mathbf{k}'-\mathbf{k})(\boldsymbol{\delta}_{p+1} - \boldsymbol{\delta}_{p'})} + e^{-i(\mathbf{k}'-\mathbf{k})(\boldsymbol{\delta}_p - \boldsymbol{\delta}_{p'+1})}) \langle a^\dagger_{\tau'\sigma'\mathbf{k}'} b_{\tau\sigma\mathbf{k}'} \rangle b^\dagger_{\tau\sigma\mathbf{k}} a_{\tau'\sigma'\mathbf{k}} \Big)
\end{aligned} \tag{5.30}
$$

$$
\begin{aligned}
U^F_{Q\times T'} = -\frac{V_0}{2\tilde{N}} \sum_{\tau,\tau'} \sum_{\sigma,\sigma'} \sum_{\mathbf{k},\mathbf{k}'} \sum_{p,p'} \frac{\alpha_1}{3} \Bigg(&[e^{-i(\mathbf{k}'-\mathbf{k})(\boldsymbol{\delta}_p - \boldsymbol{\delta}_{p'+1})} (e^{i\mathbf{k}\boldsymbol{\delta}_{p'}} - e^{i\mathbf{k}\boldsymbol{\delta}_{p'+2}}) \langle a^\dagger_{\tau'\sigma'\mathbf{k}'} b_{\tau\sigma\mathbf{k}'} \rangle \\
&\quad + e^{i(\mathbf{k}'-\mathbf{k})(\boldsymbol{\delta}_p - \boldsymbol{\delta}_{p'+1})} (e^{-i\mathbf{k}\boldsymbol{\delta}_{p'}} - e^{-i\mathbf{k}\boldsymbol{\delta}_{p'+2}}) \langle b^\dagger_{\tau'\sigma'\mathbf{k}'} a_{\tau\sigma\mathbf{k}'} \rangle] a^\dagger_{\tau\sigma\mathbf{k}} a_{\tau'\sigma'\mathbf{k}} \\
&+ [e^{i(\mathbf{k}'-\mathbf{k})(\boldsymbol{\delta}_p - \boldsymbol{\delta}_{p'+1})} (e^{i\mathbf{k}'\boldsymbol{\delta}_{p'}} - e^{i\mathbf{k}'\boldsymbol{\delta}_{p'+2}}) \langle a^\dagger_{\tau'\sigma'\mathbf{k}'} a_{\tau\sigma\mathbf{k}'} \rangle \\
&\quad + e^{-i(\mathbf{k}'-\mathbf{k})(\boldsymbol{\delta}_{p+1} - \boldsymbol{\delta}_{p'+1})} (e^{i\mathbf{k}\boldsymbol{\delta}_{p'}} - e^{i\mathbf{k}\boldsymbol{\delta}_{p'+2}}) \langle b^\dagger_{\tau'\sigma'\mathbf{k}'} b_{\tau\sigma\mathbf{k}'} \rangle] a^\dagger_{\tau\sigma\mathbf{k}} b_{\tau'\sigma'\mathbf{k}} \\
&+ [e^{i(\mathbf{k}'-\mathbf{k})(\boldsymbol{\delta}_{p+1} - \boldsymbol{\delta}_{p'+1})} (e^{i\mathbf{k}'\boldsymbol{\delta}_{p'}} - e^{i\mathbf{k}'\boldsymbol{\delta}_{p'+2}}) \langle a^\dagger_{\tau'\sigma'\mathbf{k}'} b_{\tau\sigma\mathbf{k}'} \rangle \\
&\quad + e^{-i(\mathbf{k}'-\mathbf{k})(\boldsymbol{\delta}_{p+1} - \boldsymbol{\delta}_{p'+1})} (e^{-i\mathbf{k}'\boldsymbol{\delta}_{p'}} - e^{-i\mathbf{k}'\boldsymbol{\delta}_{p'+2}}) \langle b^\dagger_{\tau'\sigma'\mathbf{k}'} a_{\tau\sigma\mathbf{k}'} \rangle] b^\dagger_{\tau\sigma\mathbf{k}} b_{\tau'\sigma'\mathbf{k}} \\
&+ [e^{-i(\mathbf{k}'-\mathbf{k})(\boldsymbol{\delta}_p - \boldsymbol{\delta}_{p'+1})} (e^{-i\mathbf{k}'\boldsymbol{\delta}_{p'}} - e^{-i\mathbf{k}'\boldsymbol{\delta}_{p'+2}}) \langle a^\dagger_{\tau'\sigma'\mathbf{k}'} a_{\tau\sigma\mathbf{k}'} \rangle \\
&\quad + e^{i(\mathbf{k}'-\mathbf{k})(\boldsymbol{\delta}_{p+1} - \boldsymbol{\delta}_{p'+1})} (e^{-i\mathbf{k}\boldsymbol{\delta}_{p'}} - e^{-i\mathbf{k}\boldsymbol{\delta}_{p'+2}}) \langle b^\dagger_{\tau'\sigma'\mathbf{k}'} b_{\tau\sigma\mathbf{k}'} \rangle] b^\dagger_{\tau\sigma\mathbf{k}} a_{\tau'\sigma'\mathbf{k}} \Bigg)
\end{aligned} \tag{5.31}
$$

$$
\begin{aligned}
U^F_{T\times Q'} = -\frac{V_0}{2\tilde{N}} \sum_{\tau,\tau'} \sum_{\sigma,\sigma'} \sum_{\mathbf{k},\mathbf{k}'} \sum_{p,p'} \frac{\alpha_1}{3} \Bigg(&[e^{i(\mathbf{k}'-\mathbf{k})(\boldsymbol{\delta}_{p'} - \boldsymbol{\delta}_{p+1})} (e^{i\mathbf{k}'\boldsymbol{\delta}_p} - e^{i\mathbf{k}'\boldsymbol{\delta}_{p+2}}) \langle a^\dagger_{\tau'\sigma'\mathbf{k}'} a_{\tau\sigma\mathbf{k}'} \rangle \\
&\quad + e^{-i(\mathbf{k}'-\mathbf{k})(\boldsymbol{\delta}_{p'+1} - \boldsymbol{\delta}_{p+1})} (e^{i\mathbf{k}\boldsymbol{\delta}_p} - e^{i\mathbf{k}\boldsymbol{\delta}_{p+2}}) \langle b^\dagger_{\tau'\sigma'\mathbf{k}'} b_{\tau\sigma\mathbf{k}'} \rangle] a^\dagger_{\tau\sigma\mathbf{k}} b_{\tau'\sigma'\mathbf{k}} \\
&+ [e^{-i(\mathbf{k}'-\mathbf{k})(\boldsymbol{\delta}_{p'} - \boldsymbol{\delta}_{p+1})} (e^{i\mathbf{k}\boldsymbol{\delta}_p} - e^{i\mathbf{k}\boldsymbol{\delta}_{p+2}}) \langle a^\dagger_{\tau'\sigma'\mathbf{k}'} b_{\tau\sigma\mathbf{k}'} \rangle
\end{aligned}
$$

$$
\begin{aligned}
&+ e^{i(\mathbf{k}'-\mathbf{k})(\boldsymbol{\delta}_{p'}-\boldsymbol{\delta}_{p+1})}(e^{-i\mathbf{k}\boldsymbol{\delta}_p} - e^{-i\mathbf{k}\boldsymbol{\delta}_{p+2}})\langle b^\dagger_{\tau'\sigma'\mathbf{k}'}a_{\tau\sigma\mathbf{k}'}\rangle]a^\dagger_{\tau\sigma\mathbf{k}}a_{\tau'\sigma'\mathbf{k}}\\
&+ [e^{i(\mathbf{k}'-\mathbf{k})(\boldsymbol{\delta}_{p'+1}-\boldsymbol{\delta}_{p+1})}(e^{i\mathbf{k}'\boldsymbol{\delta}_p} - e^{i\mathbf{k}'\boldsymbol{\delta}_{p+2}})\langle a^\dagger_{\tau'\sigma'\mathbf{k}'}b_{\tau\sigma\mathbf{k}'}\rangle\\
&\quad + e^{-i(\mathbf{k}'-\mathbf{k})(\boldsymbol{\delta}_{p'+1}-\boldsymbol{\delta}_{p+1})}(e^{-i\mathbf{k}'\boldsymbol{\delta}_p} - e^{-i\mathbf{k}'\boldsymbol{\delta}_{p+2}})\langle b^\dagger_{\tau'\sigma'\mathbf{k}'}a_{\tau\sigma\mathbf{k}'}\rangle]b^\dagger_{\tau\sigma\mathbf{k}}b_{\tau'\sigma'\mathbf{k}}\\
&+ [e^{-i(\mathbf{k}'-\mathbf{k})(\boldsymbol{\delta}_{p'}-\boldsymbol{\delta}_{p+1})}(e^{-i\mathbf{k}'\boldsymbol{\delta}_p} - e^{-i\mathbf{k}'\boldsymbol{\delta}_{p+2}})\langle a^\dagger_{\tau'\sigma'\mathbf{k}'}a_{\tau\sigma\mathbf{k}'}\rangle\\
&\quad + e^{i(\mathbf{k}'-\mathbf{k})(\boldsymbol{\delta}_{p'+1}-\boldsymbol{\delta}_{p+1})}(e^{-i\mathbf{k}\boldsymbol{\delta}_p} - e^{-i\mathbf{k}\boldsymbol{\delta}_{p+2}})\langle b^\dagger_{\tau'\sigma'\mathbf{k}'}b_{\tau\sigma\mathbf{k}'}\rangle]b^\dagger_{\tau\sigma\mathbf{k}}a_{\tau'\sigma'\mathbf{k}} \qquad (5.32)
\end{aligned}
$$

$$
\begin{aligned}
U^F_{T\times T'} = -\frac{2\alpha_1^2V_0}{2\tilde{N}}\sum_{\tau,\tau'}\sum_{\sigma,\sigma'}\sum_{\mathbf{k},\mathbf{k}'}\sum_{p,p'}\Bigg(&e^{-i(\mathbf{k}'-\mathbf{k})(\boldsymbol{\delta}_{p+1}-\boldsymbol{\delta}_{p'+1})}(e^{i\mathbf{k}'\boldsymbol{\delta}_p} - e^{i\mathbf{k}'\boldsymbol{\delta}_{p+2}})(e^{i\mathbf{k}\boldsymbol{\delta}_{p'}} - e^{i\mathbf{k}\boldsymbol{\delta}_{p'+2}})\langle a^\dagger_{\tau'\sigma'\mathbf{k}'}b_{\tau\sigma\mathbf{k}'}\rangle a^\dagger_{\tau\sigma\mathbf{k}}b_{\tau'\sigma'\mathbf{k}}\\
&+ e^{-i(\mathbf{k}'-\mathbf{k})(\boldsymbol{\delta}_{p+1}-\boldsymbol{\delta}_{p'+1})}(e^{i\mathbf{k}'\boldsymbol{\delta}_p} - e^{i\mathbf{k}'\boldsymbol{\delta}_{p+2}})(e^{-i\mathbf{k}'\boldsymbol{\delta}_{p'}} - e^{-i\mathbf{k}'\boldsymbol{\delta}_{p'+2}})\langle a^\dagger_{\tau'\sigma'\mathbf{k}'}a_{\tau\sigma\mathbf{k}'}\rangle b^\dagger_{\tau\sigma\mathbf{k}}b_{\tau'\sigma'\mathbf{k}}\\
&+ e^{i(\mathbf{k}'-\mathbf{k})(\boldsymbol{\delta}_{p+1}-\boldsymbol{\delta}_{p'+1})}(e^{i\mathbf{k}\boldsymbol{\delta}_p} - e^{i\mathbf{k}\boldsymbol{\delta}_{p+2}})(e^{-i\mathbf{k}\boldsymbol{\delta}_{p'}} - e^{-i\mathbf{k}\boldsymbol{\delta}_{p'+2}})\langle b^\dagger_{\tau'\sigma'\mathbf{k}'}b_{\tau\sigma\mathbf{k}'}\rangle a^\dagger_{\tau\sigma\mathbf{k}}a_{\tau'\sigma'\mathbf{k}}\\
&+ e^{i(\mathbf{k}'-\mathbf{k})(\boldsymbol{\delta}_{p+1}-\boldsymbol{\delta}_{p'+1})}(e^{-i\mathbf{k}'\boldsymbol{\delta}_p} - e^{-i\mathbf{k}'\boldsymbol{\delta}_{p+2}})(e^{-i\mathbf{k}\boldsymbol{\delta}_{p'}} - e^{-i\mathbf{k}\boldsymbol{\delta}_{p'+2}})\langle b^\dagger_{\tau'\sigma'\mathbf{k}'}a_{\tau\sigma\mathbf{k}'}\rangle b^\dagger_{\tau\sigma\mathbf{k}}a_{\tau'\sigma'\mathbf{k}}\Bigg). \qquad (5.33)
\end{aligned}
$$

Collecting equal operator terms and defining

$$
\begin{aligned}
A^{\alpha^\dagger\beta}_{pp'}(\mathbf{k}'-\mathbf{k}) &\equiv e^{i(\mathbf{k}'-\mathbf{k})(\boldsymbol{\delta}_p-\boldsymbol{\delta}_{p'})}\langle\alpha^\dagger_{\tau'\sigma'\mathbf{k}'}\beta_{\tau\sigma\mathbf{k}'}\rangle \qquad \text{and} \qquad (5.34)\\
B_p(\mathbf{k}) &\equiv e^{i\mathbf{k}\boldsymbol{\delta}_p} - e^{i\mathbf{k}\boldsymbol{\delta}_{p+2}}, \qquad (5.35)
\end{aligned}
$$

allows us to write the full contribution from exchange term as,

$$
\begin{aligned}
U^F = -\frac{V_0}{\tilde{N}}\sum_{\tau,\tau'}\sum_{\sigma,\sigma'}\sum_{\mathbf{k},\mathbf{k}'}\sum_{p,p'}\Big[&\frac{1}{18}[A^{a^\dagger a}_{pp'}(\mathbf{k}'-\mathbf{k}) + A^{a^\dagger a}_{pp'}(\mathbf{k}-\mathbf{k}')] + \frac{\alpha_1}{3}[A^{a^\dagger b}_{p\bar{p}'}(\mathbf{k}-\mathbf{k}')B_{p'}(\mathbf{k}) + A^{b^\dagger a}_{p\bar{p}'}(\mathbf{k}'-\mathbf{k})B_{p'}(-\mathbf{k})]\\
&+ \alpha_1^2A^{b^\dagger b}_{\bar{p}\bar{p}'}(\mathbf{k}'-\mathbf{k})B_p(\mathbf{k})B_{p'}(-\mathbf{k})\Big]a^\dagger_{\tau\sigma\mathbf{k}}a_{\tau'\sigma'\mathbf{k}}\\
+\Big[&\frac{1}{18}[A^{b^\dagger b}_{\bar{p}\bar{p}'}(\mathbf{k}'-\mathbf{k}) + A^{b^\dagger b}_{\bar{p}\bar{p}'}(\mathbf{k}-\mathbf{k}')] + \frac{\alpha_1}{3}[A^{a^\dagger b}_{\bar{p}\bar{p}'}(\mathbf{k}'-\mathbf{k})B_{p'}(\mathbf{k}') + A^{b^\dagger a}_{\bar{p}\bar{p}'}(\mathbf{k}-\mathbf{k}')B_{p'}(-\mathbf{k}')]\\
&+ \alpha_1^2A^{a^\dagger a}_{\bar{p}\bar{p}'}(\mathbf{k}-\mathbf{k}')B_p(\mathbf{k}')B_{p'}(-\mathbf{k}')\Big]b^\dagger_{\tau\sigma\mathbf{k}}b_{\tau'\sigma'\mathbf{k}}\\
+\Big[&\frac{1}{18}[A^{b^\dagger a}_{p\bar{p}'}(\mathbf{k}'-\mathbf{k}) + A^{b^\dagger a}_{\bar{p}p'}(\mathbf{k}-\mathbf{k}')] + \frac{\alpha_1}{3}[A^{a^\dagger a}_{p\bar{p}'}(\mathbf{k}'-\mathbf{k})B_{p'}(\mathbf{k}') + A^{b^\dagger b}_{\bar{p}\bar{p}'}(\mathbf{k}-\mathbf{k}')B_{p'}(\mathbf{k})]\\
&+ \alpha_1^2A^{a^\dagger b}_{\bar{p}\bar{p}'}(\mathbf{k}-\mathbf{k}')B_p(\mathbf{k}')B_{p'}(\mathbf{k})\Big]a^\dagger_{\tau\sigma\mathbf{k}}b_{\tau'\sigma'\mathbf{k}}\\
+\Big[&\frac{1}{18}[A^{a^\dagger b}_{\bar{p}p'}(\mathbf{k}'-\mathbf{k}) + A^{a^\dagger b}_{p\bar{p}'}(\mathbf{k}-\mathbf{k}')] + \frac{\alpha_1}{3}[A^{a^\dagger a}_{p\bar{p}'}(\mathbf{k}-\mathbf{k}')B_{p'}(-\mathbf{k}') + A^{b^\dagger b}_{\bar{p}\bar{p}'}(\mathbf{k}'-\mathbf{k})B_{p'}(-\mathbf{k})]\\
&+ \alpha_1^2A^{b^\dagger a}_{\bar{p}\bar{p}'}(\mathbf{k}'-\mathbf{k})B_p(-\mathbf{k}')B_{p'}(-\mathbf{k})\Big]b^\dagger_{\tau\sigma\mathbf{k}}a_{\tau'\sigma'\mathbf{k}}. \qquad (5.36)
\end{aligned}
$$

Here $\bar{p}$ ($\bar{p}'$) denote odd values of p (p'), i.e. all terms with $\boldsymbol{\delta}_{p+1}$ ($\boldsymbol{\delta}_{p'+1}$). The matrix structure is,

$$
\begin{aligned}
U^F &= -V_0\sum_{\mathbf{k}}\mathbf{f}^\dagger_{\mathbf{k}}\begin{pmatrix}\underline{\underline{M}}_1 & \underline{\underline{M}}_2\\ \underline{\underline{M}}_3 & \underline{\underline{M}}_4\end{pmatrix}\mathbf{f}_{\mathbf{k}}\\
&\equiv -V_0\sum_{\mathbf{k}}\mathbf{f}^\dagger_{\mathbf{k}}M^F\mathbf{f}_{\mathbf{k}} \qquad (5.37)
\end{aligned}
$$

with

$$
M^{\sigma'\sigma}_{1,\tau'\tau} = \frac{1}{\tilde{N}}\sum_{p,p',\mathbf{k}'}\Big[\frac{1}{18}[A^{a^\dagger a}_{pp'}(\mathbf{k}'-\mathbf{k}) + A^{a^\dagger a}_{pp'}(\mathbf{k}-\mathbf{k}')]
$$

$$+\frac{\alpha_1}{3}[A^{a^\dagger b}_{p\bar{p}'}(\mathbf{k}-\mathbf{k}')B_{p'}(\mathbf{k})+A^{b^\dagger a}_{p\bar{p}'}(\mathbf{k}'-\mathbf{k})B_{p'}(-\mathbf{k})]+\alpha_1^2A^{b^\dagger b}_{\bar{p}\bar{p}'}(\mathbf{k}'-\mathbf{k})B_p(\mathbf{k})B_{p'}(-\mathbf{k})\Big],$$

$$M^{\sigma'\sigma}_{2,\tau'\tau}=\frac{1}{\tilde{N}}\sum_{p,p',\mathbf{k}'}\Big[\frac{1}{18}[A^{b^\dagger a}_{p\bar{p}'}(\mathbf{k}'-\mathbf{k})+A^{b^\dagger a}_{\bar{p}p'}(\mathbf{k}-\mathbf{k}')]$$

$$+\frac{\alpha_1}{3}[A^{a^\dagger a}_{p\bar{p}'}(\mathbf{k}'-\mathbf{k})B_{p'}(\mathbf{k}')+A^{b^\dagger b}_{\bar{p}\bar{p}'}(\mathbf{k}-\mathbf{k}')B_{p'}(\mathbf{k})]+\alpha_1^2A^{a^\dagger b}_{\bar{p}\bar{p}'}(\mathbf{k}-\mathbf{k}')B_p(\mathbf{k}')B_{p'}(\mathbf{k})\Big],$$

$$M^{\sigma'\sigma}_{3,\tau'\tau}=\frac{1}{\tilde{N}}\sum_{p,p',\mathbf{k}'}\Big[\frac{1}{18}[A^{a^\dagger b}_{\bar{p}p'}(\mathbf{k}'-\mathbf{k})+A^{a^\dagger b}_{p\bar{p}'}(\mathbf{k}-\mathbf{k}')]$$

$$+\frac{\alpha_1}{3}[A^{a^\dagger a}_{p\bar{p}'}(\mathbf{k}-\mathbf{k}')B_{p'}(-\mathbf{k}')+A^{b^\dagger b}_{\bar{p}\bar{p}'}(\mathbf{k}'-\mathbf{k})B_{p'}(-\mathbf{k})]+\alpha_1^2A^{b^\dagger a}_{\bar{p}\bar{p}'}(\mathbf{k}'-\mathbf{k})B_p(-\mathbf{k}')B_{p'}(-\mathbf{k})\Big],$$

$$M^{\sigma'\sigma}_{4,\tau'\tau}=\frac{1}{\tilde{N}}\sum_{p,p',\mathbf{k}'}\Big[\frac{1}{18}[A^{b^\dagger b}_{\bar{p}\bar{p}'}(\mathbf{k}'-\mathbf{k})+A^{b^\dagger b}_{\bar{p}\bar{p}'}(\mathbf{k}-\mathbf{k}')]$$

$$+\frac{\alpha_1}{3}[A^{a^\dagger b}_{\bar{p}\bar{p}'}(\mathbf{k}'-\mathbf{k})B_{p'}(\mathbf{k}')+A^{b^\dagger a}_{\bar{p}\bar{p}'}(\mathbf{k}-\mathbf{k}')B_{p'}(-\mathbf{k}')]+\alpha_1^2A^{a^\dagger a}_{\bar{p}\bar{p}'}(\mathbf{k}-\mathbf{k}')B_p(\mathbf{k}')B_{p'}(-\mathbf{k}')\Big].$$

Note that $\underline{\underline{M}}_1^\dagger=\underline{\underline{M}}_1$, $\underline{\underline{M}}_4^\dagger=\underline{\underline{M}}_4$ and $\underline{\underline{M}}_2^\dagger=\underline{\underline{M}}_3$, thus $(U^F)^\dagger=U^F$ as required.

The full TBG model in reciprocal space is,

$$H=\sum_{\mathbf{k}\in BZ}\mathbf{f}^\dagger_{\mathbf{k}}\Big[\mathcal{H}_{tb}+V_0\big(M^H-M^F\big)\Big]\mathbf{f}_{\mathbf{k}}, \tag{5.38}$$

where,

$$\mathcal{H}_{tb}=[-\mu+\tilde{t_2}(\mathbf{k})]s_0\sigma_0\tau_0-i\tilde{t_2'}(\mathbf{k})s_0\sigma_0\tau_z+Re[\tilde{t_1}(\mathbf{k})]s_x\sigma_0\tau_0+Im[\tilde{t_1}(\mathbf{k})]s_y\sigma_0\tau_0\,,$$
$$M^H=\bar{n}\otimes\mathbb{1}_{8\times8}$$

and M^F is as defined in Eq. 5.37.

Chapter 6

Numerics

In this chapter we will go through the numerical solution of the TBG model. In the first section, we describe the symmetry requirements, numbering and set up of the real space model. In the subsequent section, we derive the discretization of momentum space and outline the set up of the reciprocal space model. In the final section, we discuss the self-consistent iteration scheme and argue why the preferred ground state of the system is reached upon convergence.

6.1 Real space lattice

The HF decoupling of the real space TBG model (Eq. (5.11)) performed in the last chapter reveals a complicated structure of not only independent summations over primed and unprimed indices leading to the "all-to-all" operator combinations within each hexagon, but also a coupling of each operator combination to nine different mean fields with varying strength set by $\bar{\alpha}$. The intertwined mean field couplings of the real space model is reflected in reciprocal space by an unusual amount of form factors, which must all be accounted for in the numerical solution. Aside from these intricate couplings, the honeycomb lattice further complicates the numerics. In a simple, square lattice, all system parameters are given more or less by definition: the system size can be set by side lenght L yielding an $L \times L$ matrix with a total of $N = L^2$ sites. The site numbering is intuitively given by starting in one corner and counting all sites, one row at a time, up to L^2. Additionally, all mirror and rotational symmetries are automatically respected in this $L \times L$ lattice. Unfortunately, things get less intuitive in the case of a honeycomb lattice, where the required preservation of C_{3z} symmetry prevents a square system. In this setion, we will outline the numerical set up of the symmetry-preserving real space lattice and corresponding discretization of points in the first MBZ. We will leave the detailed set up of the mean field couplings to Appendix F.

When setting up the honeycomb lattice, three goals must be achieved. *i*) We must preserve C_{3z} and C_{2y}, *ii*) in accordance with the model, the full Hamiltonian is set up as a sum over hexagon indices, which we thus need to label in a structured manner and *iii*) on top of the hexagon numbering, we must also number all individual sites, as each site must be uniquely identified by a single input in the Hamiltonian. In the description of the numbering conventions, we will ignore the valley and spin degrees of freedom for clarity.

Preservation of C_{3z} and C_{2y} with respect to the rotation center requires that each hexagon has all symmetry related partners present in the system. Thus, we consider a simple system of three hexagons, with the rotation center placed at the AA-region in one, see Fig. 6.1. It is evident that C_{3z} require hexagons adjacent to all six sides of the centered hexagon to include all symmetry partners of the non-centered hexagons. We proceed to consider valid expansions of the system by adding an additional hexagon in the bottom panel of Fig. 6.1. Though the final

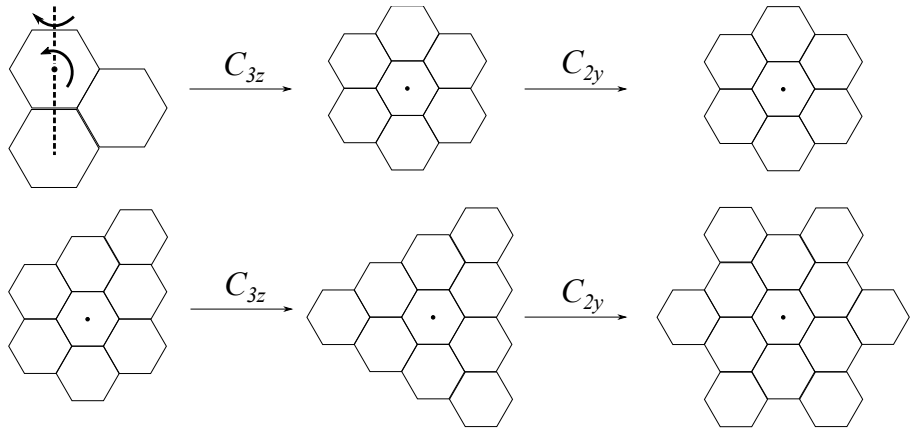

Figure 6.1: **Symmetry preservation in real space**. To obey C_{3z} and C_{2y}, each hexagon must have all symmetry related partners represented in the system and we must add hexagons in sets as depicted. Black dot is the origin of the system. Dashed line in the first figure is the y-axes and arrows indicate rotation direction of the two symmetries.

star-like system does indeed obey all symmetries, the numerics become unnecessarily involved if we allow for partially filled edges. Thus, we choose a convention where we always add hexagons along the entire perimeter on the system, when increasing the system size. Examples of such systems can be seen in Fig. 6.2. The reader might notice, that the numerical set up has been rotated by 30° compared to the derivations in the previous chapters. This is purely due to numerical details, and can of course be done without loss of generality. We define the system size, L, to be the number of hexagons along each of the six sides in the system. If we expand the system size, the added set of hexagons along the perimeter will constitute a new and larger hexagon with $L+1$ small hexagons along each side. We will refer to these sets of hexagons as rings to avoid confusion. The number of hexagons in each ring, R_r, will clearly increase with system size and is given by $R_r = 6r$, where r is the ring number defined by $r = L_r - 1$ and L_r is the side length of ring r. Note that we use zero-based indexing in accordance with the Python syntax used to perform the computations. From the definition of R_r we can easily define the total number of hexagons in the system as $R_{tot} = \sum_{r=0}^{L-1} 6r + 1$, where the additional one accounts for the single hexagon in the $r = 0$ ring. This expression can be verified from inspection of Fig. 6.2a, where $R_{tot} = \sum_{r=0}^{4} 6r + 1 = 61$ (note again the zero-indexing in the figure). Once the total number of hexagons in the system is established, we can label each hexagon by a number, R, as illustrated in Fig. 6.2a. We choose the numbering starting point and direction in each ring in accordance with the numbering starting point and direction of the $\boldsymbol{\delta}_p$ vectors (see Fig. 6.2b). With the numbering and symmetries in place, we have already accomplished goals *i*) and *ii*).

Adding a ring of hexagons to the system will naturally add additional sites to the system. However, as each site is adjacent to three different hexagons, some of the sites will already be accounted for in the previous ring. We illustrate this point in Fig. 6.2b, where orange sites belong to $r = 0$ and purple sites belong to $r = 1$. To define the total number of sites, N, let us again consider the number of added sites as a function of L_r. We find that $N_r = 12L_r - 6$, where N_r is the number of sites belonging to ring r, leading to $N = \sum_{L_r=1}^{L} 12L_r - 6$. For the case in Fig. 6.2b we have $N = \sum_{L_r=1}^{2} 12L_r - 6 = 6 + 18 = 24$ in agreement with the numbering. Should the reader not be convinced, it is easy to verify that $N = 150$ in Fig. 6.2a by counting all hexagon corners once. We number all sites in accordance with the hexagon numbering. With all sites numbered we can now define our Hamiltonian as an $N \times N$ matrix, where the input

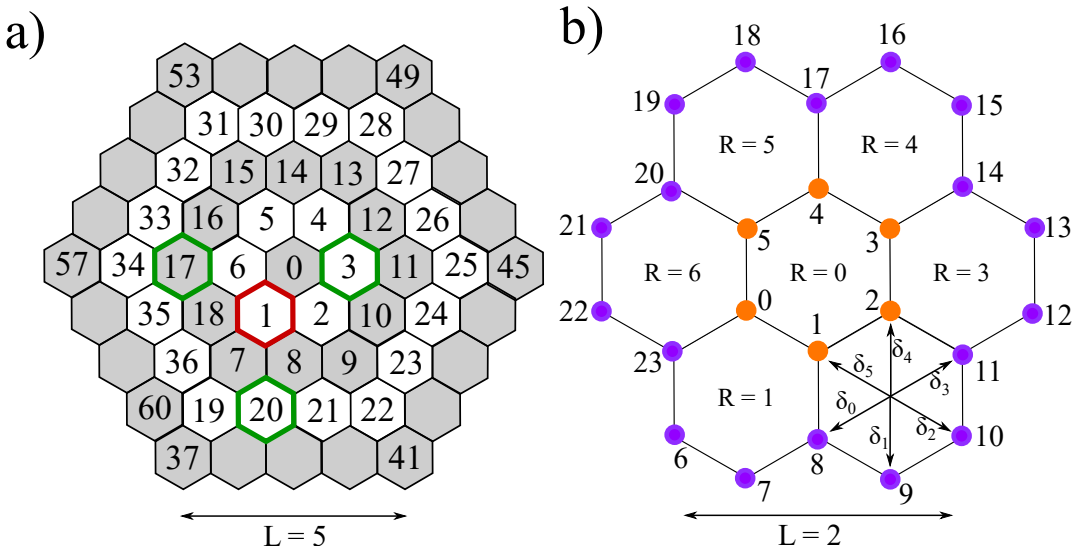

Figure 6.2: **Numbering conventions for hexagons and sites**. **a)** Numbering convention of hexagons in a system of size $L = 5$. Green hexagons are the three NNN hexagons related to the fifth NN hoppings of sites in the red hexagon. **b)** Numbering convention for the individual sites in a system of size $L = 2$. For each ring of hexagons added, we add a corresponding ring of sites. Orange sites belong to ring 0 and purple sites belong to ring 1. Both numbering conventions are chosen in accordance with the $\boldsymbol{\delta}_p$ vectors defined as depicted.

on position (n, m) defines the mean fields and hoppings related to operator combination $d_n^\dagger d_m$. Now recall that our model is set up as a sum over hexagon indices, R, and the position, p, of the site within that hexagon. Thus we write a function, $f(R)$, which takes the hexagon number as input, and returns the site numbers, n, ordered by their corresponding p index. To clarify, we consider the case for $f(R = 3)$ which returns an array, $\bar{n} = [2, 11, 12, 13, 14, 3]$, where the order of site numbers corresponds to positions $\bar{p} = [0, 1, 2, 3, 4, 5]$, see Fig. 6.2b.[1] This function enables a direct implementation of NN hopping terms, $t_1 e^{(-1)^p i\phi} d^\dagger(\mathbf{R} + \boldsymbol{\delta}_p) d(\mathbf{R} + \boldsymbol{\delta}_{p+1})$, given by $H(\bar{n}[p], \bar{n}[p+1]) = t_1 e^{(-1)^p i\phi}$, where $p = 0, ..., 5$ with periodic boundaries.

The fifth NN hoppings, $\sum_{\mathbf{R}'}[(t_2 + it_2')d^\dagger(\mathbf{R} + \boldsymbol{\delta}_p)d(\mathbf{R}' + \boldsymbol{\delta}_p) + h.c.]/3$, are interhexagon couplings relating equal p indices. To implement these terms, we write a function $g(R)$ which returns an array $\bar{R}_{NNN} = [R_0, R_1, R_2]$, where $R_{0,1,2}$ are the three NNN hexagons included in the $\mathbf{R}'$-sum. To exemplify, we consider $g(R = 1)$ which will return $R_{NNN} = [20, 3, 17]$, see Fig. 6.2a. We then compute $f(R = 1) \to \bar{n}$, $f(R = 20) \to \bar{m}_0$, $f(R = 3) \to \bar{m}_1$ and $f(R = 17) \to \bar{m}_2$, where $\bar{n}, \bar{m}_{0,1,2}$ all contain the six site numbers of the hexagon in question. The fifth NN hoppings are then implemented by setting $H(\bar{n}[p], \bar{m}_i[p]) += (t_2 + it_2')/3$ and $H(\bar{m}_i[p], \bar{n}[p]) += (t_2 - it_2')/3$ for $i = 0, 1, 2$ and $p = 0, ..., 5$. Here $+=$ is the Python syntax for adding to the value already present at $H(n, m)$, thus when performing this rutine for all R, each term will add up to $(t_2 \pm it_2')$ due to the triple counting discussed in Section 5.1. The on-site terms are trivially implemented as $H(n, n) = -\mu$. We will leave the details regarding the structure of the mean fields and implementation of the interactions to Appendix F.

As a final note on the numerical set up in real space, we comment on the consequences of including the four flavours of each site, that is $\tau = \pm$ and $\sigma = \uparrow, \downarrow$ labelling valley and spin, respectively. Each input in the Hamiltonian must be uniquely defined by a single operator combination $d^\dagger_{\tau,\sigma,n} d_{\tau',\sigma',m}$, where n, m refers to the site numbers as previous. We thus de-

[1] Note that the p-index merely defines an overall sign of the prefactors and $(-1)^{p=0} = (-1)^{p=6}$, thus the substitution to zero-indexing, $\boldsymbol{\delta}_6 \to \boldsymbol{\delta}_0$, has been made without further complications.

fine $i = 4n + flavour$ and $j = 4m + flavour$, where $flavour = 0, 1, 2, 3$ corresponds to $+\uparrow, -\uparrow, +\downarrow, -\downarrow$, respectively, and $H(n, m) \to H(i, j)$. Thus $i = 0$ all relates to $d^\dagger_{+,\uparrow,0}$, $i = 1$ relates to $d^\dagger_{-,\uparrow,0}$ etc. Each site has four rows (columns) related to creating (annihilating) an electron where each of these rows (columns) reflect a specific flavour at that given site. In this convention, the function $f(R)$ returns an array, $\bar{i}$, with 24 entries defining all i-indices of R. Alongside $\bar{i}$ it returns an array $\bar{p} = [0, 0, 0, 0, 1, 1, 1, 1, 2, ..., 5, 5, 5, 5]$ identifying the p index of $\bar{i}[l]$ (l = 0,...,24). We can use this to infer the additional valley-dependent signs, where the NN hoppings are given by $H(\bar{i}[l], \bar{i}[l + 4]) = t_1 \exp\left[(-1)^{\bar{p}[l]} i(-1)^l \phi\right]$ with periodic boundary conditions. To verify this rather tortuous expression we consider the hopping $d^\dagger_{-,\uparrow,n=0} d_{-,\uparrow,m=1}$. The set $\{-, \uparrow, n = 0\}$ is represented by $i = 4 \cdot 0 + 1 = 1$ and the set $\{-, \uparrow, m = 1\}$ is represented by $j = 4 \cdot 1 + 1 = 5$. From the tight-binding model we have that $H(1, 5)$ is given by $t_1 e^{(-1)^p i\tau\phi} = t_1 e^{(-1)^{p=0} i(-1)\phi} = t_1 e^{-i\phi}$. From the numerics we have that $H(1, 5) = t_1 \exp\left[(-1)^{\bar{p}[l]} i(-1)^l \phi\right] = t_1 \exp\left[(-1)^0 i(-1)^1 \phi\right] = t_1 e^{-i\phi}$. Indeed, the defintion fits. We can implement the valley-dependent sign of the fifth NN hoppings in a similar manner, where $H(\bar{i}[l], \bar{j}[l]) += (t_2 + (-1)^l i t_2')/3$. Overall the convention used is implemented in a Hamiltonian with dimensions $4N \times 4N$, where N is the total number of sites and the factors of four reflect the four different flavours at each site. Once the Hamiltonian is set up, we iterate the model self-consistently until all mean fields converge. Before describing the self-consistent iteration scheme, we explain the basics behind a numerical set up of the TBG model in reciprocal space.

6.2 Discretization of momentum space

To set up our Hamiltonian in reciprocal space, the primary task is to determine allowed points in momentum space. These can be determined by demanding periodic boundary conditions such that $\psi(\mathbf{r}) = \psi(\mathbf{r} + \mathbf{R})$, where $\mathbf{R} = n\mathbf{L}_1 + m\mathbf{L}_2$ translates the state across the lattice. Through Bloch's theorem we have that $\psi(\mathbf{r} + \mathbf{R}) = e^{i\mathbf{k}\mathbf{R}}\psi(\mathbf{r}) \Rightarrow e^{i\mathbf{k}\mathbf{R}} = 1 \Rightarrow \mathbf{k} \cdot \mathbf{R} = 2\pi n$ for $n \in \mathbb{Z}$. We

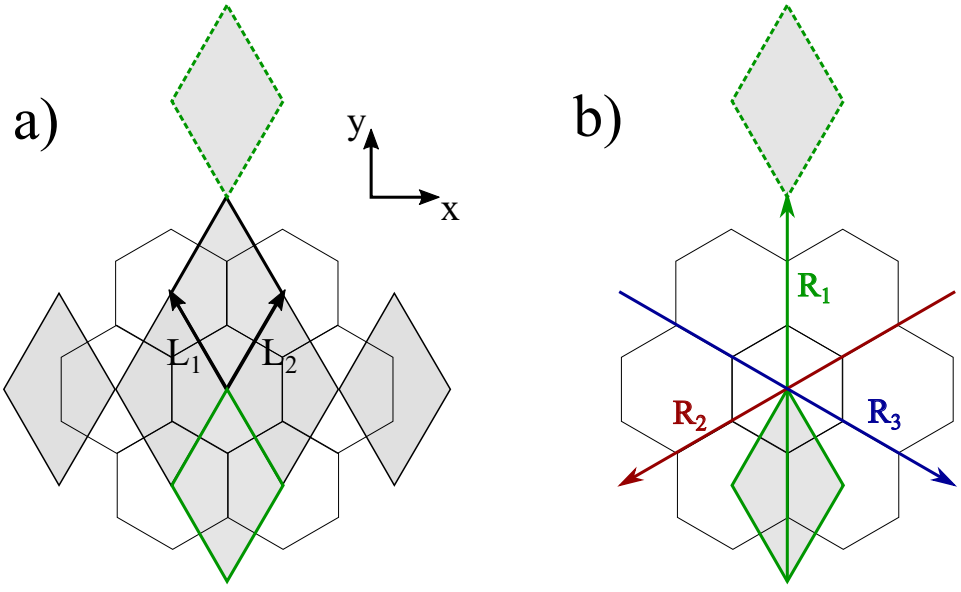

Figure 6.3: **Visualization of real space periodicity**. Filled rhombi display unit cells in a system of size $L = 2$. When imposing periodic boundary conditions unit cells marked by solid and dashed green lines are equivalent. **a)** Illustration of the number of unit cells along $\hat{x}$ (2L) and $\hat{y}$ (L). $\mathbf{L}_{1,2}$ denote the lattice vectors. **b)** Translation vector $\mathbf{R}_1 = L(\mathbf{L}_1 + \mathbf{L}_2)$ connecting equivalent unit cells along y. $\mathbf{R}_{2,3}$ are the C_{3z} related partners of $\mathbf{R}_1$. To preserve this symmetry, periodicity requirements set by $\mathbf{R}_1$ must also hold for $\mathbf{R}_{2,3}$.

will consider a small system with $L = 2$ for simplicity, see Fig. 6.3. In Fig. 6.3a, the unit cell marked by solid, green lines is repeated by the unit cell marked in dashed green lines. We define the vector connecting these two unit cells as $\mathbf{R}_1 = 2\mathbf{L}_1 + 2\mathbf{L}_2$. It is straightforward to show that, in general terms, $\mathbf{R}_1 = L(\mathbf{L}_1 + \mathbf{L}_2)$, where L is the size of the system as defined in the previous section. From trigonometric considerations, we have that $\mathbf{L}_{1,2} = (\mp 1/2, \sqrt{3}/2)^T L_M$ where $L_M = |\mathbf{L}_{1,2}|$. We thus have,

$$\mathbf{k} \cdot \mathbf{R}_1 = \mathbf{k} \cdot \begin{pmatrix} 0 \\ \sqrt{3} \end{pmatrix} L_M L = \sqrt{3} k_y L_M L = 2\pi n \Rightarrow k_y = \frac{2\pi}{\sqrt{3} L_M L} n. \tag{6.1}$$

We directly conclude, that k_y is discretized in steps of $2\pi/(\sqrt{3}L_M L)$. As we have expressed the model in the Bravais lattice picture, the number of inequivalent k_y-points should reflect the periodicity along $\hat{y}$ equal to L, see Fig. 6.3a. Thus, in the present case, we must have two different values of n where the choice of integers sets the origin.
Due to C_{3z}, the same periodicity requirement must hold for $\mathbf{R}_{2,3} = R_z^{\pm 120^\circ} \mathbf{R}_1 = (\mp 3/2, -\sqrt{3}/2)^T L_M L$ (see Fig.6.3b), where we find

$$\begin{aligned} \mathbf{k} \cdot \mathbf{R}_2 &= \mathbf{k} \cdot \begin{pmatrix} -3/2 \\ -\sqrt{3}/2 \end{pmatrix} L_M L \Rightarrow -\frac{3k_x}{2} - \frac{\sqrt{3}k_y}{2} = \frac{2\pi}{L_M L} n_2 \\ \mathbf{k} \cdot \mathbf{R}_3 &= \mathbf{k} \cdot \begin{pmatrix} 3/2 \\ -\sqrt{3}/2 \end{pmatrix} L_M L \Rightarrow \frac{3k_x}{2} - \frac{\sqrt{3}k_y}{2} = \frac{2\pi}{L_M L} n_3 \\ \Rightarrow k_x &= \frac{2\pi}{3 L_M L}(n_3 - n_2). \end{aligned} \tag{6.2}$$

We conclude that k_x is discretized in steps of $2\pi/(3L_M L)$. The number of unit cells along $\hat{x}$ is $2L$ (see Fig.6.3a), thus we have four different values of $m = (n_3 - n_2)$.

Having established the discretization in both directions, all that is left to do, is to determine the boundaries of the first MBZ. From $\mathbf{G}_i \cdot \mathbf{L}_j = 2\pi\delta_{ij}$ it is easy to show that

$$\mathbf{G}_{1,2} = \begin{pmatrix} \mp 1 \\ 1/\sqrt{3} \end{pmatrix} \frac{2\pi}{L_M}.$$

Straightforward trigonometrics yields the intervals

$$k_x = [-4\pi/(3L_M); 4\pi/(3L_M)[$$

and

$$k_y = [-2\pi/(\sqrt{3}L_M); 2\pi/(\sqrt{3}L_M)[.$$

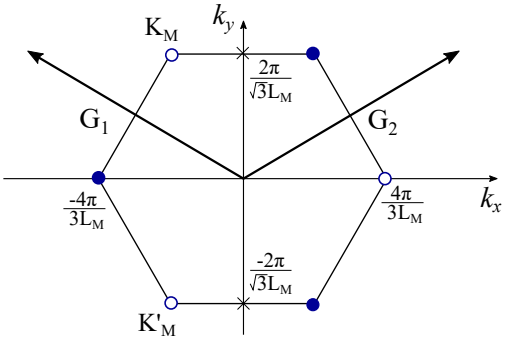

Figure 6.4: **MBZ and boundaries**. $\mathbf{G}_{1,2}$ denotes reciprocal lattice vectors. Filled and empty blue dots are the Dirac points. Minimum and maximum k_x (k_y) values are $\mp 4\pi/(3L_M)$ ($\mp 2\pi/(\sqrt{3}L_M)$), respectively.

Using again the case of $L = 2$, if we take steps according to Eqs. (6.1) and (6.2) we get for k_y that $n = -2, -1, 0, 1$ and for k_x that $m = -4, .., 3$, which does not agree with our previous conclusion that $(\#n, \#m) = (L, 2L)$. The discrepancy is due to the ambiguity in the choice of axis. C_{3z} requires that the discretization also holds for $\hat{x}'$ along $\mathbf{R}_2$ and $\hat{x}''$ along $\mathbf{R}_3$. We solve this issue numerically, by producing a grid of all $\mathbf{k}$-points along $\hat{x}, \hat{y}$. The set of $\mathbf{k}$-values are then rotated by $\pm 120^\circ$, repectively, and only coinciding points are allowed in the final grid. An example of points before and after this selection can be seen in Fig. 6.5. This proceedure will yield a set of $\tilde{N}$ inequivalent $\mathbf{k}$-points, where $\tilde{N}$ is the number of unit cells in the corresponding real space

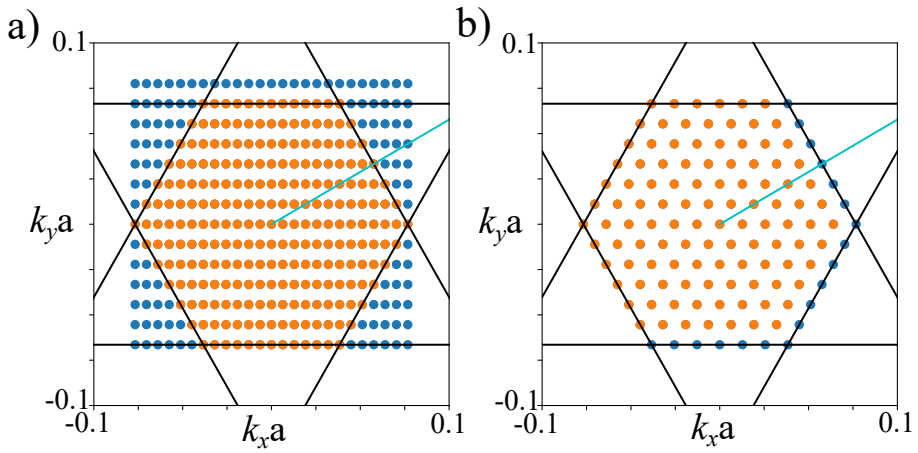

Figure 6.5: **Numerical selection of allowed k-points for** $L = 6$. Black lines mark the MBZ boundaries and cyan line is $\mathbf{G}_2$ inserted as a guide to the eye. **a)** Initial grid of $\mathbf{k}$ values with spacing according the Eqs. (6.1) and (6.2) before the selection. Here we merely sort away all values residing outside the MBZ (blue points) and keep the remaining (orange points). We include all points reciding on the six MBZ edges before the selection. **b)** Remaining points after the C_{3z} selection has been performed. Here we sort away half of the edges two avoid double counting. The orange points in **b)** is the final set of $\mathbf{k}$-points for the case of $L = 6$. $k_{x,y}$ are in units of the reciprocal monolayer unit vector length, $1/a$, and we have used that $L_M = a/(2\sin(\theta/2))$ [22].

system.

Having identified the symmetry allowed set of $\mathbf{k}$-points, the TBG model in Eq. (5.38) can be set up. We set the dimensions of the full Hamiltonian as $dim(H) = (\tilde{N}, 8, 8)$ and structure the mean field parameters in the same manner such that e.g. $\overline{MF}(0,0,0) = \langle a^\dagger_{+,\uparrow,\mathbf{k}(0)} a_{+,\uparrow,\mathbf{k}(0)} \rangle$. Here $\mathbf{k}(0)$ simply refers to the first point in an array containing all $\mathbf{k}$-points. The tight-binding model is generated by computing the $\mathbf{k}$-dependent hopping parameters according to Eq. (4.14) (with the additional gauge tranformation of $\tilde{t}_1(\mathbf{k})$) enabling a straightforward implementation of Eq. (5.16), where H_{tb} has dimensions $dim(H_{tb}) = dim(H)$. The implementation of the Hartree terms is also straightforward as $\bar{n} = \tilde{N}^{-1} \sum_{\mathbf{k}',i} \overline{MF}(\mathbf{k}', i, i)$ where $\{\mathbf{k}'\} = \{\mathbf{k}\}$ and $i = 0, .., 7$. Implementation of the Fock terms are tremendously more intricate. Here we merely sketch the set up. Each $\underline{\underline{M_s}}$ (s = 1,2,3,4) has four different form factors related to four different mean fields. Each form factor has both $\mathbf{k}'$- and $\mathbf{k}$-dependence. We set up the $4 \times 4 = 16$ form factors as arrays with dimensions $dim(\bar{M}_{st}) = (\#\mathbf{k}, \#\mathbf{k}')$ where $s, t = 1, 2, 3, 4$. We then compute the input of e.g. $a^\dagger_{i\mathbf{k}} a_{j\mathbf{k}} = -V_0 \sum_{\mathbf{k}'} \big(M_{11}(\mathbf{k}') \overline{MF}(\mathbf{k}', j, i) + M_{12}(\mathbf{k}') \overline{MF}(\mathbf{k}', j, i+4) + M_{13}(\mathbf{k}') \overline{MF}(\mathbf{k}', j+4, i) + M_{14}(\mathbf{k}') \overline{MF}(\mathbf{k}', j+4, i+4) \big)$. Here we have used that for $i, j = 0, .., 3$ ($i, j = 4, .., 7$) the sublattice is a (b). We have also directly imposed the exchange structure of the Fock terms such that the input on $a^\dagger_{i\mathbf{k}} a_{j\mathbf{k}}$ is given by inputs $\overline{MF}(\mathbf{k}', j, i)$. Finally, we note that the structure of the form factors directly enables the sum to be performed by matrix multiplication which reduces the computation times significantly.

6.3 Self-consistent solution

We have now discussed the numerical implementation of the decoupled TBG model in real as well as reciprocal space. This is of course a monumental part of solving the system. However,

we have yet to discuss how one obtains the *correct* solution of the system, i.e. the ground state. The ground state is, by definition, the state with the lowest (Helmholtz) free energy. Since the mean fields act as effective fields in the system, the free energy naturally depends on the "strength" of these fields, i.e. their values. Now, one could simply *guess* these values, but the probability of guessing the exact configuration of $R_{tot} \times 6 \cdot 4 \times 6 \cdot 4$ mean fields resulting in the lowest possible energy is obviously vanishing. Furthermore, as the mean fields are average values of operators, these averages depend on the Hamiltonian, and consequently the free energy, by definition. Thus, what we have on our hands are a set of self-consistent equations which can be solved iteratively. To see how the iteration scheme comes about, we first identify

$$\begin{aligned}\langle c_k^\dagger c_l \rangle &= \Big\langle \sum_r \gamma_r^\dagger U_{r,k}^\dagger \sum_s U_{l,s}\gamma_s \Big\rangle \\ &= \sum_{r,s} U_{r,k}^\dagger U_{l,s} \langle \gamma_r^\dagger \gamma_s \rangle \\ &= \sum_{r,s} U_{r,k}^\dagger U_{l,s} \delta_{r,s} f(E_r, \mu), \end{aligned} \tag{6.3}$$

where k, l can be any indices labelling the states, U is the unitary transformation diagonalizing H, γ's denote the eigenvectors, E_r are the eigenenergies, μ is the chemical potential and $f(E_r, \mu)$ is the Fermi-Dirac distribution. In real space r, s run over all $4N = 8\tilde{N}$ states, where, as previous, N is the number of sites and $\tilde{N}$ is the number of unit cells. In reciprocal space, we have assumed homogeneity ensuring that $\mathbf{k}$ is a good quantum number, thus r, s will only run over the eight possible flavour combinations of each $\mathbf{k}$. We specifically write the chemical potential as a variable in the Fermi-Dirac distribution, since the carrier density is given by $\langle n \rangle = \tilde{N}^{-1} \sum_{n=0}^{8\tilde{N}} f(E_n, \mu) \in [0, 8]$, where we can vary the chemical potential to set the desired filling.

The iteration scheme is sketched in Fig. 6.6. To initialize the Hamiltonian, we must asign *some* value to the mean field parameters. To avoid bias in this intialization, we choose a random value between zero and one for all parameters. These random mean fields are used to set up the Hamiltonian as described in the previous two sections. We proceed to diagonalize the Hamiltonian and obtain the eigensystem, $\{E, U\}$. Inserting this system in Eq. (6.3), we generate new values of the mean fields. The new mean fields are used to set up a new Hamiltonian, which can again be diagonalized to obtain a new set, $\{E, U\}$, used to generate a third set of mean fields etc. The proceedure of a single iteration is: Set up the Hamiltonian $\rightarrow$ Diagonalize the Hamiltonian $\rightarrow$ Generate new mean fields. After each iteration, we check if the system has converged. Due to the immense amount of various mean fields in our model, we choose to define convergence by the condition $\sum_n |E_n(m-1) - E_n(m)| < 8\tilde{N} \cdot 10^{-10} t_1$ with m denoting the iteration number, i.e. the average change of each energy in a single iteration must be less than $10^{-10} t_1$. When this requirement is met, the iterations are stopped and we can deduce the ground state from the final mean fields.
Alongside the iteration of the mean fields, we also iterate the chemical potential, μ, to set the desired filling of the system. The small proceedure is illustrated in the dashed rectangle in Fig. 6.6. From the eigensystem $\{E, U\}$ obtained through the diagonalization of H, we calculate $\langle n \rangle = \tilde{N}^{-1} \sum_{n=0}^{8\tilde{N}} f(E_n, \mu)$. We then set $\mu(m+1) = \mu(m) + \eta(\nu - \langle n \rangle)$, where $\nu \in [0, 8]$ is the target filling set by the user, η sets the size of the change and m is again the iteration number. It is evident that μ will decrease for $\nu < \langle n \rangle$ and increase for $\nu > \langle n \rangle$ as it should be. The expression also ensures fixed μ as soon as $\nu = \langle n \rangle$.

Before presenting the results obtained through this scheme, we wish to clarify why convergence of the energies reflects a minimization of the free energy. To demonstrate this concept we consider an on-site Hubbard model for simplicity. The mean field decoupled interaction of this

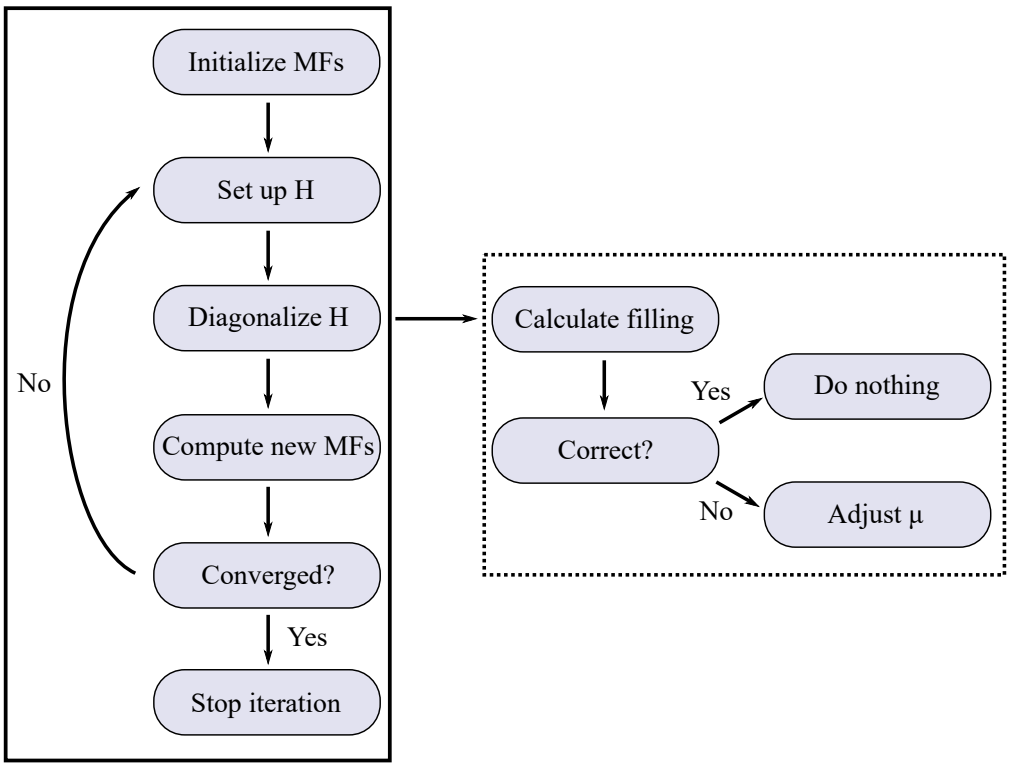

Figure 6.6: **Schematic of the self-consistent iteration scheme**. Rutine shown in the solid rectangle describes the primary iteration of the mean field parameters. Rutine in dotted rectangle show the parallel iteration of the chemical potential, μ. The abrieviations are mean field parameters (MFs) and Hamiltonian (H). See text for detailed describtion of both rutines.

model reads $U_{Hub}^{MF} = V\sum_i(\langle n_{i\downarrow}\rangle n_{i\uparrow} + n_{i\downarrow}\langle n_{i\uparrow}\rangle - \langle n_{i\downarrow}\rangle\langle n_{i\uparrow}\rangle)$, where $n_{i\sigma} = c_{i\sigma}^\dagger c_{i\sigma}$, i denotes the site and σ denotes the spin. We choose the z-direction to point along the spin without loss of generality, thus the exchange terms $\langle c_{i\uparrow}^\dagger c_{i\downarrow}\rangle = 0$. The exact form of the kinetic Hamiltonian is not important in the following.
Let us denote the mean field parameters minimizing the free energy, F_{MF}, as $\bar{n}_{i\sigma}$ ($\sigma = \uparrow, \downarrow$). We must then have that

$$\begin{aligned} 0 = \frac{dF_{MF}}{d\bar{n}_{i\sigma}} &= \frac{d}{d\bar{n}_{i\sigma}}\Big(-\frac{1}{\beta}\ln[Z_{MF}]\Big) \\ &= \frac{1}{Z_{MF}} Tr\Big[e^{-\beta H_{MF}}\frac{d}{d\bar{n}_{i\sigma}}H_{MF}\Big] \\ &= \frac{1}{Z_{MF}} Tr\Big[e^{-\beta H_{MF}}V(n_{i\bar{\sigma}} - \bar{n}_{i\bar{\sigma}})\Big] \\ &= V(\langle n_{i\bar{\sigma}}\rangle_{MF} - \bar{n}_{i\bar{\sigma}}) \end{aligned}$$

where $Z_{MF} = Tr[e^{-\beta H_{MF}}]$ is the partition function of the mean field decoupled Hamiltonian, $H_{MF} = H_{kin} + U_{Hub}^{MF}$. Now let $\langle n_{i\bar{\sigma}}\rangle_{MF}(m)$ denote the value of the mean field parameter computed in iteration m. We then have that

$$\frac{dF_{MF}(m)}{d[\langle n_{i\bar{\sigma}}\rangle_{MF}(m-1)]} = V(\langle n_{i\bar{\sigma}}\rangle_{MF}(m) - \langle n_{i\bar{\sigma}}\rangle_{MF}(m-1)) = 0$$

only when $\langle n_{i\bar{\sigma}}\rangle_{MF}(m) = \bar{n}_{i\bar{\sigma}}(m-1)$ for all i, i.e. at convergence. If $\langle n_{i\bar{\sigma}}\rangle_{MF}(m) \neq \bar{n}_{i\bar{\sigma}}(m-1) \rightarrow H_{MF}(m) \neq H_{MF}(m-1) \rightarrow \sum_n |E_n(m-1) - E_n(m)| \neq 0$, thus we conclude that convergence of the eigenenergies ensures convergence of the mean fields, which in turn ensures a minimization of the free energy.

Chapter 7

Results

In this chapter we present results obtained self-consistently from the numerical procedure described in the previous chapter. We focus on three commensurate fillings of the bands with $\nu = 2, 3, 4$ electrons per unit cell, recall that $\nu = 4$ corresponds to charge neutrality. All three commensurate fillings will be explored at low and intermediate interaction strengths. The results are computed with periodic boundary conditions unless open boundary conditions are explicitly stated. The parameters of the assisted hopping interactions, α_1 and ϕ, express the overlap of neighboring Wannier states within each hexagon. This overlap is computed in Supplementary Material of Ref. [24], thus we adopt the values $\alpha_1 = 0.23$ and $\phi = 0.743\pi$ in our computations. Note the ratio between cluster charge interactions and assisted hopping interactions is $\alpha_1/(1/3) \sim \mathcal{O}(1)$ directly expressing the extended shape of the Wannier orbitals. Remaining parameters are $N = 600 \Leftrightarrow \tilde{N} = 300$, $t_1 = t = 1.0$, $t_2 = 0.025t$, $t_2' = 0.1t$ and the temperature, $T = 2.5 \cdot 10^{-5}t$. Before presenting the results, we recall the symmetries of the system. The model is invariant under $U_v(1) \otimes SU(2) \otimes SU(2)$ representing the valley charge conservation and spin degeneracy in the two decoupled valleys. In addtion, the model exhibits spinfull and spinless TRS and the spatial symmetries are the point group D_3, the global C_{2x} and discrete translational symmetry among unit cells.

7.1 Charge neutrality

The first results we present in this thesis are obtained at filling $\nu = 4$, that is at charge neutrality (CN), where four out of the eight narrow bands are filled. The renormalized real space mean fields (MFs) for $V_0 = 6.0t$ are shown in Table 7.1. The result is homogeneous despite a completely random, inhomogeneous intialization of the MFs. We first note that all on-site MFs are unchanged when including the interactions. Furthermore, all spin/valley mixing mean fields are also unchanged. Thus the result does not break neither the spin $SU(2)$ symmetries nor the $U_v(1)$ valley symmetry. Let us first discuss the intersublattice renormalized hoppings, i.e. terms of type $\langle d^\dagger_{\tau\sigma p} d_{\tau\sigma p\pm1,3}\rangle$. While the MFs themselves might seem slightly confusing, the overall structure yields nothing but a sublattice and valley dependent phase in complete agreement with the gauge transformation. Upon inspection, it is clear that $\langle d^\dagger_{\tau\sigma p} d_{\tau\sigma p\pm1,3}\rangle = |\langle d^\dagger_{\tau\sigma p} d_{\tau\sigma p\pm1,3}\rangle| e^{(-1)^p i\tau\phi'}$, where ϕ' is the renormalized ϕ. These terms will modify the shape and width of the bands but not cause any bands splitting, crossings, gap openings or other interesting features.

The appearance of the purely imaginary $\langle d^\dagger_{\tau,\sigma,p} d_{\tau,\sigma,p\pm2}\rangle$ terms, on the other hand, cannot be understood directly from the gauge transformation, as it only affects intersublattice terms where the phases cancel. They can, however, be deduced from the exchange terms of the decoupled

$V_0 = 6t$	**AB** ($p = 0, 2, 4$) and **BA** ($p = 1, 3, 5$)			
	$d^\dagger_{+\uparrow p}$	$d^\dagger_{-\uparrow p}$	$d^\dagger_{+\downarrow p}$	$d^\dagger_{-\downarrow p}$
$d_{+\uparrow p}$	-	-	-	-
$d_{-\uparrow p}$	-	-	-	-
$d_{+\downarrow p}$	-	-	-	-
$d_{-\downarrow p}$	-	-	-	-
$d_{+\uparrow p\pm1}$	$-0.066 + (-1)^p 0.027i$	-	-	-
$d_{-\uparrow p\pm1}$	-	$-0.066 - (-1)^p 0.027i$	-	-
$d_{+\downarrow p\pm1}$	-	-	$-0.066 + (-1)^p 0.027i$	-
$d_{-\downarrow p\pm1}$	-	-	-	$-0.066 - (-1)^p 0.027i$
$d_{+\uparrow p\pm2}$	$\pm 0.084i$	-	-	-
$d_{-\uparrow p\pm2}$	-	$\mp 0.084i$	-	-
$d_{+\downarrow p\pm2}$	-	-	$\pm 0.084i$	-
$d_{-\downarrow p\pm2}$	-	-	-	$\mp 0.084i$
$d_{+\uparrow p+3}$	$0.059 - (-1)^p 0.024i$	-	-	-
$d_{-\uparrow p+3}$	-	$0.059 + (-1)^p 0.024i$	-	-
$d_{+\downarrow p+3}$	-	-	$0.059 - (-1)^p 0.024i$	-
$d_{-\downarrow p+3}$	-	-	-	$0.059 + (-1)^p 0.024i$

Table 7.1: **Renormalized MFs at $\nu = 4$ and $V_0 = 6t$.** The input on $(d_{\tau'\sigma'p'}, d^\dagger_{\tau\sigma p})$ represents the MF parameter $\langle d^\dagger_{\tau\sigma p} d_{\tau'\sigma'p'}\rangle$. The $\pm$ signs on the NNN hoppings refer to the hopping direction $p \pm 2$. As the result is homogeneous the listed values contain information about all sites. We have subtracted the bare band contributions evaluated at $\nu = 4$ and ignored all MFs with $\frac{|MF|_{max}}{|MF|} > 100$.

interaction. To see this, we consider exchange terms with $p' = p \pm 2$, and have

$$U \propto \sum_{n,m} \alpha_n(p \pm 2)\alpha_m(p)\langle d^\dagger_{p\pm2+n} d_{p+m}\rangle d^\dagger_p d_{p\pm2},$$

where we drop the spin and valley indices for simplicity and $n, m = \{-1, 0, 1\}$ as previous. As H_{tb} includes NN hoppings, we always have finite values of $\langle d^\dagger_{p\pm1} d_p\rangle$ and $\langle d^\dagger_{p\pm2} d_{p\pm1}\rangle$, where all positive (negative) signs are represented in the $p' = p + 2$ ($p' = p - 2$) term. We thus have,

$$\begin{aligned} U &\propto \left(\alpha_{\mp1}(p \pm 2)\alpha_0(p)\langle d^\dagger_{p\pm1} d_p\rangle + \alpha_0(p \pm 2)\alpha_{\pm1}(p)\langle d^\dagger_{p\pm2} d_{p\pm1}\rangle\right) d^\dagger_p d_{p\pm2} \\ &= \frac{\alpha_1}{3}|\langle NN\rangle|(\pm e^{-i\tau\phi} \mp e^{i\tau\phi}) d^\dagger_p d_{p\pm2} = \mp\frac{2i\alpha_1}{3}|\langle NN\rangle| \sin(\tau\phi) d^\dagger_p d_{p\pm2} \end{aligned} \tag{7.1}$$

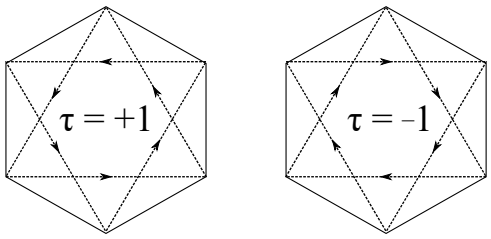

Figure 7.1: **Illustration of the emergent NNN hoppings at CN**. Arrow directions indicate the sign of the coupling. The NNN hoppings are purely imaginary with the sign determined by hopping direction and valley index. The hoppings result in an effective flux at the center of each hexagon. The fluxes of the two valleys are opposite, thus the net flux is zero.

for p even, and

$$\begin{aligned} U &\propto \frac{\alpha_1}{3}|\langle NN\rangle|(\mp e^{i\tau\phi} \pm e^{-i\tau\phi}) d^\dagger_p d_{p\pm2} \\ &= \mp\frac{2i\alpha_1}{3}|\langle NN\rangle| \sin(\tau\phi) d^\dagger_p d_{p\pm2} \end{aligned} \tag{7.2}$$

for p odd. Here we have used that H_{tb} preserves D_3, thus all NN couplings have equal magnitudes and we denote it $|\langle NN\rangle|$. It is evident that the emergence of NNN hoppings is inevitable in our model. Furthermore, the gauge transformation ensures these hoppings to be purely imaginary with an overall sign according to hopping direction and valley index, as is also evident in Table 7.1. We note that the sign is identical for p even and odd.

The NN mean fields all have either n or $m = \pm 1$ and we conclude that these purely imaginary NNN hoppings are a direct consequence of the topological assisted hopping interaction. Fig. 7.1 illustrate the imaginary hoppings, where the arrow directions indicate the sign of the coupling. It is evident that an effective flux can be associated with the center of each hexagon for each valley. The two valleys will experience opposite fluxes and the net flux is zero.
The presence of the NNN hoppings causes an instability of the Dirac semi-metallic phase at charge neutrality and the Dirac cones are gapped away, see Fig. 7.2. Here we use that the result is homogeneous, allowing for a solution of the system in reciprocal space with $\mathbf{q} = 0$ as derived in Chapter 5. The results obtained in reciprocal space are in complete quantitative agreement with the real space results. Top left plot in Fig. 7.2 show the bare, kinetic bands ($V_0 = 0$). The result is identical to the bands presented in Chapter 4. The three band structures presented with $V_0 \neq 0$ all have an energy offset defined thorugh the Hartree terms and the chemical potential, μ. The latter is marked by dashed lines in Fig. 7.2. As we shift μ to ensure $\nu = 4$, the correct filling is obtained when the offet is roughly $E_{off} \approx V_0 \sum_{\mathbf{R}} \bar{n}(\mathbf{R}) - \mu = V_0\nu - \mu = 4V_0 - 4V_0/2 = 2V_0$. This value of the offset is exact, if μ is positioned in the middle of the gap. However, since we choose to disregard the last terms of the HF decoupling, the excitation energies have an arbitrary energy reference and there is no reason to fix μ to the gap center.

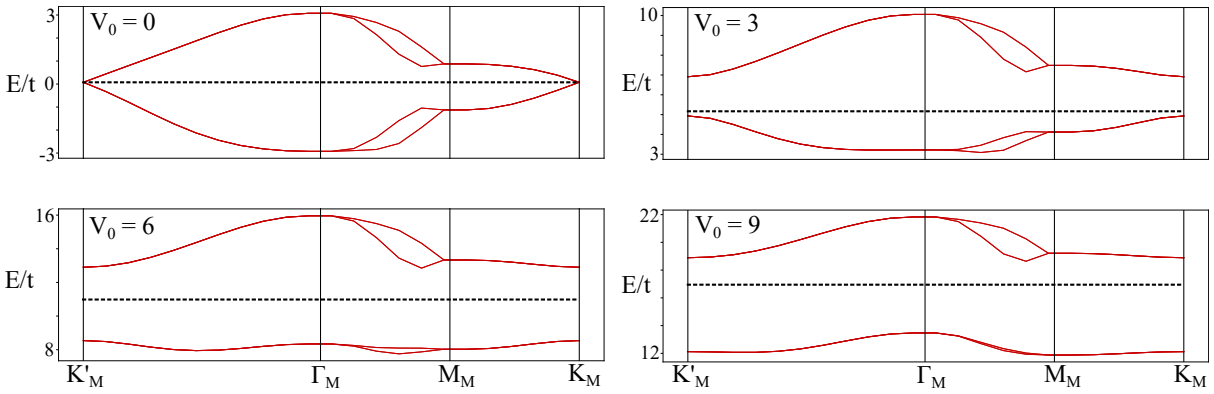

Figure 7.2: **Band structures at CN for various interaction strengths**. Top left figure show the bare bands. This structure is identical to the structure presented in Chapter 4. Remaining structures have $V_0 \neq 0$ and significant gaps are evident in all three cases. The gap size increases with increasing V_0. The shape of the occupied bands gradually shifts from concave to convex.

It is evident that a significant gap is present even at $V_0 = 3$. The gap increases with interaction strength, while the shape of the filled bands gradually shifts from a concave to a convex structure. The form factors in M^F must thus exhibit this convex shape, and the gradual shift directly expresses the competition between H_{tb} and U^{HF}. To investigate a possible critical interaction strength of this insulating phase, we plot the gap size at $\mathbf{K}_M$, $\Delta(\mathbf{K}_M)$, as a function of V_0 in Fig. 7.3. Blue line is the gap size of the full model with $\alpha_1 = 0.23$ as usual and orange line is the gap size for the $\alpha_1 = 0$ case, i.e. without the assisted hopping terms. For $\alpha_1 = 0$ the spectrum remains gapless. The slight increase in gap size is a finite size effect and $\Delta(\mathbf{K}_M, \alpha_1 = 0) \to 0$ for $N \to \infty$. For $\alpha_1 = 0.23$ the gap opens for infinitely small V_0 and the size increases linearly with V_0. Thus, the result confirms both the origin and inevitable emergence of the NNN hoppings.

The fact that the imaginary NNN hoppings opens a gap at charge neutrality should not be a surprise to the readers familiar with the Haldene model [28]. The Haldane model was the first

theoretical proposal of a topolgical insulator which produces a quantum Hall effect without any net magnetic flux through the system.

In the orignial Haldane model, a gap emerges in the graphene spectrum due to broken (spinless) time-reversal symmetry. In the present case we have four copies of the Haldane model including both valley and spin. Since the valleys are related through time-reversal and experience opposite effective fluxes (see Fig. 7.1), the result does not break (spinless or spinfull) time-reversal despite the emergence of a gap.

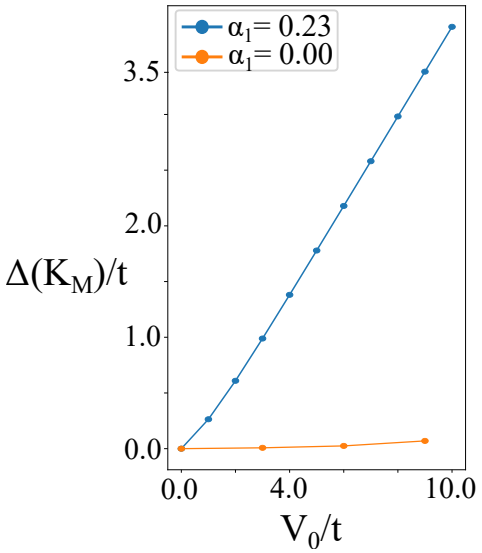

Figure 7.3: **Gap size as a function of interaction strength at CN**. Blue line is the gap size of the full TBG model and the values can be directly compared to the bands shown in Fig. 7.2. The gap opens immediatly as we include interactions, and the size of the gap increases linearly with increasing V_0. Orange line show the gap size without assisted hoppings. The slight increase in gap size with V_0 for $\alpha_1 = 0$ is a finite size effect and $\Delta(\mathbf{K}_M, \alpha_1 = 0) \to 0$ for $N \to \infty$.

Haldane showed that complex NNN hoppings on a honeycomb lattice not only causes a gap to open but also relates a Chern number, $C = \pm 1$ for $\tau = \pm 1$, to the bands in the present regime [28]. We remind the reader that the Chern number is a topological invariant which manifests itself through gapless edge modes in a topological insulator. The number of edge modes associated with each band is quantized according to the Chern number, C, and the system exhibits a quantized Hall conductance, i.e. the quantum Hall effect. Thus, following the findings of Haldane, we expect the result to exhibit quantized edge modes and we dub this phase the quantum valley Hall (QVH) phase. To investigate this feature, we derive an expression of the site-resolved local density of states, $LDOS$, as

$$\begin{aligned} LDOS(i,\omega) &= -\frac{1}{\pi} Im[G^R(i,\omega)] \\ &= -\frac{1}{\pi} Im\Big[\sum_n \frac{|U_{i,n}|^2}{\omega - E_n + i\eta}\Big], \end{aligned} \tag{7.3}$$

where i reflects both site and flavours as in the previous chapter, G^R is the retarded Green's function, U is the unitary tranformation that diagonalizes H and $\eta \to 0$. This is expression is found using that

$$\begin{aligned} \mathcal{G}(i,\tau) &= -[\theta(\tau)\langle c_i(\tau)c_i^\dagger(0)\rangle - \theta(-\tau)\langle c_i^\dagger(0)c_i(\tau)\rangle] \\ &= -[\theta(\tau)\sum_n U_{i,n}U_{n,i}^\dagger\langle\gamma_n(\tau)\gamma_n^\dagger(0)\rangle - \theta(-\tau)\sum_m U_{m,i}^\dagger U_{i,m}\langle\gamma_m^\dagger(0)\gamma_m(\tau)\rangle] \\ &= \sum_n |U_{i,n}|^2\Big(-[\theta(\tau)\langle\gamma_n\gamma_n^\dagger\rangle - \theta(-\tau)\langle\gamma_n^\dagger\gamma_n\rangle]e^{-E_n\tau}\Big) \\ &= \sum_n |U_{i,n}|^2\Big(-[\theta(\tau)(1-f(E_n)) - \theta(-\tau)f(E_n)]e^{-E_n\tau}\Big) \\ \Rightarrow \mathcal{G}(i,ik_n) &= \int_0^\beta e^{ik_n\tau}\mathcal{G}(i,\tau)d\tau \\ &= \sum_n \frac{|U_{i,n}|^2}{ik_n - E_n} \end{aligned}$$

$$\Rightarrow G^R(i,\omega) = \sum_n \frac{|U_{i,n}|^2}{\omega - E_n + i\eta}$$

where $\mathcal{G}$ is the Matsubara Green's function, τ is imaginiary time, ik_n are the Matsubara frequencies and we used analytical continuation in the last step. By opening the boundaries of the system in the QVH phase and integrating the $LDOS$ across the gap, edge localized states should appear. The result is shown in Fig. 7.4, where we present both valley and spin-resolved $LDOS$ for later comparison. For the valley-resolved (spin- resolved) results, top (bottom) panel of Fig. 7.4, we have added the contributions from both spin directions (valleys). The edge modes are clearly visible in all four cases. In the QVH phase at CN we have the valence bands of both spin directions filled for both valleys, thus the in-gap $LDOS$, $LDOS_\Delta$, is equal for $\sigma = \uparrow, \downarrow$ and $\tau = \pm 1$. While the computation of the Chern numbers, hence the quantization of the number of edge states, is left for future work, the clear evidence of gapless edge modes justifies the claim of the non-trivial topology of the QVH phase. This is a rather striking result, as it places TBG as a strong contestant in the search for interaction-induced topological phases in real phases of matter. A search which has been subject to increasing interest during recent years [29–32].

The possibility of experimental evidence of these topological edge modes at CN is, unfortunately, doubtful. According to Haldane model, the propagation direction changes with valley index while both spin directions for each valley will propagate in the same direction. Thus even if one splits the spin degeneracy by applying an external magnetic field, we will still have two counter-propagating modes with equal spin and opposite valley index yielding no net Hall conductance. At this stage, what we *can* verify from experiments is the general insulating behaviour expected at CN from the measurements performed by Lu *et al.*, Fig. 1.2. Furthermore, if the QVH is a general feature across various fillings, it could in principle lead to the supposed QAH measurement performed by Serlin *et al.*, see Fig. 1.4.

As a final note on the QVH phase at CN, we mention the findings of a direct comparison between the HF study presented in this thesis and a quantum Monte Carlo (QMC) study of the same model performed by Yuan Da Liao from the Chinese Academy of Sciences in Beijing. The preprint manuscript is attached in Appendix G. First and foremost, the QMC study confirms the QVH phase. Furthermore, we find a qualitative agreement on the linear increase in gap size with increasing V_0. Strikingly, we even find a quantitative agreement on the NNN hoppings for $\alpha_1 = 0.1$ and $V_0 = 8t$. The power of this comparison cannot be underestimated. QMC simulations offer an exact solution of the model, and the general agreement serves as a direct validation of the HF approximation in the TBG model. Additionally, QMC simulations will often encounter the so-called sign-problem which prohibits solutions. In the present case, a sign-problem free simulation can only be performed at CN with $\phi = \pi/2$. This is in strong contrast to the HF model of this thesis, as both the filling and ϕ are free parameters and can be chosen as desired. Thus the HF machinery offers a much larger exploration of the TBG phase diagram.
In the study attached in Appendix G the parameters are chosen as $\phi = \pi/2$ (to avoid a sign-problem) and $\alpha_1 = 0.45$. Thus the result also provides a general parameters check, and verifies that the QVH is stable across varying ϕ and α_1. From Eqs. (7.1) and (7.2) we assume that the magnitude of the NNN hoppings increase with α_1, which is confirmed by the results presented in Appendix G. In addition to this parameters check, we also check for finite size issues and find complete quantitative agreement between the MFs in Table 7.1, $N = 600$, and a system with $N = 1350$.

The validation of the interaction-induced QVH phase at CN from QMC raises a series of questions which can only be answered by HF calculations. Is the QVH phase stabil across several

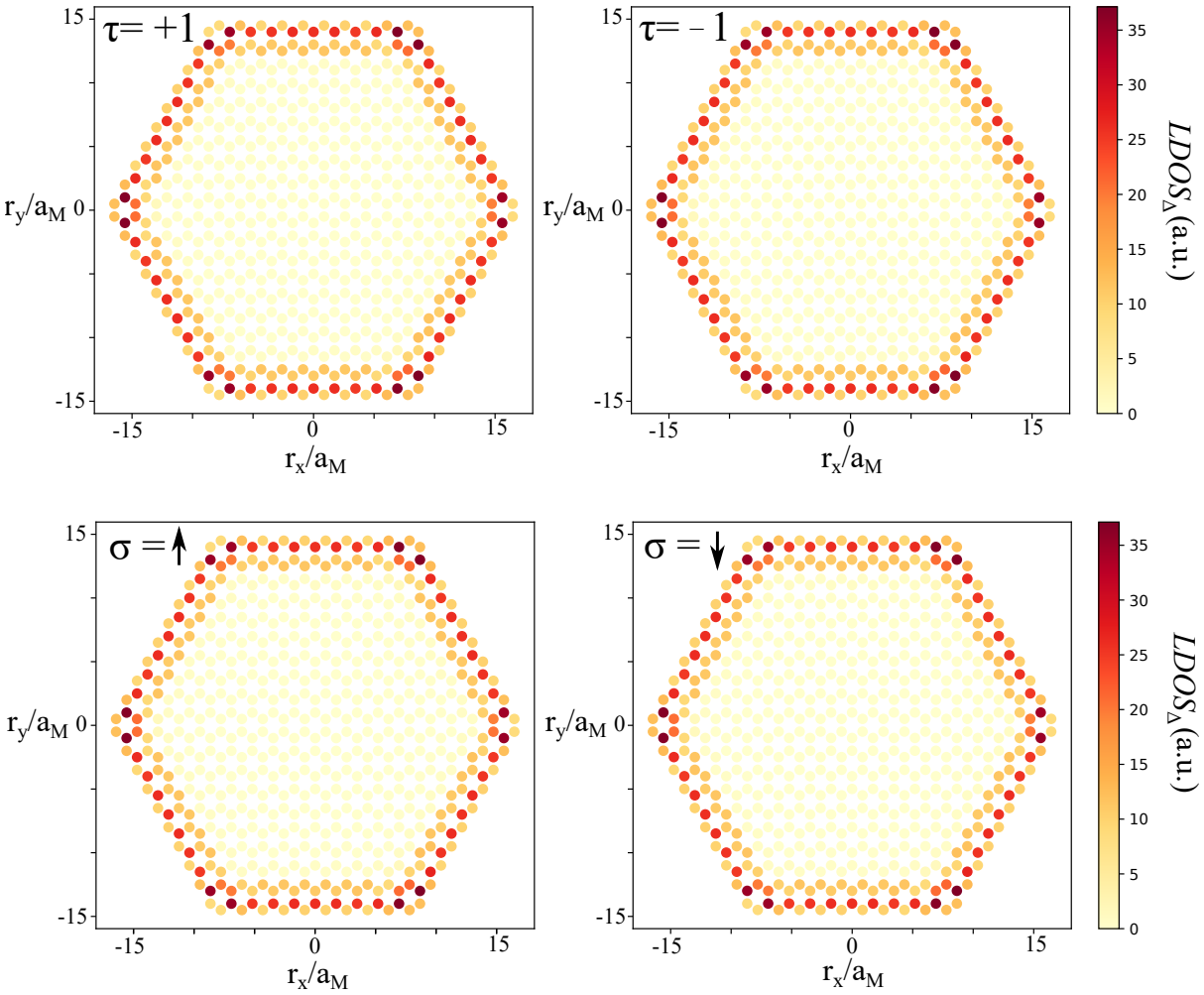

Figure 7.4: **Spin- and valley-resolved in-gap LDOS at CN for** $V_0 = 6t$. The $LDOSs$ are integrated for $8.8 \leq \omega/t \leq 11.8$ with discretisation $\Delta\omega = 10^{-2}$ and $\eta = 0.001$. Top panel show valley-resolved $LDOS(\tau, n) = \sum_\sigma LDOS(\tau, \sigma, n)$, where n is the site index. Bottom panel show the spin-resolved $LDOS(\sigma, n) = \sum_\tau LDOS(\tau, \sigma, n)$. All four plots are identical, as we have four occupied bands corresponding to one band of each flavours at CN. Units of $r_{x,y}$, $a_M = L_M/\sqrt{3}$, is the moiré lattice spacing.

of the commensurate filling regions, where the experimental evidence suggest insulating phases (Figs. 1.2, 1.3)? Is the QVH phase encountered at infinitely small interaction strengths at all fillings? And finally, can the QVH phase pose as a possible explanation of the QAH effect observed in Ref. [10]? We will attempt to answer these questions in the subsequent sections.

7.2 Three-quarters and half filling at intermediate interaction strengths

In this section we present results at three-quarters and half filling of the valence bands, i.e. $\nu = 3, 2$ electrons per unit cell, respectively. We will primarily discuss results obtained at $V_0 = 6t$ in the intermediate interaction regime. We know from the results at charge neutrality that the HF method produces strikingly realiable results in this regime at $\nu = 4$. Furthermore, we know that the order parameters of the QVH phase, that is the NNN hoppings, increase with interaction strength. Thus, it is not unreasonable to begin our exploration of new fillings

regimes and the universality of the QVH phase at this relatively high interaction strength. We find a homogeneous ground state at $\nu = 3$ and $V_0 = 6t$ and the renormalized real space MFs are shown in Table 7.2. The results are obtained with the usual parameters listed in the introduction to this chapter. We have initialized the MFs in a homogeneous, random manner, where all 24×24 MFs for each hexagon (see Appendix F) are generated randomly, but we use the same random 24×24 MFs as the initial MFs in each hexagon. We will return to the justification of this initialization later.

$V_0 = 6t$	**AB** ($p = 0, 2, 4$) and **BA** ($p = 1, 3, 5$)			
	$d^\dagger_{+\uparrow p}$	$d^\dagger_{-\uparrow p}$	$d^\dagger_{+\downarrow p}$	$d^\dagger_{-\downarrow p}$
$d_{+\uparrow p}$	0.004	-	$0.190 - 0.100i$	-
$d_{-\uparrow p}$	-	0.125	-	-
$d_{+\downarrow p}$	$0.190 + 0.100i$	-	-0.254	-
$d_{-\downarrow p}$	-	-	-	0.125
$d_{+\uparrow p\pm1}$	$-0.073 + (-1)^p 0.004i$	-	**AB**: $0.087 + 0.059i$	-
$d_{-\uparrow p\pm1}$	-	$-0.045 - (-1)^p 0.049i$	-	-
$d_{+\downarrow p\pm1}$	**AB**: $0.105i$	-	$-0.132 - (-1)^p 0.115i$	-
$d_{-\downarrow p\pm1}$	-	-	-	$-0.045 - (-1)^p 0.049i$
$d_{+\uparrow p\pm2}$	$-0.050 \pm 0.064i$	-	$\pm 0.017 \pm 0.032i$	-
$d_{-\uparrow p\pm2}$	-	$-0.050 \mp 0.084i$	-	-
$d_{+\downarrow p\pm2}$	$\mp 0.017 \pm 0.032i$	-	$-0.050 \pm 0.020i$	-
$d_{-\downarrow p\pm2}$	-	-	-	$-0.050 \mp 0.084i$
$d_{+\uparrow p+3}$	$0.011 - (-1)^p 0.040i$	-	**AB**: $0.020 - 0.034i$	-
$d_{-\uparrow p+3}$	-	$0.010 + (-1)^p 0.062i$	-	-
$d_{+\downarrow p+3}$	**AB**: $0.016 - 0.036i$	-	$0.014 + (-1)^p 0.007i$	-
$d_{-\downarrow p+3}$	-	-	-	$0.010 + (-1)^p 0.062i$

Table 7.2: **Renormalized MFs at $\nu = 3$ and $V_0 = 6t$.** The input on $(d_{\tau'\sigma'p'},\ d^\dagger_{\tau\sigma p})$ represents the MF parameter $\langle d^\dagger_{\tau\sigma p} d_{\tau'\sigma'p'}\rangle$. The $\pm$ signs on the NNN hoppings refers to the hopping direction $p \pm 2$. The NN and NNNN hoppings marked by **AB** are the values for the AB-sublattice. The BA-sublattice values are defined through hermitian conjugation, since $\langle d^\dagger_{+\uparrow p=AB} d_{+\downarrow p\pm1=BA}\rangle^\dagger = \langle d^\dagger_{+\downarrow p=BA} d_{+\uparrow p\mp1=AB}\rangle$. As the result is homogeneous, the listed values contain information about all sites. We have subtracted the bare band contributions evaluated at $\nu = 3$ and ignored all MFs with $\frac{|MF|_{max}}{|MF|} > 100$.

The structure of the renormalized MFs at $\nu = 3$ in Table 7.2 is slightly more complicated than the result at CN. However, the result preserves $U_v(1)$ and we can inspect the result one valley at a time. For $\tau = -1$ the renormalization affects the same MFs as the previous result at CN with an additional renormalization of the densities. For $\nu = 3$ in the bare band case, we enter at metallic phase and the chemical potential is positioned in the valence bands (see Fig. 7.2). The increase in carrier density evident in the diagonal on-site terms implies a band modification lowering the bands. We will confirm this assertion later. Furthermore, we note that seemingly real component of the NNN hoppings is solely due to the subtraction of the bare bands, and the full value of e.g. $\langle d^\dagger_{+\uparrow p} d_{+\uparrow p\pm2}\rangle = \pm 0.064i$. The result for $\tau = -1$ preserves the internal $SU(2)$.

For $\tau = +1$ the interaction induces non-zero $\sigma_{x,z,y}$-components, that is $\langle d^\dagger_{+\uparrow p} d_{+\uparrow p}\rangle - \langle d^\dagger_{+\downarrow p} d_{+\downarrow p}\rangle \neq 0$ and $\langle d^\dagger_{+\uparrow p} d_{+\downarrow p}\rangle - \langle d^\dagger_{+\downarrow p} d_{+\uparrow p}\rangle \neq 0$, thus we have a finite magnetization in this valley and the result breaks the internal $SU(2)$ symmetry. Since the model does not include any mechanisms coupling to the spin (e.g. magnetic field or spin-orbit coupling), it points along an arbitrary direction in the $SU(2)$ Bloch sphere. The direction is equal for all sites, hence it is ferromagnetic. The ferromagnetism naturally also induces non-zero $\sigma_{x,y,z}$-components in the hoppings.

We show this valley selective ferromagnetism in Fig. 7.5a, where we choose to plot the σ_z-component without loss of generality. The ferromagnetism is clearly present (absent) in $\tau = +1$ ($\tau = -1$). Additionally, as opposed to $\tau = -1$, the interactions decrease the total density of $\tau = +1$. Thus we must have significant valley polarization, as is indeed evident from Fig. 7.5b. Finally, we note that the QVH structure of the NNN hoppings is also present for $\tau = +1$. We dub this phase a QVH phase with valley selective ferromagnetism.

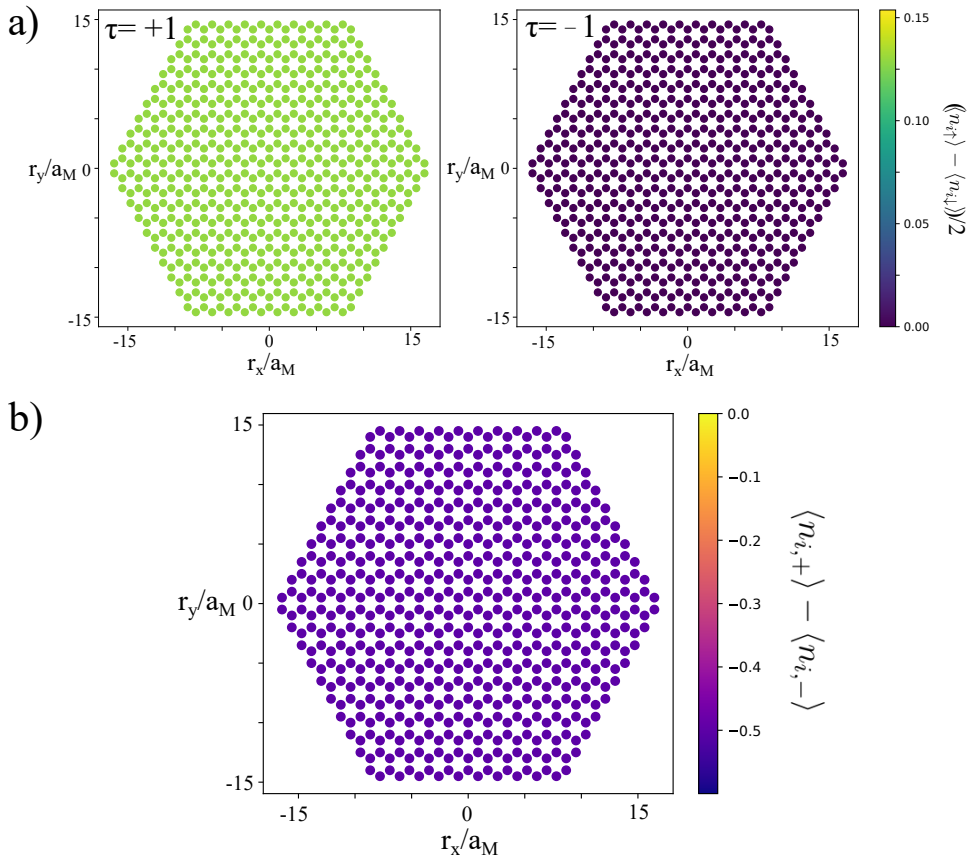

Figure 7.5: **Spin and valley polarization at $\nu = 3$ and $V_0 = 6t$. a)** Spin polarization along $\hat{z}$ of the two valleys. Valley $+1$ has non-zero ferromagnetic spin polarization. Valley -1 has no spin polarization. **b)** Valley polarization, $\sum_\sigma(\langle n_{n,\sigma,+}\rangle - \langle n_{n,\sigma,-}\rangle) \equiv \langle n_{i,+}\rangle - \langle n_{i,-}\rangle = -0.5$, yielding two occupied bands with $\tau = -1$ and a single occupancied band with $\tau = +1$.

The emergent ferromagnetism is the justification for the homogeneous initilization of the MFs. As the reader may be aware, a random initialization of the individual spins in a ferromagnetic system will usually lead to domains of different spin directions. In the present case, we accidentally managed to construct a homogeneous ferromagnet from an inhomogeneous initialization. However, the reproducibility of the ferromagnetic phase from an inhomogeneous initialization with only a single domain, i.e. spin direction, was poor and computation times were unnecessarily long. We found by the homogeneous, yet random, initialization that the results presented here are highly reproducible, though the magnetism can shift to $\tau = -1$ and the spin direction naturally differs from computation to computaion. Both of these variations are to be expected from $SU(2)$ and the random aspect of the initialization.

The results obtained at $\nu = 3, 4$ implies a strikingly simple interpretation depicted in Fig. 7.6. In this interpretation we consider eight completely decoupled bands. The four upper bands are

the conduction bands and the four lower bands are the valence bands. Each conduction/valence band can be labelled with a particular flavour. Here we assume a rotation of the spin subspace has been performed such that $\uparrow$ really points along the spin in the $SU(2)$ Bloch sphere.

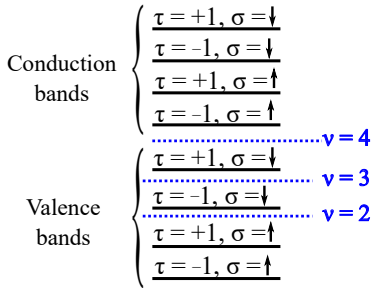

Figure 7.6: **Schematic representation of bands and occupancies at various fillings**. Labelling each band by its flavour, we find at CN that we have two bands of opposite spin filled in each valley. The bands are spin degenerate, thus $SU(2)$ is preserved within each valley. At $\nu = 3$ we have two spin degenerate bands filled for $\tau = -1$ and a single spin $\uparrow$ band filled for $\tau = +1$. Thus the total system is valley and spin polarized. At $\nu = 2$ we have one band filled in each valley. Both bands have $\sigma = \uparrow$ and $SU(2)$ is broken independently in each valley.

At CN ($\nu = 4$) we have all valence bands filled, and the system exhibits neither spin nor valley polarization. At three-quarter filling ($\nu = 3$) we have both spin directions of $\tau = -1$ filled, and this valley will have no net magnetization. However, as we can only fill three bands, the second valley must be completely spin polarized. This picture certainly agrees with our findings so far. Following this line of thought, we have two options at $\nu = 2$. Either the system pushes the band labelled by $\{\tau = +1, \sigma = \uparrow\}$ above the chemical potential and thereby finds a completely valley polarized phase with no net magnetization or the system pushes the band labelled by $\{\tau = -1, \sigma = \downarrow\}$ above the chemical potential and has one band filled for each valley with finite magnetization in both valleys. Indeed, when computing the results at $\nu = 2$ we find the latter of the two as indicated in Fig. 7.6.

We present the renormalized MFs at $\nu = 2$ in Table 7.3 and the σ_z-component of the valley-resolved ferromagnetism in Fig. 7.7a. The result still preserves the $U_v(1)$ symmetry, thus each valley break $SU(2)$ independently and pick two different, arbitrary directions in the Bloch sphere. We note from Table 7.3 that the magnitude of the spin is equal in both valleys as $\sqrt{0.056^2 + 0.191^2 + 0.151^2} = \sqrt{0.142^2 + 0.168^2 + (-0.120)^2} = 0.25$. Adding the contributions from both valleys, we indeed get a total ferromagnetic spin of $|\bar{\sigma}| = 1/2$, yielding a complete spin polarization of the bands. For completeness we plot the valley polarization in Fig. 7.7b, where we merely confirm an equal occupation of both valleys as expected. The QVH structure of the NNN hoppings is evident from the MFs yet again and we dub the phase found at $\nu = 2$ with $V_0 = 6t$ a ferromagnetic QVH phase.

Throughout the analysis of the preferred electronic phases at $\nu = 2, 3$ and $V_0 = 6t$ we have hinted at the emergence of a gap and even dubbed the phases accordingly. However, we have yet to establish the presence of an insulating gap. Thus we display the modified band structures of the two in Fig. 7.8. These are obtained by performing a Fourier tranformation of all the real space MFs, use these as inputs in the self-consistent **k**-space computation and plot the bands upon convergence.

An insulating gap has clearly emerged in the structures. The position of the chemical potential just below the empty bands is a consequence of the very low temperature regime (recall $T = 2.5 \cdot 10^{-5} t$) effectively causing the Fermi-Dirac distribution to be a step function. Thus, as soon as the chemical potential is below a given band the occupancy of said band is zero. As before, the exact position of the chemical potential within the gap has no significance. For $\nu = 3$ we have three filled bands, two from valley $\tau = -1$ and one from valley $\tau = +1$. The two

$V_0 = 6t$	**AB** ($p = 0, 2, 4$) and **BA** ($p = 1, 3, 5$)			
	$d^\dagger_{+\uparrow p}$	$d^\dagger_{-\uparrow p}$	$d^\dagger_{+\downarrow p}$	$d^\dagger_{-\downarrow p}$
$d_{+\uparrow p}$	0.056	-	$0.191 - 0.151i$	-
$d_{-\uparrow p}$	-	0.142	-	$0.168 + 0.120i$
$d_{+\downarrow p}$	$0.191 + 0.151i$	-	-0.055	-
$d_{-\downarrow p}$	-	$0.168 - 0.120i$	-	-0.141
$d_{+\uparrow p\pm1}$	$-0.053 + (-1)^p 0.003i$	-	**AB**: $0.110 + 0.048i$	-
$d_{-\uparrow p\pm1}$	-	$-0.034 - (-1)^p 0.040i$	-	**AB**: $0.091 - 0.045i$
$d_{+\downarrow p\pm1}$	**AB**: $-0.021 + 0.118i$	-	$-0.079 - (-1)^p 0.045i$	-
$d_{-\downarrow p\pm1}$	-	**AB**: $-0.013 - 0.100i$	-	$-0.099 + (-1)^p 0.083i$
$d_{+\uparrow p\pm2}$	$-0.078 \pm 0.051i$	-	$\pm 0.025 \pm 0.032i$	-
$d_{-\uparrow p\pm2}$	-	$-0.078 \mp 0.066i$	-	$0.020 - 0.028i$
$d_{+\downarrow p\pm2}$	$\mp 0.025 \pm 0.032i$	-	$-0.078 \pm 0.033i$	-
$d_{-\downarrow p\pm2}$	-	$-0.020 \mp 0.028i$	-	$-0.078 \mp 0.018i$
$d_{+\uparrow p+3}$	$-0.045 - (-1)^p 0.067i$	-	**AB**:$-0.030 - 0.033i$	-
$d_{-\uparrow p+3}$	-	$-0.046 + (-1)^p 0.083i$	-	**AB**: $-0.024 + 0.029i$
$d_{+\downarrow p+3}$	**AB**:$0.026 - 0.037i$	-	$-0.043 - (-1)^p 0.047i$	-
$d_{-\downarrow p+3}$	-	**AB**: $0.020 + 0.032i$	-	$-0.042 + (-1)^p 0.031i$

Table 7.3: **Renormalized MFs at $\nu = 2$ and $V_0 = 6t$.** The input on ($d_{\tau'\sigma'p'}$, $d^\dagger_{\tau\sigma p}$) represents the MF parameter $\langle d^\dagger_{\tau\sigma p} d_{\tau'\sigma'p'}\rangle$. The $\pm$ signs on the NNN hoppings refers to the hopping direction $p \pm 2$. The NN and NNNN hoppings marked by **AB** are the values for the AB-sublattice. The BA-sublattice values are defined through hermitian conjugation, since $\langle d^\dagger_{+\uparrow p=AB} d_{+\downarrow p\pm1=BA}\rangle^\dagger = \langle d^\dagger_{+\downarrow p=BA} d_{+\uparrow p\mp1=AB}\rangle$. As the result is homogeneous, the listed values contain information about all sites. We have subtracted the bare band contributions evaluated at $\nu = 2$ and ignored all MFs with $\frac{|MF|_{max}}{|MF|} > 100$.

bands with $\tau = -1$ preserves $SU(2)$ within that valley and are degenerate. A residual splitting along $\mathbf{\Gamma}_M\mathbf{M}_M$ from the bare bands splits the degenerate $\tau = -1$ bands from the $\tau = +1$ band. For $\nu = 2$ we have two filled bands, one from each valley, and a residual splitting along $\mathbf{\Gamma}_M\mathbf{M}_M$ remains.

At CN it was reasonable to assume the gap to have non-trivial topology due to the almost direct applicabilty of the Haldane model. We further argued for this non-trivial topology of the bands through the emergence of gapless edge states. The emergence of insulating gaps at $\nu = 2, 3$ enable an investigation of the in-gap $LDOS$ at the two fillings. The results are obtained in the same manner as described in the previous section. The valley- and spin-resolved results are shown in Figs. 7.9 and 7.10.

The emergence of gapless edge modes is indisputable at both fillings. At $\nu = 2$ (Fig. 7.9), the in-gap $LDOSs$ are equivalent for both valleys. This agrees well with the band structure and MFs, where one (spin polarized) band from each valley is occupied. Since the two valleys are completely decoupled, we must have that each gapless mode connects the bulk bands labelled by $\sigma = \uparrow, \downarrow$ within the same valley. From the MFs we know that both bands are primarily spin $\uparrow$ along $\hat{z}$. Thus the spin can be expected to rotate from $\uparrow$ to $\downarrow$ when moving from the bottom to the top of the gap. This should in principle yield an equal contribution from both spin directions. On the contrary, Fig. 7.9 show a dominating spin $\downarrow$ contribution. However, upon further inspection, we *do* find that

$$\frac{\sum_n \int_{-\Delta}^{-\Delta+0.1} LDOS(\omega, n\uparrow) d\omega}{\sum_n \int_{-\Delta}^{-\Delta+0.1} LDOS(\omega, n\downarrow) d\omega} = 2.28,$$

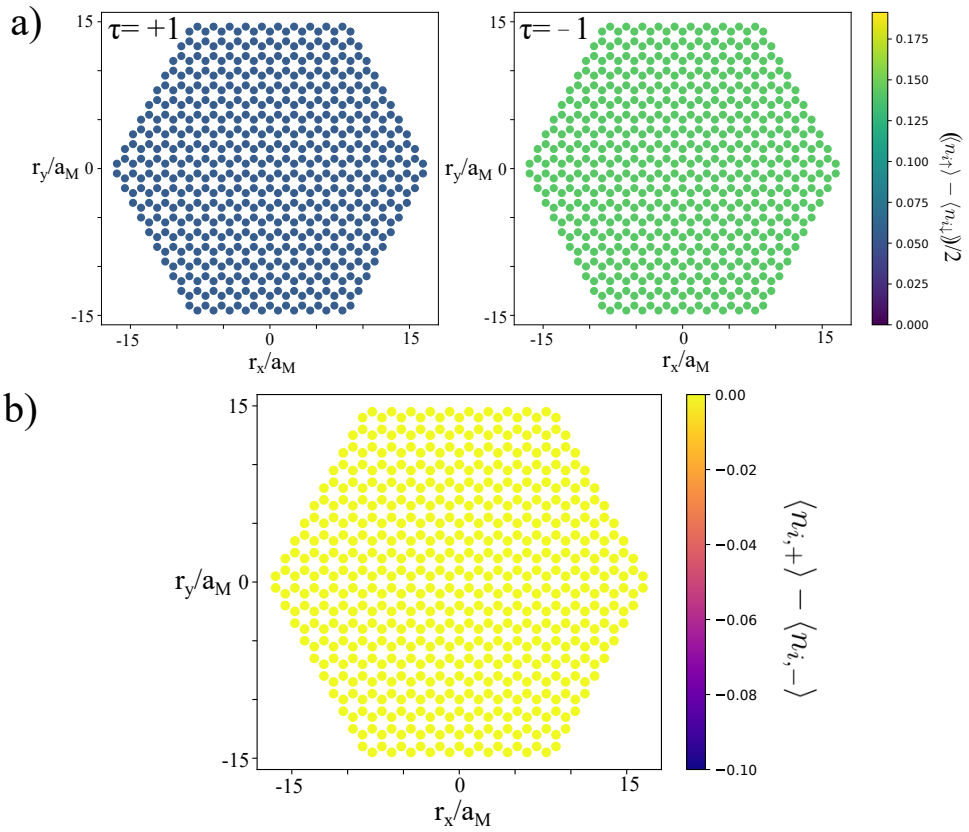

Figure 7.7: **Spin and valley polarization at $\nu = 2$ and $V_0 = 6t$.** **a)** Spin polarization along $\hat{z}$ of the two valleys. Both valleys are ferromagnetic. The two valleys are decoupled and break $SU(2)$ independently, thus the magnitude of the spin along $\hat{z}$ is different for the two. **b)** Valley polarization $\sum_\sigma(\langle n_{n,\sigma,+}\rangle - \langle n_{n,\sigma,-}\rangle) \equiv \langle n_{i,+}\rangle - \langle n_{i,-}\rangle = 0.0$ yielding no valley polarization and equal occupancy of a single band for each valley.

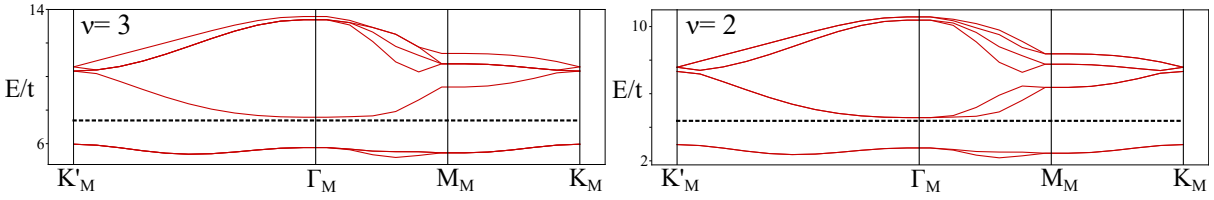

Figure 7.8: **Band structures of $\nu = 2, 3$ with $V_0 = 6t$.** An insulating gap has emergered in both band structure. At $\nu = 3$ the two $\tau = -1$ bands are degenerate while a single $\tau = +1$ band is evident from the residual splitting from H_{tb} along $\mathbf{\Gamma}_M\mathbf{M}_M$. At $\nu = 2$ a single band is occupied in each valley. These bands also split along $\mathbf{\Gamma}_M\mathbf{M}_M$.

and,

$$\frac{\sum_n \int_{\Delta-0.1}^{\Delta} LDOS(\omega, n\uparrow)d\omega}{\sum_n \int_{\Delta-0.1}^{\Delta} LDOS(\omega, n\downarrow)d\omega} = 0.71,$$

where we have suppressed the τ summation for simplicity, n indicates the site and $\pm\Delta$ are the energies at the upper and lower gap edge, respectively. Thus we do indeed have a larger spin $\uparrow$ contribution near the lower band and a larger spin $\downarrow$ contribution near the upper band. Furthermore, we find upon inspection of the energy spectrum that the in-gap excitation energies are not equidistant and two excitation energies recide in the interval $-\Delta < \omega < -\Delta + 0.1$ while six excitation energies reside within $\Delta - 0.1 < \omega < \Delta$. Thus the spin polarization could be a

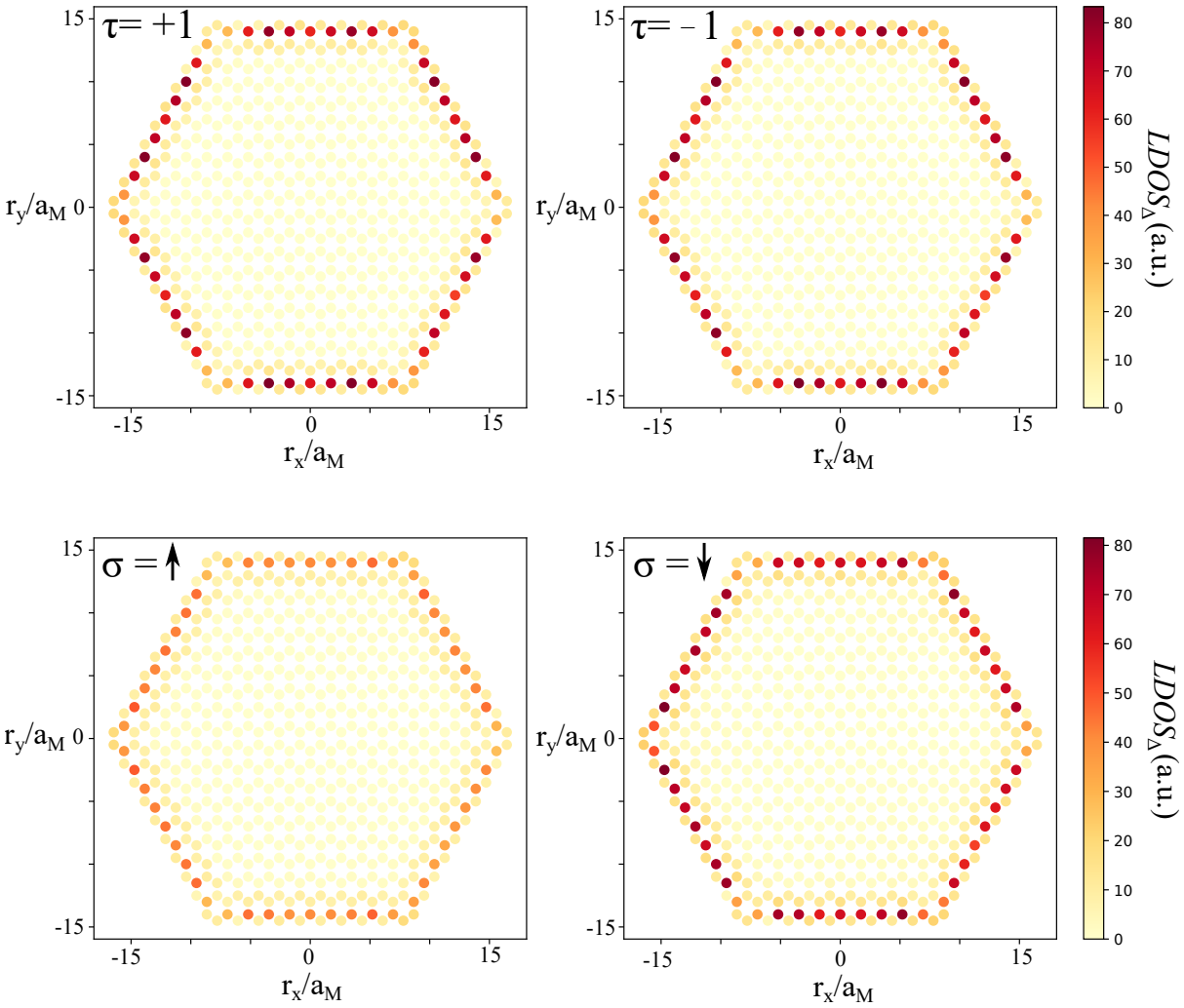

Figure 7.9: **Spin- and valley-resolved in-gap LDOS at** $\nu = 2$. The $LDOSs$ are integrated for $3.38 \leq \omega/t \leq 4.74$ with discretisation $\Delta\omega = 4.5 \cdot 10^{-3}$ and $\eta = 0.001$. Top panel show valley-resolved $LDOS(\tau, n) = \sum_\sigma LDOS(\tau, \sigma, n)$, where n is the site index. Bottom panel show the spin-resolved $LDOS(\sigma, n) = \sum_\tau LDOS(\tau, \sigma, n)$. Valley-resolved plots are identical, as we have one occupied bands from each valley. Units of $r_{x,y}$, $a_M = L_M/\sqrt{3}$, is the moiré lattice spacing

finite size artifact. A further exploration of this is left for future work.
The result in Fig. 7.9 suggests that the ferromagnetic QVH phase does indeed exhibit non-trivial topology as was the case for the non-magnetic QVH phase at CN. However, the Hall conductance in the Haldane model is derived at CN from the gap-closing-and-opening at $\mathbf{K}_M$ ($\mathbf{K}'_M$) and the results are not applicable at $\nu = 2$. Nonetheless, we can state is that the ferromagnetism breaks spinfull time-reversal, $\mathcal{T}$, while spinless $\mathcal{T}$ is still preserved. If we still have $|C| = 1$ for all bands and the propagation direction of the edge mode is still defined by the valley index, the two modes will counter-propagate and the total Hall conductance is zero despite the broken spinfull $\mathcal{T}$. To investigate this hypothesis, one must perform a proper topological analysis. This requires a computation of the Berry curvature of each occupied band, $\Omega_n(\mathbf{k})$, where the associated Chern number can then be calculated as $C_n = \frac{1}{2\pi} \int_{BZ} d\mathbf{k}\, \Omega_n(\mathbf{k})$ [33]. The analysis is left for future work.

At $\nu = 3$ we have two bands with $\tau = -1$ and a single band with $\tau = +1$ occupied. As the valleys are still decoupled, one would intuitively assume from the result at CN that the in-gap

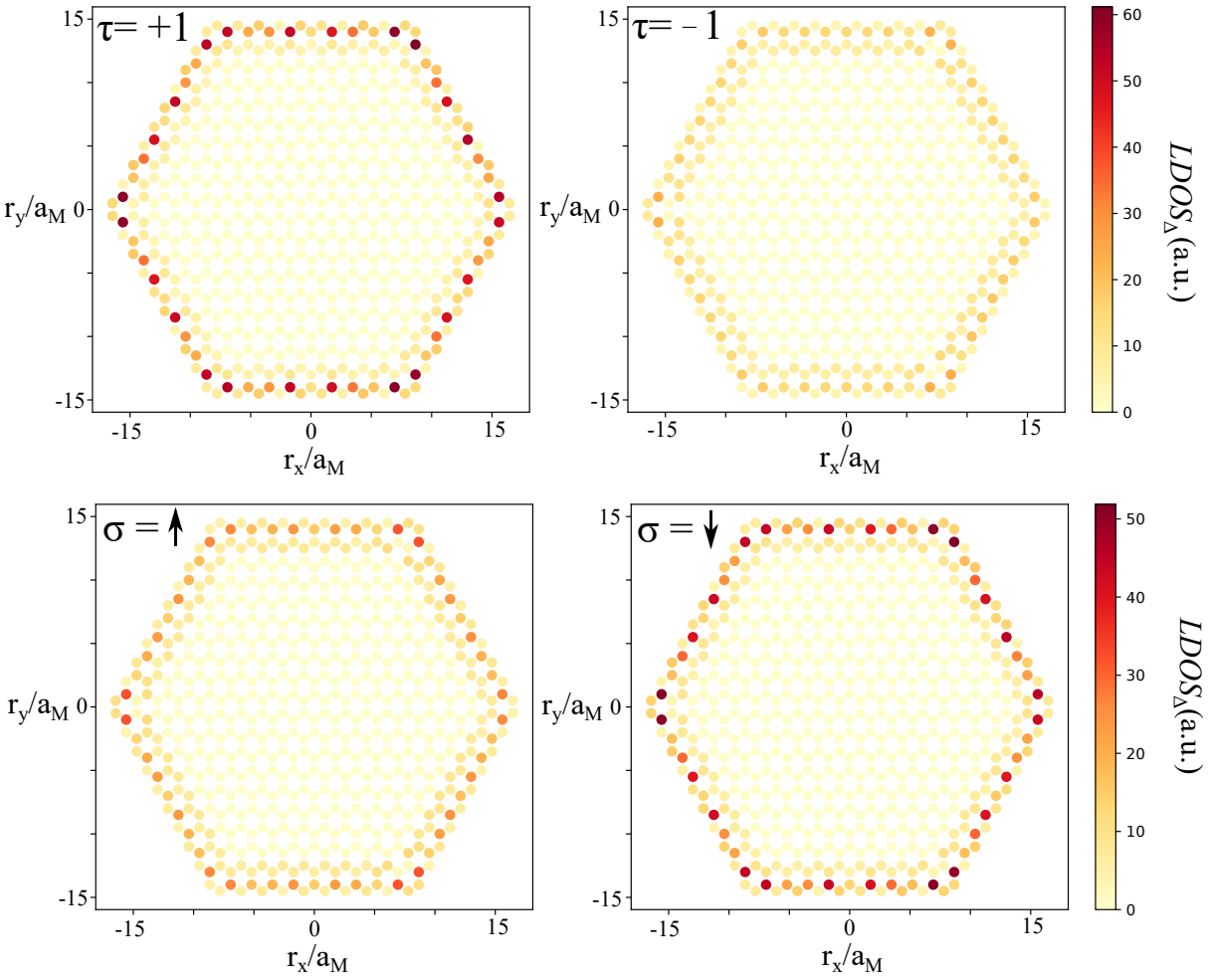

Figure 7.10: **Spin- and valley-resolved in-gap LDOS at** $\nu = 3$. The $LDOSs$ are integrated for $6.45 \leq \omega/t \leq 7.81$ with discretisation $\Delta\omega = 4.5 \cdot 10^{-3}$ and $\eta = 0.001$. Top panel show valley-resolved $LDOS(\tau, n) = \sum_\sigma LDOS(\tau, \sigma, n)$, where n is the site index. Bottom panel show the spin-resolved $LDOS(\sigma, n) = \sum_\tau LDOS(\tau, \sigma, n)$. Units of $r_{x,y}$, $a_M = L_M/\sqrt{3}$, is the moiré lattice spacing

$LDOS$ of valley -1 would be roughly twice as large as the in-gap $LDOS$ for valley $+1$. Interestingly, we find quite the contrary conclusion in Fig. 7.10. Without a proper topological analysis, one can only conjucture at this discrepancy. What we can confirm is a visible difference in the valley-resolved in-gap $LDOS$. This difference presumably refers to the spontanously broken (spinfull *and* spinless) $\mathcal{T}$ and suggests the possibility of a finite, quantized, net Hall conductance without external magnetic field, i.e. a quantum anomalous Hall (QAH) effect. Since we have approximate particle-hole symmetry of the bare bands (broken by the small $t_2 = 0.025$) it is not unreasonable to conjecture that the proposed QAH at $\nu = 7$ (three-quarters filling of the conduction bands) presented in Ref. [10] and discussed in Chapter 1 might be closely related to the results presented here at $\nu = 3$. We also note the apparent spin polarization of the gapless edge modes. This is most likely caused by the mechanisms discussed for the $\nu = 2$ case.

We end the discussion of the results at $\nu = 2, 3$ with an investigation of the V_0 dependence. From the results at CN we know that a decrease in V_0 causes the bands to gradually bend upwards, see Fig. 7.2. For Fig. 7.8 one can imagine how this modification in shape alongside a decrease of the gap will cause the occupied bands to overlap in energy with the empty bands,

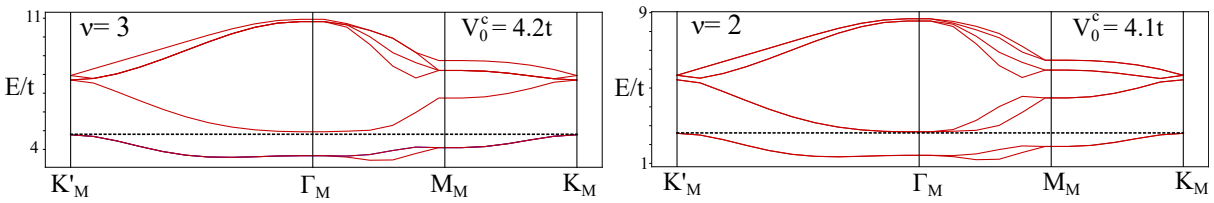

Figure 7.11: **Band structures for V_0^c at $\nu = 2, 3$.** Reducing V_0 will cause an upwards bending of the occupied bands and a decrease of the band gap. Combining these two effects leads to a critical interaction strength required to open an insulating gap. Upon further reduction of V_0 in the present two structure, the chemical potential can no longer avoid a band crossing.

thus closing the gap at a critical interaction strength V_0^c. We find at $\nu = 3$ that $V_0^c = 4.2t$ and at $\nu = 2$ that $V_0^c = 4.1t$, see Fig. 7.11. It is clear that upon further upwards bending of the bands at $\mathbf{K}_M$ ($\mathbf{K}'_M$) and reduction of the gap, the chemical potential can no longer avoid band crossings. This is in stark contrast to the results at CN, where an arbitrarily small splitting of the bands will open an insulating gap. We will discuss the results at $\nu = 2, 3$ below the critical interaction strength in the following, last section of this chapter.

7.3 Three-quarters and half filling at low interaction strengths

When the insulating gap closes at $\nu = 2, 3$, distinct phases occur upon variations of V_0. We will begin by stating the two common properties of the phases presented in this section: *i)* all phases are inhomogeneous and *ii)* all phases are metallic, i.e. the insulating gap does not reemerge with the inhomogeneous structures. Due to the inhomogeneity, we will spare the reader of endless tables listing all of the MFs and restrict our discussion to figures displaying the inhomogeneous structures. Additionally, since $\mathbf{q} \neq 0$, we do not have access to the modified band structures with the current machinery. The metallic behaviour is thus established from the real space excitation energy spectra and yields an important agreement with experiments. Recall Fig. 1.3 where increasing the screening, i.e. decreasing the interactions, suppresses the resitivity at fillings $\nu = 2, 3$. While an agreement on general transport properties is neat, the overall goal from a theoretical point of view must be to determine the full electronic ground state. As a multitude of electronic phases, e.g. charge density wave, spin density waves, (anti)ferromagnets etc., can all be metallic, the transport properties merely serve as motivation to explore the phase diagram in the low V_0 regime.

We first present results at $\nu = 3$ with $V_0 = 2t, 3t$. The results are obtained with a random, homogeneous initialization of the MFs as in the previous section. In Fig. 7.12a we display the site- and valley-resolved σ_y-component of the spin for $V_0 = 2t$. All valley mixing MFs are zero, thus the result preserves $U_v(1)$ and the valleys remain decoupled. Valley $+1$ preserves $SU(2)$ while valley -1 breaks it. To investigate the spin modulation of $\tau = -1$ we perform a Fourier analysis, using that

$$M_i(\mathbf{q}) = \frac{1}{N} \sum_{\mathbf{r}} e^{i\mathbf{q}\mathbf{r}} M_i(\mathbf{r}), \tag{7.4}$$

where $\mathbf{r}$ is the position of the site, N is the total number of the sites, $\mathbf{q} = \mathbf{k} - \mathbf{k}'$ and $M_i(\mathbf{r}) = \langle \mathbf{d}^\dagger{}_\tau(\mathbf{r}) \sigma_i(\mathbf{r}) \mathbf{d}_\tau(\mathbf{r}) \rangle$ for $i = x, y, z$ and $\mathbf{d}^\dagger{}_\tau(\mathbf{r}) = (d^\dagger_{\tau\uparrow}(\mathbf{r}), d^\dagger_{\tau\downarrow}(\mathbf{r}))$. $M_i(\mathbf{q})$ will peak at $\mathbf{q}$-points corresponding to the modulation of $M_i(\mathbf{r})$. $M_y(\mathbf{q})$ of Fig. 7.12a with $\tau = -1$ can be seen in Fig. 7.13a, where we subtract the average magnetization along $\hat{y}$ to avoid a peak at $\mathbf{\Gamma}_M$. We find three inequivalent $\mathbf{q}$-vectors related by C_{3z}. Interestingly, the modulation directions are sligthy

rotated with respects to the original $\hat{x}$ which breaks C_{2y}. The angle of rotation is $\theta = 11°$. Fig. 7.13b depict the spin modulations obtained through an inverse Fourier transformation only including the six dominating **q**-vectors with an overlay of the modulation's contour lines. We find that the wave length of the modulation is $\lambda = 6.54a_M = 3.77L_M$. This length scale sets the size of the modulation unit cells. However, due to the relative rotation between the modulations and the underlying lattice, translational symmetry is not preserved among the modulation unit cells. As we have seen previous, the slight relative rotation should induce a moiré pattern with length scale $\sim \mathcal{O}(L_M/\theta) = 5.2L_M$. However, as we also find incommensurate length scales the lattice and spin modulations, this estimate no longer holds and a moiré pattern is not guaranteed. *If* an enhanced, well-defined, unit cell exists, the lenght scale is $>> L = 10$ (recall the definition of the system size from the previous chapter). Generally, when modulation length scales are $\gtrsim L$, the system cannot display the full structure due to periodic boundaries. Thus the result in Fig. 7.12a is expected to be highly system size dependent.

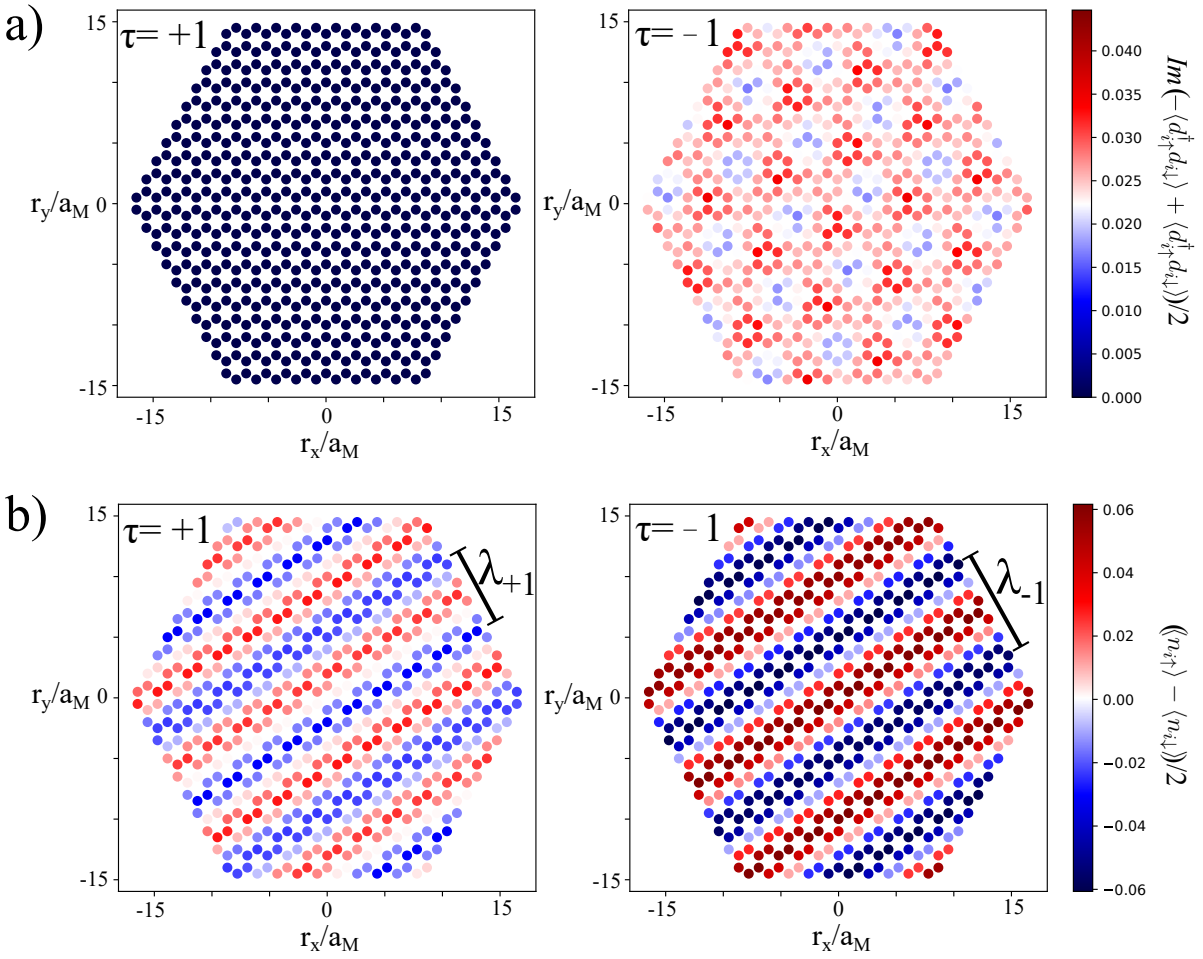

Figure 7.12: **Site- and valley-resolved dominating spin components at $\nu = 3$. a)** Spin component along $\hat{y}$ with $V_0 = 2t$. The result preserves $U_v(1)$. Valley $+1$ has no spin polarization. Valley -1 is ferromagnetic with modulations breaking spatial symmetries. **b)** Spin component along $\hat{z}$ with $V_0 = 3t$. The result breaks $U_v(1)$ and substantial valley mixing is present. Both figures show striped, antiferromagnetic spin modulations. The modulation lengths are indicated by $\lambda_{\pm 1}$. Due to valley mixing, the two modulations will interfere and the combined modulation has $\lambda_{int} \sim 15L_M > L = 10$.

We conclude that the result at $\nu = 3$ for $V_0 = 2t$ suggests that a spin density wave (SDW) could be energetically favorable. The result further indicates that the spin modulation will only

be present in one of the valleys, and that this valley will spontanously break the translational symmetry and possibly enhance the TBG moiré unit cell to an even larger superstructure.

For $V_0 = 3t$ the result alters significantly. In Fig. 7.12b we plot the site- and valley-resolved σ_z-component. This result has substantial valley mixing with $|\tau_x|, |\tau_y| \approx 0.1$ (where $\tau_{x,y}$ are the Pauli matrices in valley space) and thus breaks $U_v(1)$. The fact that the valleys mix is a new feature not previously encountered in this thesis. This leads us to suspect that the valley mixing phase might be merely a local minimum in the free energy landscape trapping the MFs. Interestingly, we find that even when using the converged MFs of the result for $V_0 = 2t$ as input in the $V_0 = 3t$ computation, the valley mixing MFs are quickly induced, and the result moves towards the striped spin modulation in Fig. 7.12b. This finding suggests that the valley mixing phase is really a global minimum and further implies a highly involved phase diagram at $\nu = 3$ in the low V_0 regime, where it is reasonable to assume that more phases might emerge with a complete sweep of V_0. In addition to the valley mixing, Fig. 7.12b show significant striped spin modulations breaking C_{3z} while preserving C_2 along $\mathbf{q}$. By Fourier analysis we find wave lengths $\lambda_{+1} = |2\pi/\mathbf{q}_{+1}| = 3.75L_M$ and $\lambda_{-1} = 5.0L_M$ as indicated in the figure. However, as the valleys are not decoupled, the separation is meaningless and the true modulation length is defined from the inteference of the two patterns. Here we note that, on top of the different wave lengths, the two modulation structures has a relative phase shift evident by comparing the two structures in Fig. 7.12b. We find that the interference has $\lambda_{int} \sim 15 > L = 10$, thus the result is again expected to be system size dependent
While further investigation is needed to draw certain conclusion, both results in Fig. 7.12 suggest that broken spatial symmetries and SDWs could be a general feature at $\nu = 3$ in the low V_0 regime.

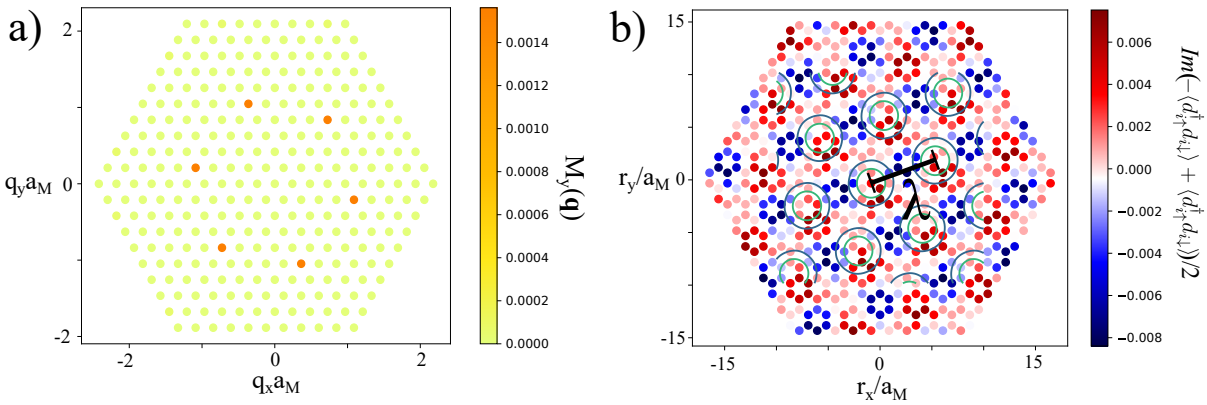

Figure 7.13: **Fourier spectrum and dominating $2\pi/\mathbf{q}$ modulations along σ_y for $\nu = 3$, $\tau = -1$ and $V_0 = 2t$.** **a)** Fourier spectrum of the spin modulations depicted in Fig. 7.12a for $\tau = -1$. The spectrum peaks at three distinct $\mathbf{q}$-vectors related by C_{3z}. The peaks are rotated by $\theta = 11°$ with respect to the C_{3z} related axis of the MBZ. We have subtracted the average magnetization along $\hat{y}$ to avoid a peak at $\mathbf{q} = (0, 0)$. **b)** Inverse FT of the six peaks in **a)**. The spin modulations has a strong resemblance to the total modulations in Fig. 7.12a for $\tau = -1$. Overlay is a contour plot of the interference pattern of all three modulation waves with interference wave length $\lambda = 3.77L_M$.

At $\nu = 2$, the low V_0 regime proves even more intricate. Initiating the MFs homogeneously as previous immediately traps the system in a local minimum of the free energy landscape, where convergence at commensurate filling $\nu = 2$ is impossible with the current iteration scheme. Thus

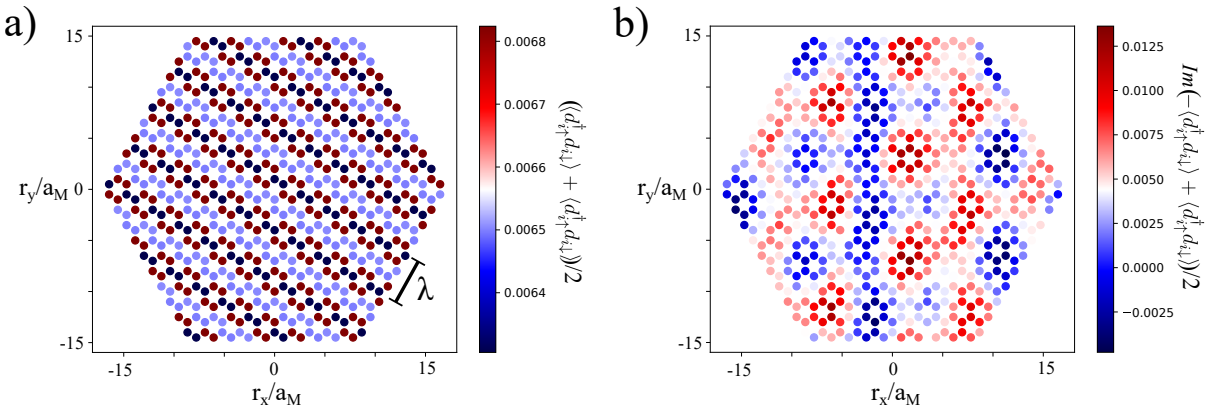

Figure 7.14: **Site-resolved dominating spin components at** $\nu = 2$. Both result has valley mixing. **a)** Spin component along $\hat{x}$ with $V_0 = 2t$. Striped, ferromagnetic spin modulations reminiscent of the result at $\nu = 3$ and $V_0 = 3t$ are evident. Fourier analysis yields the modulation length $\lambda = 2.5L_M$ **b)** Spin component along $\hat{y}$ with $V_0 = 3t$. The result suggest a domain wall along r_y with $r_x/a_M \sim -1$. The domain wall obscures the modulation pattern. The result breaks translational symmetry and the modulations could be similar to the pattern in $\tau = -1$ at $\nu = 3$ for $V_0 = 2t$.

we initiate the MFs in a random and *in*homogeneous manner. The site-resolved spin along $\hat{x}$ for $V_0 = 2t, 3t$ is shown in Fig. 7.14. We have not resolved the results in the valley degree of freedom due to significant valley mixing of $|\tau_{x,y}| \sim 0.01, 0.03$ for $V_0 = 2t, 3t$, respectively. The results are reminiscent of the preceeding results at $\nu = 3$ with two notable differences: *i)* both results exhibit significant valley mixing and *ii)* the spin modulations are exchanged in terms of interaction strength such that the striped SDW is now present for $V_0 = 2t$ and moiré superstructure SDW is (questionably) present for $V_0 = 3t$. We also note that the result for $V_0 = 3t$ suggests the presence of a domain wall around $r_x/a_M \sim -1$. As we have previously discussed the likely emergence of domain walls in spin structures with an inhomogeneous initialization, it is not an unexpected outcome. However, it further complicates the analysis of the spin modulations for $V_0 = 3t$, as no well-defined pattern is evident. Fourier analysis of this result yields a multitude of different **q**-peaks, reflecting the lack of universal structure. In contrast, a Fourier analysis of Fig. 7.14a yields a single modulation length of $\lambda = 2.5L_M$ fully consistent with the visible SDW. As $\lambda < L = 10$, the result is expected to be system size independent. While further investigations are desirable at $V_0 = 3t$, the result at $V_0 = 2t$ is fully reproducible between random initilization and seems reliable. We again note that the quite different results at $V_0 = 2t, 3t$ points towards a highly complicated phase diagram and investigations at additional interaction strengths is needed to make general conclusions. Though nothing definite can be deduced before these investigations have been performed, we choose to include the results due to a recent experiment presented Ref. [34]. Here Cao *et al.* reports finite transverse resistance of TBG samples with $\nu \sim 2$. The transverse resistance suggests an anisotropic resistivity tensor with non-zero off-diagonal components. Cao *et al.* uses this to conjecture that the correlated electronic state might be either a nematic phase or a (charge/spin) density wave. This conjecture agrees with our preliminary results at $\nu = 2$ and serves as a strong motivation of further investigations in this parameter range. Since spin structures are measurable in neutron scattering experiments, it opens the possibility of direct comparison between theoretical preditions and experimental evidence.

With this intriguing prospect, we finalize the results presented in this thesis. The results suggests a wide range of interaction-induced electronic phases in TBG and indicate that further

investigations of parameter space will add new and exotic phases to the phase diagram. In particular, the results imply that the topological QVH phase is a general feature of the TBG model for intermediate interactions strengths which places TBG as a promising candidate of an experimental realization of interaction-induced topological phases of matter.

Chapter 8

Conclusion and Outlook

Throughout this thesis we contructed a model reflecting the symmetries and extended nature of the Wannier orbitals in "magic" angle TBG. We further performed a Hartree-Fock decoupling of said model and implemented a self-consistent solution numerically. The self-consistent minimization of the free energy yielded a general feature of the TBG model with interaction-induced imaginary next-nearest neighbor hoppings reminiscent of the Haldane model. The imaginary hoppings generated an insulating gap in the band structure where a clear presence of edge modes in the gap suggests a non-trivial topology of the phases. These quantum valley Hall (QVH) phases was identified across several band fillings and interaction strength. In particular, we found a strong stability of the QVH phase at charge neutrality across all low-intermediate interaction strengths. This finding ties well into the experimental evidence of a clear insulating gap persistent across several interaction strengths [9].
At three-quarters and half filling of the valence bands we found that the signatures of the QVH phase disappeared below critical values of the interaction strength. In this low interaction strength regime, we found significant variations of the phases across narrow regions. The variations suggest a highly complex phase diagram reflecting the numerous symmetries all subject to spontanous breaking. Despite the variations, all phases found at low interaction strengths exhibited an anisotropy in the form of spin density waves which is in general agreement with new experimental evidence [8]. A further investigation of this regime is an intriguing opportunity to identify the fundamental mechanism driving the spin density waves thereby opening the possiblity of a direct comparison to neutron scattering experiments.

While further analysis of the results presented in this thesis alone could be instructive, the constructed model offers a much wider exploration of the TBG platform. In particular, a decoupling in the superconducting channels could yield compelling exotic phenomenons. Currently, the theoretical predictions of the superconducting pairing mechanisms in TBG are pointing in all directions, to say the least. Unconventional $p + ip$-, $d + id$- and extended s-wave pairings have all been proposed [35–39] alongside studies predicting a conventional phonon-driven superconductivity [40, 41]. However, many of these studies does not go beyond the on-site Hubbard interaction [35, 39, 40], thus an exploration of the possible pairing mechanisms in our lattice model which directly reflects the shape of the Wannier orbitals could prove valuable. If superconductivity can be self-consistently stabilized, an additional investigation of the interplay between superconductiviting and insulating phases might yield tremendous insight into the electronic behaviour in strongly correlated materials and, if dreams really do come true, lay a piece in the unsolved scientific puzzle of high-T_c superconductivity.

Bibliography

[1] Cyril Proust and Louis Taillefer. The remarkable underlying ground states of cuprate superconductors. *Annual Review of Condensed Matter Physics*, 10(1):409–429, 2019.

[2] J. M. B. Lopes dos Santos, N. M. R. Peres, and A. H. Castro Neto. Graphene bilayer with a twist: Electronic structure. *Phys. Rev. Lett.*, 99:256802, Dec 2007.

[3] G. Trambly de Laissardiere, D. Mayou, and L. Magaud. Localization of dirac electrons in rotated graphene bilayers. *Nano Letters*, 10(3):804–808, Mar 2010.

[4] E. Suárez Morell, J. D. Correa, P. Vargas, M. Pacheco, and Z. Barticevic. Flat bands in slightly twisted bilayer graphene: Tight-binding calculations. *Physical Review B*, 82(12), Sep 2010.

[5] R. Bistritzer and A. H. MacDonald. Moire bands in twisted double-layer graphene. *Proceedings of the National Academy of Sciences*, 108(30):12233–12237, Jul 2011.

[6] Yuan Cao, Valla Fatemi, Ahmet Demir, Shiang Fang, Spencer L. Tomarken, Jason Y. Luo, Javier D. Sanchez-Yamagishi, Kenji Watanabe, Takashi Taniguchi, Efthimios Kaxiras, and et al. Correlated insulator behaviour at half-filling in magic-angle graphene superlattices. *Nature*, 556(7699):80–84, Mar 2018.

[7] Xiaobo Lu, Petr Stepanov, Wei Yang, Ming Xie, Mohammed Ali Aamir, Ipsita Das, Carles Urgell, Kenji Watanabe, Takashi Taniguchi, Guangyu Zhang, and et al. Superconductors, orbital magnets and correlated states in magic-angle bilayer graphene. *Nature*, 574(7780):653–657, Oct 2019.

[8] Rafael M. Fernandes and Jörn W. F. Venderbos. Nematicity with a twist: rotational symmetry breaking in a moiré superlattice. *arXiv:1911.11367*, 2019.

[9] Petr Stepanov, Ipsita Das, Xiaobo Lu, Ali Fahimniya, Kenji Watanabe, Takashi Taniguchi, Frank H. L. Koppens, Johannes Lischner, Leonid Levitov, and Dmitri K. Efetov. The interplay of insulating and superconducting orders in magic-angle graphene bilayers. *arXiv:1911.09198*, 2019.

[10] M. Serlin, C. L. Tschirhart, H. Polshyn, Y. Zhang, J. Zhu, K. Watanabe, T. Taniguchi, L. Balents, and A. F. Young. Intrinsic quantized anomalous hall effect in a moiré heterostructure. *Science*, 367(6480):900–903, Dec 2019.

[11] Hiroki Isobe, Noah F. Q. Yuan, and Liang Fu. Unconventional superconductivity and density waves in twisted bilayer graphene. *Physical Review X*, 8(4), Dec 2018.

[12] T. M. R. Wolf, J. L. Lado, G. Blatter, and O. Zilberberg. Electrically tunable flat bands and magnetism in twisted bilayer graphene. *Physical Review Letters*, 123(9), Aug 2019.

[13] Xiaogan Liang. Chapter 19 - transition from tubes to sheets—a comparison of the properties and applications of carbon nanotubes and graphene. In Mark J. Schulz, Vesselin N. Shanov, and Zhangzhang Yin, editors, *Nanotube Superfiber Materials*, pages 519 – 568. William Andrew Publishing, Boston, 2014.

[14] N. M. R. Peres. Colloquium: The transport properties of graphene: An introduction. *Rev. Mod. Phys.*, 82:2673–2700, Sep 2010.

[15] Neil W. Ashcroft and N. David Mermin. *Solid state physics*. Brooks/Cole Cengage Learning Learning, 2018.

[16] Huijuan Cui Yuli Huang, Xiaoyun Li and Zhen Zhou. Bi-layer graphene: Structure, properties, preparation and prospects. *Current Graphene Science*, 2(2):97–105, 2018.

[17] Liujun Zou, Hoi Chun Po, Ashvin Vishwanath, and T. Senthil. Band structure of twisted bilayer graphene: Emergent symmetries, commensurate approximants, and wannier obstructions. *Physical Review B*, 98(8), Aug 2018.

[18] Nguyen N. T. Nam and Mikito Koshino. Lattice relaxation and energy band modulation in twisted bilayer graphene. *Phys. Rev. B*, 96:075311, Aug 2017.

[19] Noah F. Q. Yuan and Liang Fu. Model for the metal-insulator transition in graphene superlattices and beyond. *Phys. Rev. B*, 98:045103, Jul 2018.

[20] M. S. Dresselhaus, G. Dresselhaus, and A. Jorio. *Group theory: application to the physics of condensed matter*. Springer-Verlag, 2008.

[21] Alexander Kerelsky, Leo J. McGilly, Dante M. Kennes, Lede Xian, Matthew Yankowitz, Shaowen Chen, K. Watanabe, T. Taniguchi, James Hone, Cory Dean, and et al. Maximized electron interactions at the magic angle in twisted bilayer graphene. *Nature*, 572(7767):95–100, Jul 2019.

[22] Mikito Koshino, Noah F. Q. Yuan, Takashi Koretsune, Masayuki Ochi, Kazuhiko Kuroki, and Liang Fu. Maximally localized wannier orbitals and the extended hubbard model for twisted bilayer graphene. *Phys. Rev. X*, 8:031087, Sep 2018.

[23] Jian Kang and Oskar Vafek. Symmetry, maximally localized wannier states, and a low-energy model for twisted bilayer graphene narrow bands. *Phys. Rev. X*, 8:031088, Sep 2018.

[24] Jian Kang and Oskar Vafek. Strong coupling phases of partially filled twisted bilayer graphene narrow bands. *Physical Review Letters*, 122(24), Jun 2019.

[25] Hoi Chun Po, Liujun Zou, Ashvin Vishwanath, and T. Senthil. Origin of mott insulating behavior and superconductivity in twisted bilayer graphene. *Physical Review X*, 8(3), Sep 2018.

[26] Hoi Chun Po, Liujun Zou, T. Senthil, and Ashvin Vishwanath. Faithful tight-binding models and fragile topology of magic-angle bilayer graphene. *Physical Review B*, 99(19), May 2019.

[27] Henrik Bruus and Karsten Flensberg. *Many-body quantum theory in condensed matter physics: an introduction*. Oxford University Press, 2017.

[28] F. D. M. Haldane. Model for a quantum hall effect without landau levels: Condensed-matter realization of the "parity anomaly". *Phys. Rev. Lett.*, 61:2015–2018, Oct 1988.

[29] Lei Wang, Xi Dai, and X. C. Xie. Interaction-induced topological phase transition in the bernevig-hughes-zhang model. *EPL (Europhysics Letters)*, 98(5):57001, May 2012.

[30] Jörn W. F. Venderbos, Marco Manzardo, Dmitry V. Efremov, Jeroen van den Brink, and Carmine Ortix. Engineering interaction-induced topological insulators in a3×3substrate-induced honeycomb superlattice. *Physical Review B*, 93(4), Jan 2016.

[31] Pramod Kumar, Thomas Mertz, and Walter Hofstetter. Interaction-induced topological and magnetic phases in the hofstadter-hubbard model. *Physical Review B*, 94(11), Sep 2016.

[32] Daniel González-Cuadra, Alejandro Bermudez, Przemysław R. Grzybowski, Maciej Lewenstein, and Alexandre Dauphin. Intertwined topological phases induced by emergent symmetry protection. *Nature Communications*, 10(1), Jun 2019.

[33] Yugui Yao, Leonard Kleinman, A. H. MacDonald, Jairo Sinova, T. Jungwirth, Ding-sheng Wang, Enge Wang, and Qian Niu. First principles calculation of anomalous hall conductivity in ferromagnetic bcc fe. *Physical Review Letters*, 92(3), Jan 2004.

[34] Yuan Cao, Daniel Rodan-Legrain, Jeong Min Park, Fanqi Noah Yuan, Kenji Watanabe, Takashi Taniguchi, Rafael M. Fernandes, Liang Fu, and Pablo Jarillo-Herrero. Nematicity and competing orders in superconducting magic-angle graphene. *arXiv:2004.04148*, 2020.

[35] Dante M. Kennes, Johannes Lischner, and Christoph Karrasch. Strong correlations and d+id superconductivity in twisted bilayer graphene. *Physical Review B*, 98(24), Dec 2018.

[36] Sujay Ray, Jeil Jung, and Tanmoy Das. Wannier pairs in superconducting twisted bilayer graphene and related systems. *Physical Review B*, 99(13), Apr 2019.

[37] Cenke Xu and Leon Balents. Topological superconductivity in twisted multilayer graphene. *Physical Review Letters*, 121(8), Aug 2018.

[38] Tongyun Huang, Lufeng Zhang, and Tianxing Ma. Antiferromagnetically ordered mott insulator and d+id superconductivity in twisted bilayer graphene: a quantum monte carlo study. *Science Bulletin*, 64(5):310–314, Mar 2019.

[39] Bitan Roy and Vladimir Juričić. Unconventional superconductivity in nearly flat bands in twisted bilayer graphene. *Physical Review B*, 99(12), Mar 2019.

[40] Teemu J. Peltonen, Risto Ojajärvi, and Tero T. Heikkilä. Mean-field theory for superconductivity in twisted bilayer graphene. *Physical Review B*, 98(22), Dec 2018.

[41] Biao Lian, Zhijun Wang, and B. Andrei Bernevig. Twisted bilayer graphene: A phonon-driven superconductor. *Physical Review Letters*, 122(25), Jun 2019.

Appendices

Appendix A

Fourier transformation of the tight-binding model

In this appendix, we perform a Fourier tranformation of H_{tb}.
We define the transformations as follows,

$$\begin{aligned}
\mathbf{a}_{i+\boldsymbol{\alpha}} &= \frac{1}{\sqrt{\tilde{N}}} \sum_{\mathbf{k}\in BZ} e^{i\mathbf{k}(\mathbf{R}_i+\boldsymbol{\alpha})} \mathbf{a}_{\mathbf{k}}, \\
\mathbf{a}^{\dagger}_{i+\boldsymbol{\alpha}} &= \frac{1}{\sqrt{\tilde{N}}} \sum_{\mathbf{k}\in BZ} e^{-i\mathbf{k}(\mathbf{R}_i+\boldsymbol{\alpha})} \mathbf{a}^{\dagger}_{\mathbf{k}}, \\
\mathbf{b}_{i+2\boldsymbol{\alpha}} &= \frac{1}{\sqrt{\tilde{N}}} \sum_{\mathbf{k}\in BZ} e^{i\mathbf{k}(\mathbf{R}_i+2\boldsymbol{\alpha})} \mathbf{b}_{\mathbf{k}}, \\
\mathbf{b}^{\dagger}_{i+2\boldsymbol{\alpha}} &= \frac{1}{\sqrt{\tilde{N}}} \sum_{\mathbf{k}\in BZ} e^{-i\mathbf{k}(\mathbf{R}_i+2\boldsymbol{\alpha})} \mathbf{b}^{\dagger}_{\mathbf{k}},
\end{aligned} \tag{A.1}$$

where $\tilde{N}$ is the number of unit cells in the system.
Inserting into Eq. (4.7) yields,

$$\begin{aligned}
H_0 &= -\mu \sum_{\mathbf{R}_i} [\mathbf{a}^{\dagger}_{i+\boldsymbol{\alpha}} \cdot \mathbf{a}_{i+\boldsymbol{\alpha}} + \mathbf{b}^{\dagger}_{i+2\boldsymbol{\alpha}} \cdot \mathbf{b}_{i+2\boldsymbol{\alpha}}] \\
&= -\frac{\mu}{\tilde{N}} \sum_{\mathbf{R}_i} \sum_{\mathbf{k},\mathbf{k}'\in BZ} \left[e^{-i\mathbf{k}(\mathbf{R}_i+\boldsymbol{\alpha})} e^{i\mathbf{k}'(\mathbf{R}_i+\boldsymbol{\alpha})} \mathbf{a}^{\dagger}_{\mathbf{k}} \cdot \mathbf{a}_{\mathbf{k}'} + e^{-i\mathbf{k}(\mathbf{R}_i+2\boldsymbol{\alpha})} e^{i\mathbf{k}'(\mathbf{R}_i+2\boldsymbol{\alpha})} \mathbf{b}^{\dagger}_{\mathbf{k}} \cdot \mathbf{b}_{\mathbf{k}'} \right] \\
&= -\frac{\mu}{\tilde{N}} \sum_{\mathbf{k},\mathbf{k}'\in BZ} \sum_{\mathbf{R}_i} e^{-i(\mathbf{k}-\mathbf{k}')\mathbf{R}_i} \left[e^{-i(\mathbf{k}-\mathbf{k}')\boldsymbol{\alpha}} \mathbf{a}^{\dagger}_{\mathbf{k}} \cdot \mathbf{a}_{\mathbf{k}'} + e^{-i(\mathbf{k}-\mathbf{k}')2\boldsymbol{\alpha}} \mathbf{b}^{\dagger}_{\mathbf{k}} \cdot \mathbf{b}_{\mathbf{k}'} \right] \\
&= -\frac{\mu}{\tilde{N}} \sum_{\mathbf{k},\mathbf{k}'\in BZ} \sum_{\mathbf{G}} \delta_{\mathbf{k}',\mathbf{k}+\mathbf{G}} \left[e^{-i(\mathbf{k}-\mathbf{k}')\boldsymbol{\alpha}} \mathbf{a}^{\dagger}_{\mathbf{k}} \cdot \mathbf{a}_{\mathbf{k}} + e^{-i(\mathbf{k}-\mathbf{k}')2\boldsymbol{\alpha}} \mathbf{b}^{\dagger}_{\mathbf{k}} \cdot \mathbf{b}_{\mathbf{k}} \right] \\
&= -\frac{\mu}{\tilde{N}} \sum_{\mathbf{k}\in BZ} \sum_{\mathbf{G}} \left[e^{i\mathbf{G}\boldsymbol{\alpha}} \mathbf{a}^{\dagger}_{\mathbf{k}} \cdot \mathbf{a}_{\mathbf{k}+\mathbf{G}} + e^{i\mathbf{G}2\boldsymbol{\alpha}} \mathbf{b}^{\dagger}_{\mathbf{k}} \cdot \mathbf{b}_{\mathbf{k}+\mathbf{G}} \right],
\end{aligned} \tag{A.2}$$

where $\mathbf{G} = r\mathbf{K}_1 + s\mathbf{K}_2$, $r, s \in \mathbb{Z}$, are the reciprocal lattice vectors.
From the definition in Eq. (A.1) we have,

$$\begin{aligned}
\mathbf{a}_{\mathbf{k}+\mathbf{G}} &= \frac{1}{\sqrt{\tilde{N}}} \sum_{\mathbf{R}_i} e^{-i(\mathbf{k}+\mathbf{G})(\mathbf{R}_i+\boldsymbol{\alpha})} \mathbf{a}_{i+\boldsymbol{\alpha}} \\
&= \frac{1}{\sqrt{\tilde{N}}} \sum_{\mathbf{R}_i} e^{-i\mathbf{k}(\mathbf{R}_i+\boldsymbol{\alpha})} \mathbf{a}_{i+\boldsymbol{\alpha}} e^{-i\mathbf{G}\boldsymbol{\alpha}} \\
&= \mathbf{a}_{\mathbf{k}} e^{-i\mathbf{G}\boldsymbol{\alpha}}.
\end{aligned} \tag{A.3}$$

Likewise we have $\mathbf{b}_{\mathbf{k}+\mathbf{G}} = \mathbf{b}_{\mathbf{k}} e^{-i\mathbf{G}2\boldsymbol{\alpha}}$. The result is general for $\boldsymbol{\alpha}$ being any shift of position relative to $\mathbf{R}_i$. Inserting into Eq. (A.2) we get,

$$\begin{aligned} H_0 &= -\frac{\mu}{\tilde{N}} \sum_{\mathbf{k}\in BZ} \sum_{\mathbf{G}} \left[e^{i\mathbf{G}\boldsymbol{\alpha}} e^{-i\mathbf{G}\boldsymbol{\alpha}} \mathbf{a}_{\mathbf{k}}^{\dagger} \cdot \mathbf{a}_{\mathbf{k}} + e^{i\mathbf{G}2\boldsymbol{\alpha}} e^{-i\mathbf{G}2\boldsymbol{\alpha}} \mathbf{b}_{\mathbf{k}}^{\dagger} \cdot \mathbf{b}_{\mathbf{k}} \right] \\ &= -\frac{\mu}{\tilde{N}} \sum_{\mathbf{k}\in BZ} \sum_{\mathbf{G}} \left[\mathbf{a}_{\mathbf{k}}^{\dagger} \cdot \mathbf{a}_{\mathbf{k}} + \mathbf{b}_{\mathbf{k}}^{\dagger} \cdot \mathbf{b}_{\mathbf{k}} \right] \\ &= -\mu \sum_{\mathbf{k}\in BZ} [\mathbf{a}_{\mathbf{k}}^{\dagger} \cdot \mathbf{a}_{\mathbf{k}} + \mathbf{b}_{\mathbf{k}}^{\dagger} \cdot \mathbf{b}_{\mathbf{k}}], \end{aligned} \tag{A.4}$$

since we have $\tilde{N}$ distinct reciprocal lattice vectors. Using the definitions of Eq. (A.1) in the second term (Eq. (4.8)), we get

$$\begin{aligned} H_1 &= t_1 \sum_{\mathbf{R}_i} [\mathbf{a}_{i+\boldsymbol{\alpha}}^{\dagger} \cdot (\mathbf{b}_{i+2\boldsymbol{\alpha}} + \mathbf{b}_{i+2\boldsymbol{\alpha}-\mathbf{L}_1} + \mathbf{b}_{i+2\boldsymbol{\alpha}-\mathbf{L}_2}) + h.c.] \\ &= \frac{t_1}{\tilde{N}} \sum_{\mathbf{R}_i} \sum_{\mathbf{k},\mathbf{k}'\in BZ} \big[e^{-i\mathbf{k}(\mathbf{R}_i+\boldsymbol{\alpha})} \mathbf{a}_{\mathbf{k}}^{\dagger} \cdot (e^{i\mathbf{k}'(\mathbf{R}_i+2\boldsymbol{\alpha})} + e^{i\mathbf{k}'(\mathbf{R}_i+2\boldsymbol{\alpha}-\mathbf{L}_1)} + e^{i\mathbf{k}'(\mathbf{R}_i+2\boldsymbol{\alpha}-\mathbf{L}_2)}) \mathbf{b}_{\mathbf{k}'} \\ &\qquad + (e^{-i\mathbf{k}'(\mathbf{R}_i+2\boldsymbol{\alpha})} + e^{-i\mathbf{k}'(\mathbf{R}_i+2\boldsymbol{\alpha}-\mathbf{L}_1)} + e^{-i\mathbf{k}'(\mathbf{R}_i+2\boldsymbol{\alpha}-\mathbf{L}_2)}) \mathbf{b}_{\mathbf{k}'}^{\dagger} \cdot e^{i\mathbf{k}(\mathbf{R}_i+\boldsymbol{\alpha})} \mathbf{a}_{\mathbf{k}} \big] \\ &= \frac{t_1}{\tilde{N}} \sum_{\mathbf{k},\mathbf{k}'\in BZ} \sum_{\mathbf{R}_i} \big[e^{-i(\mathbf{k}-\mathbf{k}')\mathbf{R}_i} e^{-i\mathbf{k}\boldsymbol{\alpha}} (e^{i\mathbf{k}'2\boldsymbol{\alpha}} + e^{i\mathbf{k}'(2\boldsymbol{\alpha}-\mathbf{L}_1)} + e^{i\mathbf{k}'(2\boldsymbol{\alpha}-\mathbf{L}_2)}) \mathbf{a}_{\mathbf{k}}^{\dagger} \cdot \mathbf{b}_{\mathbf{k}'} \\ &\qquad + e^{i(\mathbf{k}-\mathbf{k}')\mathbf{R}_i} e^{i\mathbf{k}\boldsymbol{\alpha}} (e^{-i\mathbf{k}'2\boldsymbol{\alpha}} + e^{-i\mathbf{k}'(2\boldsymbol{\alpha}-\mathbf{L}_1)} + e^{-i\mathbf{k}'(2\boldsymbol{\alpha}-\mathbf{L}_2)}) \mathbf{b}_{\mathbf{k}'}^{\dagger} \cdot \mathbf{a}_{\mathbf{k}} \big] \\ &= \frac{t_1}{\tilde{N}} \sum_{\mathbf{k},\mathbf{k}'\in BZ} \sum_{\mathbf{G}} \boldsymbol{\delta}_{\mathbf{k}',\mathbf{k}+\mathbf{G}} \big[e^{-i\mathbf{k}\boldsymbol{\alpha}} (e^{i\mathbf{k}'2\boldsymbol{\alpha}} + e^{i\mathbf{k}'(2\boldsymbol{\alpha}-\mathbf{L}_1)} + e^{i\mathbf{k}'(2\boldsymbol{\alpha}-\mathbf{L}_2)}) \mathbf{a}_{\mathbf{k}}^{\dagger} \cdot \mathbf{b}_{\mathbf{k}'} \\ &\qquad + e^{i\mathbf{k}\boldsymbol{\alpha}} (e^{-i\mathbf{k}'2\boldsymbol{\alpha}} + e^{-i\mathbf{k}'(2\boldsymbol{\alpha}-\mathbf{L}_1)} + e^{-i\mathbf{k}'(2\boldsymbol{\alpha}-\mathbf{L}_2)}) \mathbf{b}_{\mathbf{k}}^{\dagger} \cdot \mathbf{a}_{\mathbf{k}'} \big] \\ &= \frac{t_1}{\tilde{N}} \sum_{\mathbf{k}\in BZ} \sum_{\mathbf{G}} \big[e^{-i\mathbf{k}\boldsymbol{\alpha}} (e^{i(\mathbf{k}+\mathbf{G})2\boldsymbol{\alpha}} + e^{i(\mathbf{k}+\mathbf{G})(2\boldsymbol{\alpha}-\mathbf{L}_1)} + e^{i(\mathbf{k}+\mathbf{G})(2\boldsymbol{\alpha}-\mathbf{L}_2)}) \mathbf{a}_{\mathbf{k}}^{\dagger} \cdot \mathbf{b}_{\mathbf{k}+\mathbf{G}} \\ &\qquad + e^{i\mathbf{k}\boldsymbol{\alpha}} (e^{-i(\mathbf{k}+\mathbf{G})2\boldsymbol{\alpha}} + e^{-i(\mathbf{k}+\mathbf{G})(2\boldsymbol{\alpha}-\mathbf{L}_1)} + e^{-i(\mathbf{k}+\mathbf{G})(2\boldsymbol{\alpha}-\mathbf{L}_2)}) \mathbf{b}_{\mathbf{k}+\mathbf{G}}^{\dagger} \cdot \mathbf{a}_{\mathbf{k}} \big] \end{aligned} \tag{A.5}$$

Recalling that each phase has its origin in individual FTs with different shifts in real space, we can follow the same procedure as in Eq. (A.3) and get,

$$\begin{aligned} H_1 &= \frac{t_1}{\tilde{N}} \sum_{\mathbf{k}\in BZ} \sum_{\mathbf{G}} \big[e^{-i\mathbf{k}\boldsymbol{\alpha}} (e^{i(\mathbf{k}+\mathbf{G})2\boldsymbol{\alpha}} e^{-i\mathbf{G}2\boldsymbol{\alpha}} + e^{i(\mathbf{k}+\mathbf{G})(2\boldsymbol{\alpha}-\mathbf{L}_1)} e^{-i\mathbf{G}(2\boldsymbol{\alpha}-\mathbf{L}_1)} + e^{i(\mathbf{k}+\mathbf{G})(2\boldsymbol{\alpha}-\mathbf{L}_2)} e^{-i\mathbf{G}(2\boldsymbol{\alpha}-\mathbf{L}_2)}) \mathbf{a}_{\mathbf{k}}^{\dagger} \cdot \mathbf{b}_{\mathbf{k}} \\ &\qquad + e^{i\mathbf{k}\boldsymbol{\alpha}} (e^{-i(\mathbf{k}+\mathbf{G})2\boldsymbol{\alpha}} e^{i\mathbf{G}2\boldsymbol{\alpha}} + e^{-i(\mathbf{k}+\mathbf{G})(2\boldsymbol{\alpha}-\mathbf{L}_1)} e^{i\mathbf{G}(2\boldsymbol{\alpha}-\mathbf{L}_1)} + e^{-i(\mathbf{k}+\mathbf{G})(2\boldsymbol{\alpha}-\mathbf{L}_2)} e^{i\mathbf{G}(2\boldsymbol{\alpha}-\mathbf{L}_2)}) \mathbf{b}_{\mathbf{k}}^{\dagger} \cdot \mathbf{a}_{\mathbf{k}} \big] \\ &= \frac{t_1}{\tilde{N}} \sum_{\mathbf{k}\in BZ} \tilde{N} \big[e^{-i\mathbf{k}\boldsymbol{\alpha}} (e^{i\mathbf{k}2\boldsymbol{\alpha}} + e^{i\mathbf{k}(2\boldsymbol{\alpha}-\mathbf{L}_1))} + e^{i\mathbf{k}(2\boldsymbol{\alpha}-\mathbf{L}_2)}) \mathbf{a}_{\mathbf{k}}^{\dagger} \cdot \mathbf{b}_{\mathbf{k}} \\ &\qquad + e^{i\mathbf{k}\boldsymbol{\alpha}} (e^{-i\mathbf{k}2\boldsymbol{\alpha}} + e^{-i\mathbf{k}(2\boldsymbol{\alpha}-\mathbf{L}_1)} + e^{-i\mathbf{k}(2\boldsymbol{\alpha}-\mathbf{L}_1)}) \mathbf{b}_{\mathbf{k}}^{\dagger} \cdot \mathbf{a}_{\mathbf{k}} \big] \\ &= t_1 \sum_{\mathbf{k}\in BZ} \big[e^{i\mathbf{k}\boldsymbol{\alpha}} (1 + e^{-i\mathbf{k}\mathbf{L}_1} + e^{-i\mathbf{k}\mathbf{L}_2}) \mathbf{a}_{\mathbf{k}}^{\dagger} \cdot \mathbf{b}_{\mathbf{k}} + h.c. \big] \end{aligned} \tag{A.6}$$

Proceeding to the third term of the Hamiltonian, Eq. (4.9), we get

$$\begin{aligned} H_2 = t_2 \sum_{\mathbf{R}_i} \big[& \mathbf{a}_{i+\boldsymbol{\alpha}}^{\dagger} \cdot (\mathbf{a}_{i+\boldsymbol{\alpha}-\mathbf{L}_1+2\mathbf{L}_2} + \mathbf{a}_{i+\boldsymbol{\alpha}-\mathbf{L}_1-\mathbf{L}_2} + \mathbf{a}_{i+\boldsymbol{\alpha}+2\mathbf{L}_1-\mathbf{L}_2}) \\ & + \mathbf{b}_{i+2\boldsymbol{\alpha}}^{\dagger} \cdot (\mathbf{b}_{i+2\boldsymbol{\alpha}-\mathbf{L}_1+2\mathbf{L}_2} + \mathbf{b}_{i+2\boldsymbol{\alpha}-\mathbf{L}_1-\mathbf{L}_2} + \mathbf{b}_{i+2\boldsymbol{\alpha}+2\mathbf{L}_1-\mathbf{L}_2}) + h.c. \big] \end{aligned}$$

$$
\begin{aligned}
&= \frac{t_2}{\tilde{N}} \sum_{\mathbf{R}_i} \sum_{\mathbf{k},\mathbf{k}'\in BZ} \big[e^{-i\mathbf{k}(\mathbf{R}_i+\boldsymbol{\alpha})} \big(e^{i\mathbf{k}'(\mathbf{R}_i+\boldsymbol{\alpha}-\mathbf{L}_1+2\mathbf{L}_2)} + e^{i\mathbf{k}'(\mathbf{R}_i+\boldsymbol{\alpha}-\mathbf{L}_1-\mathbf{L}_2)} + e^{i\mathbf{k}'(\mathbf{R}_i+\boldsymbol{\alpha}+2\mathbf{L}_1-\mathbf{L}_2)} \big) \mathbf{a}_{\mathbf{k}}^\dagger \cdot \mathbf{a}_{\mathbf{k}'} \\
&\quad + e^{-i\mathbf{k}(\mathbf{R}_i+2\boldsymbol{\alpha})} \big(e^{i\mathbf{k}'(\mathbf{R}_i+2\boldsymbol{\alpha}-\mathbf{L}_1+2\mathbf{L}_2)} + e^{i\mathbf{k}'(\mathbf{R}_i+2\boldsymbol{\alpha}-\mathbf{L}_1-\mathbf{L}_2)} + e^{i\mathbf{k}'(\mathbf{R}_i+2\boldsymbol{\alpha}+2\mathbf{L}_1-\mathbf{L}_2)} \big) \mathbf{b}_{\mathbf{k}}^\dagger \cdot \mathbf{b}_{\mathbf{k}'} \\
&\quad + e^{i\mathbf{k}(\mathbf{R}_i+\boldsymbol{\alpha})} \big(e^{-i\mathbf{k}'(\mathbf{R}_i+\boldsymbol{\alpha}-\mathbf{L}_1+2\mathbf{L}_2)} + e^{-i\mathbf{k}'(\mathbf{R}_i+\boldsymbol{\alpha}-\mathbf{L}_1-\mathbf{L}_2)} + e^{-i\mathbf{k}'(\mathbf{R}_i+\boldsymbol{\alpha}+2\mathbf{L}_1-\mathbf{L}_2)} \big) \mathbf{a}_{\mathbf{k}'}^\dagger \cdot \mathbf{a}_{\mathbf{k}} \\
&\quad + e^{i\mathbf{k}(\mathbf{R}_i+2\boldsymbol{\alpha})} \big(e^{-i\mathbf{k}'(\mathbf{R}_i+2\boldsymbol{\alpha}-\mathbf{L}_1+2\mathbf{L}_2)} + e^{-i\mathbf{k}'(\mathbf{R}_i+2\boldsymbol{\alpha}-\mathbf{L}_1-\mathbf{L}_2)} + e^{-i\mathbf{k}'(\mathbf{R}_i+2\boldsymbol{\alpha}+2\mathbf{L}_1-\mathbf{L}_2)} \big) \mathbf{b}_{\mathbf{k}'}^\dagger \cdot \mathbf{b}_{\mathbf{k}} \big] \\
&= \frac{t_2}{\tilde{N}} \sum_{\mathbf{R}_i} \sum_{\mathbf{k},\mathbf{k}'\in BZ} \big[e^{-i(\mathbf{k}-\mathbf{k}')\mathbf{R}_i} e^{-i\mathbf{k}\boldsymbol{\alpha}} \big(e^{i\mathbf{k}'(\boldsymbol{\alpha}-\mathbf{L}_1+2\mathbf{L}_2)} + e^{i\mathbf{k}'(\boldsymbol{\alpha}-\mathbf{L}_1-\mathbf{L}_2)} + e^{i\mathbf{k}'(+\boldsymbol{\alpha}+2\mathbf{L}_1-\mathbf{L}_2)} \big) \mathbf{a}_{\mathbf{k}}^\dagger \cdot \mathbf{a}_{\mathbf{k}'} \\
&\quad + e^{-i(\mathbf{k}-\mathbf{k}')\mathbf{R}_i} e^{-i\mathbf{k}2\boldsymbol{\alpha}} \big(e^{i\mathbf{k}'(2\boldsymbol{\alpha}-\mathbf{L}_1+2\mathbf{L}_2)} + e^{i\mathbf{k}'(2\boldsymbol{\alpha}-\mathbf{L}_1-\mathbf{L}_2)} + e^{i\mathbf{k}'(2\boldsymbol{\alpha}+2\mathbf{L}_1-\mathbf{L}_2)} \big) \mathbf{b}_{\mathbf{k}}^\dagger \cdot \mathbf{b}_{\mathbf{k}'} \\
&\quad + \big[e^{i(\mathbf{k}-\mathbf{k}')\mathbf{R}_i} e^{i\mathbf{k}\boldsymbol{\alpha}} \big(e^{-i\mathbf{k}'(\boldsymbol{\alpha}-\mathbf{L}_1+2\mathbf{L}_2)} + e^{-i\mathbf{k}'(\boldsymbol{\alpha}-\mathbf{L}_1-\mathbf{L}_2)} + e^{-i\mathbf{k}'(+\boldsymbol{\alpha}+2\mathbf{L}_1-\mathbf{L}_2)} \big) \mathbf{a}_{\mathbf{k}'}^\dagger \cdot \mathbf{a}_{\mathbf{k}} \\
&\quad + e^{i(\mathbf{k}-\mathbf{k}')\mathbf{R}_i} e^{i\mathbf{k}2\boldsymbol{\alpha}} \big(e^{-i\mathbf{k}'(2\boldsymbol{\alpha}-\mathbf{L}_1+2\mathbf{L}_2)} + e^{-i\mathbf{k}'(2\boldsymbol{\alpha}-\mathbf{L}_1-\mathbf{L}_2)} + e^{-i\mathbf{k}'(2\boldsymbol{\alpha}+2\mathbf{L}_1-\mathbf{L}_2)} \big) \mathbf{b}_{\mathbf{k}'}^\dagger \cdot \mathbf{b}_{\mathbf{k}} \big] \\
&= \frac{t_2}{\tilde{N}} \sum_{\mathbf{k}\in BZ} \sum_{\mathbf{G}} \big[e^{-i\mathbf{k}\boldsymbol{\alpha}} \big(e^{i(\mathbf{k}+\mathbf{G})(\boldsymbol{\alpha}-\mathbf{L}_1+2\mathbf{L}_2)} + e^{i(\mathbf{k}+\mathbf{G})(\boldsymbol{\alpha}-\mathbf{L}_1-\mathbf{L}_2)} + e^{i(\mathbf{k}+\mathbf{G})(\boldsymbol{\alpha}+2\mathbf{L}_1-\mathbf{L}_2)} \big) \mathbf{a}_{\mathbf{k}}^\dagger \cdot \mathbf{a}_{\mathbf{k}+\mathbf{G}} \\
&\quad + e^{-i\mathbf{k}2\boldsymbol{\alpha}} \big(e^{i(\mathbf{k}+\mathbf{G})(2\boldsymbol{\alpha}-\mathbf{L}_1+2\mathbf{L}_2)} + e^{i(\mathbf{k}+\mathbf{G})(2\boldsymbol{\alpha}-\mathbf{L}_1-\mathbf{L}_2)} + e^{i(\mathbf{k}+\mathbf{G})(2\boldsymbol{\alpha}+2\mathbf{L}_1-\mathbf{L}_2)} \big) \mathbf{b}_{\mathbf{k}}^\dagger \cdot \mathbf{b}_{\mathbf{k}+\mathbf{G}} \\
&\quad + e^{i\mathbf{k}\boldsymbol{\alpha}} \big(e^{-i(\mathbf{k}+\mathbf{G})(\boldsymbol{\alpha}-\mathbf{L}_1+2\mathbf{L}_2)} + e^{-i(\mathbf{k}+\mathbf{G})(\boldsymbol{\alpha}-\mathbf{L}_1-\mathbf{L}_2)} + e^{-i(\mathbf{k}+\mathbf{G})(\boldsymbol{\alpha}+2\mathbf{L}_1-\mathbf{L}_2)} \big) \mathbf{a}_{\mathbf{k}+\mathbf{G}}^\dagger \cdot \mathbf{a}_{\mathbf{k}} \\
&\quad + e^{i\mathbf{k}2\boldsymbol{\alpha}} \big(e^{-i(\mathbf{k}+\mathbf{G})(2\boldsymbol{\alpha}-\mathbf{L}_1+2\mathbf{L}_2)} + e^{-i(\mathbf{k}+\mathbf{G})(2\boldsymbol{\alpha}-\mathbf{L}_1-\mathbf{L}_2)} + e^{-i(\mathbf{k}+\mathbf{G})(2\boldsymbol{\alpha}+2\mathbf{L}_1-\mathbf{L}_2)} \big) \mathbf{b}_{\mathbf{k}+\mathbf{G}}^\dagger \cdot \mathbf{b}_{\mathbf{k}} \big] \\
&= \frac{t_2}{\tilde{N}} \sum_{\mathbf{k}\in BZ} \tilde{N} \big[(e^{i\mathbf{k}(-\mathbf{L}_1+2\mathbf{L}_2)} + e^{i\mathbf{k}(-\mathbf{L}_1-\mathbf{L}_2)} + e^{i\mathbf{k}(2\mathbf{L}_1-\mathbf{L}_2)}) \mathbf{a}_{\mathbf{k}}^\dagger \cdot \mathbf{a}_{\mathbf{k}} \\
&\quad + (e^{i\mathbf{k}(-\mathbf{L}_1+2\mathbf{L}_2)} + e^{i\mathbf{k}(-\mathbf{L}_1-\mathbf{L}_2)} + e^{i\mathbf{k}(2\mathbf{L}_1-\mathbf{L}_2)}) \mathbf{b}_{\mathbf{k}}^\dagger \cdot \mathbf{b}_{\mathbf{k}} \\
&\quad + (e^{-i\mathbf{k}(-\mathbf{L}_1+2\mathbf{L}_2)} + e^{-i\mathbf{k}(-\mathbf{L}_1-\mathbf{L}_2)} + e^{-i\mathbf{k}(2\mathbf{L}_1-\mathbf{L}_2)}) \mathbf{a}_{\mathbf{k}}^\dagger \cdot \mathbf{a}_{\mathbf{k}} \\
&\quad + (e^{-i\mathbf{k}(-\mathbf{L}_1+2\mathbf{L}_2)} + e^{-i\mathbf{k}(-\mathbf{L}_1-\mathbf{L}_2)} + e^{-i\mathbf{k}(2\mathbf{L}_1-\mathbf{L}_2)}) \mathbf{b}_{\mathbf{k}}^\dagger \cdot \mathbf{b}_{\mathbf{k}} \big] \\
&= 2t_2 \sum_{\mathbf{k}\in BZ} \big[\cos\big(\mathbf{k}\cdot(-\mathbf{L}_1+2\mathbf{L}_2)\big) + \cos\big(\mathbf{k}\cdot(-\mathbf{L}_1-\mathbf{L}_2)\big) + \cos\big(\mathbf{k}\cdot(2\mathbf{L}_1-\mathbf{L}_2)\big) \big] (\mathbf{a}_{\mathbf{k}}^\dagger \cdot \mathbf{a}_{\mathbf{k}} + \mathbf{b}_{\mathbf{k}}^\dagger \cdot \mathbf{b}_{\mathbf{k}}).
\end{aligned}
\tag{A.7}
$$

Finally we turn our attention to the fourth and last term of the Hamiltonian, Eq. (4.10),

$$
\begin{aligned}
H_{2'} = t_2' \sum_{\mathbf{R}_i} \Big[& \big[\mathbf{a}_{i+\boldsymbol{\alpha}}^\dagger \times (\mathbf{a}_{i+\boldsymbol{\alpha}-\mathbf{L}_1+2\mathbf{L}_2} + \mathbf{a}_{i+\boldsymbol{\alpha}-\mathbf{L}_1-\mathbf{L}_2} + \mathbf{a}_{i+\boldsymbol{\alpha}-2\mathbf{L}_1+\mathbf{L}_2}) \big]_z \\
& + \big[\mathbf{b}_{i+2\boldsymbol{\alpha}}^\dagger \times (\mathbf{b}_{i+2\boldsymbol{\alpha}-\mathbf{L}_1+2\mathbf{L}_2} + \mathbf{b}_{i+2\boldsymbol{\alpha}-\mathbf{L}_1-\mathbf{L}_2} + \mathbf{b}_{i+2\boldsymbol{\alpha}-2\mathbf{L}_1+\mathbf{L}_2}) \big]_z \\
& - \big[(\mathbf{a}_{i+\boldsymbol{\alpha}-\mathbf{L}_1+2\mathbf{L}_2}^\dagger + \mathbf{a}_{i+\boldsymbol{\alpha}-\mathbf{L}_1-\mathbf{L}_2}^\dagger + \mathbf{a}_{i+\boldsymbol{\alpha}-2\mathbf{L}_1+\mathbf{L}_2}^\dagger) \times \mathbf{a}_{i+\boldsymbol{\alpha}} \big]_z \\
& - \big[(\mathbf{b}_{i+2\boldsymbol{\alpha}-\mathbf{L}_1+2\mathbf{L}_2}^\dagger + \mathbf{b}_{i+2\boldsymbol{\alpha}-\mathbf{L}_1-\mathbf{L}_2}^\dagger + \mathbf{b}_{i+2\boldsymbol{\alpha}-2\mathbf{L}_1+\mathbf{L}_2}^\dagger) \times \mathbf{b}_{i+2\boldsymbol{\alpha}} \big]_z \Big],
\end{aligned}
$$

where we used that $\Big([\mathbf{a}_i^\dagger \times \mathbf{a}_j]_z\Big)^\dagger = -[\mathbf{a}_j^\dagger \times \mathbf{a}_i]_z$, which can easily be verified.

$$
\begin{aligned}
H_{2'} &= \frac{t_2'}{\tilde{N}} \sum_{\mathbf{R}_i} \sum_{\mathbf{k},\mathbf{k}'\in BZ} \Big[\big[e^{-i\mathbf{k}(\mathbf{R}_i+\boldsymbol{\alpha})} \mathbf{a}_{\mathbf{k}}^\dagger \times (e^{i\mathbf{k}'(\mathbf{R}_i+\boldsymbol{\alpha}-\mathbf{L}_1+2\mathbf{L}_2)} \mathbf{a}_{\mathbf{k}'} + e^{i\mathbf{k}'(\mathbf{R}_i+\boldsymbol{\alpha}-\mathbf{L}_1-\mathbf{L}_2)} \mathbf{a}_{\mathbf{k}'} + e^{i\mathbf{k}'(\mathbf{R}_i+\boldsymbol{\alpha}+2\mathbf{L}_1-\mathbf{L}_2)} \mathbf{a}_{\mathbf{k}'}) \big]_z \\
&\quad + \big[e^{-i\mathbf{k}(\mathbf{R}_i+2\boldsymbol{\alpha})} \mathbf{b}_{\mathbf{k}}^\dagger \times (e^{i\mathbf{k}'(\mathbf{R}_i+2\boldsymbol{\alpha}-\mathbf{L}_1+2\mathbf{L}_2)} \mathbf{b}_{\mathbf{k}'} + e^{i\mathbf{k}'(\mathbf{R}_i+2\boldsymbol{\alpha}-\mathbf{L}_1-\mathbf{L}_2)} \mathbf{b}_{\mathbf{k}'} + e^{i\mathbf{k}'(\mathbf{R}_i+2\boldsymbol{\alpha}+2\mathbf{L}_1-\mathbf{L}_2)} \mathbf{b}_{\mathbf{k}'}) \big]_z \\
&\quad - \big[(e^{-i\mathbf{k}'(\mathbf{R}_i+\boldsymbol{\alpha}-\mathbf{L}_1+2\mathbf{L}_2)} \mathbf{a}_{\mathbf{k}'} + e^{-i\mathbf{k}'(\mathbf{R}_i+\boldsymbol{\alpha}-\mathbf{L}_1-\mathbf{L}_2)} \mathbf{a}_{\mathbf{k}'} + e^{-i\mathbf{k}'(\mathbf{R}_i+\boldsymbol{\alpha}+2\mathbf{L}_1-\mathbf{L}_2)} \mathbf{a}_{\mathbf{k}'}) \times e^{i\mathbf{k}(\mathbf{R}_i+\boldsymbol{\alpha})} \mathbf{a}_{\mathbf{k}}^\dagger \big]_z \\
&\quad - \big[(e^{-i\mathbf{k}'(\mathbf{R}_i+2\boldsymbol{\alpha}-\mathbf{L}_1+2\mathbf{L}_2)} \mathbf{b}_{\mathbf{k}'} + e^{-i\mathbf{k}'(\mathbf{R}_i+2\boldsymbol{\alpha}-\mathbf{L}_1-\mathbf{L}_2)} \mathbf{b}_{\mathbf{k}'} + e^{-i\mathbf{k}'(\mathbf{R}_i+2\boldsymbol{\alpha}+2\mathbf{L}_1-\mathbf{L}_2)} \mathbf{b}_{\mathbf{k}'}) \times e^{i\mathbf{k}(\mathbf{R}_i+2\boldsymbol{\alpha})} \mathbf{b}_{\mathbf{k}}^\dagger \big]_z \Big] \\
&= \frac{t_2'}{\tilde{N}} \sum_{\mathbf{R}_i} \sum_{\mathbf{k},\mathbf{k}'\in BZ} \Big[e^{-i(\mathbf{k}-\mathbf{k}')\mathbf{R}_i} e^{-i\mathbf{k}\boldsymbol{\alpha}} \big(e^{i\mathbf{k}'(\boldsymbol{\alpha}-\mathbf{L}_1+2\mathbf{L}_2)} + e^{i\mathbf{k}'(\boldsymbol{\alpha}-\mathbf{L}_1-\mathbf{L}_2)} + e^{i\mathbf{k}'(\boldsymbol{\alpha}+2\mathbf{L}_1-\mathbf{L}_2)} \big) \big[\mathbf{a}_{\mathbf{k}}^\dagger \times \mathbf{a}_{\mathbf{k}'} \big]_z
\end{aligned}
$$

$$
\begin{aligned}
&+ e^{-i(\mathbf{k}-\mathbf{k}')\mathbf{R}_i} e^{i\mathbf{k}2\boldsymbol{\alpha}} \big(e^{i\mathbf{k}'(2\boldsymbol{\alpha}-\mathbf{L}_1+2\mathbf{L}_2)} + e^{i\mathbf{k}'(2\boldsymbol{\alpha}-\mathbf{L}_1-\mathbf{L}_2)} + e^{i\mathbf{k}'(2\boldsymbol{\alpha}+2\mathbf{L}_1-\mathbf{L}_2)}\big) \big[\mathbf{b}_{\mathbf{k}}^\dagger \times \mathbf{b}_{\mathbf{k}'}\big]_z \\
&- e^{i(\mathbf{k}-\mathbf{k}')\mathbf{R}_i} e^{i\mathbf{k}\boldsymbol{\alpha}} \big(e^{-i\mathbf{k}'(\boldsymbol{\alpha}-\mathbf{L}_1+2\mathbf{L}_2)} + e^{-i\mathbf{k}'(\boldsymbol{\alpha}-\mathbf{L}_1-\mathbf{L}_2)} + e^{-i\mathbf{k}'(\boldsymbol{\alpha}+2\mathbf{L}_1-\mathbf{L}_2)}\big) \big[\mathbf{a}_{\mathbf{k}'}^\dagger \times \mathbf{a}_{\mathbf{k}}\big]_z \\
&- e^{i(\mathbf{k}-\mathbf{k}')\mathbf{R}_i} e^{-i\mathbf{k}2\boldsymbol{\alpha}} \big(e^{-i\mathbf{k}'(2\boldsymbol{\alpha}-\mathbf{L}_1+2\mathbf{L}_2)} + e^{-i\mathbf{k}'(2\boldsymbol{\alpha}-\mathbf{L}_1-\mathbf{L}_2)} + e^{-i\mathbf{k}'(2\boldsymbol{\alpha}+2\mathbf{L}_1-\mathbf{L}_2)}\big) \big[\mathbf{b}_{\mathbf{k}'}^\dagger \times \mathbf{b}_{\mathbf{k}}\big]_z \\
&= \frac{t_2'}{\tilde{N}} \sum_{\mathbf{k}\in BZ} \sum_{\mathbf{G}} \Big[e^{-i\mathbf{k}\boldsymbol{\alpha}} \big(e^{i(\mathbf{k}+\mathbf{G})(\boldsymbol{\alpha}-\mathbf{L}_1+2\mathbf{L}_2)} + e^{i(\mathbf{k}+\mathbf{G})(\boldsymbol{\alpha}-\mathbf{L}_1-\mathbf{L}_2)} + e^{i(\mathbf{k}+\mathbf{G})(\boldsymbol{\alpha}+2\mathbf{L}_1-\mathbf{L}_2)}\big) \big[\mathbf{a}_{\mathbf{k}}^\dagger \times \mathbf{a}_{\mathbf{k}+\mathbf{G}}\big]_z \\
&\quad + e^{-i\mathbf{k}2\boldsymbol{\alpha}} \big(e^{i(\mathbf{k}+\mathbf{G})(2\boldsymbol{\alpha}-\mathbf{L}_1+2\mathbf{L}_2)} + e^{i(\mathbf{k}+\mathbf{G})(2\boldsymbol{\alpha}-\mathbf{L}_1-\mathbf{L}_2)} + e^{i(\mathbf{k}+\mathbf{G})(2\boldsymbol{\alpha}+2\mathbf{L}_1-\mathbf{L}_2)}\big) \big[\mathbf{b}_{\mathbf{k}}^\dagger \times \mathbf{b}_{\mathbf{k}+\mathbf{G}}\big]_z \\
&\quad - e^{i\mathbf{k}\boldsymbol{\alpha}} \big(e^{-i(\mathbf{k}+\mathbf{G})(\boldsymbol{\alpha}-\mathbf{L}_1+2\mathbf{L}_2)} + e^{-i(\mathbf{k}+\mathbf{G})(\boldsymbol{\alpha}-\mathbf{L}_1-\mathbf{L}_2)} + e^{-i(\mathbf{k}+\mathbf{G})(\boldsymbol{\alpha}+2\mathbf{L}_1-\mathbf{L}_2)}\big) \big[\mathbf{a}_{\mathbf{k}+\mathbf{G}}^\dagger \times \mathbf{a}_{\mathbf{k}}\big]_z \\
&\quad - e^{i\mathbf{k}2\boldsymbol{\alpha}} \big(e^{-i(\mathbf{k}+\mathbf{G})(2\boldsymbol{\alpha}-\mathbf{L}_1+2\mathbf{L}_2)} + e^{-i(\mathbf{k}+\mathbf{G})(2\boldsymbol{\alpha}-\mathbf{L}_1-\mathbf{L}_2)} + e^{-i(\mathbf{k}+\mathbf{G})(2\boldsymbol{\alpha}+2\mathbf{L}_1-\mathbf{L}_2)}\big) \big[\mathbf{b}_{\mathbf{k}+\mathbf{G}}^\dagger \times \mathbf{b}_{\mathbf{k}}\big]_z \\
&= \frac{t_2'}{\tilde{N}} \sum_{\mathbf{k}\in BZ} \tilde{N} \Big[\big(e^{i\mathbf{k}(-\mathbf{L}_1+2\mathbf{L}_2)} + e^{i\mathbf{k}(-\mathbf{L}_1-\mathbf{L}_2)} + e^{i\mathbf{k}(2\mathbf{L}_1-\mathbf{L}_2)}\big) \big[\mathbf{a}_{\mathbf{k}}^\dagger \times \mathbf{a}_{\mathbf{k}}\big]_z \\
&\quad + \big(e^{i\mathbf{k}(-\mathbf{L}_1+2\mathbf{L}_2)} + e^{i\mathbf{k}(-\mathbf{L}_1-\mathbf{L}_2)} + e^{i\mathbf{k}(2\mathbf{L}_1-\mathbf{L}_2)}\big) \big[\mathbf{b}_{\mathbf{k}}^\dagger \times \mathbf{b}_{\mathbf{k}}\big]_z \\
&\quad - \big(e^{-i\mathbf{k}(-\mathbf{L}_1+2\mathbf{L}_2)} + e^{-i\mathbf{k}(-\mathbf{L}_1-\mathbf{L}_2)} + e^{-i\mathbf{k}(2\mathbf{L}_1-\mathbf{L}_2)}\big) \big[\mathbf{a}_{\mathbf{k}}^\dagger \times \mathbf{a}_{\mathbf{k}}\big]_z \\
&\quad - \big(e^{-i\mathbf{k}(-\mathbf{L}_1+2\mathbf{L}_2)} + e^{-i\mathbf{k}(-\mathbf{L}_1-\mathbf{L}_2)} + e^{-i\mathbf{k}(2\mathbf{L}_1-\mathbf{L}_2)}\big) \big[\mathbf{b}_{\mathbf{k}}^\dagger \times \mathbf{b}_{\mathbf{k}}\big]_z \\
&= 2it_2' \sum_{\mathbf{k}\in BZ} \big[\sin\big(\mathbf{k}\cdot(-\mathbf{L}_1+2\mathbf{L}_2)\big) + \sin\big(\mathbf{k}\cdot(-\mathbf{L}_1-\mathbf{L}_2)\big) + \sin\big(\mathbf{k}\cdot(2\mathbf{L}_1-\mathbf{L}_2)\big)\big] \\
&\qquad\qquad \cdot \big(\big[\mathbf{a}_{\mathbf{k}}^\dagger \times \mathbf{a}_{\mathbf{k}}\big]_z + \big[\mathbf{b}_{\mathbf{k}}^\dagger \times \mathbf{b}_{\mathbf{k}}\big]_z\big). \qquad \text{(A.8)}
\end{aligned}
$$

Combining the results, the tight-binding Hamiltonian in $\mathbf{k}$-space is

$$
\begin{aligned}
H_{tb} = \sum_{\mathbf{k}\in BZ} \Bigg(& -\mu[\mathbf{a}_{\mathbf{k}}^\dagger \cdot \mathbf{a}_{\mathbf{k}} + \mathbf{b}_{\mathbf{k}}^\dagger \cdot \mathbf{b}_{\mathbf{k}}] + t_1\big[e^{i\mathbf{k}\boldsymbol{\alpha}}(1 + e^{-i\mathbf{k}\mathbf{L}_1} + e^{-i\mathbf{k}\mathbf{L}_2})\mathbf{a}_{\mathbf{k}}^\dagger \cdot \mathbf{b}_{\mathbf{k}} + h.c.\big] \\
& + 2t_2\big[\cos\big(\mathbf{k}\cdot(-\mathbf{L}_1+2\mathbf{L}_2)\big) + \cos\big(\mathbf{k}\cdot(-\mathbf{L}_1-\mathbf{L}_2)\big) + \cos\big(\mathbf{k}\cdot(2\mathbf{L}_1-\mathbf{L}_2)\big)\big](\mathbf{a}_{\mathbf{k}}^\dagger \cdot \mathbf{a}_{\mathbf{k}} + \mathbf{b}_{\mathbf{k}}^\dagger \cdot \mathbf{b}_{\mathbf{k}}) \\
& + 2it_2'\big[\sin\big(\mathbf{k}\cdot(-\mathbf{L}_1+2\mathbf{L}_2)\big) + \sin\big(\mathbf{k}\cdot(-\mathbf{L}_1-\mathbf{L}_2)\big) + \sin\big(\mathbf{k}\cdot(2\mathbf{L}_1-\mathbf{L}_2)\big)\big] \cdot \big(\big[\mathbf{a}_{\mathbf{k}}^\dagger \times \mathbf{a}_{\mathbf{k}}\big]_z + \big[\mathbf{b}_{\mathbf{k}}^\dagger \times \mathbf{b}_{\mathbf{k}}\big]_z\big)\Bigg).
\end{aligned} \qquad \text{(A.9)}
$$

Writing this in terms of the basis $\mathbf{f}_{\mathbf{k}}^\dagger = (a_{\mathbf{k},x}^\dagger, a_{\mathbf{k},y}^\dagger, b_{\mathbf{k},x}^\dagger, b_{\mathbf{k},y}^\dagger)$, we have

$$
H_{tb} = \sum_{\mathbf{k}\in BZ} \mathbf{f}_{\mathbf{k}}^\dagger \begin{pmatrix} -\mu + \tilde{t_2}(\mathbf{k}) & \tilde{t_2'}(\mathbf{k}) & \tilde{t_1}(\mathbf{k}) & 0 \\ -\tilde{t_2'}(\mathbf{k}) & -\mu + \tilde{t_2}(\mathbf{k}) & 0 & \tilde{t_1}(\mathbf{k}) \\ \tilde{t_1^*}(\mathbf{k}) & 0 & -\mu + \tilde{t_2}(\mathbf{k}) & \tilde{t_2'}(\mathbf{k}) \\ 0 & \tilde{t_1^*}(\mathbf{k}) & -\tilde{t_2'}(\mathbf{k}) & -\mu + \tilde{t_2}(\mathbf{k}) \end{pmatrix} \mathbf{f}_{\mathbf{k}}, \qquad \text{(A.10)}
$$

where,

$$
\begin{aligned}
\tilde{t_1}(\mathbf{k}) &= t_1\big[e^{i\mathbf{k}\boldsymbol{\alpha}}(1 + e^{-i\mathbf{k}\mathbf{L}_1} + e^{-i\mathbf{k}\mathbf{L}_2})\big], \\
\tilde{t_2}(\mathbf{k}) &= 2t_2\big[\cos\big(\mathbf{k}\cdot(-\mathbf{L}_1+2\mathbf{L}_2)\big) + \cos\big(\mathbf{k}\cdot(-\mathbf{L}_1-\mathbf{L}_2)\big) + \cos\big(\mathbf{k}\cdot(2\mathbf{L}_1-\mathbf{L}_2)\big)\big], \\
\tilde{t_2'}(\mathbf{k}) &= 2it_2'\big[\sin\big(\mathbf{k}\cdot(-\mathbf{L}_1+2\mathbf{L}_2)\big) + \sin\big(\mathbf{k}\cdot(-\mathbf{L}_1-\mathbf{L}_2)\big) + \sin\big(\mathbf{k}\cdot(2\mathbf{L}_1-\mathbf{L}_2)\big)\big]. \qquad \text{(A.11)}
\end{aligned}
$$

Appendix B

Fourier transformation of the interaction model

In this appendix, we derive the Fourier transformation (FT) of

$$U = \frac{V_0}{2}\sum_{\mathbf{R}}\sum_{j,j'}\sum_{\sigma,\sigma'}\left(\frac{1}{3}Q_{j,\sigma}(\mathbf{R}) + \alpha_1 T_{j,\sigma}(\mathbf{R})\right)\left(\frac{1}{3}Q_{j',\sigma'}(\mathbf{R}) + \alpha_1 T_{j',\sigma'}(\mathbf{R})\right). \tag{B.1}$$

We define the Fourier transformations as follows,

$$\begin{aligned} d_{j,\sigma}(\mathbf{R}+\boldsymbol{\delta}_p) &= \frac{1}{\sqrt{N}}\sum_{\mathbf{k}\in BZ} e^{i\mathbf{k}(\mathbf{R}+\boldsymbol{\delta}_p)} c_{j,\sigma,\mathbf{k}}\,, \\ d^{\dagger}_{j,\sigma}(\mathbf{R}+\boldsymbol{\delta}_p) &= \frac{1}{\sqrt{N}}\sum_{\mathbf{k}\in BZ} e^{-i\mathbf{k}(\mathbf{R}+\boldsymbol{\delta}_p)} c^{\dagger}_{j,\sigma,\mathbf{k}} \end{aligned} \tag{B.2}$$

where N is the total number of sites and $\mathbf{k} = (k_x, k_y)$ are points within the first Brillouin zone defined by the reciprocal vectors of $\mathbf{L}_{1,2}$.
We perform the FT of each term individually,

$$\begin{aligned} Q_{j,\sigma}(\mathbf{R}) &= \frac{1}{N}\sum_{p=1}^{6}\sum_{\mathbf{k},\mathbf{k}'} e^{-i\mathbf{k}(\mathbf{R}+\boldsymbol{\delta}_p)} e^{i\mathbf{k}'(\mathbf{R}+\boldsymbol{\delta}_p)} c^{\dagger}_{j,\sigma,\mathbf{k}} c_{j,\sigma,\mathbf{k}'} \\ &= \frac{1}{N}\sum_{p=1}^{6}\sum_{\mathbf{k},\mathbf{k}'} e^{-i(\mathbf{k}-\mathbf{k}')(\mathbf{R}+\boldsymbol{\delta}_p)} c^{\dagger}_{j,\sigma,\mathbf{k}} c_{j,\sigma,\mathbf{k}'} \\ &= \frac{1}{N}\sum_{p=1}^{6}\sum_{\mathbf{k},\mathbf{q}} e^{i\mathbf{q}(\mathbf{R}+\boldsymbol{\delta}_p)} c^{\dagger}_{j,\sigma,\mathbf{k}} c_{j,\sigma,\mathbf{k}+\mathbf{q}}, \end{aligned}$$

where $\mathbf{q} = \mathbf{k}' - \mathbf{k}$. Likewise,

$$\begin{aligned} T_{j,\sigma}(\mathbf{R}) &= \frac{1}{N}\sum_{p=1}^{6}(-1)^{p-1}\sum_{\mathbf{k},\mathbf{k}'}\left(e^{-i\mathbf{k}(\mathbf{R}+\boldsymbol{\delta}_p)} e^{i\mathbf{k}'(\mathbf{R}+\boldsymbol{\delta}_{p+1})} c^{\dagger}_{j,\sigma,\mathbf{k}} c_{j,\sigma,\mathbf{k}'} + h.c.\right) \\ &= \frac{1}{N}\sum_{p=1}^{6}(-1)^{p-1}\sum_{\mathbf{k},\mathbf{k}'}\left(e^{-i(\mathbf{k}-\mathbf{k}')\mathbf{R}} e^{-i\mathbf{k}\cdot\boldsymbol{\delta}_p} e^{i\mathbf{k}'\cdot\boldsymbol{\delta}_{p+1}} c^{\dagger}_{j,\sigma,\mathbf{k}} c_{j,\sigma,\mathbf{k}'} + e^{i(\mathbf{k}-\mathbf{k}')\mathbf{R}} e^{i\mathbf{k}\cdot\boldsymbol{\delta}_p} e^{-i\mathbf{k}'\cdot\boldsymbol{\delta}_{p+1}} c^{\dagger}_{j,\sigma,\mathbf{k}'} c_{j,\sigma,\mathbf{k}}\right) \\ &= \frac{1}{N}\sum_{p=1}^{6}(-1)^{p-1}\sum_{\mathbf{k},\mathbf{q}}\left(e^{i\mathbf{q}\mathbf{R}} e^{-i\mathbf{k}\cdot\boldsymbol{\delta}_p} e^{i(\mathbf{k}+\mathbf{q})\cdot\boldsymbol{\delta}_{p+1}} c^{\dagger}_{j,\sigma,\mathbf{k}} c_{j,\sigma,\mathbf{k}+\mathbf{q}} + e^{-i\mathbf{q}\mathbf{R}} e^{i\mathbf{k}\cdot\boldsymbol{\delta}_p} e^{-i(\mathbf{k}+\mathbf{q})\cdot\boldsymbol{\delta}_{p+1}} c^{\dagger}_{j,\sigma,\mathbf{k}+\mathbf{q}} c_{j,\sigma,\mathbf{k}}\right) \end{aligned}$$

$$= \frac{1}{N}\sum_{p=1}^{6}(-1)^{p-1}\sum_{\mathbf{k},\mathbf{q}}\left(e^{i\mathbf{q}\cdot(\mathbf{R}+\boldsymbol{\delta}_{p+1})}e^{i\mathbf{k}\cdot(\boldsymbol{\delta}_{p+1}-\boldsymbol{\delta}_p)}c^\dagger_{j,\sigma,\mathbf{k}}c_{j,\sigma,\mathbf{k}+\mathbf{q}} + e^{-i\mathbf{q}(\mathbf{R}+\boldsymbol{\delta}_{p+1})}e^{-i\mathbf{k}\cdot(\boldsymbol{\delta}_{p+1}-\boldsymbol{\delta}_p)}c^\dagger_{j,\sigma,\mathbf{k}+\mathbf{q}}c_{j,\sigma,\mathbf{k}}\right)$$

where we have suppressed the restriction on the $\mathbf{k},\mathbf{q}$-sums.
Inserting in Eq. (B.1), we get

$$\begin{aligned}
U &= \frac{V_0}{2N^2}\sum_{\mathbf{R}}\sum_{j,j'}\sum_{\sigma,\sigma'}\sum_{\substack{\mathbf{k},\mathbf{k}'\\ \mathbf{q},\mathbf{q}'}}\sum_{p,p'}\Bigg(\frac{1}{3}e^{i\mathbf{q}\cdot(\mathbf{R}+\boldsymbol{\delta}_p)}c^\dagger_{j,\sigma,\mathbf{k}}c_{j,\sigma,\mathbf{k}+\mathbf{q}} + \alpha_1(-1)^{p-1}\\
&\quad\times\left(e^{i\mathbf{q}\cdot(\mathbf{R}+\boldsymbol{\delta}_{p+1})}e^{i\mathbf{k}\cdot(\boldsymbol{\delta}_{p+1}-\boldsymbol{\delta}_p)}c^\dagger_{j,\sigma,\mathbf{k}}c_{j,\sigma,\mathbf{k}+\mathbf{q}} + e^{-i\mathbf{q}\cdot(\mathbf{R}+\boldsymbol{\delta}_{p+1})}e^{-i\mathbf{k}\cdot(\boldsymbol{\delta}_{p+1}-\boldsymbol{\delta}_p)}c^\dagger_{j,\sigma,\mathbf{k}+\mathbf{q}}c_{j,\sigma,\mathbf{k}}\right)\Bigg)\\
&\quad\times\Bigg(\frac{1}{3}e^{i\mathbf{q}'\cdot(\mathbf{R}+\boldsymbol{\delta}_{p'})}c^\dagger_{j',\sigma',\mathbf{k}'}c_{j',\sigma',\mathbf{k}'+\mathbf{q}'} + \alpha_1(-1)^{p'-1}\\
&\quad\times\left(e^{i\mathbf{q}'\cdot(\mathbf{R}+\boldsymbol{\delta}_{p'+1})}e^{i\mathbf{k}'\cdot(\boldsymbol{\delta}_{p'+1}-\boldsymbol{\delta}_{p'})}c^\dagger_{j',\sigma',\mathbf{k}'}c_{j',\sigma',\mathbf{k}'+\mathbf{q}'} + e^{-i\mathbf{q}'\cdot(\mathbf{R}+\boldsymbol{\delta}_{p'+1})}e^{-i\mathbf{k}'\cdot(\boldsymbol{\delta}_{p'+1}-\boldsymbol{\delta}_{p'})}c^\dagger_{j',\sigma',\mathbf{k}'+\mathbf{q}'}c_{j',\sigma',\mathbf{k}'}\right)\Bigg)\\
&= \frac{V_0}{2N^2}\sum_{\mathbf{R}}\sum_{j,j'}\sum_{\sigma,\sigma'}\sum_{\substack{\mathbf{k},\mathbf{k}'\\ \mathbf{q},\mathbf{q}'}}\sum_{p,p'}\Bigg(e^{i\mathbf{q}\cdot\mathbf{R}}\Big(\frac{1}{3}e^{i\mathbf{q}\cdot\boldsymbol{\delta}_p} + \alpha_1(-1)^{p-1}e^{i\mathbf{q}\cdot\boldsymbol{\delta}_{p+1}}e^{i\mathbf{k}\cdot(\boldsymbol{\delta}_{p+1}-\boldsymbol{\delta}_p)}\Big)c^\dagger_{j,\sigma,\mathbf{k}}c_{j,\sigma,\mathbf{k}+\mathbf{q}}\\
&\quad + e^{-i\mathbf{q}\cdot\mathbf{R}}\alpha_1(-1)^{p-1}e^{-i\mathbf{q}\cdot\boldsymbol{\delta}_{p+1}}e^{-i\mathbf{k}\cdot(\boldsymbol{\delta}_{p+1}-\boldsymbol{\delta}_p)}c^\dagger_{j,\sigma,\mathbf{k}+\mathbf{q}}c_{j,\sigma,\mathbf{k}}\Bigg)\\
&\quad\times\Bigg(e^{i\mathbf{q}'\cdot\mathbf{R}}\Big(\frac{1}{3}e^{i\mathbf{q}'\cdot\boldsymbol{\delta}_{p'}} + \alpha_1(-1)^{p'-1}e^{i\mathbf{q}'\cdot\boldsymbol{\delta}_{p'+1}}e^{i\mathbf{k}'\cdot(\boldsymbol{\delta}_{p'+1}-\boldsymbol{\delta}_{p'})}\Big)c^\dagger_{j',\sigma',\mathbf{k}'}c_{j',\sigma',\mathbf{k}'+\mathbf{q}'}\\
&\quad + e^{-i\mathbf{q}'\cdot\mathbf{R}}\alpha_1(-1)^{p'-1}e^{-i\mathbf{q}'\boldsymbol{\delta}_{p'+1}}e^{-i\mathbf{k}'\cdot(\boldsymbol{\delta}_{p'+1}-\boldsymbol{\delta}_{p'})}c^\dagger_{j',\sigma',\mathbf{k}'+\mathbf{q}'}c_{j',\sigma',\mathbf{k}'}\Bigg)\\
&= \frac{V_0}{2N^2}\sum_{\mathbf{R}}\sum_{j,j'}\sum_{\sigma,\sigma'}\sum_{\substack{\mathbf{k},\mathbf{k}'\\ \mathbf{q},\mathbf{q}'}}\sum_{p,p'}\Bigg(e^{i(\mathbf{q}+\mathbf{q}')\cdot\mathbf{R}}\Big(\frac{1}{3}e^{i\mathbf{q}\cdot\boldsymbol{\delta}_p} + \alpha_1(-1)^{p-1}e^{i\mathbf{q}\cdot\boldsymbol{\delta}_{p+1}}e^{i\mathbf{k}\cdot(\boldsymbol{\delta}_{p+1}-\boldsymbol{\delta}_p)}\Big)\\
&\quad\times\Big(\frac{1}{3}e^{i\mathbf{q}'\cdot\boldsymbol{\delta}_{p'}} + \alpha_1(-1)^{p'-1}e^{i\mathbf{q}'\cdot\boldsymbol{\delta}_{p'+1}}e^{i\mathbf{k}'\cdot(\boldsymbol{\delta}_{p'+1}-\boldsymbol{\delta}_{p'})}\Big)c^\dagger_{j,\sigma,\mathbf{k}}c_{j,\sigma,\mathbf{k}+\mathbf{q}}c^\dagger_{j',\sigma',\mathbf{k}'}c_{j',\sigma',\mathbf{k}'+\mathbf{q}'}\\
&\quad + e^{-i(\mathbf{q}-\mathbf{q}')\cdot\mathbf{R}}\Big(\alpha_1(-1)^{p-1}e^{-i\mathbf{q}\cdot\boldsymbol{\delta}_{p+1}}e^{-i\mathbf{k}\cdot(\boldsymbol{\delta}_{p+1}-\boldsymbol{\delta}_p)}\Big)\\
&\quad\times\Big(\frac{1}{3}e^{i\mathbf{q}'\cdot\boldsymbol{\delta}_{p'}} + \alpha_1(-1)^{p'-1}e^{i\mathbf{q}'\cdot\boldsymbol{\delta}_{p'+1}}e^{i\mathbf{k}'\cdot(\boldsymbol{\delta}_{p'+1}-\boldsymbol{\delta}_{p'})}\Big)c^\dagger_{j,\sigma,\mathbf{k}+\mathbf{q}}c_{j,\sigma,\mathbf{k}}c^\dagger_{j',\sigma',\mathbf{k}'}c_{j',\sigma',\mathbf{k}'+\mathbf{q}'}\\
&\quad + e^{i(\mathbf{q}-\mathbf{q}')\cdot\mathbf{R}}\Big(\frac{1}{3}e^{i\mathbf{q}\cdot\boldsymbol{\delta}_p} + \alpha_1(-1)^{p-1}e^{i\mathbf{q}\cdot\boldsymbol{\delta}_{p+1}}e^{i\mathbf{k}\cdot(\boldsymbol{\delta}_{p+1}-\boldsymbol{\delta}_p)}\Big)\\
&\quad\times\Big(\alpha_1(-1)^{p'-1}e^{-i\mathbf{q}'\cdot\boldsymbol{\delta}_{p'+1}}e^{-i\mathbf{k}'\cdot(\boldsymbol{\delta}_{p'+1}-\boldsymbol{\delta}_{p'})}\Big)c^\dagger_{j,\sigma,\mathbf{k}}c_{j,\sigma,\mathbf{k}+\mathbf{q}}c^\dagger_{j',\sigma',\mathbf{k}'+\mathbf{q}'}c_{j',\sigma',\mathbf{k}'}\\
&\quad + e^{-i(\mathbf{q}+\mathbf{q}')\cdot\mathbf{R}}\Big(\alpha_1(-1)^{p-1}e^{-i\mathbf{q}\cdot\boldsymbol{\delta}_{p+1}}e^{-i\mathbf{k}\cdot(\boldsymbol{\delta}_{p+1}-\boldsymbol{\delta}_p)}\Big)\\
&\quad\times\Big(\alpha_1(-1)^{p'-1}e^{-i\mathbf{q}'\cdot\boldsymbol{\delta}_{p'+1}}e^{-i\mathbf{k}'\cdot(\boldsymbol{\delta}_{p'+1}-\boldsymbol{\delta}_{p'})}\Big)c^\dagger_{j,\sigma,\mathbf{k}+\mathbf{q}}c_{j,\sigma,\mathbf{k}}c^\dagger_{j',\sigma',\mathbf{k}'+\mathbf{q}'}c_{j',\sigma',\mathbf{k}'}\Bigg).
\end{aligned}\tag{B.3}$$

Performing the summation over $\mathbf{R}$ eliminates the $\mathbf{q}'$-sum, since $\sum_{\mathbf{R}} e^{(-)i(\mathbf{q}\pm\mathbf{q}')\mathbf{R}} = \sum_{\mathbf{G}}\delta_{\mathbf{q}',\mp(\mathbf{q}+\mathbf{G})}$, where $\mathbf{G}$ are the reciprocal lattice vectors. The effect of this substitution is similar in all four terms and can be evaluated individually. To avoid long expressions we merely study the $\mathbf{G}$-

summation performed on the first term and fix all other variables.

$$
\begin{aligned}
&\sum_{\mathbf{G}} \delta_{\mathbf{q}',-(\mathbf{q}+\mathbf{G})} \Bigg(\Big(\frac{1}{3} e^{i\mathbf{q}\cdot\boldsymbol{\delta}_p} + \alpha_1 (-1)^{p-1} e^{i\mathbf{q}\cdot\boldsymbol{\delta}_{p+1}} e^{i\mathbf{k}\cdot(\boldsymbol{\delta}_{p+1}-\boldsymbol{\delta}_p)} \Big) \\
&\qquad \times \Big(\frac{1}{3} e^{i\mathbf{q}'\cdot\boldsymbol{\delta}_{p'}} + \alpha_1 (-1)^{p'-1} e^{i\mathbf{q}'\cdot\boldsymbol{\delta}_{p'+1}} e^{i\mathbf{k}'\cdot(\boldsymbol{\delta}_{p'+1}-\boldsymbol{\delta}_{p'})} \Big) c^\dagger_{j,\sigma,\mathbf{k}} c_{j,\sigma,\mathbf{k}+\mathbf{q}} c^\dagger_{j',\sigma',\mathbf{k}'} c_{j',\sigma',\mathbf{k}'+\mathbf{q}'} \\
&= \sum_{\mathbf{G}} \Bigg(\Big(\frac{1}{3} e^{i\mathbf{q}\cdot\boldsymbol{\delta}_p} + \alpha_1 (-1)^{p-1} e^{i\mathbf{q}\cdot\boldsymbol{\delta}_{p+1}} e^{i\mathbf{k}\cdot(\boldsymbol{\delta}_{p+1}-\boldsymbol{\delta}_p)} \Big) \\
&\qquad \times \Big(\frac{1}{3} e^{-i(\mathbf{q}+\mathbf{G})\cdot\boldsymbol{\delta}_{p'}} + \alpha_1 (-1)^{p'-1} e^{-i(\mathbf{q}+\mathbf{G})\cdot\boldsymbol{\delta}_{p'+1}} e^{i\mathbf{k}'\cdot(\boldsymbol{\delta}_{p'+1}-\boldsymbol{\delta}_{p'})} \Big) c^\dagger_{j,\sigma,\mathbf{k}} c_{j,\sigma,\mathbf{k}+\mathbf{q}} c^\dagger_{j',\sigma',\mathbf{k}'} c_{j',\sigma',\mathbf{k}'-\mathbf{q}-\mathbf{G}} \\
&= \sum_{\mathbf{G}} \Bigg(\Big(\frac{1}{3} e^{i\mathbf{q}\cdot\boldsymbol{\delta}_p} + \alpha_1 (-1)^{p-1} e^{i\mathbf{q}\cdot\boldsymbol{\delta}_{p+1}} e^{i\mathbf{k}\cdot(\boldsymbol{\delta}_{p+1}-\boldsymbol{\delta}_p)} \Big) c^\dagger_{j,\sigma,\mathbf{k}} c_{j,\sigma,\mathbf{k}+\mathbf{q}} \\
&\qquad \times \Big(\frac{1}{3} e^{-i(\mathbf{q}+\mathbf{G})\cdot\boldsymbol{\delta}_{p'}} c^\dagger_{j',\sigma',\mathbf{k}'} c_{j',\sigma',\mathbf{k}'-\mathbf{G}-\mathbf{q}} + \alpha_1 (-1)^{p'-1} e^{-i(\mathbf{q}+\mathbf{G})\cdot\boldsymbol{\delta}_{p'+1}} e^{i\mathbf{k}'\cdot(\boldsymbol{\delta}_{p'+1}-\boldsymbol{\delta}_{p'})} c^\dagger_{j',\sigma',\mathbf{k}'} c_{j',\sigma',\mathbf{k}'-\mathbf{G}-\mathbf{q}} \Big) \\
&= \Bigg(\Big(\frac{1}{3} e^{i\mathbf{q}\cdot\boldsymbol{\delta}_p} + \alpha_1 (-1)^{p-1} e^{i\mathbf{q}\cdot\boldsymbol{\delta}_{p+1}} e^{i\mathbf{k}\cdot(\boldsymbol{\delta}_{p+1}-\boldsymbol{\delta}_p)} \Big) c^\dagger_{j,\sigma,\mathbf{k}} c_{j,\sigma,\mathbf{k}+\mathbf{q}} \\
&\qquad \times \sum_{\mathbf{G}} \Big(\frac{1}{3} e^{-i(\mathbf{q}+\mathbf{G})\cdot\boldsymbol{\delta}_{p'}} c^\dagger_{j',\sigma',\mathbf{k}'} c_{j',\sigma',\mathbf{k}'-\mathbf{G}-\mathbf{q}} + \alpha_1 (-1)^{p'-1} e^{-i(\mathbf{q}+\mathbf{G})\cdot\boldsymbol{\delta}_{p'+1}} e^{i\mathbf{k}'\cdot(\boldsymbol{\delta}_{p'+1}-\boldsymbol{\delta}_{p'})} c^\dagger_{j',\sigma',\mathbf{k}'} c_{j',\sigma',\mathbf{k}'-\mathbf{G}-\mathbf{q}} \Big)
\end{aligned}
\tag{B.4}
$$

We wish to let $c_{j',\sigma',\mathbf{k}'-\mathbf{G}-\mathbf{q}} \to c_{j',\sigma',\mathbf{k}'-\mathbf{q}}$, which can be usually be done without further consideration in the case of single-site unit cells with the atom at $\mathbf{R}$. In our slightly more complicated case, we must return to the definitions in Eq. (B.2) and get

$$
\begin{aligned}
c_{j',\sigma',\mathbf{k}'-\mathbf{G}-\mathbf{q}} &= \frac{1}{\sqrt{N}} \sum_{\mathbf{R}} e^{-i(\mathbf{k}'-\mathbf{G}-\mathbf{q})(\mathbf{R}+\beta)} d_{j',\sigma'}(\mathbf{R}+\beta) \\
&= \frac{1}{\sqrt{N}} \sum_{\mathbf{R}} e^{-i(\mathbf{k}'-\mathbf{q})(\mathbf{R}+\beta)} d_{j',\sigma'}(\mathbf{R}+\beta) e^{i\mathbf{G}(\mathbf{R}+\beta)} \\
&= \frac{1}{\sqrt{N}} \sum_{\mathbf{R}} e^{-i(\mathbf{k}'-\mathbf{q})(\mathbf{R}+\beta)} d_{j',\sigma'}(\mathbf{R}+\beta) e^{i\mathbf{G}\beta} \\
&= c_{j',\sigma',\mathbf{k}'-\mathbf{q}} e^{i\mathbf{G}\beta},
\end{aligned}
\tag{B.5}
$$

where β must be obtained from the original real-space operator prior to the Fourier transformation.

The result is general such that $c_{j,\sigma,\tilde{k}\pm\mathbf{G}} = c_{j,\sigma,\tilde{k}} e^{\mp i\mathbf{G}\beta}$ and $c^\dagger_{j,\sigma,\tilde{k}\pm\mathbf{G}} = c^\dagger_{j,\sigma,\tilde{k}} e^{\pm i\mathbf{G}\beta}$. Keeping track of original operators from Eq. (B.1) and inserting into Eq. (B.4) one finds (disregarding the $\mathbf{G}$-independent prefactor),

$$
\begin{aligned}
&\sum_{\mathbf{G}} \Big(\frac{1}{3} e^{-i(\mathbf{q}+\mathbf{G})\cdot\boldsymbol{\delta}_{p'}} c^\dagger_{j',\sigma',\mathbf{k}'} e^{i\mathbf{G}\cdot\boldsymbol{\delta}_{p'}} c_{j',\sigma',\mathbf{k}'-\mathbf{q}} + \alpha_1 (-1)^{p'-1} e^{-i(\mathbf{q}+\mathbf{G})\cdot\boldsymbol{\delta}_{p'+1}} e^{i\mathbf{k}'\cdot(\boldsymbol{\delta}_{p'+1}-\boldsymbol{\delta}_{p'})} c^\dagger_{j',\sigma',\mathbf{k}'} e^{i\mathbf{G}\cdot\boldsymbol{\delta}_{p'+1}} c_{j',\sigma',\mathbf{k}'-\mathbf{q}} \Big) \\
&= \sum_{\mathbf{G}} \Big(\frac{1}{3} e^{-i\mathbf{q}\cdot\boldsymbol{\delta}_{p'}} c^\dagger_{j',\sigma',\mathbf{k}'} c_{j',\sigma',\mathbf{k}'-\mathbf{q}} + \alpha_1 (-1)^{p'-1} e^{-i\mathbf{q}\cdot\boldsymbol{\delta}_{p'+1}} e^{i\mathbf{k}'\cdot(\boldsymbol{\delta}_{p'+1}-\boldsymbol{\delta}_{p'})} c^\dagger_{j',\sigma',\mathbf{k}'} c_{j',\sigma',\mathbf{k}'-\mathbf{q}} \Big) \\
&= N \Big(\frac{1}{3} e^{-i\mathbf{q}\cdot\boldsymbol{\delta}_{p'}} c^\dagger_{j',\sigma',\mathbf{k}'} c_{j',\sigma',\mathbf{k}'-\mathbf{q}} + \alpha_1 (-1)^{p'-1} e^{-i\mathbf{q}\cdot\boldsymbol{\delta}_{p'+1}} e^{i\mathbf{k}'\cdot(\boldsymbol{\delta}_{p'+1}-\boldsymbol{\delta}_{p'})} c^\dagger_{j',\sigma',\mathbf{k}'} c_{j',\sigma',\mathbf{k}'-\mathbf{q}} \Big),
\end{aligned}
\tag{B.6}
$$

where we use that the number of distinct reciprocal lattice vectors is equal to the number of sites.

Repeating this procedure on the remaining three terms of Eq. (B.3) yields,

$$
U = \frac{V_0}{2N} \sum_{j,j'} \sum_{\sigma,\sigma'} \sum_{\mathbf{k},\mathbf{k}',\mathbf{q}} \sum_{p,p'} \Bigg(\Big(\frac{1}{3} e^{i\mathbf{q}\cdot\boldsymbol{\delta}_p} + \alpha_1 (-1)^{p-1} e^{i\mathbf{q}\cdot\boldsymbol{\delta}_{p+1}} e^{i\mathbf{k}\cdot(\boldsymbol{\delta}_{p+1}-\boldsymbol{\delta}_p)} \Big)
$$

$$
\begin{aligned}
&\times \left(\frac{1}{3}e^{-i\mathbf{q}\cdot\boldsymbol{\delta}_{p'}} + \alpha_1(-1)^{p'-1}e^{-i\mathbf{q}\cdot\boldsymbol{\delta}_{p'+1}}e^{i\mathbf{k}'\cdot(\boldsymbol{\delta}_{p'+1}-\boldsymbol{\delta}_{p'})}\right)c^{\dagger}_{j,\sigma,\mathbf{k}}c_{j,\sigma,\mathbf{k}+\mathbf{q}}c^{\dagger}_{j',\sigma',\mathbf{k}'}c_{j',\sigma',\mathbf{k}'-\mathbf{q}} \\
&+ \left(\alpha_1(-1)^{p-1}e^{-i\mathbf{q}\cdot\boldsymbol{\delta}_{p+1}}e^{-i\mathbf{k}\cdot(\boldsymbol{\delta}_{p+1}-\boldsymbol{\delta}_{p})}\right) \\
&\times \left(\frac{1}{3}e^{i\mathbf{q}\cdot\boldsymbol{\delta}_{p'}} + \alpha_1(-1)^{p'-1}e^{i\mathbf{q}\cdot\boldsymbol{\delta}_{p'+1}}e^{i\mathbf{k}'\cdot(\boldsymbol{\delta}_{p'+1}-\boldsymbol{\delta}_{p'})}\right)c^{\dagger}_{j,\sigma,\mathbf{k}+\mathbf{q}}c_{j,\sigma,\mathbf{k}}c^{\dagger}_{j',\sigma',\mathbf{k}'}c_{j',\sigma',\mathbf{k}'+\mathbf{q}} \\
&+ \left(\frac{1}{3}e^{i\mathbf{q}\cdot\boldsymbol{\delta}_{p}} + \alpha_1(-1)^{p-1}e^{i\mathbf{q}\cdot\boldsymbol{\delta}_{p+1}}e^{i\mathbf{k}\cdot(\boldsymbol{\delta}_{p+1}-\boldsymbol{\delta}_{p})}\right) \\
&\times \left(\alpha_1(-1)^{p'-1}e^{-i\mathbf{q}\cdot\boldsymbol{\delta}_{p'+1}}e^{-i\mathbf{k}'\cdot(\boldsymbol{\delta}_{p'+1}-\boldsymbol{\delta}_{p'})}\right)c^{\dagger}_{j,\sigma,\mathbf{k}}c_{j,\sigma,\mathbf{k}+\mathbf{q}}c^{\dagger}_{j',\sigma',\mathbf{k}'+\mathbf{q}}c_{j',\sigma',\mathbf{k}'} \\
&+ \left(\alpha_1(-1)^{p-1}e^{-i\mathbf{q}\cdot\boldsymbol{\delta}_{p+1}}e^{-i\mathbf{k}\cdot(\boldsymbol{\delta}_{p+1}-\boldsymbol{\delta}_{p})}\right) \\
&\times \left(\alpha_1(-1)^{p'-1}e^{i\mathbf{q}\cdot\boldsymbol{\delta}_{p'+1}}e^{-i\mathbf{k}'\cdot(\boldsymbol{\delta}_{p'+1}-\boldsymbol{\delta}_{p'})}\right)c^{\dagger}_{j,\sigma,\mathbf{k}+\mathbf{q}}c_{j,\sigma,\mathbf{k}}c^{\dagger}_{j',\sigma',\mathbf{k}'-\mathbf{q}}c_{j',\sigma',\mathbf{k}'}\Bigg),
\end{aligned}
\tag{B.7}
$$

which can be readily verified.

Appendix C

Momentum shift of U

In this appendix we study the consequences of a momentum shift on individual terms of U. The FT of U reads,

$$
\begin{aligned}
U \quad = \frac{V_0}{2N} \sum_{\tau,\tau'} \sum_{\sigma,\sigma'} \sum_{\mathbf{k},\mathbf{k}',\mathbf{q}} \sum_{p,p'} \Bigg(& \Big(\frac{1}{3} e^{i\mathbf{q}\cdot\boldsymbol{\delta}_p} + \alpha_1 (-1)^{p-1} e^{i\mathbf{q}\cdot\boldsymbol{\delta}_{p+1}} e^{i\mathbf{k}\cdot(\boldsymbol{\delta}_{p+1}-\boldsymbol{\delta}_p)}\Big) \\
& \times \Big(\frac{1}{3} e^{-i\mathbf{q}\cdot\boldsymbol{\delta}_{p'}} + \alpha_1 (-1)^{p'-1} e^{-i\mathbf{q}\cdot\boldsymbol{\delta}_{p'+1}} e^{i\mathbf{k}'\cdot(\boldsymbol{\delta}_{p'+1}-\boldsymbol{\delta}_{p'})}\Big) c^\dagger_{\tau,\sigma,\mathbf{k}} c_{\tau,\sigma,\mathbf{k}+\mathbf{q}} c^\dagger_{\tau',\sigma',\mathbf{k}'} c_{\tau',\sigma',\mathbf{k}'-\mathbf{q}} \\
& + \Big(\alpha_1 (-1)^{p-1} e^{-i\mathbf{q}\cdot\boldsymbol{\delta}_{p+1}} e^{-i\mathbf{k}\cdot(\boldsymbol{\delta}_{p+1}-\boldsymbol{\delta}_p)}\Big) \\
& \times \Big(\frac{1}{3} e^{i\mathbf{q}\cdot\boldsymbol{\delta}_{p'}} + \alpha_1 (-1)^{p'-1} e^{i\mathbf{q}\cdot\boldsymbol{\delta}_{p'+1}} e^{i\mathbf{k}'\cdot(\boldsymbol{\delta}_{p'+1}-\boldsymbol{\delta}_{p'})}\Big) c^\dagger_{\tau,\sigma,\mathbf{k}+\mathbf{q}} c_{\tau,\sigma,\mathbf{k}} c^\dagger_{\tau',\sigma',\mathbf{k}'} c_{\tau',\sigma',\mathbf{k}'+\mathbf{q}} \\
& + \Big(\frac{1}{3} e^{i\mathbf{q}\cdot\boldsymbol{\delta}_p} + \alpha_1 (-1)^{p-1} e^{i\mathbf{q}\cdot\boldsymbol{\delta}_{p+1}} e^{i\mathbf{k}\cdot(\boldsymbol{\delta}_{p+1}-\boldsymbol{\delta}_p)}\Big) \\
& \times \Big(\alpha_1 (-1)^{p'-1} e^{-i\mathbf{q}\cdot\boldsymbol{\delta}_{p'+1}} e^{-i\mathbf{k}'\cdot(\boldsymbol{\delta}_{p'+1}-\boldsymbol{\delta}_{p'})}\Big) c^\dagger_{\tau,\sigma,\mathbf{k}} c_{\tau,\sigma,\mathbf{k}+\mathbf{q}} c^\dagger_{\tau',\sigma',\mathbf{k}'+\mathbf{q}} c_{\tau',\sigma',\mathbf{k}'} \\
& + \Big(\alpha_1 (-1)^{p-1} e^{-i\mathbf{q}\cdot\boldsymbol{\delta}_{p+1}} e^{-i\mathbf{k}\cdot(\boldsymbol{\delta}_{p+1}-\boldsymbol{\delta}_p)}\Big) \\
& \times \Big(\alpha_1 (-1)^{p'-1} e^{i\mathbf{q}\cdot\boldsymbol{\delta}_{p'+1}} e^{-i\mathbf{k}'\cdot(\boldsymbol{\delta}_{p'+1}-\boldsymbol{\delta}_{p'})}\Big) c^\dagger_{\tau,\sigma,\mathbf{k}+\mathbf{q}} c_{\tau,\sigma,\mathbf{k}} c^\dagger_{\tau',\sigma',\mathbf{k}'-\mathbf{q}} c_{\tau',\sigma',\mathbf{k}'} \Bigg)
\end{aligned}
\tag{C.1}
$$

An identical shift of $\mathbf{k}' \to \tilde{\mathbf{k}} - \mathbf{q}$ must be performed on the second and third term to obtain a restriction on $\mathbf{q}$ in the HF decoupling .
As we wish to shift $\mathbf{k}'$ we will consider the possible interactions for fixed $\mathbf{k}$ and $\mathbf{q}$. Two cases will be studied, *i*) the simple case for $\mathbf{k}, \mathbf{k}+\mathbf{q}, \mathbf{k}', \mathbf{k}'+\mathbf{q} \in$ BZ and *ii*) the case for $\mathbf{k}, \mathbf{k}+\mathbf{q}, \mathbf{k}' \in$ BZ and $\mathbf{k}'+\mathbf{q} \notin$ BZ. We will not study the case for $\mathbf{k}+\mathbf{q} \notin$ BZ, as these terms will remain unchanged. The essential details to consider are first whether all interactions are represented after performing the shift and second whether the phases on each interaction are identical to the phases before the shift.

An illustration of the first case with all points within the first BZ can be seen in Fig. C.1. As evident from the figure, we now consider interactions from the second term in U, however as the interactions in the third term simply have creation and annihilation operators (filled and empty circles respectively) interchanged, the result will apply to both terms. As $\mathbf{k}'$, and hence $\tilde{\mathbf{k}}$, run through all values within the first BZ for fixed $\mathbf{k}$ all interactions will be taken into account after performing a shift. This is illustrated in Fig. C.1b, where $\tilde{\mathbf{k}}$ is clearly different from $\mathbf{k}'$ in Fig. C.1a, thus this interaction certainly appears at a different time when performing the sum. The orders of the terms are, however, insignificant as long as all values of $\tilde{\mathbf{k}}$ are present for fixed $\mathbf{k}$. To ensure the consistency of the phases, we consider a generic form of the interaction terms $e^{i\mathbf{q}\cdot\mathbf{a}} e^{i\mathbf{k}\cdot\mathbf{b}} e^{i\mathbf{q}\cdot\mathbf{a}'} e^{i\mathbf{k}'\cdot\mathbf{b}'} c^\dagger_{\mathbf{k}+\mathbf{q}} c_{\mathbf{k}} c^\dagger_{\mathbf{k}'} c_{\mathbf{k}'+\mathbf{q}} \to e^{i\mathbf{q}\cdot\mathbf{a}} e^{i\mathbf{k}\cdot\mathbf{b}} e^{i\mathbf{q}\cdot\mathbf{a}'} e^{i(\tilde{\mathbf{k}}-\mathbf{q})\cdot\mathbf{b}'} c^\dagger_{\mathbf{k}+\mathbf{q}} c_{\mathbf{k}} c^\dagger_{\tilde{\mathbf{k}}-\mathbf{q}} c_{\tilde{\mathbf{k}}}$. The momentum of

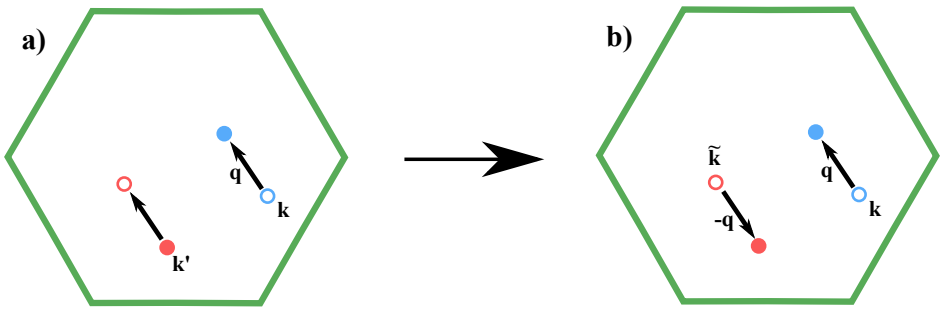

Figure C.1: Illustration of interaction term with $\mathbf{k}, \mathbf{k}+\mathbf{q}, \mathbf{k}', \mathbf{k}'+\mathbf{q} \in$ BZ. Filled circles are creation operators whereas empty circles are annihilation operators. **a)** depicts an interaction in the original term while **b)** depict the same interaction after the shift. The terms will appear at different times in the $\mathbf{k}'/\tilde{\mathbf{k}}$ sum.

the phase still relates to the momentum of the creation operator while all other phases are unchanged. We conclude that for the first case, where all points reside inside the first BZ, a shift of $\mathbf{k}' \to \tilde{\mathbf{k}} - \mathbf{q}$ can be performed with no further complications.

We now turn our attention to the slightly more complicated case, for $\mathbf{k}'+\mathbf{q} \notin$ BZ, see Fig. C.2. $\mathbf{k}+\mathbf{q}$ and $\tilde{\mathbf{k}}-\mathbf{q}$ reside outside the first BZ and are folded back in with $\mathbf{G}_1$ and $\mathbf{G}_2$, respectively. Note that $\mathbf{k}'$ and $\tilde{\mathbf{k}}$ still reside inside the first BZ as required by the restriction on the associated sums. As for the first case, since the entire summation of $\mathbf{k}'$ ($\tilde{\mathbf{k}}$) is performed for fixed $\mathbf{k}$, all interactions will be taken into account. The important difference in these types of terms is the folding, since $\mathbf{G}_1 \neq \mathbf{G}_2$. Thus we must ensure that the phases are individually unaffected by the folding.

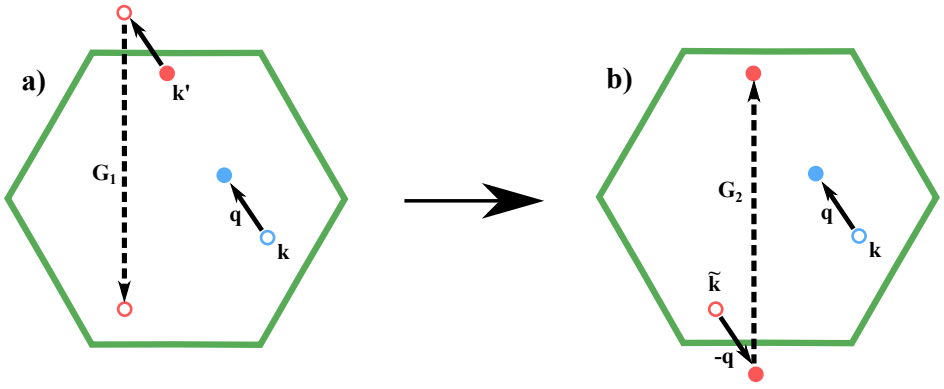

Figure C.2: Illustration of interaction term with $\mathbf{k}, \mathbf{k}+\mathbf{q}, \mathbf{k}' \in$ BZ and $\mathbf{k}'+\mathbf{q} \notin$ BZ. Filled circles are creation operators and empty are annihilation operators. **a)** depicts an interaction in the original term while **b)** depict the same interaction after the shift. As $\mathbf{k}+\mathbf{q}$ ($\tilde{\mathbf{k}}-\mathbf{q}$) reside outside the first BZ it is folded back in with a reciprocal vector. Note that $\mathbf{G}_1 \neq \mathbf{G}_2$.

In general we must have that $U(\mathbf{q}) = U(\mathbf{q}+\mathbf{G})$ since the Hamiltonian should obey the discrete translational symmetry of the Bravais lattice. To investigate if the terms satisfies this equality individually, we study one term at a time (denoted $U^{(i)}$, $i = 1, 2, 3, 4$), perform the shift $\mathbf{q} \to \mathbf{q}+\mathbf{G}$ and employ the generalized result of Eq. (B.5).

$$U_{\mathbf{q}}^{(1)} \propto \sum_{\mathbf{k},\mathbf{k}',\mathbf{q}} \left(\frac{1}{3} e^{i\mathbf{q}\cdot\boldsymbol{\delta}_p} + \alpha_1 (-1)^{p-1} e^{i\mathbf{q}\cdot\boldsymbol{\delta}_{p+1}} e^{i\mathbf{k}\cdot(\boldsymbol{\delta}_{p+1}-\boldsymbol{\delta}_p)}\right)\left(\frac{1}{3} e^{-i\mathbf{q}\cdot\boldsymbol{\delta}_{p'}} + \alpha_1 (-1)^{p'-1} e^{-i\mathbf{q}\cdot\boldsymbol{\delta}_{p'+1}} e^{i\mathbf{k}'\cdot(\boldsymbol{\delta}_{p'+1}-\boldsymbol{\delta}_{p'})}\right)$$
$$\times\, c^\dagger_{j,\sigma,\mathbf{k}} c_{j,\sigma,\mathbf{k}+\mathbf{q}} c^\dagger_{j',\sigma',\mathbf{k}'} c_{j',\sigma',\mathbf{k}'-\mathbf{q}}$$

$$
\begin{aligned}
\rightarrow U^{(1)}_{\mathbf{q}+\mathbf{G}} \propto & \sum_{\mathbf{k},\mathbf{k}',\mathbf{q}} \Big(\frac{1}{3}e^{i(\mathbf{q}+\mathbf{G})\cdot\boldsymbol{\delta}_p} + \alpha_1(-1)^{p-1}e^{i(\mathbf{q}+\mathbf{G})\cdot\boldsymbol{\delta}_{p+1}}e^{i\mathbf{k}\cdot(\boldsymbol{\delta}_{p+1}-\boldsymbol{\delta}_p)}\Big)c^\dagger_{j,\sigma,\mathbf{k}}c_{j,\sigma,\mathbf{k}+(\mathbf{q}+\mathbf{G})} \\
& \times \Big(\frac{1}{3}e^{-i(\mathbf{q}+\mathbf{G})\cdot\boldsymbol{\delta}_{p'}} + \alpha_1(-1)^{p'-1}e^{-i(\mathbf{q}+\mathbf{G})\cdot\boldsymbol{\delta}_{p'+1}}e^{i\mathbf{k}'\cdot(\boldsymbol{\delta}_{p'+1}-\boldsymbol{\delta}_{p'})}\Big)c^\dagger_{j',\sigma',\mathbf{k}'}c_{j',\sigma',\mathbf{k}'-(\mathbf{q}+\mathbf{G})} \\
= & \sum_{\mathbf{k},\mathbf{k}',\mathbf{q}} \Big(\frac{1}{3}e^{i(\mathbf{q}+\mathbf{G})\cdot\boldsymbol{\delta}_p}c^\dagger_{j,\sigma,\mathbf{k}}e^{-i\mathbf{G}\boldsymbol{\delta}_p}c_{j,\sigma,\mathbf{k}+\mathbf{q}} + \alpha_1(-1)^{p-1}e^{i(\mathbf{q}+\mathbf{G})\cdot\boldsymbol{\delta}_{p+1}}e^{i\mathbf{k}\cdot(\boldsymbol{\delta}_{p+1}-\boldsymbol{\delta}_p)}c^\dagger_{j,\sigma,\mathbf{k}}e^{-i\mathbf{G}\boldsymbol{\delta}_{p+1}}c_{j,\sigma,\mathbf{k}+\mathbf{q}}\Big) \\
& \times \Big(\frac{1}{3}e^{-i(\mathbf{q}+\mathbf{G})\cdot\boldsymbol{\delta}_{p'}}c^\dagger_{j',\sigma',\mathbf{k}'}e^{i\mathbf{G}\boldsymbol{\delta}_{p'}}c_{j',\sigma',\mathbf{k}'-\mathbf{q}} + \alpha_1(-1)^{p'-1}e^{-i(\mathbf{q}+\mathbf{G})\cdot\boldsymbol{\delta}_{p'+1}}e^{i\mathbf{k}'\cdot(\boldsymbol{\delta}_{p'+1}-\boldsymbol{\delta}_{p'})}c^\dagger_{j',\sigma',\mathbf{k}'}e^{i\mathbf{G}\boldsymbol{\delta}_{p'+1}}c_{j',\sigma',\mathbf{k}'-\mathbf{q}}\Big) \\
= & \sum_{\mathbf{k},\mathbf{k}',\mathbf{q}} \Big(\frac{1}{3}e^{i\mathbf{q}\cdot\boldsymbol{\delta}_p} + \alpha_1(-1)^{p-1}e^{i\mathbf{q}\cdot\boldsymbol{\delta}_{p+1}}e^{i\mathbf{k}\cdot(\boldsymbol{\delta}_{p+1}-\boldsymbol{\delta}_p)}\Big)\Big(\frac{1}{3}e^{-i\mathbf{q}\cdot\boldsymbol{\delta}_{p'}} + \alpha_1(-1)^{p'-1}e^{-i\mathbf{q}\cdot\boldsymbol{\delta}_{p'+1}}e^{i\mathbf{k}'\cdot(\boldsymbol{\delta}_{p'+1}-\boldsymbol{\delta}_{p'})}\Big) \\
& \times c^\dagger_{j,\sigma,\mathbf{k}}c_{j,\sigma,\mathbf{k}+\mathbf{q}}c^\dagger_{j',\sigma',\mathbf{k}'}c_{j',\sigma',\mathbf{k}'-\mathbf{q}}
\end{aligned}
\tag{C.2}
$$

$$
\begin{aligned}
U^{(2)}_{\mathbf{q}} \propto & \sum_{\mathbf{k},\mathbf{k}',\mathbf{q}} \Big(\alpha_1(-1)^{p-1}e^{-i\mathbf{q}\cdot\boldsymbol{\delta}_{p+1}}e^{-i\mathbf{k}\cdot(\boldsymbol{\delta}_{p+1}-\boldsymbol{\delta}_p)}\Big)\Big(\frac{1}{3}e^{i\mathbf{q}\cdot\boldsymbol{\delta}_{p'}} + \alpha_1(-1)^{p'-1}e^{i\mathbf{q}\cdot\boldsymbol{\delta}_{p'+1}}e^{i\mathbf{k}'\cdot(\boldsymbol{\delta}_{p'+1}-\boldsymbol{\delta}_{p'})}\Big) \\
& \times c^\dagger_{j,\sigma,\mathbf{k}+\mathbf{q}}c_{j,\sigma,\mathbf{k}}c^\dagger_{j',\sigma',\mathbf{k}'}c_{j',\sigma',\mathbf{k}'+\mathbf{q}} \\
\rightarrow U^{(2)}_{\mathbf{q}+\mathbf{G}} \propto & \sum_{\mathbf{k},\mathbf{k}',\mathbf{q}} \Big(\alpha_1(-1)^{p-1}e^{-i(\mathbf{q}+\mathbf{G})\cdot\boldsymbol{\delta}_{p+1}}e^{-i\mathbf{k}\cdot(\boldsymbol{\delta}_{p+1}-\boldsymbol{\delta}_p)}\Big)c^\dagger_{j,\sigma,\mathbf{k}+(\mathbf{q}+\mathbf{G})}c_{j,\sigma,\mathbf{k}} \\
& \times \Big(\frac{1}{3}e^{i(\mathbf{q}+\mathbf{G})\cdot\boldsymbol{\delta}_{p'}} + \alpha_1(-1)^{p'-1}e^{i(\mathbf{q}+\mathbf{G})\cdot\boldsymbol{\delta}_{p'+1}}e^{i\mathbf{k}'\cdot(\boldsymbol{\delta}_{p'+1}-\boldsymbol{\delta}_{p'})}\Big)c^\dagger_{j',\sigma',\mathbf{k}'}c_{j',\sigma',\mathbf{k}'+(\mathbf{q}+\mathbf{G})} \\
= & \sum_{\mathbf{k},\mathbf{k}',\mathbf{q}} \Big(\alpha_1(-1)^{p-1}e^{-i(\mathbf{q}+\mathbf{G})\cdot\boldsymbol{\delta}_{p+1}}e^{-i\mathbf{k}\cdot(\boldsymbol{\delta}_{p+1}-\boldsymbol{\delta}_p)}\Big)e^{i\mathbf{G}\boldsymbol{\delta}_{p+1}}c^\dagger_{j,\sigma,\mathbf{k}+\mathbf{q}}c_{j,\sigma,\mathbf{k}} \\
& \times \Big(\frac{1}{3}e^{i(\mathbf{q}+\mathbf{G})\cdot\boldsymbol{\delta}_{p'}}c^\dagger_{j',\sigma',\mathbf{k}'}e^{-i\mathbf{G}\boldsymbol{\delta}_{p'}}c_{j',\sigma',\mathbf{k}'+} + \alpha_1(-1)^{p'-1}e^{i(\mathbf{q}+\mathbf{G})\cdot\boldsymbol{\delta}_{p'+1}}e^{i\mathbf{k}'\cdot(\boldsymbol{\delta}_{p'+1}-\boldsymbol{\delta}_{p'})}c^\dagger_{j',\sigma',\mathbf{k}'}e^{-i\mathbf{G}\boldsymbol{\delta}_{p'+1}}c_{j',\sigma',\mathbf{k}'+\mathbf{q}}\Big) \\
= & \sum_{\mathbf{k},\mathbf{k}',\mathbf{q}} \Big(\alpha_1(-1)^{p-1}e^{-i\mathbf{q}\cdot\boldsymbol{\delta}_{p+1}}e^{-i\mathbf{k}\cdot(\boldsymbol{\delta}_{p+1}-\boldsymbol{\delta}_p)}\Big)\Big(\frac{1}{3}e^{i\mathbf{q}\cdot\boldsymbol{\delta}_{p'}} + \alpha_1(-1)^{p'-1}e^{i\mathbf{q}\cdot\boldsymbol{\delta}_{p'+1}}e^{i\mathbf{k}'\cdot(\boldsymbol{\delta}_{p'+1}-\boldsymbol{\delta}_{p'})}\Big) \\
& \times c^\dagger_{j,\sigma,\mathbf{k}+\mathbf{q}}c_{j,\sigma,\mathbf{k}}c^\dagger_{j',\sigma',\mathbf{k}'}c_{j',\sigma',\mathbf{k}'+\mathbf{q}}
\end{aligned}
\tag{C.3}
$$

$$
\begin{aligned}
U^{(3)}_{\mathbf{q}} \propto & \sum_{\mathbf{k},\mathbf{k}',\mathbf{q}} \Big(\frac{1}{3}e^{i\mathbf{q}\cdot\boldsymbol{\delta}_p} + \alpha_1(-1)^{p-1}e^{i\mathbf{q}\cdot\boldsymbol{\delta}_{p+1}}e^{i\mathbf{k}\cdot(\boldsymbol{\delta}_{p+1}-\boldsymbol{\delta}_p)}\Big)\Big(\alpha_1(-1)^{p'-1}e^{-i\mathbf{q}\cdot\boldsymbol{\delta}_{p'+1}}e^{-i\mathbf{k}'\cdot(\boldsymbol{\delta}_{p'+1}-\boldsymbol{\delta}_{p'})}\Big) \\
& \times c^\dagger_{j,\sigma,\mathbf{k}}c_{j,\sigma,\mathbf{k}+\mathbf{q}}c^\dagger_{j',\sigma',\mathbf{k}'+\mathbf{q}}c_{j',\sigma',\mathbf{k}'} \\
\rightarrow U^{(3)}_{\mathbf{q}+\mathbf{G}} \propto & \sum_{\mathbf{k},\mathbf{k}',\mathbf{q}} \Big(\frac{1}{3}e^{i(\mathbf{q}+\mathbf{G})\cdot\boldsymbol{\delta}_p} + \alpha_1(-1)^{p-1}e^{i(\mathbf{q}+\mathbf{G})\cdot\boldsymbol{\delta}_{p+1}}e^{i\mathbf{k}\cdot(\boldsymbol{\delta}_{p+1}-\boldsymbol{\delta}_p)}\Big)c^\dagger_{j,\sigma,\mathbf{k}}c_{j,\sigma,\mathbf{k}+(\mathbf{q}+\mathbf{G})} \\
& \times \Big(\alpha_1(-1)^{p'-1}e^{-i(\mathbf{q}+\mathbf{G})\cdot\boldsymbol{\delta}_{p'+1}}e^{-i\mathbf{k}'\cdot(\boldsymbol{\delta}_{p'+1}-\boldsymbol{\delta}_{p'})}\Big)c^\dagger_{j',\sigma',\mathbf{k}'+(\mathbf{q}+\mathbf{G})}c_{j',\sigma',\mathbf{k}'} \\
= & \sum_{\mathbf{k},\mathbf{k}',\mathbf{q}} \Big(\frac{1}{3}e^{i(\mathbf{q}+\mathbf{G})\cdot\boldsymbol{\delta}_p}c^\dagger_{j,\sigma,\mathbf{k}}e^{-i\mathbf{G}\boldsymbol{\delta}_p}c_{j,\sigma,\mathbf{k}+\mathbf{q}} + \alpha_1(-1)^{p-1}e^{i(\mathbf{q}+\mathbf{G})\cdot\boldsymbol{\delta}_{p+1}}e^{i\mathbf{k}\cdot(\boldsymbol{\delta}_{p+1}-\boldsymbol{\delta}_p)}c^\dagger_{j,\sigma,\mathbf{k}}e^{-i\mathbf{G}\boldsymbol{\delta}_{p+1}}c_{j,\sigma,\mathbf{k}+\mathbf{q}}\Big) \\
& \times \Big(\alpha_1(-1)^{p'-1}e^{-i(\mathbf{q}+\mathbf{G})\cdot\boldsymbol{\delta}_{p'+1}}e^{-i\mathbf{k}'\cdot(\boldsymbol{\delta}_{p'+1}-\boldsymbol{\delta}_{p'})}\Big)e^{i\mathbf{G}\boldsymbol{\delta}_{p'+1}}c^\dagger_{j',\sigma',\mathbf{k}'+\mathbf{q}}c_{j',\sigma',\mathbf{k}'} \\
= & \sum_{\mathbf{k},\mathbf{k}',\mathbf{q}} \Big(\frac{1}{3}e^{i\mathbf{q}\cdot\boldsymbol{\delta}_p} + \alpha_1(-1)^{p-1}e^{i\mathbf{q}\cdot\boldsymbol{\delta}_{p+1}}e^{i\mathbf{k}\cdot(\boldsymbol{\delta}_{p+1}-\boldsymbol{\delta}_p)}\Big)\Big(\alpha_1(-1)^{p'-1}e^{-i\mathbf{q}\cdot\boldsymbol{\delta}_{p'+1}}e^{-i\mathbf{k}'\cdot(\boldsymbol{\delta}_{p'+1}-\boldsymbol{\delta}_{p'})}\Big) \\
& \times c^\dagger_{j,\sigma,\mathbf{k}}c_{j,\sigma,\mathbf{k}+\mathbf{q}}c^\dagger_{j',\sigma',\mathbf{k}'+\mathbf{q}}c_{j',\sigma',\mathbf{k}'}
\end{aligned}
\tag{C.4}
$$

$$
\begin{aligned}
U^{(4)}_{\mathbf{q}} \propto \sum_{\mathbf{k},\mathbf{k}',\mathbf{q}} & \Big(\alpha_1(-1)^{p-1} e^{-i\mathbf{q}\cdot\boldsymbol{\delta}_{p+1}} e^{-i\mathbf{k}\cdot(\boldsymbol{\delta}_{p+1}-\boldsymbol{\delta}_p)}\Big)\Big(\alpha_1(-1)^{p'-1} e^{i\mathbf{q}\cdot\boldsymbol{\delta}_{p'+1}} e^{-i\mathbf{k}'\cdot(\boldsymbol{\delta}_{p'+1}-\boldsymbol{\delta}_{p'})}\Big) \\
& \times c^\dagger_{j,\sigma,\mathbf{k}+\mathbf{q}} c_{j,\sigma,\mathbf{k}} c^\dagger_{j',\sigma',\mathbf{k}'-\mathbf{q}} c_{j',\sigma',\mathbf{k}'}\Big) \\
\rightarrow U^{(4)}_{\mathbf{q}+\mathbf{G}} \propto \sum_{\mathbf{k},\mathbf{k}',\mathbf{q}} & \Big(\alpha_1(-1)^{p-1} e^{-i(\mathbf{q}+\mathbf{G})\cdot\boldsymbol{\delta}_{p+1}} e^{-i\mathbf{k}\cdot(\boldsymbol{\delta}_{p+1}-\boldsymbol{\delta}_p)}\Big) c^\dagger_{j,\sigma,\mathbf{k}+(\mathbf{q}+\mathbf{G})} c_{j,\sigma,\mathbf{k}} \\
& \times \Big(\alpha_1(-1)^{p'-1} e^{i(\mathbf{q}+\mathbf{G})\cdot\boldsymbol{\delta}_{p'+1}} e^{-i\mathbf{k}'\cdot(\boldsymbol{\delta}_{p'+1}-\boldsymbol{\delta}_{p'})}\Big) c^\dagger_{j',\sigma',\mathbf{k}'-(\mathbf{q}+\mathbf{G})} c_{j',\sigma',\mathbf{k}'}\Big) \\
= \sum_{\mathbf{k},\mathbf{k}',\mathbf{q}} & \Big(\alpha_1(-1)^{p-1} e^{-i(\mathbf{q}+\mathbf{G})\cdot\boldsymbol{\delta}_{p+1}} e^{-i\mathbf{k}\cdot(\boldsymbol{\delta}_{p+1}-\boldsymbol{\delta}_p)}\Big) e^{i\mathbf{G}\boldsymbol{\delta}_{p+1}} c^\dagger_{j,\sigma,\mathbf{k}+\mathbf{q}} c_{j,\sigma,\mathbf{k}} \\
& \times \Big(\alpha_1(-1)^{p'-1} e^{i(\mathbf{q}+\mathbf{G})\cdot\boldsymbol{\delta}_{p'+1}} e^{-i\mathbf{k}'\cdot(\boldsymbol{\delta}_{p'+1}-\boldsymbol{\delta}_{p'})}\Big) e^{-i\mathbf{G}\boldsymbol{\delta}_{p'+1}} c^\dagger_{j',\sigma',\mathbf{k}'-\mathbf{q}} c_{j',\sigma',\mathbf{k}'}\Big) \\
= \sum_{\mathbf{k},\mathbf{k}',\mathbf{q}} & \Big(\alpha_1(-1)^{p-1} e^{-i\mathbf{q}\cdot\boldsymbol{\delta}_{p+1}} e^{-i\mathbf{k}\cdot(\boldsymbol{\delta}_{p+1}-\boldsymbol{\delta}_p)}\Big)\Big(\alpha_1(-1)^{p'-1} e^{i\mathbf{q}\cdot\boldsymbol{\delta}_{p'+1}} e^{-i\mathbf{k}'\cdot(\boldsymbol{\delta}_{p'+1}-\boldsymbol{\delta}_{p'})}\Big) \\
& \times c^\dagger_{j,\sigma,\mathbf{k}+\mathbf{q}} c_{j,\sigma,\mathbf{k}} c^\dagger_{j',\sigma',\mathbf{k}'-\mathbf{q}} c_{j',\sigma',\mathbf{k}'}\Big)
\end{aligned}
\tag{C.5}
$$

The results are general and do not depend on either $\mathbf{k}, \mathbf{k}'$, $\mathbf{q}$ or $\mathbf{G}$. With the knowledge that folding of one term is independent of folding in the three remaining terms, we can reduce our further investigation of folding effects of the shifted terms to the second and third term. We drop valley and spin indices for readability.

$$
\begin{aligned}
U^{(2)}_{\mathbf{q}} \propto \sum_{\mathbf{k},\tilde{\mathbf{k}},\mathbf{q}} & \Big(\frac{1}{3} e^{i\mathbf{q}\cdot\boldsymbol{\delta}_p} + \alpha_1(-1)^{p-1} e^{i\mathbf{q}\cdot\boldsymbol{\delta}_{p+1}} e^{i\mathbf{k}\cdot(\boldsymbol{\delta}_{p+1}-\boldsymbol{\delta}_p)}\Big)\Big(\alpha_1(-1)^{p'-1} e^{-i\mathbf{q}\cdot\boldsymbol{\delta}_{p'+1}} e^{-i(\tilde{\mathbf{k}}-\mathbf{q})\cdot(\boldsymbol{\delta}_{p'+1}-\boldsymbol{\delta}_{p'})}\Big) c^\dagger_{\mathbf{k}+\mathbf{q}} c_{\mathbf{k}} c^\dagger_{\tilde{\mathbf{k}}-\mathbf{q}} c_{\tilde{\mathbf{k}}} \\
\rightarrow U^{(2)}_{\mathbf{q}+\mathbf{G}} \propto \sum_{\mathbf{k},\tilde{\mathbf{k}},\mathbf{q}} & \Big(\alpha_1(-1)^{p-1} e^{-i(\mathbf{q}+\mathbf{G})\cdot\boldsymbol{\delta}_{p+1}} e^{-i\mathbf{k}\cdot(\boldsymbol{\delta}_{p+1}-\boldsymbol{\delta}_p)}\Big) c^\dagger_{\mathbf{k}+(\mathbf{q}+\mathbf{G})} c_{\mathbf{k}} \\
& \times \Big(\frac{1}{3} e^{i(\mathbf{q}+\mathbf{G})\cdot\boldsymbol{\delta}_{p'}} + \alpha_1(-1)^{p'-1} e^{i(\mathbf{q}+\mathbf{G})\cdot\boldsymbol{\delta}_{p'+1}} e^{i(\tilde{\mathbf{k}}-\mathbf{q}-\mathbf{G})\cdot(\boldsymbol{\delta}_{p'+1}-\boldsymbol{\delta}_{p'})}\Big) c^\dagger_{\tilde{\mathbf{k}}-\mathbf{q}-\mathbf{G}} c_{\tilde{\mathbf{k}}} \\
= \sum_{\mathbf{k},\tilde{\mathbf{k}},\mathbf{q}} & \Big(\alpha_1(-1)^{p-1} e^{-i\mathbf{q}\cdot\boldsymbol{\delta}_{p+1}} e^{-i\mathbf{k}\cdot(\boldsymbol{\delta}_{p+1}-\boldsymbol{\delta}_p)}\Big) c^\dagger_{\mathbf{k}+\mathbf{q}} c_{\mathbf{k}} \\
& \times \Big(\frac{1}{3} e^{i(\mathbf{q}+\mathbf{G})\cdot\boldsymbol{\delta}_{p'}} + \alpha_1(-1)^{p'-1} e^{i\mathbf{q}\cdot\boldsymbol{\delta}_{p'+1}} e^{i\mathbf{G}\cdot\boldsymbol{\delta}_{p'}} e^{i(\tilde{\mathbf{k}}-\mathbf{q})\cdot(\boldsymbol{\delta}_{p'+1}-\boldsymbol{\delta}_{p'})}\Big) c^\dagger_{\tilde{\mathbf{k}}-\mathbf{q}-\mathbf{G}} c_{\tilde{\mathbf{k}}} \\
= \sum_{\mathbf{k},\tilde{\mathbf{k}},\mathbf{q}} & \Big(\alpha_1(-1)^{p-1} e^{-i\mathbf{q}\cdot\boldsymbol{\delta}_{p+1}} e^{-i\mathbf{k}\cdot(\boldsymbol{\delta}_{p+1}-\boldsymbol{\delta}_p)}\Big) c^\dagger_{\mathbf{k}+\mathbf{q}} c_{\mathbf{k}} \\
& \times \Big(\frac{1}{3} e^{i(\mathbf{q}+\mathbf{G})\cdot\boldsymbol{\delta}_{p'}} + \alpha_1(-1)^{p'-1} e^{i\mathbf{q}\cdot\boldsymbol{\delta}_{p'+1}} e^{i\mathbf{G}\cdot\boldsymbol{\delta}_{p'}} e^{i(\tilde{\mathbf{k}}-\mathbf{q})\cdot(\boldsymbol{\delta}_{p'+1}-\boldsymbol{\delta}_{p'})}\Big) e^{-i\mathbf{G}\cdot\boldsymbol{\delta}_{p'}} c^\dagger_{\tilde{\mathbf{k}}-\mathbf{q}} c_{\tilde{\mathbf{k}}} \\
= \sum_{\mathbf{k},\tilde{\mathbf{k}},\mathbf{q}} & \Big(\alpha_1(-1)^{p-1} e^{-i\mathbf{q}\cdot\boldsymbol{\delta}_{p+1}} e^{-i\mathbf{k}\cdot(\boldsymbol{\delta}_{p+1}-\boldsymbol{\delta}_p)}\Big)\Big(\frac{1}{3} e^{i\mathbf{q}\cdot\boldsymbol{\delta}_{p'}} + \alpha_1(-1)^{p'-1} e^{i\mathbf{q}\cdot\boldsymbol{\delta}_{p'+1}} e^{i(\tilde{\mathbf{k}}-\mathbf{q})\cdot(\boldsymbol{\delta}_{p'+1}-\boldsymbol{\delta}_{p'})}\Big) \\
& \times c^\dagger_{\mathbf{k}+\mathbf{q}} c_{\mathbf{k}} c^\dagger_{\tilde{\mathbf{k}}-\mathbf{q}} c_{\tilde{\mathbf{k}}}
\end{aligned}
\tag{C.6}
$$

where the phase from the annihilation operator in the last two terms are identical. This can be verified by going back to the original real space definitions in Eq. (5.18). The result is independent of $\mathbf{G}$, hence there is no consequence of folding with different reciprocal vectors as

illustrated in Fig. C.2.
Comparing to Eq. (C.3) it is clear that this resembles the first case, hence it is possible to let $\mathbf{k}' \to \tilde{\mathbf{k}} - \mathbf{q}$ without additional phases. For completeness we repeat the calculation for third term.

$$
\begin{aligned}
U^{(3)}_{\mathbf{q}} &\propto \sum_{\mathbf{k},\tilde{\mathbf{k}},\mathbf{q}} \left(\frac{1}{3} e^{i\mathbf{q}\cdot\boldsymbol{\delta}_p} + \alpha_1 (-1)^{p-1} e^{i\mathbf{q}\cdot\boldsymbol{\delta}_{p+1}} e^{i\mathbf{k}\cdot(\boldsymbol{\delta}_{p+1}-\boldsymbol{\delta}_p)}\right)\left(\alpha_1 (-1)^{p'-1} e^{-i\mathbf{q}\cdot\boldsymbol{\delta}_{p'+1}} e^{-i(\tilde{\mathbf{k}}-\mathbf{q})\cdot(\boldsymbol{\delta}_{p'+1}-\boldsymbol{\delta}_{p'})}\right) c^\dagger_{\mathbf{k}} c_{\mathbf{k}+\mathbf{q}} c^\dagger_{\tilde{\mathbf{k}}} c_{\tilde{\mathbf{k}}-\mathbf{q}} \\
\to U^{(3)}_{\mathbf{q}+\mathbf{G}} &\propto \sum_{\mathbf{k},\tilde{\mathbf{k}},\mathbf{q}} \left(\frac{1}{3} e^{i(\mathbf{q}+\mathbf{G})\cdot\boldsymbol{\delta}_p} + \alpha_1 (-1)^{p-1} e^{i(\mathbf{q}+\mathbf{G})\cdot\boldsymbol{\delta}_{p+1}} e^{i\mathbf{k}\cdot(\boldsymbol{\delta}_{p+1}-\boldsymbol{\delta}_p)}\right) c^\dagger_{\mathbf{k}} c_{\mathbf{k}+\mathbf{q}+\mathbf{G}} \\
&\qquad \times \left(\alpha_1 (-1)^{p'-1} e^{-i(\mathbf{q}+\mathbf{G})\cdot\boldsymbol{\delta}_{p'+1}} e^{-i(\tilde{\mathbf{k}}-\mathbf{q}-\mathbf{G})\cdot(\boldsymbol{\delta}_{p'+1}-\boldsymbol{\delta}_{p'})}\right) c^\dagger_{\tilde{\mathbf{k}}} c_{\tilde{\mathbf{k}}-\mathbf{q}-\mathbf{G}} \\
&= \sum_{\mathbf{k},\tilde{\mathbf{k}},\mathbf{q}} \left(\frac{1}{3} e^{i\mathbf{q}\cdot\boldsymbol{\delta}_p} + \alpha_1 (-1)^{p-1} e^{i\mathbf{q}\cdot\boldsymbol{\delta}_{p+1}} e^{i\mathbf{k}\cdot(\boldsymbol{\delta}_{p+1}-\boldsymbol{\delta}_p)}\right) c^\dagger_{\mathbf{k}} c_{\mathbf{k}+\mathbf{q}} \\
&\qquad \times \left(\alpha_1 (-1)^{p'-1} e^{-i\mathbf{q}\cdot\boldsymbol{\delta}_{p'+1}} e^{-i\mathbf{G}\cdot\boldsymbol{\delta}_{p'}} e^{-i(\tilde{\mathbf{k}}-\mathbf{q})\cdot(\boldsymbol{\delta}_{p'+1}-\boldsymbol{\delta}_{p'})}\right) c^\dagger_{\tilde{\mathbf{k}}} e^{i\mathbf{G}\cdot\boldsymbol{\delta}_{p'}} c_{\tilde{\mathbf{k}}-\mathbf{q}} \\
&= \sum_{\mathbf{k},\tilde{\mathbf{k}},\mathbf{q}} \left(\frac{1}{3} e^{i\mathbf{q}\cdot\boldsymbol{\delta}_p} + \alpha_1 (-1)^{p-1} e^{i\mathbf{q}\cdot\boldsymbol{\delta}_{p+1}} e^{i\mathbf{k}\cdot(\boldsymbol{\delta}_{p+1}-\boldsymbol{\delta}_p)}\right)\left(\alpha_1 (-1)^{p'-1} e^{-i\mathbf{q}\cdot\boldsymbol{\delta}_{p'+1}} e^{-i(\tilde{\mathbf{k}}-\mathbf{q})\cdot(\boldsymbol{\delta}_{p'+1}-\boldsymbol{\delta}_{p'})}\right) c^\dagger_{\mathbf{k}} c_{\mathbf{k}+\mathbf{q}} c^\dagger_{\tilde{\mathbf{k}}} c_{\tilde{\mathbf{k}}-\mathbf{q}}.
\end{aligned}
\tag{C.7}
$$

The conclusion remains. We can perform the shift on the second and third term with no additional phases arising and no ambiguity between shifted and non-shifted terms. In the proceeding we rename $\tilde{\mathbf{k}} \to \mathbf{k}'$.

Appendix D

Interaction model in the Bravais lattice picture

To represent U^{HF} in the $\mathbf{f}^\dagger_{\mathbf{k}}$ basis, we must return to the original real space representation of U which reads,

$$U = \frac{V_0}{2}\sum_{\mathbf{R}}\sum_{j,j'}\sum_{\sigma,\sigma'}\left(\frac{1}{3}Q_{j,\sigma}(\mathbf{R}) + \alpha_1 T_{j,\sigma}(\mathbf{R})\right)\left(\frac{1}{3}Q_{j',\sigma'}(\mathbf{R}) + \alpha_1 T_{j',\sigma'}(\mathbf{R})\right), \quad \text{where} \tag{D.1}$$

$$Q_{j,\sigma}(\mathbf{R}) = \sum_{p=1}^{6} d^\dagger_{j,\sigma}(\mathbf{R}+\boldsymbol{\delta}_p)d_{j,\sigma}(\mathbf{R}+\boldsymbol{\delta}_p), \qquad \text{and}$$

$$T_{j,\sigma}(\mathbf{R}) = \sum_{p=1}^{6}(-1)^{p-1}\Big(d^\dagger_{j,\sigma}(\mathbf{R}+\boldsymbol{\delta}_p)d_{j,\sigma}(\mathbf{R}+\boldsymbol{\delta}_{p+1}) + h.c.\Big).$$

$\mathbf{R}$ is the center of each honeycomb thus $\mathbf{R}_i$ of the tight-binding model and $\mathbf{R}$ are identical. By inspecting Figs. 4.5 and 4.8, we can identify $p = 1, 3, 5$ as BA-sites and $p = 2, 4, 6$ as AB-sites (represented by b-operators and a-operators, respectively).
We thus have,

$$\begin{aligned} Q_{j,\sigma}(\mathbf{R}) &= \sum_{p\,\text{even}} a^\dagger_{j,\sigma}(\mathbf{R}+\boldsymbol{\delta}_p)a_{j,\sigma}(\mathbf{R}+\boldsymbol{\delta}_p) + \sum_{p\,\text{odd}} b^\dagger_{j,\sigma}(\mathbf{R}+\boldsymbol{\delta}_p)b_{j,\sigma}(\mathbf{R}+\boldsymbol{\delta}_p) \\ &= \sum_{p=2,4,6}(a^\dagger_{j,\sigma}(\mathbf{R}+\boldsymbol{\delta}_p)a_{j,\sigma}(\mathbf{R}+\boldsymbol{\delta}_p) + b^\dagger_{j,\sigma}(\mathbf{R}+\boldsymbol{\delta}_{p+1})b_{j,\sigma}(\mathbf{R}+\boldsymbol{\delta}_{p+1})), \end{aligned} \tag{D.2}$$

and,

$$\begin{aligned} T_{j,\sigma}(\mathbf{R}) &= -\sum_{p\,\text{even}}\Big(a^\dagger_{j,\sigma}(\mathbf{R}+\boldsymbol{\delta}_p)b_{j,\sigma}(\mathbf{R}+\boldsymbol{\delta}_{p+1}) + h.c.\Big) + \sum_{p\,\text{odd}}\Big(b^\dagger_{j,\sigma}(\mathbf{R}+\boldsymbol{\delta}_p)a_{j,\sigma}(\mathbf{R}+\boldsymbol{\delta}_{p+1}) + h.c.\Big) \\ &= \sum_{p=2,4,6}\Big[-a^\dagger_{j,\sigma}(\mathbf{R}+\boldsymbol{\delta}_p)b_{j,\sigma}(\mathbf{R}+\boldsymbol{\delta}_{p+1}) + b^\dagger_{j,\sigma}(\mathbf{R}+\boldsymbol{\delta}_{p+1})a_{j,\sigma}(\mathbf{R}+\boldsymbol{\delta}_{p+2}) + h.c.\Big] \end{aligned} \tag{D.3}$$

Note the periodic boundary conditions. Using the same Fourier transformations as in Eq. (4.11) with $\boldsymbol{\alpha}$ replaced by the $\boldsymbol{\delta}$ in question, we have

$$\begin{aligned} Q_{j,\sigma}(\mathbf{R}) &= \frac{1}{N}\sum_{\mathbf{k},\mathbf{k}'}\sum_{p=2,4,6}\big(e^{-i\mathbf{k}(\mathbf{R}+\boldsymbol{\delta}_p)}e^{i\mathbf{k}'(\mathbf{R}+\boldsymbol{\delta}_p)}a^\dagger_{j\sigma\mathbf{k}}a_{j\sigma\mathbf{k}'} + e^{-i\mathbf{k}(\mathbf{R}+\boldsymbol{\delta}_{p+1})}e^{i\mathbf{k}'(\mathbf{R}+\boldsymbol{\delta}_{p+1})}b^\dagger_{j\sigma\mathbf{k}}b_{j\sigma\mathbf{k}'}\big) \\ &= \frac{1}{N}\sum_{\mathbf{k},\mathbf{q}}\sum_{p=2,4,6}\big(e^{i\mathbf{q}(\mathbf{R}+\boldsymbol{\delta}_p)}a^\dagger_{j\sigma\mathbf{k}}a_{j\sigma\mathbf{k}+\mathbf{q}} + e^{i\mathbf{q}(\mathbf{R}+\boldsymbol{\delta}_{p+1})}b^\dagger_{j\sigma\mathbf{k}}b_{j\sigma\mathbf{k}+\mathbf{q}}\big), \qquad \text{and,} \end{aligned}$$

$$
\begin{aligned}
T_{j,\sigma}(\mathbf{R}) = \frac{1}{N}\sum_{\mathbf{k},\mathbf{k}'}\sum_{p=2,4,6}\big(& - e^{-i\mathbf{k}(\mathbf{R}+\boldsymbol{\delta}_p)}e^{i\mathbf{k}'(\mathbf{R}+\boldsymbol{\delta}_{p+1})}a^\dagger_{j\sigma\mathbf{k}}b_{j\sigma\mathbf{k}'} - e^{i\mathbf{k}(\mathbf{R}+\boldsymbol{\delta}_p)}e^{-i\mathbf{k}'(\mathbf{R}+\boldsymbol{\delta}_{p+1})}b^\dagger_{j\sigma\mathbf{k}'}a_{j\sigma\mathbf{k}} \\
& + e^{-i\mathbf{k}'(\mathbf{R}+\boldsymbol{\delta}_{p+1})}e^{i\mathbf{k}(\mathbf{R}+\boldsymbol{\delta}_{p+2})}b^\dagger_{j\sigma\mathbf{k}'}a_{j\sigma\mathbf{k}} + e^{i\mathbf{k}'(\mathbf{R}+\boldsymbol{\delta}_{p+1})}e^{-i\mathbf{k}(\mathbf{R}+\boldsymbol{\delta}_{p+2})}a^\dagger_{j\sigma\mathbf{k}}b_{j\sigma\mathbf{k}'}\big) \\
= \frac{1}{N}\sum_{\mathbf{k},\mathbf{k}'}\sum_{p=2,4,6}\Big[& \big(e^{i\mathbf{k}'(\mathbf{R}+\boldsymbol{\delta}_{p+1})}e^{-i\mathbf{k}(\mathbf{R}+\boldsymbol{\delta}_{p+2})} - e^{-i\mathbf{k}(\mathbf{R}+\boldsymbol{\delta}_p)}e^{i\mathbf{k}'(\mathbf{R}+\boldsymbol{\delta}_{p+1})}\big)a^\dagger_{j\sigma\mathbf{k}}b_{j\sigma\mathbf{k}'} \\
& + \big(e^{-i\mathbf{k}'(\mathbf{R}+\boldsymbol{\delta}_{p+1})}e^{i\mathbf{k}(\mathbf{R}+\boldsymbol{\delta}_{p+2})} - e^{i\mathbf{k}(\mathbf{R}+\boldsymbol{\delta}_p)}e^{-i\mathbf{k}'(\mathbf{R}+\boldsymbol{\delta}_{p+1})}\big)b^\dagger_{j\sigma\mathbf{k}'}a_{j\sigma\mathbf{k}}\Big] \\
= \frac{1}{N}\sum_{\mathbf{k},\mathbf{q}}\sum_{p=2,4,6}\Big[& e^{i\mathbf{q}\mathbf{R}}e^{i\mathbf{q}\boldsymbol{\delta}_{p+1}}(e^{i\mathbf{k}(\boldsymbol{\delta}_{p+1}-\boldsymbol{\delta}_{p+2})} - e^{i\mathbf{k}(\boldsymbol{\delta}_{p+1}-\boldsymbol{\delta}_p)})a^\dagger_{j\sigma\mathbf{k}}b_{j\sigma\mathbf{k}+\mathbf{q}} \\
& + e^{-i\mathbf{q}\mathbf{R}}e^{-i\mathbf{q}\boldsymbol{\delta}_{p+1}}(e^{-i\mathbf{k}(\boldsymbol{\delta}_{p+1}-\boldsymbol{\delta}_{p+2})} - e^{-i\mathbf{k}(\boldsymbol{\delta}_{p+1}-\boldsymbol{\delta}_p)})b^\dagger_{j\sigma\mathbf{k}+\mathbf{q}}a_{j\sigma\mathbf{k}}\Big] \\
= \frac{1}{N}\sum_{\mathbf{k},\mathbf{q}}\sum_{p=2,4,6}\Big[& e^{i\mathbf{q}\mathbf{R}}e^{i\mathbf{q}\boldsymbol{\delta}_{p+1}}(e^{i\mathbf{k}\boldsymbol{\delta}_p} - e^{i\mathbf{k}\boldsymbol{\delta}_{p+2}})a^\dagger_{j\sigma\mathbf{k}}b_{j\sigma\mathbf{k}+\mathbf{q}} \\
& + e^{-i\mathbf{q}\mathbf{R}}e^{-i\mathbf{q}\boldsymbol{\delta}_{p+1}}(e^{-i\mathbf{k}\boldsymbol{\delta}_p} - e^{-i\mathbf{k}\boldsymbol{\delta}_{p+2}})b^\dagger_{j\sigma\mathbf{k}+\mathbf{q}}a_{j\sigma\mathbf{k}}\Big]
\end{aligned}
\tag{D.4}
$$

where $\mathbf{q} = \mathbf{k}' - \mathbf{k}$ and N is the number of unit cells. In the last equality we used that $\boldsymbol{\delta}_{p+1} - \boldsymbol{\delta}_p = \boldsymbol{\delta}_{p+2}$. With these expression we obtain,

$$
\begin{aligned}
U = \frac{V_0}{2N^2}\sum_{\mathbf{R}}\sum_{j,j'}\sum_{\sigma,\sigma'}\sum_{\substack{\mathbf{k},\mathbf{k}'\\ \mathbf{q},\mathbf{q}'}}\sum_{p,p'=2,4,6}\Bigg(& \frac{1}{3}\big(e^{i\mathbf{q}(\mathbf{R}+\boldsymbol{\delta}_p)}a^\dagger_{j\sigma\mathbf{k}}a_{j\sigma\mathbf{k}+\mathbf{q}} + e^{i\mathbf{q}(\mathbf{R}+\boldsymbol{\delta}_{p+1})}b^\dagger_{j\sigma\mathbf{k}}b_{j\sigma\mathbf{k}+\mathbf{q}}\big) \\
& + \alpha_1\Big[e^{i\mathbf{q}\mathbf{R}}e^{i\mathbf{q}\boldsymbol{\delta}_{p+1}}(e^{i\mathbf{k}\boldsymbol{\delta}_p} - e^{i\mathbf{k}\boldsymbol{\delta}_{p+2}})a^\dagger_{j\sigma\mathbf{k}}b_{j\sigma\mathbf{k}+\mathbf{q}} \\
& + e^{-i\mathbf{q}\mathbf{R}}e^{-i\mathbf{q}\boldsymbol{\delta}_{p+1}}(e^{-i\mathbf{k}\boldsymbol{\delta}_p} - e^{-i\mathbf{k}\boldsymbol{\delta}_{p+2}})b^\dagger_{j\sigma\mathbf{k}+\mathbf{q}}a_{j\sigma\mathbf{k}}\Big]\Bigg) \\
\times\Bigg(& \frac{1}{3}\big(e^{i\mathbf{q}'(\mathbf{R}+\boldsymbol{\delta}_{p'})}a^\dagger_{j'\sigma'\mathbf{k}'}a_{j'\sigma'\mathbf{k}'+\mathbf{q}'} + e^{i\mathbf{q}'(\mathbf{R}+\boldsymbol{\delta}_{p'+1})}b^\dagger_{j'\sigma'\mathbf{k}'}b_{j'\sigma'\mathbf{k}'+\mathbf{q}'}\big) \\
& + \alpha_1\Big[e^{i\mathbf{q}'\mathbf{R}}e^{i\mathbf{q}'\boldsymbol{\delta}_{p'+1}}(e^{i\mathbf{k}'\boldsymbol{\delta}_{p'}} - e^{i\mathbf{k}'\boldsymbol{\delta}_{p'+2}})a^\dagger_{j'\sigma'\mathbf{k}'}b_{j'\sigma'\mathbf{k}'+\mathbf{q}'} \\
& + e^{-i\mathbf{q}'\mathbf{R}}e^{-i\mathbf{q}'\boldsymbol{\delta}_{p'+1}}(e^{-i\mathbf{k}'\boldsymbol{\delta}_{p'}} - e^{-i\mathbf{k}'\boldsymbol{\delta}_{p'+2}})b^\dagger_{j'\sigma'\mathbf{k}'+\mathbf{q}'}a_{j'\sigma'\mathbf{k}'}\Big]\Bigg).
\end{aligned}
\tag{D.5}
$$

Term by term we get

$$
\begin{aligned}
U_{Q\times Q'} = \frac{V_0}{2N^2}\sum_{\mathbf{R}}\sum_{j,j'}\sum_{\sigma,\sigma'}\sum_{\substack{\mathbf{k},\mathbf{k}'\\ \mathbf{q},\mathbf{q}'}}\sum_{p,p'=2,4,6}\frac{1}{9} & \big(e^{i\mathbf{q}(\mathbf{R}+\boldsymbol{\delta}_p)}a^\dagger_{j\sigma\mathbf{k}}a_{j\sigma\mathbf{k}+\mathbf{q}} + e^{i\mathbf{q}(\mathbf{R}+\boldsymbol{\delta}_{p+1})}b^\dagger_{j\sigma\mathbf{k}}b_{j\sigma\mathbf{k}+\mathbf{q}}\big) \\
& \times\big(e^{i\mathbf{q}'(\mathbf{R}+\boldsymbol{\delta}_{p'})}a^\dagger_{j'\sigma'\mathbf{k}'}a_{j'\sigma'\mathbf{k}'+\mathbf{q}'} + e^{i\mathbf{q}'(\mathbf{R}+\boldsymbol{\delta}_{p'+1})}b^\dagger_{j'\sigma'\mathbf{k}'}b_{j'\sigma'\mathbf{k}'+\mathbf{q}'}\big) \\
= \frac{V_0}{2N^2}\sum_{\mathbf{R}}\sum_{j,j'}\sum_{\sigma,\sigma'}\sum_{\substack{\mathbf{k},\mathbf{k}'\\ \mathbf{q},\mathbf{q}'}}\sum_{p,p'=2,4,6}\frac{1}{9}e^{i(\mathbf{q}+\mathbf{q}')\mathbf{R}}\Big(& e^{i\mathbf{q}\boldsymbol{\delta}_p}e^{i\mathbf{q}'\boldsymbol{\delta}_{p'}}a^\dagger_{j\sigma\mathbf{k}}a_{j\sigma\mathbf{k}+\mathbf{q}}a^\dagger_{j'\sigma'\mathbf{k}'}a_{j'\sigma'\mathbf{k}'+\mathbf{q}'} \\
& + e^{i\mathbf{q}\boldsymbol{\delta}_{p+1}}e^{i\mathbf{q}'\boldsymbol{\delta}_{p'+1}}b^\dagger_{j\sigma\mathbf{k}}b_{j\sigma\mathbf{k}+\mathbf{q}}b^\dagger_{j'\sigma'\mathbf{k}'}b_{j'\sigma'\mathbf{k}'+\mathbf{q}'} \\
& + e^{i\mathbf{q}\boldsymbol{\delta}_p}e^{i\mathbf{q}'\boldsymbol{\delta}_{p'+1}}a^\dagger_{j\sigma\mathbf{k}}a_{j\sigma\mathbf{k}+\mathbf{q}}b^\dagger_{j'\sigma'\mathbf{k}'}b_{j'\sigma'\mathbf{k}'+\mathbf{q}'} \\
& + e^{i\mathbf{q}\boldsymbol{\delta}_{p+1}}e^{i\mathbf{q}'\boldsymbol{\delta}_{p'}}b^\dagger_{j\sigma\mathbf{k}}b_{j\sigma\mathbf{k}+\mathbf{q}}a^\dagger_{j'\sigma'\mathbf{k}'}a_{j'\sigma'\mathbf{k}'+\mathbf{q}'}\Big)
\end{aligned}
\tag{D.6}
$$

Using that $\sum_{\mathbf{R}} e^{i(\mathbf{q}+\mathbf{q}')\mathbf{R}} = \sum_{\mathbf{G}} \delta_{\mathbf{q}',-(\mathbf{q}+\mathbf{G})}$, adopting the result from Eq. (B.5) and performing the same calculations as in Eqs. (B.6), (B.7) one finds,

$$\begin{aligned} U_{Q\times Q'} = \frac{V_0}{2N} \sum_{j,j'} \sum_{\sigma,\sigma'} \sum_{\mathbf{k},\mathbf{k}',\mathbf{q}} \sum_{p,p'=2,4,6} \frac{1}{9} \Big(& e^{i\mathbf{q}(\boldsymbol{\delta}_p - \boldsymbol{\delta}_{p'})} a^\dagger_{j\sigma\mathbf{k}} a_{j\sigma\mathbf{k}+\mathbf{q}} a^\dagger_{j'\sigma'\mathbf{k}'} a_{j'\sigma'\mathbf{k}'-\mathbf{q}} \\ & + e^{i\mathbf{q}(\boldsymbol{\delta}_{p+1} - \boldsymbol{\delta}_{p'+1})} b^\dagger_{j\sigma\mathbf{k}} b_{j\sigma\mathbf{k}+\mathbf{q}} b^\dagger_{j'\sigma'\mathbf{k}'} b_{j'\sigma'\mathbf{k}'-\mathbf{q}} \\ & + e^{i\mathbf{q}(\boldsymbol{\delta}_p - \boldsymbol{\delta}_{p'+1})} a^\dagger_{j\sigma\mathbf{k}} a_{j\sigma\mathbf{k}+\mathbf{q}} b^\dagger_{j'\sigma'\mathbf{k}'} b_{j'\sigma'\mathbf{k}'-\mathbf{q}} \\ & + e^{i\mathbf{q}(\boldsymbol{\delta}_{p+1} - \boldsymbol{\delta}_{p'})} b^\dagger_{j\sigma\mathbf{k}} b_{j\sigma\mathbf{k}+\mathbf{q}} a^\dagger_{j'\sigma'\mathbf{k}'} a_{j'\sigma'\mathbf{k}'-\mathbf{q}} \Big). \end{aligned} \tag{D.7}$$

Proceeding to the next term, we get

$$\begin{aligned} U_{Q\times T'} = & \frac{V_0}{2N^2} \sum_{\mathbf{R}} \sum_{j,j'} \sum_{\sigma,\sigma'} \sum_{\substack{\mathbf{k},\mathbf{k}' \\ \mathbf{q},\mathbf{q}'}} \sum_{p,p'=2,4,6} \frac{\alpha_1}{3} \left(e^{i\mathbf{q}(\mathbf{R}+\boldsymbol{\delta}_p)} a^\dagger_{j\sigma\mathbf{k}} a_{j\sigma\mathbf{k}+\mathbf{q}} + e^{i\mathbf{q}(\mathbf{R}+\boldsymbol{\delta}_{p+1})} b^\dagger_{j\sigma\mathbf{k}} b_{j\sigma\mathbf{k}+\mathbf{q}} \right) \\ & \times \Big[e^{i\mathbf{q}'\mathbf{R}} e^{i\mathbf{q}'\boldsymbol{\delta}_{p'+1}} (e^{i\mathbf{k}'\boldsymbol{\delta}_{p'}} - e^{i\mathbf{k}'\boldsymbol{\delta}_{p'+2}}) a^\dagger_{j'\sigma'\mathbf{k}'} b_{j'\sigma'\mathbf{k}'+\mathbf{q}'} \\ & + e^{-i\mathbf{q}'\mathbf{R}} e^{-i\mathbf{q}'\boldsymbol{\delta}_{p'+1}} (e^{-i\mathbf{k}'\boldsymbol{\delta}_{p'}} - e^{-i\mathbf{k}'\boldsymbol{\delta}_{p'+2}}) b^\dagger_{j'\sigma'\mathbf{k}'+\mathbf{q}'} a_{j'\sigma'\mathbf{k}'} \Big] \\ = & \frac{V_0}{2N^2} \sum_{\mathbf{R}} \sum_{j,j'} \sum_{\sigma,\sigma'} \sum_{\substack{\mathbf{k},\mathbf{k}' \\ \mathbf{q},\mathbf{q}'}} \sum_{p,p'=2,4,6} \frac{\alpha_1}{3} \Bigg(e^{i(\mathbf{q}+\mathbf{q}')\mathbf{R}} \Big[e^{i\mathbf{q}\boldsymbol{\delta}_p} e^{i\mathbf{q}'\boldsymbol{\delta}_{p'+1}} (e^{i\mathbf{k}'\boldsymbol{\delta}_{p'}} - e^{i\mathbf{k}'\boldsymbol{\delta}_{p'+2}}) a^\dagger_{j\sigma\mathbf{k}} a_{j\sigma\mathbf{k}+\mathbf{q}} a^\dagger_{j'\sigma'\mathbf{k}'} b_{j'\sigma'\mathbf{k}'+\mathbf{q}'} \\ & + e^{i\mathbf{q}\boldsymbol{\delta}_{p+1}} e^{i\mathbf{q}'\boldsymbol{\delta}_{p'+1}} (e^{i\mathbf{k}'\boldsymbol{\delta}_{p'}} - e^{i\mathbf{k}'\boldsymbol{\delta}_{p'+2}}) b^\dagger_{j\sigma\mathbf{k}} b_{j\sigma\mathbf{k}+\mathbf{q}} a^\dagger_{j'\sigma'\mathbf{k}'} b_{j'\sigma'\mathbf{k}'+\mathbf{q}'} \Big] \\ & + e^{i(\mathbf{q}-\mathbf{q}')\mathbf{R}} \Big[e^{i\mathbf{q}\boldsymbol{\delta}_p} e^{-i\mathbf{q}'\boldsymbol{\delta}_{p'+1}} (e^{-i\mathbf{k}'\boldsymbol{\delta}_{p'}} - e^{-i\mathbf{k}'\boldsymbol{\delta}_{p'+2}}) a^\dagger_{j\sigma\mathbf{k}} a_{j\sigma\mathbf{k}+\mathbf{q}} b^\dagger_{j'\sigma'\mathbf{k}'+\mathbf{q}'} a_{j'\sigma'\mathbf{k}'} \\ & + e^{i\mathbf{q}\boldsymbol{\delta}_{p+1}} e^{-i\mathbf{q}'\boldsymbol{\delta}_{p'+1}} (e^{-i\mathbf{k}'\boldsymbol{\delta}_{p'}} - e^{-i\mathbf{k}'\boldsymbol{\delta}_{p'+2}}) b^\dagger_{j\sigma\mathbf{k}} b_{j\sigma\mathbf{k}+\mathbf{q}} b^\dagger_{j'\sigma'\mathbf{k}'+\mathbf{q}'} a_{j'\sigma'\mathbf{k}'} \Big] \Bigg) \\ = & \frac{V_0}{2N} \sum_{j,j'} \sum_{\sigma,\sigma'} \sum_{\mathbf{k},\mathbf{k}',\mathbf{q}} \sum_{p,p'=2,4,6} \frac{\alpha_1}{3} \Bigg(e^{i\mathbf{q}(\boldsymbol{\delta}_p - \boldsymbol{\delta}_{p'+1})} (e^{i\mathbf{k}'\boldsymbol{\delta}_{p'}} - e^{i\mathbf{k}'\boldsymbol{\delta}_{p'+2}}) a^\dagger_{j\sigma\mathbf{k}} a_{j\sigma\mathbf{k}+\mathbf{q}} a^\dagger_{j'\sigma'\mathbf{k}'} b_{j'\sigma'\mathbf{k}'-\mathbf{q}} \\ & + e^{i\mathbf{q}(\boldsymbol{\delta}_{p+1} - \boldsymbol{\delta}_{p'+1})} (e^{i\mathbf{k}'\boldsymbol{\delta}_{p'}} - e^{i\mathbf{k}'\boldsymbol{\delta}_{p'+2}}) b^\dagger_{j\sigma\mathbf{k}} b_{j\sigma\mathbf{k}+\mathbf{q}} a^\dagger_{j'\sigma'\mathbf{k}'} b_{j'\sigma'\mathbf{k}'-\mathbf{q}} \\ & + e^{i\mathbf{q}(\boldsymbol{\delta}_p - \boldsymbol{\delta}_{p'+1})} (e^{-i\mathbf{k}'\boldsymbol{\delta}_{p'}} - e^{-i\mathbf{k}'\boldsymbol{\delta}_{p'+2}}) a^\dagger_{j\sigma\mathbf{k}} a_{j\sigma\mathbf{k}+\mathbf{q}} b^\dagger_{j'\sigma'\mathbf{k}'+\mathbf{q}} a_{j'\sigma'\mathbf{k}'} \\ & + e^{i\mathbf{q}(\boldsymbol{\delta}_{p+1} - \boldsymbol{\delta}_{p'+1})} (e^{-i\mathbf{k}'\boldsymbol{\delta}_{p'}} - e^{-i\mathbf{k}'\boldsymbol{\delta}_{p'+2}}) b^\dagger_{j\sigma\mathbf{k}} b_{j\sigma\mathbf{k}+\mathbf{q}} b^\dagger_{j'\sigma'\mathbf{k}'+\mathbf{q}} a_{j'\sigma'\mathbf{k}'} \Bigg). \end{aligned} \tag{D.8}$$

As described in Section 5.2.1, we need to perform a shift in momentum of the third and fourth term to obtain $\mathbf{q}$-restrictions in the exchange terms of the HF decoupling. This can be done without complication, which can be readily verified by following the proceedure in Appendix C. We thus get

$$\begin{aligned} U_{Q\times T'} = \frac{V_0}{2N} \sum_{j,j'} \sum_{\sigma,\sigma'} \sum_{\mathbf{k},\mathbf{k}',\mathbf{q}} \sum_{p,p'=2,4,6} \frac{\alpha_1}{3} \Bigg(& e^{i\mathbf{q}(\boldsymbol{\delta}_p - \boldsymbol{\delta}_{p'+1})} (e^{i\mathbf{k}'\boldsymbol{\delta}_{p'}} - e^{i\mathbf{k}'\boldsymbol{\delta}_{p'+2}}) a^\dagger_{j\sigma\mathbf{k}} a_{j\sigma\mathbf{k}+\mathbf{q}} a^\dagger_{j'\sigma'\mathbf{k}'} b_{j'\sigma'\mathbf{k}'-\mathbf{q}} \\ & + e^{i\mathbf{q}(\boldsymbol{\delta}_{p+1} - \boldsymbol{\delta}_{p'+1})} (e^{i\mathbf{k}'\boldsymbol{\delta}_{p'}} - e^{i\mathbf{k}'\boldsymbol{\delta}_{p'+2}}) b^\dagger_{j\sigma\mathbf{k}} b_{j\sigma\mathbf{k}+\mathbf{q}} a^\dagger_{j'\sigma'\mathbf{k}'} b_{j'\sigma'\mathbf{k}'-\mathbf{q}} \\ & + e^{i\mathbf{q}(\boldsymbol{\delta}_p - \boldsymbol{\delta}_{p'+1})} (e^{-i(\mathbf{k}'-\mathbf{q})\boldsymbol{\delta}_{p'}} - e^{-i(\mathbf{k}'-\mathbf{q})\boldsymbol{\delta}_{p'+2}}) a^\dagger_{j\sigma\mathbf{k}} a_{j\sigma\mathbf{k}+\mathbf{q}} b^\dagger_{j'\sigma'\mathbf{k}'} a_{j'\sigma'\mathbf{k}'-\mathbf{q}} \\ & + e^{i\mathbf{q}(\boldsymbol{\delta}_{p+1} - \boldsymbol{\delta}_{p'+1})} (e^{-i(\mathbf{k}'-\mathbf{q})\boldsymbol{\delta}_{p'}} - e^{-i(\mathbf{k}'-\mathbf{q})\boldsymbol{\delta}_{p'+2}}) b^\dagger_{j\sigma\mathbf{k}} b_{j\sigma\mathbf{k}+\mathbf{q}} b^\dagger_{j'\sigma'\mathbf{k}'} a_{j'\sigma'\mathbf{k}'-\mathbf{q}} \Bigg). \end{aligned} \tag{D.9}$$

Likewise,

$$
\begin{aligned}
U_{T\times Q'} = \frac{V_0}{2N^2}\sum_{\mathbf{R}}\sum_{j,j'}\sum_{\sigma,\sigma'}\sum_{\substack{\mathbf{k},\mathbf{k}'\\ \mathbf{q},\mathbf{q}'}}\sum_{p,p'=2,4,6}\frac{\alpha_1}{3}\Big[&e^{i\mathbf{q}\mathbf{R}}e^{i\mathbf{q}\boldsymbol{\delta}_{p+1}}(e^{i\mathbf{k}\boldsymbol{\delta}_p}-e^{i\mathbf{k}\boldsymbol{\delta}_{p+2}})a^\dagger_{j\sigma\mathbf{k}}b_{j\sigma\mathbf{k}+\mathbf{q}}\\
&+e^{-i\mathbf{q}\mathbf{R}}e^{-i\mathbf{q}\boldsymbol{\delta}_{p+1}}(e^{-i\mathbf{k}\boldsymbol{\delta}_p}-e^{-i\mathbf{k}\boldsymbol{\delta}_{p+2}})b^\dagger_{j\sigma\mathbf{k}+\mathbf{q}}a_{j\sigma\mathbf{k}}\Big]\\
&\times\Big[e^{i\mathbf{q}'(\mathbf{R}+\boldsymbol{\delta}_{p'})}a^\dagger_{j'\sigma'\mathbf{k}'}a_{j'\sigma'\mathbf{k}'+\mathbf{q}'}+e^{i\mathbf{q}'(\mathbf{R}+\boldsymbol{\delta}_{p'+1})}b^\dagger_{j'\sigma'\mathbf{k}'}b_{j'\sigma'\mathbf{k}'+\mathbf{q}'}\Big]\\
=\frac{V_0}{2N^2}\sum_{\mathbf{R}}\sum_{j,j'}\sum_{\sigma,\sigma'}\sum_{\substack{\mathbf{k},\mathbf{k}'\\ \mathbf{q},\mathbf{q}'}}\sum_{p,p'=2,4,6}\frac{\alpha_1}{3}\Bigg(&e^{i(\mathbf{q}+\mathbf{q}')\mathbf{R}}\Big[e^{i\mathbf{q}'\boldsymbol{\delta}_{p'}}e^{i\mathbf{q}\boldsymbol{\delta}_{p+1}}(e^{i\mathbf{k}\boldsymbol{\delta}_p}-e^{i\mathbf{k}\boldsymbol{\delta}_{p+2}})a^\dagger_{j\sigma\mathbf{k}}b_{j\sigma\mathbf{k}+\mathbf{q}}a^\dagger_{j'\sigma'\mathbf{k}'}a_{j'\sigma'\mathbf{k}'+\mathbf{q}'}\\
&+e^{i\mathbf{q}'\boldsymbol{\delta}_{p'+1}}e^{i\mathbf{q}\boldsymbol{\delta}_{p+1}}(e^{i\mathbf{k}\boldsymbol{\delta}_p}-e^{i\mathbf{k}\boldsymbol{\delta}_{p+2}})a^\dagger_{j\sigma\mathbf{k}}b_{j\sigma\mathbf{k}+\mathbf{q}}b^\dagger_{j'\sigma'\mathbf{k}'}b_{j'\sigma'\mathbf{k}'+\mathbf{q}'}\Big]\\
&+\Bigg(e^{-i(\mathbf{q}-\mathbf{q}')\mathbf{R}}\Big[e^{i\mathbf{q}'\boldsymbol{\delta}_{p'}}e^{-i\mathbf{q}\boldsymbol{\delta}_{p+1}}(e^{-i\mathbf{k}\boldsymbol{\delta}_p}-e^{-i\mathbf{k}\boldsymbol{\delta}_{p+2}})b^\dagger_{j\sigma\mathbf{k}+\mathbf{q}}a_{j\sigma\mathbf{k}}a^\dagger_{j'\sigma'\mathbf{k}'}a_{j'\sigma'\mathbf{k}'+\mathbf{q}'}\\
&+e^{i\mathbf{q}'\boldsymbol{\delta}_{p'+1}}e^{-i\mathbf{q}\boldsymbol{\delta}_{p+1}}(e^{-i\mathbf{k}\boldsymbol{\delta}_p}-e^{-i\mathbf{k}\boldsymbol{\delta}_{p+2}})b^\dagger_{j\sigma\mathbf{k}+\mathbf{q}}a_{j\sigma\mathbf{k}+\mathbf{q}}b^\dagger_{j'\sigma'\mathbf{k}'}b_{j'\sigma'\mathbf{k}'+\mathbf{q}'}\Big]\Bigg)\\
=\frac{V_0}{2N}\sum_{j,j'}\sum_{\sigma,\sigma'}\sum_{\mathbf{k},\mathbf{k}',\mathbf{q}}\sum_{p,p'=2,4,6}\frac{\alpha_1}{3}\Bigg(&e^{-i\mathbf{q}(\boldsymbol{\delta}_{p'}-\boldsymbol{\delta}_{p+1})}(e^{i\mathbf{k}\boldsymbol{\delta}_p}-e^{i\mathbf{k}\boldsymbol{\delta}_{p+2}})a^\dagger_{j\sigma\mathbf{k}}b_{j\sigma\mathbf{k}+\mathbf{q}}a^\dagger_{j'\sigma'\mathbf{k}'}a_{j'\sigma'\mathbf{k}'-\mathbf{q}}\\
&+e^{-i\mathbf{q}(\boldsymbol{\delta}_{p'+1}-\boldsymbol{\delta}_{p+1})}(e^{i\mathbf{k}\boldsymbol{\delta}_p}-e^{i\mathbf{k}\boldsymbol{\delta}_{p+2}})a^\dagger_{j\sigma\mathbf{k}}b_{j\sigma\mathbf{k}+\mathbf{q}}b^\dagger_{j'\sigma'\mathbf{k}'}b_{j'\sigma'\mathbf{k}'-\mathbf{q}}\\
&+e^{i\mathbf{q}(\boldsymbol{\delta}_{p'}-\boldsymbol{\delta}_{p+1})}(e^{-i\mathbf{k}\boldsymbol{\delta}_p}-e^{-i\mathbf{k}\boldsymbol{\delta}_{p+2}})b^\dagger_{j\sigma\mathbf{k}+\mathbf{q}}a_{j\sigma\mathbf{k}}a^\dagger_{j'\sigma'\mathbf{k}'}a_{j'\sigma'\mathbf{k}'+\mathbf{q}}\\
&+e^{i\mathbf{q}(\boldsymbol{\delta}_{p'+1}-\boldsymbol{\delta}_{p+1})}(e^{-i\mathbf{k}\boldsymbol{\delta}_p}-e^{-i\mathbf{k}\boldsymbol{\delta}_{p+2}})b^\dagger_{j\sigma\mathbf{k}+\mathbf{q}}a_{j\sigma\mathbf{k}}b^\dagger_{j'\sigma'\mathbf{k}'}b_{j'\sigma'\mathbf{k}'+\mathbf{q}}\Bigg)\\
=\frac{V_0}{2N}\sum_{j,j'}\sum_{\sigma,\sigma'}\sum_{\mathbf{k},\mathbf{k}',\mathbf{q}}\sum_{p,p'=2,4,6}\frac{\alpha_1}{3}\Bigg(&e^{-i\mathbf{q}(\boldsymbol{\delta}_{p'}-\boldsymbol{\delta}_{p+1})}(e^{i\mathbf{k}\boldsymbol{\delta}_p}-e^{i\mathbf{k}\boldsymbol{\delta}_{p+2}})a^\dagger_{j\sigma\mathbf{k}}b_{j\sigma\mathbf{k}+\mathbf{q}}a^\dagger_{j'\sigma'\mathbf{k}'}a_{j'\sigma'\mathbf{k}'-\mathbf{q}}\\
&+e^{-i\mathbf{q}(\boldsymbol{\delta}_{p'+1}-\boldsymbol{\delta}_{p+1})}(e^{i\mathbf{k}\boldsymbol{\delta}_p}-e^{i\mathbf{k}\boldsymbol{\delta}_{p+2}})a^\dagger_{j\sigma\mathbf{k}}b_{j\sigma\mathbf{k}+\mathbf{q}}b^\dagger_{j'\sigma'\mathbf{k}'}b_{j'\sigma'\mathbf{k}'-\mathbf{q}}\\
&+e^{i\mathbf{q}(\boldsymbol{\delta}_{p'}-\boldsymbol{\delta}_{p+1})}(e^{-i\mathbf{k}\boldsymbol{\delta}_p}-e^{-i\mathbf{k}\boldsymbol{\delta}_{p+2}})b^\dagger_{j\sigma\mathbf{k}+\mathbf{q}}a_{j\sigma\mathbf{k}}a^\dagger_{j'\sigma'\mathbf{k}'-\mathbf{q}}a_{j'\sigma'\mathbf{k}'}\\
&+e^{i\mathbf{q}(\boldsymbol{\delta}_{p'+1}-\boldsymbol{\delta}_{p+1})}(e^{-i\mathbf{k}\boldsymbol{\delta}_p}-e^{-i\mathbf{k}\boldsymbol{\delta}_{p+2}})b^\dagger_{j\sigma\mathbf{k}+\mathbf{q}}a_{j\sigma\mathbf{k}}b^\dagger_{j'\sigma'\mathbf{k}'-\mathbf{q}}b_{j'\sigma'\mathbf{k}'}\Bigg).
\end{aligned}
\tag{D.10}
$$

Finally, we have

$$
\begin{aligned}
U_{T\times T'} = \frac{V_0}{2N^2}\sum_{\mathbf{R}}\sum_{\substack{j,j'\\ \sigma,\sigma'}}\sum_{\substack{\mathbf{k},\mathbf{k}'\\ \mathbf{q},\mathbf{q}'}}\sum_{p,p'=2,4,6}\alpha_1^2\Big[&e^{i\mathbf{q}\mathbf{R}}e^{i\mathbf{q}\boldsymbol{\delta}_{p+1}}(e^{i\mathbf{k}\boldsymbol{\delta}_p}-e^{i\mathbf{k}\boldsymbol{\delta}_{p+2}})a^\dagger_{j\sigma\mathbf{k}}b_{j\sigma\mathbf{k}+\mathbf{q}}\\
&+e^{-i\mathbf{q}\mathbf{R}}e^{-i\mathbf{q}\boldsymbol{\delta}_{p+1}}(e^{-i\mathbf{k}\boldsymbol{\delta}_p}-e^{-i\mathbf{k}\boldsymbol{\delta}_{p+2}})b^\dagger_{j\sigma\mathbf{k}+\mathbf{q}}a_{j\sigma\mathbf{k}}\Big]\\
&\times\Big[e^{i\mathbf{q}'\mathbf{R}}e^{i\mathbf{q}'\boldsymbol{\delta}_{p'+1}}(e^{i\mathbf{k}'\boldsymbol{\delta}_{p'}}-e^{i\mathbf{k}'\boldsymbol{\delta}_{p'+2}})a^\dagger_{j'\sigma'\mathbf{k}'}b_{j'\sigma'\mathbf{k}'+\mathbf{q}'}\\
&+e^{-i\mathbf{q}'\mathbf{R}}e^{-i\mathbf{q}'\boldsymbol{\delta}_{p'+1}}(e^{-i\mathbf{k}'\boldsymbol{\delta}_{p'}}-e^{-i\mathbf{k}'\boldsymbol{\delta}_{p'+2}})b^\dagger_{j'\sigma'\mathbf{k}'+\mathbf{q}'}a_{j'\sigma'\mathbf{k}'}\Big]\\
=\frac{\alpha_1^2V_0}{2N^2}\sum_{\mathbf{R}}\sum_{\substack{j,j'\\ \sigma,\sigma'}}\sum_{\substack{\mathbf{k},\mathbf{k}'\\ \mathbf{q},\mathbf{q}'}}\sum_{p,p'}\Big[&e^{i(\mathbf{q}+\mathbf{q}')\mathbf{R}}e^{i\mathbf{q}\boldsymbol{\delta}_{p+1}}e^{i\mathbf{q}'\boldsymbol{\delta}_{p'+1}}(e^{i\mathbf{k}\boldsymbol{\delta}_p}-e^{i\mathbf{k}\boldsymbol{\delta}_{p+2}})(e^{i\mathbf{k}'\boldsymbol{\delta}_{p'}}-e^{i\mathbf{k}'\boldsymbol{\delta}_{p'+2}})a^\dagger_{j\sigma\mathbf{k}}b_{j\sigma\mathbf{k}+\mathbf{q}}a^\dagger_{j'\sigma'\mathbf{k}'}b_{j'\sigma'\mathbf{k}'+\mathbf{q}'}\\
&+e^{i(\mathbf{q}-\mathbf{q}')\mathbf{R}}e^{i\mathbf{q}\boldsymbol{\delta}_{p+1}}e^{-i\mathbf{q}'\boldsymbol{\delta}_{p'+1}}(e^{i\mathbf{k}\boldsymbol{\delta}_p}-e^{i\mathbf{k}\boldsymbol{\delta}_{p+2}})(e^{-i\mathbf{k}'\boldsymbol{\delta}_{p'}}-e^{-i\mathbf{k}'\boldsymbol{\delta}_{p'+2}})a^\dagger_{j\sigma\mathbf{k}}b_{j\sigma\mathbf{k}+\mathbf{q}}b^\dagger_{j'\sigma'\mathbf{k}'+\mathbf{q}'}a_{j'\sigma'\mathbf{k}'}
\end{aligned}
$$

$$
\begin{aligned}
&+ e^{-i(\mathbf{q}-\mathbf{q}')\mathbf{R}} e^{-i\mathbf{q}\boldsymbol{\delta}_{p+1}} e^{i\mathbf{q}'\boldsymbol{\delta}_{p'+1}} (e^{-i\mathbf{k}\boldsymbol{\delta}_p} - e^{-i\mathbf{k}\boldsymbol{\delta}_{p+2}})(e^{i\mathbf{k}'\boldsymbol{\delta}_{p'}} - e^{i\mathbf{k}'\boldsymbol{\delta}_{p'+2}}) b^\dagger_{j\sigma\mathbf{k}+\mathbf{q}} a_{j\sigma\mathbf{k}} a^\dagger_{j'\sigma'\mathbf{k}'} b_{j'\sigma'\mathbf{k}'+\mathbf{q}'} \\
&+ e^{-i(\mathbf{q}+\mathbf{q}')\mathbf{R}} e^{-i\mathbf{q}\boldsymbol{\delta}_{p+1}} e^{-i\mathbf{q}'\boldsymbol{\delta}_{p'+1}} (e^{-i\mathbf{k}\boldsymbol{\delta}_p} - e^{-i\mathbf{k}\boldsymbol{\delta}_{p+2}})(e^{-i\mathbf{k}'\boldsymbol{\delta}_{p'}} - e^{-i\mathbf{k}'\boldsymbol{\delta}_{p'+2}}) b^\dagger_{j\sigma\mathbf{k}+\mathbf{q}} a_{j\sigma\mathbf{k}} b^\dagger_{j'\sigma'\mathbf{k}'+\mathbf{q}'} a_{j'\sigma'\mathbf{k}'} \Big] \\
= \frac{V_0}{2N} \sum_{j,j'} \sum_{\sigma,\sigma'} \sum_{\mathbf{k},\mathbf{k}',\mathbf{q}} \sum_{p,p'=2,4,6} \alpha_1^2 \Big[& e^{i\mathbf{q}(\boldsymbol{\delta}_{p+1}-\boldsymbol{\delta}_{p'+1})} (e^{i\mathbf{k}\boldsymbol{\delta}_p} - e^{i\mathbf{k}\boldsymbol{\delta}_{p+2}})(e^{i\mathbf{k}'\boldsymbol{\delta}_{p'}} - e^{i\mathbf{k}'\boldsymbol{\delta}_{p'+2}}) a^\dagger_{j\sigma\mathbf{k}} b_{j\sigma\mathbf{k}+\mathbf{q}} a^\dagger_{j'\sigma'\mathbf{k}'} b_{j'\sigma'\mathbf{k}'-\mathbf{q}} \\
&+ e^{i\mathbf{q}(\boldsymbol{\delta}_{p+1}-\boldsymbol{\delta}_{p'+1})} (e^{i\mathbf{k}\boldsymbol{\delta}_p} - e^{i\mathbf{k}\boldsymbol{\delta}_{p+2}})(e^{-i\mathbf{k}'\boldsymbol{\delta}_{p'}} - e^{-i\mathbf{k}'\boldsymbol{\delta}_{p'+2}}) a^\dagger_{j\sigma\mathbf{k}} b_{j\sigma\mathbf{k}+\mathbf{q}} b^\dagger_{j'\sigma'\mathbf{k}'+\mathbf{q}} a_{j'\sigma'\mathbf{k}'} \\
&+ e^{-i\mathbf{q}(\boldsymbol{\delta}_{p+1}-\boldsymbol{\delta}_{p'+1})} (e^{-i\mathbf{k}\boldsymbol{\delta}_p} - e^{-i\mathbf{k}\boldsymbol{\delta}_{p+2}})(e^{i\mathbf{k}'\boldsymbol{\delta}_{p'}} - e^{i\mathbf{k}'\boldsymbol{\delta}_{p'+2}}) b^\dagger_{j\sigma\mathbf{k}+\mathbf{q}} a_{j\sigma\mathbf{k}} a^\dagger_{j'\sigma'\mathbf{k}'} b_{j'\sigma'\mathbf{k}'+\mathbf{q}} \\
&+ e^{-i\mathbf{q}(\boldsymbol{\delta}_{p+1}-\boldsymbol{\delta}_{p'+1})} (e^{-i\mathbf{k}\boldsymbol{\delta}_p} - e^{-i\mathbf{k}\boldsymbol{\delta}_{p+2}})(e^{-i\mathbf{k}'\boldsymbol{\delta}_{p'}} - e^{-i\mathbf{k}'\boldsymbol{\delta}_{p'+2}}) b^\dagger_{j\sigma\mathbf{k}+\mathbf{q}} a_{j\sigma\mathbf{k}} b^\dagger_{j'\sigma'\mathbf{k}'-\mathbf{q}} a_{j'\sigma'\mathbf{k}'} \Big] \\
= \frac{V_0}{2N} \sum_{j,j'} \sum_{\sigma,\sigma'} \sum_{\mathbf{k},\mathbf{k}',\mathbf{q}} \sum_{p,p'=2,4,6} \alpha_1^2 \Big[& e^{i\mathbf{q}(\boldsymbol{\delta}_{p+1}-\boldsymbol{\delta}_{p'+1})} (e^{i\mathbf{k}\boldsymbol{\delta}_p} - e^{i\mathbf{k}\boldsymbol{\delta}_{p+2}})(e^{i\mathbf{k}'\boldsymbol{\delta}_{p'}} - e^{i\mathbf{k}'\boldsymbol{\delta}_{p'+2}}) a^\dagger_{j\sigma\mathbf{k}} b_{j\sigma\mathbf{k}+\mathbf{q}} a^\dagger_{j'\sigma'\mathbf{k}'} b_{j'\sigma'\mathbf{k}'-\mathbf{q}} \\
&+ e^{i\mathbf{q}(\boldsymbol{\delta}_{p+1}-\boldsymbol{\delta}_{p'+1})} (e^{i\mathbf{k}\boldsymbol{\delta}_p} - e^{i\mathbf{k}\boldsymbol{\delta}_{p+2}})(e^{-i(\mathbf{k}'-\mathbf{q})\boldsymbol{\delta}_{p'}} - e^{-i(\mathbf{k}'-\mathbf{q})\boldsymbol{\delta}_{p'+2}}) a^\dagger_{j\sigma\mathbf{k}} b_{j\sigma\mathbf{k}+\mathbf{q}} b^\dagger_{j'\sigma'\mathbf{k}'} a_{j'\sigma'\mathbf{k}'-\mathbf{q}} \\
&+ e^{-i\mathbf{q}(\boldsymbol{\delta}_{p+1}-\boldsymbol{\delta}_{p'+1})} (e^{-i\mathbf{k}\boldsymbol{\delta}_p} - e^{-i\mathbf{k}\boldsymbol{\delta}_{p+2}})(e^{i(\mathbf{k}'-\mathbf{q})\boldsymbol{\delta}_{p'}} - e^{i(\mathbf{k}'-\mathbf{q})\boldsymbol{\delta}_{p'+2}}) b^\dagger_{j\sigma\mathbf{k}+\mathbf{q}} a_{j\sigma\mathbf{k}} a^\dagger_{j'\sigma'\mathbf{k}'-\mathbf{q}} b_{j'\sigma'\mathbf{k}'} \\
&+ e^{-i\mathbf{q}(\boldsymbol{\delta}_{p+1}-\boldsymbol{\delta}_{p'+1})} (e^{-i\mathbf{k}\boldsymbol{\delta}_p} - e^{-i\mathbf{k}\boldsymbol{\delta}_{p+2}})(e^{-i\mathbf{k}'\boldsymbol{\delta}_{p'}} - e^{-i\mathbf{k}'\boldsymbol{\delta}_{p'+2}}) b^\dagger_{j\sigma\mathbf{k}+\mathbf{q}} a_{j\sigma\mathbf{k}} b^\dagger_{j'\sigma'\mathbf{k}'-\mathbf{q}} a_{j'\sigma'\mathbf{k}'} \Big].
\end{aligned}
\tag{D.11}
$$

Appendix E

Fock terms in the Bravais lattice picture

In this appendix we derive the Fock terms of the interaction model in the Bravais lattice picture. The exchange terms will contain contributions from all four combinations in Eqs. (5.24)-(5.27). We thus begin by writing the exchange terms of each part individually with the homogeneity condition applied.

$$
\begin{aligned}
U^F_{Q\times Q'} = -\frac{V_0}{2N}\sum_{j,j'}\sum_{\sigma,\sigma'}\sum_{\mathbf{k},\mathbf{k}',\mathbf{q}}\sum_{p,p'}\frac{\delta_{\mathbf{k}',\mathbf{k}+\mathbf{q}}}{9}\Big(&e^{i\mathbf{q}(\boldsymbol{\delta}_p-\boldsymbol{\delta}_{p'})}[\langle a^\dagger_{j\sigma\mathbf{k}}a_{j'\sigma'\mathbf{k}'-\mathbf{q}}\rangle a^\dagger_{j'\sigma'\mathbf{k}'}a_{j\sigma\mathbf{k}+\mathbf{q}} + a^\dagger_{j\sigma\mathbf{k}}a_{j'\sigma'\mathbf{k}'-\mathbf{q}}\langle a^\dagger_{j'\sigma'\mathbf{k}'}a_{j\sigma\mathbf{k}+\mathbf{q}}\rangle]\\
&+ e^{i\mathbf{q}(\boldsymbol{\delta}_{p+1}-\boldsymbol{\delta}_{p'+1})}[\langle b^\dagger_{j\sigma\mathbf{k}}b_{j'\sigma'\mathbf{k}'-\mathbf{q}}\rangle b^\dagger_{j'\sigma'\mathbf{k}'}b_{j\sigma\mathbf{k}+\mathbf{q}} + b^\dagger_{j\sigma\mathbf{k}}b_{j'\sigma'\mathbf{k}'-\mathbf{q}}\langle b^\dagger_{j'\sigma'\mathbf{k}'}b_{j\sigma\mathbf{k}+\mathbf{q}}\rangle]\\
&+ e^{i\mathbf{q}(\boldsymbol{\delta}_{p}-\boldsymbol{\delta}_{p'+1})}[\langle a^\dagger_{j\sigma\mathbf{k}}b_{j'\sigma'\mathbf{k}'-\mathbf{q}}\rangle b^\dagger_{j'\sigma'\mathbf{k}'}a_{j\sigma\mathbf{k}+\mathbf{q}} + a^\dagger_{j\sigma\mathbf{k}}b_{j'\sigma'\mathbf{k}'-\mathbf{q}}\langle b^\dagger_{j'\sigma'\mathbf{k}'}a_{j\sigma\mathbf{k}+\mathbf{q}}\rangle]\\
&+ e^{i\mathbf{q}(\boldsymbol{\delta}_{p+1}-\boldsymbol{\delta}_{p'})}[\langle b^\dagger_{j\sigma\mathbf{k}}a_{j'\sigma'\mathbf{k}'-\mathbf{q}}\rangle a^\dagger_{j'\sigma'\mathbf{k}'}b_{j\sigma\mathbf{k}+\mathbf{q}} + b^\dagger_{j\sigma\mathbf{k}}a_{j'\sigma'\mathbf{k}'-\mathbf{q}}\langle a^\dagger_{j'\sigma'\mathbf{k}'}b_{j\sigma\mathbf{k}+\mathbf{q}}\rangle]\Big)\\
= -\frac{V_0}{2N}\sum_{j,j'}\sum_{\sigma,\sigma'}\sum_{\mathbf{k},\mathbf{k}'}\sum_{p,p'}\frac{1}{9}\Big(&e^{i(\mathbf{k}'-\mathbf{k})(\boldsymbol{\delta}_p-\boldsymbol{\delta}_{p'})}[\langle a^\dagger_{j\sigma\mathbf{k}}a_{j'\sigma'\mathbf{k}}\rangle a^\dagger_{j'\sigma'\mathbf{k}'}a_{j\sigma\mathbf{k}'} + a^\dagger_{j\sigma\mathbf{k}}a_{j'\sigma'\mathbf{k}}\langle a^\dagger_{j'\sigma'\mathbf{k}'}a_{j\sigma\mathbf{k}'}\rangle]\\
&+ e^{i(\mathbf{k}'-\mathbf{k})(\boldsymbol{\delta}_{p+1}-\boldsymbol{\delta}_{p'+1})}[\langle b^\dagger_{j\sigma\mathbf{k}}b_{j'\sigma'\mathbf{k}}\rangle b^\dagger_{j'\sigma'\mathbf{k}'}b_{j\sigma\mathbf{k}'} + b^\dagger_{j\sigma\mathbf{k}}b_{j'\sigma'\mathbf{k}}\langle b^\dagger_{j'\sigma'\mathbf{k}'}b_{j\sigma\mathbf{k}'}\rangle]\\
&+ e^{i(\mathbf{k}'-\mathbf{k})(\boldsymbol{\delta}_{p}-\boldsymbol{\delta}_{p'+1})}[\langle a^\dagger_{j\sigma\mathbf{k}}b_{j'\sigma'\mathbf{k}}\rangle b^\dagger_{j'\sigma'\mathbf{k}'}a_{j\sigma\mathbf{k}'} + a^\dagger_{j\sigma\mathbf{k}}b_{j'\sigma'\mathbf{k}}\langle b^\dagger_{j'\sigma'\mathbf{k}'}a_{j\sigma\mathbf{k}'}\rangle]\\
&+ e^{i(\mathbf{k}'-\mathbf{k})(\boldsymbol{\delta}_{p+1}-\boldsymbol{\delta}_{p'})}[\langle b^\dagger_{j\sigma\mathbf{k}}a_{j'\sigma'\mathbf{k}}\rangle a^\dagger_{j'\sigma'\mathbf{k}'}b_{j\sigma\mathbf{k}'} + b^\dagger_{j\sigma\mathbf{k}}a_{j'\sigma'\mathbf{k}}\langle a^\dagger_{j'\sigma'\mathbf{k}'}b_{j\sigma\mathbf{k}'}\rangle]\Big)\\
= -\frac{V_0}{2N}\sum_{j,j'}\sum_{\sigma,\sigma'}\sum_{\mathbf{k},\mathbf{k}'}\sum_{p,p'}\frac{1}{9}\Big(&(e^{i(\mathbf{k}'-\mathbf{k})(\boldsymbol{\delta}_p-\boldsymbol{\delta}_{p'})} + e^{-i(\mathbf{k}'-\mathbf{k})(\boldsymbol{\delta}_p-\boldsymbol{\delta}_{p'})})\langle a^\dagger_{j'\sigma'\mathbf{k}'}a_{j\sigma\mathbf{k}'}\rangle a^\dagger_{j\sigma\mathbf{k}}a_{j'\sigma'\mathbf{k}}\\
&+ (e^{i(\mathbf{k}'-\mathbf{k})(\boldsymbol{\delta}_{p+1}-\boldsymbol{\delta}_{p'+1})} + e^{-i(\mathbf{k}'-\mathbf{k})(\boldsymbol{\delta}_{p+1}-\boldsymbol{\delta}_{p'+1})})\langle b^\dagger_{j'\sigma'\mathbf{k}'}b_{j\sigma\mathbf{k}'}\rangle b^\dagger_{j\sigma\mathbf{k}}b_{j'\sigma'\mathbf{k}}\\
&+ (e^{i(\mathbf{k}'-\mathbf{k})(\boldsymbol{\delta}_{p}-\boldsymbol{\delta}_{p'+1})} + e^{-i(\mathbf{k}'-\mathbf{k})(\boldsymbol{\delta}_{p+1}-\boldsymbol{\delta}_{p'})})\langle b^\dagger_{j'\sigma'\mathbf{k}'}a_{j\sigma\mathbf{k}'}\rangle a^\dagger_{j\sigma\mathbf{k}}b_{j'\sigma'\mathbf{k}}\\
&+ (e^{i(\mathbf{k}'-\mathbf{k})(\boldsymbol{\delta}_{p+1}-\boldsymbol{\delta}_{p'})} + e^{-i(\mathbf{k}'-\mathbf{k})(\boldsymbol{\delta}_{p}-\boldsymbol{\delta}_{p'+1})})\langle a^\dagger_{j'\sigma'\mathbf{k}'}b_{j\sigma\mathbf{k}'}\rangle b^\dagger_{j\sigma\mathbf{k}}a_{j'\sigma'\mathbf{k}}
\end{aligned}
\tag{E.1}
$$

$$
\begin{aligned}
U^F_{Q\times T'} = -\frac{V_0}{2N}\sum_{j,j'}\sum_{\sigma,\sigma'}\sum_{\mathbf{k},\mathbf{k}',\mathbf{q}}\sum_{p,p'}\frac{\alpha_1}{3}\delta_{\mathbf{k}',\mathbf{k}+\mathbf{q}}\Bigg(&e^{i\mathbf{q}(\boldsymbol{\delta}_p-\boldsymbol{\delta}_{p'+1})}(e^{i\mathbf{k}'\boldsymbol{\delta}_{p'}} - e^{i\mathbf{k}'\boldsymbol{\delta}_{p'+2}})\\
&\times[\langle a^\dagger_{j\sigma\mathbf{k}}b_{j'\sigma'\mathbf{k}'-\mathbf{q}}\rangle a^\dagger_{j'\sigma'\mathbf{k}'}a_{j\sigma\mathbf{k}+\mathbf{q}} + \langle a^\dagger_{j'\sigma'\mathbf{k}'}a_{j\sigma\mathbf{k}+\mathbf{q}}\rangle a^\dagger_{j\sigma\mathbf{k}}b_{j'\sigma'\mathbf{k}'-\mathbf{q}}]\\
&+ e^{i\mathbf{q}(\boldsymbol{\delta}_{p+1}-\boldsymbol{\delta}_{p'+1})}(e^{i\mathbf{k}'\boldsymbol{\delta}_{p'}} - e^{i\mathbf{k}'\boldsymbol{\delta}_{p'+2}})\\
&\times[\langle b^\dagger_{j\sigma\mathbf{k}}b_{j'\sigma'\mathbf{k}'-\mathbf{q}}\rangle a^\dagger_{j'\sigma'\mathbf{k}'}b_{j\sigma\mathbf{k}+\mathbf{q}} + \langle a^\dagger_{j'\sigma'\mathbf{k}'}b_{j\sigma\mathbf{k}+\mathbf{q}}\rangle b^\dagger_{j\sigma\mathbf{k}}b_{j'\sigma'\mathbf{k}'-\mathbf{q}}]\\
&+ e^{i\mathbf{q}(\boldsymbol{\delta}_p-\boldsymbol{\delta}_{p'+1})}(e^{-i(\mathbf{k}'-\mathbf{q})\boldsymbol{\delta}_{p'}} - e^{-i(\mathbf{k}'-\mathbf{q})\boldsymbol{\delta}_{p'+2}})
\end{aligned}
$$

$$
\begin{aligned}
&\times [\langle a^\dagger_{j\sigma\mathbf{k}} a_{j'\sigma'\mathbf{k'}-\mathbf{q}}\rangle b^\dagger_{j'\sigma'\mathbf{k'}} a_{j\sigma\mathbf{k}+\mathbf{q}} + \langle b^\dagger_{j'\sigma'\mathbf{k'}} a_{j\sigma\mathbf{k}+\mathbf{q}}\rangle a^\dagger_{j\sigma\mathbf{k}} a_{j'\sigma'\mathbf{k'}-\mathbf{q}}] \\
&+ e^{i\mathbf{q}(\boldsymbol{\delta}_{p+1}-\boldsymbol{\delta}_{p'+1})}(e^{-i(\mathbf{k'}-\mathbf{q})\boldsymbol{\delta}_{p'}} - e^{-i(\mathbf{k'}-\mathbf{q})\boldsymbol{\delta}_{p'+2}}) \\
&\times [\langle b^\dagger_{j\sigma\mathbf{k}} a_{j'\sigma'\mathbf{k'}-\mathbf{q}}\rangle b^\dagger_{j'\sigma'\mathbf{k'}} b_{j\sigma\mathbf{k}+\mathbf{q}} + \langle b^\dagger_{j'\sigma'\mathbf{k'}} b_{j\sigma\mathbf{k}+\mathbf{q}}\rangle b^\dagger_{j\sigma\mathbf{k}} a_{j'\sigma'\mathbf{k'}-\mathbf{q}}]\Bigg) \\
= -\frac{V_0}{2N}\sum_{j,j'}\sum_{\sigma,\sigma'}\sum_{\mathbf{k},\mathbf{k'}}\sum_{p,p'}\frac{\alpha_1}{3}\Bigg(&e^{i(\mathbf{k'}-\mathbf{k})(\boldsymbol{\delta}_p-\boldsymbol{\delta}_{p'+1})}(e^{i\mathbf{k'}\boldsymbol{\delta}_{p'}} - e^{i\mathbf{k'}\boldsymbol{\delta}_{p'+2}}) \\
&\times [\langle a^\dagger_{j\sigma\mathbf{k}} b_{j'\sigma'\mathbf{k}}\rangle a^\dagger_{j'\sigma'\mathbf{k'}} a_{j\sigma\mathbf{k'}} + \langle a^\dagger_{j'\sigma'\mathbf{k'}} a_{j\sigma\mathbf{k'}}\rangle a^\dagger_{j\sigma\mathbf{k}} b_{j'\sigma'\mathbf{k}}] \\
&+ e^{i(\mathbf{k'}-\mathbf{k})(\boldsymbol{\delta}_{p+1}-\boldsymbol{\delta}_{p'+1})}(e^{i\mathbf{k'}\boldsymbol{\delta}_{p'}} - e^{i\mathbf{k'}\boldsymbol{\delta}_{p'+2}}) \\
&\times [\langle b^\dagger_{j\sigma\mathbf{k}} b_{j'\sigma'\mathbf{k}}\rangle a^\dagger_{j'\sigma'\mathbf{k'}} b_{j\sigma\mathbf{k'}} + \langle a^\dagger_{j'\sigma'\mathbf{k'}} b_{j\sigma\mathbf{k'}}\rangle b^\dagger_{j\sigma\mathbf{k}} b_{j'\sigma'\mathbf{k}}] \\
&+ e^{i(\mathbf{k'}-\mathbf{k})(\boldsymbol{\delta}_{p}-\boldsymbol{\delta}_{p'+1})}(e^{-i\mathbf{k}\boldsymbol{\delta}_{p'}} - e^{-i\mathbf{k}\boldsymbol{\delta}_{p'+2}}) \\
&\times [\langle a^\dagger_{j\sigma\mathbf{k}} a_{j'\sigma'\mathbf{k}}\rangle b^\dagger_{j'\sigma'\mathbf{k'}} a_{j\sigma\mathbf{k'}} + \langle b^\dagger_{j'\sigma'\mathbf{k'}} a_{j\sigma\mathbf{k'}}\rangle a^\dagger_{j\sigma\mathbf{k}} a_{j'\sigma'\mathbf{k}}] \\
&+ e^{i(\mathbf{k'}-\mathbf{k})(\boldsymbol{\delta}_{p+1}-\boldsymbol{\delta}_{p'+1})}(e^{-i\mathbf{k}\boldsymbol{\delta}_{p'}} - e^{-i\mathbf{k}\boldsymbol{\delta}_{p'+2}}) \\
&\times [\langle b^\dagger_{j\sigma\mathbf{k}} a_{j'\sigma'\mathbf{k}}\rangle b^\dagger_{j'\sigma'\mathbf{k'}} b_{j\sigma\mathbf{k'}} + \langle b^\dagger_{j'\sigma'\mathbf{k'}} b_{j\sigma\mathbf{k'}}\rangle b^\dagger_{j\sigma\mathbf{k}} a_{j'\sigma'\mathbf{k}}]\Bigg) \\
= -\frac{V_0}{2N}\sum_{j,j'}\sum_{\sigma,\sigma'}\sum_{\mathbf{k},\mathbf{k'}}\sum_{p,p'}\frac{\alpha_1}{3}\Bigg(&[e^{-i(\mathbf{k'}-\mathbf{k})(\boldsymbol{\delta}_p-\boldsymbol{\delta}_{p'+1})}(e^{i\mathbf{k}\boldsymbol{\delta}_{p'}} - e^{i\mathbf{k}\boldsymbol{\delta}_{p'+2}})\langle a^\dagger_{j'\sigma'\mathbf{k'}} b_{j\sigma\mathbf{k'}}\rangle \\
&+ e^{i(\mathbf{k'}-\mathbf{k})(\boldsymbol{\delta}_p-\boldsymbol{\delta}_{p'+1})}(e^{-i\mathbf{k}\boldsymbol{\delta}_{p'}} - e^{-i\mathbf{k}\boldsymbol{\delta}_{p'+2}})\langle b^\dagger_{j'\sigma'\mathbf{k'}} a_{j\sigma\mathbf{k'}}\rangle] a^\dagger_{j\sigma\mathbf{k}} a_{j'\sigma'\mathbf{k}} \\
&+ [e^{i(\mathbf{k'}-\mathbf{k})(\boldsymbol{\delta}_p-\boldsymbol{\delta}_{p'+1})}(e^{i\mathbf{k'}\boldsymbol{\delta}_{p'}} - e^{i\mathbf{k'}\boldsymbol{\delta}_{p'+2}})\langle a^\dagger_{j'\sigma'\mathbf{k'}} a_{j\sigma\mathbf{k'}}\rangle \\
&+ e^{-i(\mathbf{k'}-\mathbf{k})(\boldsymbol{\delta}_{p+1}-\boldsymbol{\delta}_{p'+1})}(e^{i\mathbf{k}\boldsymbol{\delta}_{p'}} - e^{i\mathbf{k}\boldsymbol{\delta}_{p'+2}})\langle b^\dagger_{j'\sigma'\mathbf{k'}} b_{j\sigma\mathbf{k'}}\rangle] a^\dagger_{j\sigma\mathbf{k}} b_{j'\sigma'\mathbf{k}} \\
&+ [e^{i(\mathbf{k'}-\mathbf{k})(\boldsymbol{\delta}_{p+1}-\boldsymbol{\delta}_{p'+1})}(e^{i\mathbf{k'}\boldsymbol{\delta}_{p'}} - e^{i\mathbf{k'}\boldsymbol{\delta}_{p'+2}})\langle a^\dagger_{j'\sigma'\mathbf{k'}} b_{j\sigma\mathbf{k'}}\rangle \\
&+ e^{-i(\mathbf{k'}-\mathbf{k})(\boldsymbol{\delta}_{p+1}-\boldsymbol{\delta}_{p'+1})}(e^{-i\mathbf{k'}\boldsymbol{\delta}_{p'}} - e^{-i\mathbf{k'}\boldsymbol{\delta}_{p'+2}})\langle b^\dagger_{j'\sigma'\mathbf{k'}} a_{j\sigma\mathbf{k'}}\rangle] b^\dagger_{j\sigma\mathbf{k}} b_{j'\sigma'\mathbf{k}} \\
&+ [e^{-i(\mathbf{k'}-\mathbf{k})(\boldsymbol{\delta}_p-\boldsymbol{\delta}_{p'+1})}(e^{-i\mathbf{k'}\boldsymbol{\delta}_{p'}} - e^{-i\mathbf{k'}\boldsymbol{\delta}_{p'+2}})\langle a^\dagger_{j'\sigma'\mathbf{k'}} a_{j\sigma\mathbf{k'}}\rangle \\
&+ e^{i(\mathbf{k'}-\mathbf{k})(\boldsymbol{\delta}_{p+1}-\boldsymbol{\delta}_{p'+1})}(e^{-i\mathbf{k}\boldsymbol{\delta}_{p'}} - e^{-i\mathbf{k}\boldsymbol{\delta}_{p'+2}})\langle b^\dagger_{j'\sigma'\mathbf{k'}} b_{j\sigma\mathbf{k'}}\rangle] b^\dagger_{j\sigma\mathbf{k}} a_{j'\sigma'\mathbf{k}}\Bigg) \qquad \text{(E.2)}
\end{aligned}
$$

$$
\begin{aligned}
U^F_{T\times Q'} = -\frac{V_0}{2N}\sum_{j,j'}\sum_{\sigma,\sigma'}\sum_{\mathbf{k},\mathbf{k'},\mathbf{q}}\sum_{p,p'}\frac{\alpha_1}{3}\delta_{\mathbf{k'},\mathbf{k}+\mathbf{q}}\Bigg(&e^{-i\mathbf{q}(\boldsymbol{\delta}_{p'}-\boldsymbol{\delta}_{p+1})}(e^{i\mathbf{k}\boldsymbol{\delta}_p} - e^{i\mathbf{k}\boldsymbol{\delta}_{p+2}}) \\
&\times [\langle a^\dagger_{j\sigma\mathbf{k}} a_{j'\sigma'\mathbf{k'}-\mathbf{q}}\rangle a^\dagger_{j'\sigma'\mathbf{k'}} b_{j\sigma\mathbf{k}+\mathbf{q}} + \langle a^\dagger_{j'\sigma'\mathbf{k'}} b_{j\sigma\mathbf{k}+\mathbf{q}}\rangle a^\dagger_{j\sigma\mathbf{k}} a_{j'\sigma'\mathbf{k'}-\mathbf{q}}] \\
&+ e^{-i\mathbf{q}(\boldsymbol{\delta}_{p'+1}-\boldsymbol{\delta}_{p+1})}(e^{i\mathbf{k}\boldsymbol{\delta}_p} - e^{i\mathbf{k}\boldsymbol{\delta}_{p+2}}) \\
&\times [\langle a^\dagger_{j\sigma\mathbf{k}} b_{j'\sigma'\mathbf{k'}-\mathbf{q}}\rangle b^\dagger_{j'\sigma'\mathbf{k'}} b_{j\sigma\mathbf{k}+\mathbf{q}} + \langle b^\dagger_{j'\sigma'\mathbf{k'}} b_{j\sigma\mathbf{k}+\mathbf{q}}\rangle a^\dagger_{j\sigma\mathbf{k}} b_{j'\sigma'\mathbf{k'}-\mathbf{q}}] \\
&+ e^{i\mathbf{q}(\boldsymbol{\delta}_{p'}-\boldsymbol{\delta}_{p+1})}(e^{-i\mathbf{k}\boldsymbol{\delta}_p} - e^{-i\mathbf{k}\boldsymbol{\delta}_{p+2}}) \\
&\times [\langle b^\dagger_{j\sigma\mathbf{k}+\mathbf{q}} a_{j'\sigma'\mathbf{k'}}\rangle a^\dagger_{j'\sigma'\mathbf{k'}-\mathbf{q}} a_{j\sigma\mathbf{k}} + \langle a^\dagger_{j'\sigma'\mathbf{k'}-\mathbf{q}} a_{j\sigma\mathbf{k}}\rangle b^\dagger_{j\sigma\mathbf{k}+\mathbf{q}} a_{j'\sigma'\mathbf{k'}}] \\
&+ e^{i\mathbf{q}(\boldsymbol{\delta}_{p'+1}-\boldsymbol{\delta}_{p+1})}(e^{-i\mathbf{k}\boldsymbol{\delta}_p} - e^{-i\mathbf{k}\boldsymbol{\delta}_{p+2}}) \\
&\times [\langle b^\dagger_{j\sigma\mathbf{k}+\mathbf{q}} b_{j'\sigma'\mathbf{k'}}\rangle b^\dagger_{j'\sigma'\mathbf{k'}-\mathbf{q}} a_{j\sigma\mathbf{k}} + \langle b^\dagger_{j'\sigma'\mathbf{k'}-\mathbf{q}} a_{j\sigma\mathbf{k}}\rangle b^\dagger_{j\sigma\mathbf{k}+\mathbf{q}} b_{j'\sigma'\mathbf{k'}}]\Bigg) \\
= -\frac{V_0}{2N}\sum_{j,j'}\sum_{\sigma,\sigma'}\sum_{\mathbf{k},\mathbf{k'}}\sum_{p,p'}\frac{\alpha_1}{3}\Bigg(&e^{-i(\mathbf{k'}-\mathbf{k})(\boldsymbol{\delta}_{p'}-\boldsymbol{\delta}_{p+1})}(e^{i\mathbf{k}\boldsymbol{\delta}_p} - e^{i\mathbf{k}\boldsymbol{\delta}_{p+2}}) \\
&\times [\langle a^\dagger_{j\sigma\mathbf{k}} a_{j'\sigma'\mathbf{k}}\rangle a^\dagger_{j'\sigma'\mathbf{k'}} b_{j\sigma\mathbf{k'}} + \langle a^\dagger_{j'\sigma'\mathbf{k'}} b_{j\sigma\mathbf{k'}}\rangle a^\dagger_{j\sigma\mathbf{k}} a_{j'\sigma'\mathbf{k}}]
\end{aligned}
$$

$$
\begin{aligned}
&+ e^{-i(\mathbf{k}'-\mathbf{k})(\boldsymbol{\delta}_{p'+1}-\boldsymbol{\delta}_{p+1})}(e^{i\mathbf{k}\boldsymbol{\delta}_p} - e^{i\mathbf{k}\boldsymbol{\delta}_{p+2}}) \\
&\qquad \times [\langle a^\dagger_{j\sigma\mathbf{k}} b_{j'\sigma'\mathbf{k}}\rangle b^\dagger_{j'\sigma'\mathbf{k}'} b_{j\sigma\mathbf{k}'} + \langle b^\dagger_{j'\sigma'\mathbf{k}'} b_{j\sigma\mathbf{k}'}\rangle a^\dagger_{j\sigma\mathbf{k}} b_{j'\sigma'\mathbf{k}}] \\
&+ e^{i(\mathbf{k}'-\mathbf{k})(\boldsymbol{\delta}_{p'}-\boldsymbol{\delta}_{p+1})}(e^{-i\mathbf{k}\boldsymbol{\delta}_p} - e^{-i\mathbf{k}\boldsymbol{\delta}_{p+2}}) \\
&\qquad \times [\langle b^\dagger_{j\sigma\mathbf{k}'} a_{j'\sigma'\mathbf{k}'}\rangle a^\dagger_{j'\sigma'\mathbf{k}} a_{j\sigma\mathbf{k}} + \langle a^\dagger_{j'\sigma'\mathbf{k}} a_{j\sigma\mathbf{k}}\rangle b^\dagger_{j\sigma\mathbf{k}'} a_{j'\sigma'\mathbf{k}'}] \\
&+ e^{i(\mathbf{k}'-\mathbf{k})(\boldsymbol{\delta}_{p'+1}-\boldsymbol{\delta}_{p+1})}(e^{-i\mathbf{k}\boldsymbol{\delta}_p} - e^{-i\mathbf{k}\boldsymbol{\delta}_{p+2}}) \\
&\qquad \times [\langle b^\dagger_{j\sigma\mathbf{k}'} b_{j'\sigma'\mathbf{k}'}\rangle b^\dagger_{j'\sigma'\mathbf{k}} a_{j\sigma\mathbf{k}} + \langle b^\dagger_{j'\sigma'\mathbf{k}} a_{j\sigma\mathbf{k}}\rangle b^\dagger_{j\sigma\mathbf{k}'} b_{j'\sigma'\mathbf{k}'}] \Bigg) \\
= -\frac{V_0}{2N} \sum_{j,j'} \sum_{\sigma,\sigma'} \sum_{\mathbf{k},\mathbf{k}'} \sum_{p,p'} \frac{\alpha_1}{3} \Bigg(& [e^{i(\mathbf{k}'-\mathbf{k})(\boldsymbol{\delta}_{p'}-\boldsymbol{\delta}_{p+1})}(e^{i\mathbf{k}'\boldsymbol{\delta}_p} - e^{i\mathbf{k}'\boldsymbol{\delta}_{p+2}})\langle a^\dagger_{j'\sigma'\mathbf{k}'} a_{j\sigma\mathbf{k}'}\rangle \\
&\qquad + e^{-i(\mathbf{k}'-\mathbf{k})(\boldsymbol{\delta}_{p'+1}-\boldsymbol{\delta}_{p+1})}(e^{i\mathbf{k}\boldsymbol{\delta}_p} - e^{i\mathbf{k}\boldsymbol{\delta}_{p+2}})\langle b^\dagger_{j'\sigma'\mathbf{k}'} b_{j\sigma\mathbf{k}'}\rangle] a^\dagger_{j\sigma\mathbf{k}} b_{j'\sigma'\mathbf{k}} \\
&+ [e^{-i(\mathbf{k}'-\mathbf{k})(\boldsymbol{\delta}_{p'}-\boldsymbol{\delta}_{p+1})}(e^{i\mathbf{k}\boldsymbol{\delta}_p} - e^{i\mathbf{k}\boldsymbol{\delta}_{p+2}})\langle a^\dagger_{j'\sigma'\mathbf{k}'} b_{j\sigma\mathbf{k}'}\rangle \\
&\qquad + e^{i(\mathbf{k}'-\mathbf{k})(\boldsymbol{\delta}_{p'}-\boldsymbol{\delta}_{p+1})}(e^{-i\mathbf{k}\boldsymbol{\delta}_p} - e^{-i\mathbf{k}\boldsymbol{\delta}_{p+2}})\langle b^\dagger_{j'\sigma'\mathbf{k}'} a_{j\sigma\mathbf{k}'}\rangle] a^\dagger_{j\sigma\mathbf{k}} a_{j'\sigma'\mathbf{k}} \\
&+ [e^{i(\mathbf{k}'-\mathbf{k})(\boldsymbol{\delta}_{p'+1}-\boldsymbol{\delta}_{p+1})}(e^{i\mathbf{k}'\boldsymbol{\delta}_p} - e^{i\mathbf{k}'\boldsymbol{\delta}_{p+2}})\langle a^\dagger_{j'\sigma'\mathbf{k}'} b_{j\sigma\mathbf{k}'}\rangle \\
&\qquad + e^{-i(\mathbf{k}'-\mathbf{k})(\boldsymbol{\delta}_{p'+1}-\boldsymbol{\delta}_{p+1})}(e^{-i\mathbf{k}'\boldsymbol{\delta}_p} - e^{-i\mathbf{k}'\boldsymbol{\delta}_{p+2}})\langle b^\dagger_{j'\sigma'\mathbf{k}'} a_{j\sigma\mathbf{k}'}\rangle] b^\dagger_{j\sigma\mathbf{k}} b_{j'\sigma'\mathbf{k}} \\
&+ [e^{-i(\mathbf{k}'-\mathbf{k})(\boldsymbol{\delta}_{p'}-\boldsymbol{\delta}_{p+1})}(e^{-i\mathbf{k}'\boldsymbol{\delta}_p} - e^{-i\mathbf{k}'\boldsymbol{\delta}_{p+2}})\langle a^\dagger_{j'\sigma'\mathbf{k}'} a_{j\sigma\mathbf{k}'}\rangle \\
&\qquad + e^{i(\mathbf{k}'-\mathbf{k})(\boldsymbol{\delta}_{p'+1}-\boldsymbol{\delta}_{p+1})}(e^{-i\mathbf{k}\boldsymbol{\delta}_p} - e^{-i\mathbf{k}\boldsymbol{\delta}_{p+2}})\langle b^\dagger_{j'\sigma'\mathbf{k}'} b_{j\sigma\mathbf{k}'}\rangle] b^\dagger_{j\sigma\mathbf{k}} a_{j'\sigma'\mathbf{k}} \qquad \text{(E.3)}
\end{aligned}
$$

$$
\begin{aligned}
U^F_{T\times T'} = -\frac{V_0}{2N} \sum_{j,j'} \sum_{\sigma,\sigma'} \sum_{\mathbf{k},\mathbf{k}',\mathbf{q}} \sum_{p,p'} \alpha_1^2\, \delta_{\mathbf{k}',\mathbf{k}+\mathbf{q}} \Bigg(& e^{i\mathbf{q}(\boldsymbol{\delta}_{p+1}-\boldsymbol{\delta}_{p'+1})}(e^{i\mathbf{k}\boldsymbol{\delta}_p} - e^{i\mathbf{k}\boldsymbol{\delta}_{p+2}})(e^{i\mathbf{k}'\boldsymbol{\delta}_{p'}} - e^{i\mathbf{k}'\boldsymbol{\delta}_{p'+2}}) \\
&\qquad \times [\langle a^\dagger_{j\sigma\mathbf{k}} b_{j'\sigma'\mathbf{k}'-\mathbf{q}}\rangle a^\dagger_{j'\sigma'\mathbf{k}'} b_{j\sigma\mathbf{k}+\mathbf{q}} + \langle a^\dagger_{j'\sigma'\mathbf{k}'} b_{j\sigma\mathbf{k}+\mathbf{q}}\rangle a^\dagger_{j\sigma\mathbf{k}} b_{j'\sigma'\mathbf{k}'-\mathbf{q}}] \\
&+ e^{i\mathbf{q}(\boldsymbol{\delta}_{p+1}-\boldsymbol{\delta}_{p'+1})}(e^{i\mathbf{k}\boldsymbol{\delta}_p} - e^{i\mathbf{k}\boldsymbol{\delta}_{p+2}})(e^{-i(\mathbf{k}'-\mathbf{q})\boldsymbol{\delta}_{p'}} - e^{-i(\mathbf{k}'-\mathbf{q})\boldsymbol{\delta}_{p'+2}}) \\
&\qquad \times [\langle a^\dagger_{j\sigma\mathbf{k}} a_{j'\sigma'\mathbf{k}'-\mathbf{q}}\rangle b^\dagger_{j'\sigma'\mathbf{k}'} b_{j\sigma\mathbf{k}+\mathbf{q}} + \langle b^\dagger_{j'\sigma'\mathbf{k}'} b_{j\sigma\mathbf{k}+\mathbf{q}}\rangle a^\dagger_{j\sigma\mathbf{k}} a_{j'\sigma'\mathbf{k}'-\mathbf{q}}] \\
&+ e^{-i\mathbf{q}(\boldsymbol{\delta}_{p+1}-\boldsymbol{\delta}_{p'+1})}(e^{-i\mathbf{k}\boldsymbol{\delta}_p} - e^{-i\mathbf{k}\boldsymbol{\delta}_{p+2}})(e^{i(\mathbf{k}'-\mathbf{q})\boldsymbol{\delta}_{p'}} - e^{i(\mathbf{k}'-\mathbf{q})\boldsymbol{\delta}_{p'+2}}) \\
&\qquad \times [\langle b^\dagger_{j\sigma\mathbf{k}+\mathbf{q}} b_{j'\sigma'\mathbf{k}'}\rangle a^\dagger_{j'\sigma'\mathbf{k}'-\mathbf{q}} a_{j\sigma\mathbf{k}} + \langle a^\dagger_{j'\sigma'\mathbf{k}'-\mathbf{q}} a_{j\sigma\mathbf{k}}\rangle b^\dagger_{j\sigma\mathbf{k}+\mathbf{q}} b_{j'\sigma'\mathbf{k}'}] \\
&+ e^{-i\mathbf{q}(\boldsymbol{\delta}_{p+1}-\boldsymbol{\delta}_{p'+1})}(e^{-i\mathbf{k}\boldsymbol{\delta}_p} - e^{-i\mathbf{k}\boldsymbol{\delta}_{p+2}})(e^{-i\mathbf{k}'\boldsymbol{\delta}_{p'}} - e^{-i\mathbf{k}'\boldsymbol{\delta}_{p'+2}}) \\
&\qquad \times [\langle b^\dagger_{j\sigma\mathbf{k}+\mathbf{q}} a_{j'\sigma'\mathbf{k}'}\rangle b^\dagger_{j'\sigma'\mathbf{k}'-\mathbf{q}} a_{j\sigma\mathbf{k}} + \langle b^\dagger_{j'\sigma'\mathbf{k}'-\mathbf{q}} a_{j\sigma\mathbf{k}}\rangle b^\dagger_{j\sigma\mathbf{k}+\mathbf{q}} a_{j'\sigma'\mathbf{k}'}] \Bigg) \\
= -\frac{V_0}{2N} \sum_{j,j'} \sum_{\sigma,\sigma'} \sum_{\mathbf{k},\mathbf{k}'} \sum_{p,p'} \alpha_1^2 \Bigg(& e^{i(\mathbf{k}'-\mathbf{k})(\boldsymbol{\delta}_{p+1}-\boldsymbol{\delta}_{p'+1})}(e^{i\mathbf{k}\boldsymbol{\delta}_p} - e^{i\mathbf{k}\boldsymbol{\delta}_{p+2}})(e^{i\mathbf{k}'\boldsymbol{\delta}_{p'}} - e^{i\mathbf{k}'\boldsymbol{\delta}_{p'+2}}) \\
&\qquad \times [\langle a^\dagger_{j\sigma\mathbf{k}} b_{j'\sigma'\mathbf{k}}\rangle a^\dagger_{j'\sigma'\mathbf{k}'} b_{j\sigma\mathbf{k}'} + \langle a^\dagger_{j'\sigma'\mathbf{k}'} b_{j\sigma\mathbf{k}'}\rangle a^\dagger_{j\sigma\mathbf{k}} b_{j'\sigma'\mathbf{k}}] \\
&+ e^{i(\mathbf{k}'-\mathbf{k})(\boldsymbol{\delta}_{p+1}-\boldsymbol{\delta}_{p'+1})}(e^{i\mathbf{k}\boldsymbol{\delta}_p} - e^{i\mathbf{k}\boldsymbol{\delta}_{p+2}})(e^{-i\mathbf{k}\boldsymbol{\delta}_{p'}} - e^{-i\mathbf{k}\boldsymbol{\delta}_{p'+2}}) \\
&\qquad \times [\langle a^\dagger_{j\sigma\mathbf{k}} a_{j'\sigma'\mathbf{k}}\rangle b^\dagger_{j'\sigma'\mathbf{k}'} b_{j\sigma\mathbf{k}'} + \langle b^\dagger_{j'\sigma'\mathbf{k}'} b_{j\sigma\mathbf{k}'}\rangle a^\dagger_{j\sigma\mathbf{k}} a_{j'\sigma'\mathbf{k}}] \\
&+ e^{-i(\mathbf{k}'-\mathbf{k})(\boldsymbol{\delta}_{p+1}-\boldsymbol{\delta}_{p'+1})}(e^{-i\mathbf{k}\boldsymbol{\delta}_p} - e^{-i\mathbf{k}\boldsymbol{\delta}_{p+2}})(e^{i\mathbf{k}\boldsymbol{\delta}_{p'}} - e^{i\mathbf{k}\boldsymbol{\delta}_{p'+2}}) \\
&\qquad \times [\langle b^\dagger_{j\sigma\mathbf{k}'} b_{j'\sigma'\mathbf{k}'}\rangle a^\dagger_{j'\sigma'\mathbf{k}} a_{j\sigma\mathbf{k}} + \langle a^\dagger_{j'\sigma'\mathbf{k}} a_{j\sigma\mathbf{k}}\rangle b^\dagger_{j\sigma\mathbf{k}'} b_{j'\sigma'\mathbf{k}'}] \\
&+ e^{-i(\mathbf{k}'-\mathbf{k})(\boldsymbol{\delta}_{p+1}-\boldsymbol{\delta}_{p'+1})}(e^{-i\mathbf{k}\boldsymbol{\delta}_p} - e^{-i\mathbf{k}\boldsymbol{\delta}_{p+2}})(e^{-i\mathbf{k}'\boldsymbol{\delta}_{p'}} - e^{-i\mathbf{k}'\boldsymbol{\delta}_{p'+2}}) \\
&\qquad \times [\langle b^\dagger_{j\sigma\mathbf{k}'} a_{j'\sigma'\mathbf{k}'}\rangle b^\dagger_{j'\sigma'\mathbf{k}} a_{j\sigma\mathbf{k}} + \langle b^\dagger_{j'\sigma'\mathbf{k}} a_{j\sigma\mathbf{k}}\rangle b^\dagger_{j\sigma\mathbf{k}'} a_{j'\sigma'\mathbf{k}'}] \Bigg)
\end{aligned}
$$

$$
\begin{aligned}
&= -\frac{V_0}{2N}\sum_{j,j'}\sum_{\sigma,\sigma'}\sum_{\mathbf{k},\mathbf{k}'}\sum_{p,p'}\alpha_1^2\Big(\big[e^{-i(\mathbf{k}'-\mathbf{k})(\boldsymbol{\delta}_{p+1}-\boldsymbol{\delta}_{p'+1})}(e^{i\mathbf{k}'\boldsymbol{\delta}_p}-e^{i\mathbf{k}'\boldsymbol{\delta}_{p+2}})(e^{i\mathbf{k}\boldsymbol{\delta}_{p'}}-e^{i\mathbf{k}\boldsymbol{\delta}_{p'+2}})\langle a^\dagger_{j'\sigma'\mathbf{k}'}b_{j\sigma\mathbf{k}'}\rangle\\
&\qquad + e^{i(\mathbf{k}'-\mathbf{k})(\boldsymbol{\delta}_{p+1}-\boldsymbol{\delta}_{p'+1})}(e^{i\mathbf{k}\boldsymbol{\delta}_p}-e^{i\mathbf{k}\boldsymbol{\delta}_{p+2}})(e^{i\mathbf{k}'\boldsymbol{\delta}_{p'}}-e^{i\mathbf{k}'\boldsymbol{\delta}_{p'+2}})\langle a^\dagger_{j'\sigma'\mathbf{k}'}b_{j\sigma\mathbf{k}'}\rangle\big]a^\dagger_{j\sigma\mathbf{k}}b_{j'\sigma'\mathbf{k}}\\
&\quad + \big[e^{-i(\mathbf{k}'-\mathbf{k})(\boldsymbol{\delta}_{p+1}-\boldsymbol{\delta}_{p'+1})}(e^{i\mathbf{k}'\boldsymbol{\delta}_p}-e^{i\mathbf{k}'\boldsymbol{\delta}_{p+2}})(e^{-i\mathbf{k}'\boldsymbol{\delta}_{p'}}-e^{-i\mathbf{k}'\boldsymbol{\delta}_{p'+2}})\langle a^\dagger_{j'\sigma'\mathbf{k}'}a_{j\sigma\mathbf{k}'}\rangle\\
&\qquad + e^{i(\mathbf{k}'-\mathbf{k})(\boldsymbol{\delta}_{p+1}-\boldsymbol{\delta}_{p'+1})}(e^{-i\mathbf{k}'\boldsymbol{\delta}_p}-e^{-i\mathbf{k}'\boldsymbol{\delta}_{p+2}})(e^{i\mathbf{k}'\boldsymbol{\delta}_{p'}}-e^{i\mathbf{k}'\boldsymbol{\delta}_{p'+2}})\langle a^\dagger_{j'\sigma'\mathbf{k}'}a_{j\sigma\mathbf{k}'}\rangle\big]b^\dagger_{j\sigma\mathbf{k}}b_{j'\sigma'\mathbf{k}}\\
&\quad + \big[e^{i(\mathbf{k}'-\mathbf{k})(\boldsymbol{\delta}_{p+1}-\boldsymbol{\delta}_{p'+1})}(e^{i\mathbf{k}\boldsymbol{\delta}_p}-e^{i\mathbf{k}\boldsymbol{\delta}_{p+2}})(e^{-i\mathbf{k}\boldsymbol{\delta}_{p'}}-e^{-i\mathbf{k}\boldsymbol{\delta}_{p'+2}})\langle b^\dagger_{j'\sigma'\mathbf{k}'}b_{j\sigma\mathbf{k}'}\rangle\\
&\qquad + e^{-i(\mathbf{k}'-\mathbf{k})(\boldsymbol{\delta}_{p+1}-\boldsymbol{\delta}_{p'+1})}(e^{-i\mathbf{k}\boldsymbol{\delta}_p}-e^{-i\mathbf{k}\boldsymbol{\delta}_{p+2}})(e^{i\mathbf{k}\boldsymbol{\delta}_{p'}}-e^{i\mathbf{k}\boldsymbol{\delta}_{p'+2}})\langle b^\dagger_{j'\sigma'\mathbf{k}'}b_{j\sigma\mathbf{k}'}\rangle\big]a^\dagger_{j\sigma\mathbf{k}}a_{j'\sigma'\mathbf{k}}\\
&\quad + \big[e^{-i(\mathbf{k}'-\mathbf{k})(\boldsymbol{\delta}_{p+1}-\boldsymbol{\delta}_{p'+1})}(e^{-i\mathbf{k}\boldsymbol{\delta}_p}-e^{-i\mathbf{k}\boldsymbol{\delta}_{p+2}})(e^{-i\mathbf{k}'\boldsymbol{\delta}_{p'}}-e^{-i\mathbf{k}'\boldsymbol{\delta}_{p'+2}})\langle b^\dagger_{j'\sigma'\mathbf{k}'}a_{j\sigma\mathbf{k}'}\rangle\\
&\qquad + e^{i(\mathbf{k}'-\mathbf{k})(\boldsymbol{\delta}_{p+1}-\boldsymbol{\delta}_{p'+1})}(e^{-i\mathbf{k}'\boldsymbol{\delta}_p}-e^{-i\mathbf{k}'\boldsymbol{\delta}_{p+2}})(e^{-i\mathbf{k}\boldsymbol{\delta}_{p'}}-e^{-i\mathbf{k}\boldsymbol{\delta}_{p'+2}})\langle b^\dagger_{j'\sigma'\mathbf{k}'}a_{j\sigma\mathbf{k}'}\rangle\big]b^\dagger_{j\sigma\mathbf{k}}a_{j'\sigma'\mathbf{k}}\Big)\\
&= -\frac{2\alpha_1^2V_0}{2N}\sum_{j,j'}\sum_{\sigma,\sigma'}\sum_{\mathbf{k},\mathbf{k}'}\sum_{p,p'}\Big(e^{-i(\mathbf{k}'-\mathbf{k})(\boldsymbol{\delta}_{p+1}-\boldsymbol{\delta}_{p'+1})}(e^{i\mathbf{k}'\boldsymbol{\delta}_p}-e^{i\mathbf{k}'\boldsymbol{\delta}_{p+2}})(e^{i\mathbf{k}\boldsymbol{\delta}_{p'}}-e^{i\mathbf{k}\boldsymbol{\delta}_{p'+2}})\langle a^\dagger_{j'\sigma'\mathbf{k}'}b_{j\sigma\mathbf{k}'}\rangle a^\dagger_{j\sigma\mathbf{k}}b_{j'\sigma'\mathbf{k}}\\
&\quad + e^{-i(\mathbf{k}'-\mathbf{k})(\boldsymbol{\delta}_{p+1}-\boldsymbol{\delta}_{p'+1})}(e^{i\mathbf{k}'\boldsymbol{\delta}_p}-e^{i\mathbf{k}'\boldsymbol{\delta}_{p+2}})(e^{-i\mathbf{k}'\boldsymbol{\delta}_{p'}}-e^{-i\mathbf{k}'\boldsymbol{\delta}_{p'+2}})\langle a^\dagger_{j'\sigma'\mathbf{k}'}a_{j\sigma\mathbf{k}'}\rangle b^\dagger_{j\sigma\mathbf{k}}b_{j'\sigma'\mathbf{k}}\\
&\quad + e^{i(\mathbf{k}'-\mathbf{k})(\boldsymbol{\delta}_{p+1}-\boldsymbol{\delta}_{p'+1})}(e^{i\mathbf{k}\boldsymbol{\delta}_p}-e^{i\mathbf{k}\boldsymbol{\delta}_{p+2}})(e^{-i\mathbf{k}\boldsymbol{\delta}_{p'}}-e^{-i\mathbf{k}\boldsymbol{\delta}_{p'+2}})\langle b^\dagger_{j'\sigma'\mathbf{k}'}b_{j\sigma\mathbf{k}'}\rangle a^\dagger_{j\sigma\mathbf{k}}a_{j'\sigma'\mathbf{k}}\\
&\quad + e^{i(\mathbf{k}'-\mathbf{k})(\boldsymbol{\delta}_{p+1}-\boldsymbol{\delta}_{p'+1})}(e^{-i\mathbf{k}'\boldsymbol{\delta}_p}-e^{-i\mathbf{k}'\boldsymbol{\delta}_{p+2}})(e^{-i\mathbf{k}\boldsymbol{\delta}_{p'}}-e^{-i\mathbf{k}\boldsymbol{\delta}_{p'+2}})\langle b^\dagger_{j'\sigma'\mathbf{k}'}a_{j\sigma\mathbf{k}'}\rangle b^\dagger_{j\sigma\mathbf{k}}a_{j'\sigma'\mathbf{k}}\Big)
\end{aligned}
\tag{E.4}
$$

Collecting terms and defining

$$A^{\alpha^\dagger\beta}_{pp'}(\mathbf{k}'-\mathbf{k}) \equiv e^{i(\mathbf{k}'-\mathbf{k})(\boldsymbol{\delta}_p-\boldsymbol{\delta}_{p'})}\langle\alpha^\dagger_{j'\sigma'\mathbf{k}'}\beta_{j\sigma\mathbf{k}'}\rangle \qquad \text{and} \tag{E.5}$$

$$B_p(\mathbf{k}) \equiv e^{i\mathbf{k}\boldsymbol{\delta}_p}-e^{i\mathbf{k}\boldsymbol{\delta}_{p+2}}, \tag{E.6}$$

allows us to write the full contribution from exchange term as,

$$
\begin{aligned}
U^F = -\frac{V_0}{N}\sum_{j,j'}\sum_{\sigma,\sigma'}\sum_{\mathbf{k},\mathbf{k}'}\sum_{p,p'}\Big[&\frac{1}{18}[A^{a^\dagger a}_{pp'}(\mathbf{k}'-\mathbf{k})+A^{a^\dagger a}_{pp'}(\mathbf{k}-\mathbf{k}')]+\frac{\alpha_1}{3}[A^{a^\dagger b}_{p\bar{p}'}(\mathbf{k}-\mathbf{k}')B_{p'}(\mathbf{k})+A^{b^\dagger a}_{p\bar{p}'}(\mathbf{k}'-\mathbf{k})B_{p'}(-\mathbf{k})]\\
&+\alpha_1^2A^{b^\dagger b}_{\bar{p}\bar{p}'}(\mathbf{k}'-\mathbf{k})B_p(\mathbf{k})B_{p'}(-\mathbf{k})\Big]a^\dagger_{j\sigma\mathbf{k}}a_{j'\sigma'\mathbf{k}}\\
+\Big[&\frac{1}{18}[A^{b^\dagger b}_{\bar{p}\bar{p}'}(\mathbf{k}'-\mathbf{k})+A^{b^\dagger b}_{\bar{p}\bar{p}'}(\mathbf{k}-\mathbf{k}')]+\frac{\alpha_1}{3}[A^{a^\dagger b}_{\bar{p}\bar{p}'}(\mathbf{k}'-\mathbf{k})B_{p'}(\mathbf{k}')+A^{b^\dagger a}_{\bar{p}\bar{p}'}(\mathbf{k}-\mathbf{k}')B_{p'}(-\mathbf{k}')]\\
&+\alpha_1^2A^{a^\dagger a}_{\bar{p}\bar{p}'}(\mathbf{k}-\mathbf{k}')B_p(\mathbf{k}')B_{p'}(-\mathbf{k}')\Big]b^\dagger_{j\sigma\mathbf{k}}b_{j'\sigma'\mathbf{k}}\\
+\Big[&\frac{1}{18}[A^{b^\dagger a}_{p\bar{p}'}(\mathbf{k}'-\mathbf{k})+A^{b^\dagger a}_{\bar{p}p'}(\mathbf{k}-\mathbf{k}')]+\frac{\alpha_1}{3}[A^{a^\dagger a}_{p\bar{p}'}(\mathbf{k}'-\mathbf{k})B_{p'}(\mathbf{k}')+A^{b^\dagger b}_{\bar{p}\bar{p}'}(\mathbf{k}-\mathbf{k}')B_{p'}(\mathbf{k})]\\
&+\alpha_1^2A^{a^\dagger b}_{\bar{p}\bar{p}'}(\mathbf{k}-\mathbf{k}')B_p(\mathbf{k}')B_{p'}(\mathbf{k})\Big]a^\dagger_{j\sigma\mathbf{k}}b_{j'\sigma'\mathbf{k}}\\
+\Big[&\frac{1}{18}[A^{a^\dagger b}_{\bar{p}p'}(\mathbf{k}'-\mathbf{k})+A^{a^\dagger b}_{p\bar{p}'}(\mathbf{k}-\mathbf{k}')]+\frac{\alpha_1}{3}[A^{a^\dagger a}_{p\bar{p}'}(\mathbf{k}-\mathbf{k}')B_{p'}(-\mathbf{k}')+A^{b^\dagger b}_{\bar{p}\bar{p}'}(\mathbf{k}'-\mathbf{k})B_{p'}(-\mathbf{k})]\\
&+\alpha_1^2A^{b^\dagger a}_{\bar{p}\bar{p}'}(\mathbf{k}'-\mathbf{k})B_p(-\mathbf{k}')B_{p'}(-\mathbf{k})\Big]b^\dagger_{j\sigma\mathbf{k}}a_{j'\sigma'\mathbf{k}}.
\end{aligned}
\tag{E.7}
$$

Here $\bar{p}$ ($\bar{p}'$) denote odd values of p (p'), i.e. all terms with $\boldsymbol{\delta}_{p+1}$ ($\boldsymbol{\delta}_{p'+1}$). The matrix structure is,

$$U^F = -V_0\sum_{\mathbf{k}}\mathbf{f}^\dagger_{\mathbf{k}}\begin{pmatrix}\underline{\underline{M_1}} & \underline{\underline{M_2}}\\ \underline{\underline{M_3}} & \underline{\underline{M_4}}\end{pmatrix}\mathbf{f}_{\mathbf{k}}$$

$$\equiv -V_0 \sum_{\mathbf{k}} \mathbf{f}_{\mathbf{k}}^{\dagger} M^F \mathbf{f}_{\mathbf{k}} \tag{E.8}$$

with

$$\begin{aligned}
M^{\sigma'\sigma}_{1,j'j} = \frac{1}{N}\sum_{p,p',\mathbf{k}'} \Big[& \frac{1}{18}[A^{a^\dagger a}_{pp'}(\mathbf{k}'-\mathbf{k}) + A^{a^\dagger a}_{pp'}(\mathbf{k}-\mathbf{k}')] \\
& + \frac{\alpha_1}{3}[A^{a^\dagger b}_{p\bar{p}'}(\mathbf{k}-\mathbf{k}')B_{p'}(\mathbf{k}) + A^{b^\dagger a}_{p\bar{p}'}(\mathbf{k}'-\mathbf{k})B_{p'}(-\mathbf{k})] + \alpha_1^2 A^{b^\dagger b}_{\bar{p}\bar{p}'}(\mathbf{k}'-\mathbf{k})B_p(\mathbf{k})B_{p'}(-\mathbf{k})\Big], \\
M^{\sigma'\sigma}_{2,j'j} = \frac{1}{N}\sum_{p,p',\mathbf{k}'} \Big[& \frac{1}{18}[A^{b^\dagger a}_{p\bar{p}'}(\mathbf{k}'-\mathbf{k}) + A^{b^\dagger a}_{\bar{p}p'}(\mathbf{k}-\mathbf{k}')] \\
& + \frac{\alpha_1}{3}[A^{a^\dagger a}_{p\bar{p}'}(\mathbf{k}'-\mathbf{k})B_{p'}(\mathbf{k}') + A^{b^\dagger b}_{\bar{p}\bar{p}'}(\mathbf{k}-\mathbf{k}')B_{p'}(\mathbf{k})] + \alpha_1^2 A^{a^\dagger b}_{\bar{p}\bar{p}'}(\mathbf{k}-\mathbf{k}')B_p(\mathbf{k}')B_{p'}(\mathbf{k})\Big], \\
M^{\sigma'\sigma}_{3,j'j} = \frac{1}{N}\sum_{p,p',\mathbf{k}'} \Big[& \frac{1}{18}[A^{a^\dagger b}_{\bar{p}p'}(\mathbf{k}'-\mathbf{k}) + A^{a^\dagger b}_{p\bar{p}'}(\mathbf{k}-\mathbf{k}')] \\
& + \frac{\alpha_1}{3}[A^{a^\dagger a}_{p\bar{p}'}(\mathbf{k}-\mathbf{k}')B_{p'}(-\mathbf{k}') + A^{b^\dagger b}_{\bar{p}\bar{p}'}(\mathbf{k}'-\mathbf{k})B_{p'}(-\mathbf{k})] + \alpha_1^2 A^{b^\dagger a}_{\bar{p}\bar{p}'}(\mathbf{k}'-\mathbf{k})B_p(-\mathbf{k}')B_{p'}(-\mathbf{k})\Big], \\
M^{\sigma'\sigma}_{4,j'j} = \frac{1}{N}\sum_{p,p',\mathbf{k}'} \Big[& \frac{1}{18}[A^{b^\dagger b}_{\bar{p}\bar{p}'}(\mathbf{k}'-\mathbf{k}) + A^{b^\dagger b}_{\bar{p}\bar{p}'}(\mathbf{k}-\mathbf{k}')] \\
& + \frac{\alpha_1}{3}[A^{a^\dagger b}_{\bar{p}\bar{p}'}(\mathbf{k}'-\mathbf{k})B_{p'}(\mathbf{k}') + A^{b^\dagger a}_{\bar{p}\bar{p}'}(\mathbf{k}-\mathbf{k}')B_{p'}(-\mathbf{k}')] + \alpha_1^2 A^{a^\dagger a}_{\bar{p}\bar{p}'}(\mathbf{k}-\mathbf{k}')B_p(\mathbf{k}')B_{p'}(-\mathbf{k}')\Big].
\end{aligned} \tag{E.9}$$

Appendix F

Numerical implementation of interactions in real space

In this appendix we will describe the numerical implementation of the HF decoupled interactions in real space. The interactions read,

$$U^{HF} = V_0 \sum_{\mathbf{R}} \Big[\bar{n}(\mathbf{R})(Q+T) - \sum_{\text{all}} \Big[\sum_{n,m} \alpha_n(p')\alpha_m(p) \langle d^\dagger_{\tau'\sigma'p'+n} d_{\tau\sigma p+m} \rangle \Big] d^\dagger_{\tau\sigma p} d_{\tau'\sigma'p'} \Big], \tag{F.1}$$

where $\sum_{\text{all}} = \Big(\sum_{\tau\tau'} \sum_{\sigma\sigma'} \sum_{pp'} \Big)$, $n, m = \{-1, 0, 1\}$ and we have defined,

$$\bar{n}(\mathbf{R}) = \sum_{\tau'\sigma'p'} \Big(\alpha_0(p') \langle d^\dagger_{\tau',\sigma',p'} d_{\tau',\sigma',p'} \rangle + \alpha_{+1}(p') [\langle d^\dagger_{\tau',\sigma',p'} d_{\tau',\sigma',p'+1} \rangle + \langle d^\dagger_{\tau',\sigma',p'+1} d_{\tau',\sigma',p'} \rangle] \Big), \tag{F.2}$$

$$\bar{\alpha}(p) = \begin{pmatrix} \alpha_{-1} \\ \alpha_0 \\ \alpha_{+1} \end{pmatrix} = \begin{pmatrix} \alpha_1(-1)^p \\ 1/3 \\ \alpha_1(-1)^{p-1} \end{pmatrix}.$$

As the interactions are defined by a sum over all hexagons, $\mathbf{R}$, it is natural to structure the mean fields accordingly. Thus we set up an array with dimensions $dim(\overline{MF}) = (R_{tot}, 6 \times 4, 6 \times 4)$. Here each of the R_{tot} layers contain all mean field parameters related to each hexagon, $R = 0, ..., R_{tot} - 1$. As we have six sites associated with each hexagon and four flavours associated with each site, $\overline{MF}(R)$ has 24×24 inputs where $\overline{MF}(R, i', j') = \langle d^\dagger_{i'} d_{j'} \rangle$ for $i', j' = \{\tau = \pm 1; \sigma = \uparrow, \downarrow; p = 0, .., 5\} = 0, ..., 24$. With this structure of the mean fields, it is sufficient to consider a general method of computing the Hartree and Fock terms within a single hexagon which can easily be extended to the entire system by looping over all R.

We begin by considering the Hartree terms visualized in Fig. F.1a. These terms do not mix primed and unprimed indices, and we only need to compute a single parameter, $\bar{n}(R)$, for each hexagon. The first term of $\bar{n}(R)$ contains all diagonal terms of $\overline{MF}(R)$, $\overline{MF}(R, i', i')$, while the latter two contain all terms with equal flavours but shifted by ± 1 site, respectively, equivalent to $\overline{MF}(R, i', i' + 4) + \overline{MF}(R, i' + 4, i')$. The last two terms of $\bar{n}(R)$ will thus be represented by elements along the shifted diagonals as depicted in Fig. F.1a, where green areas are all $\langle d^\dagger_{\tau',\sigma',p'} d_{\tau',\sigma',p'+1} \rangle$ and blue areas are all $\langle d^\dagger_{\tau',\sigma',p'+1} d_{\tau',\sigma',p'} \rangle$. Periodic boundary conditions are imposed by including the small diagonals in bottom left ($\langle d^\dagger_{\tau',\sigma',p'=5} d_{\tau',\sigma',p'+1=0} \rangle$) and top right ($\langle d^\dagger_{\tau',\sigma',p'+1=0} d_{\tau',\sigma',p'=5} \rangle$) corners. We sum over a total of $3 \times 24 = 72$ terms for each $\bar{n}(R)$ in accordance with Eq. (F.2). $\bar{n}(R)$ is added to $H(i, i), H(i, i + 4)$ and $H(i + 4, i)$, where i is defined from the unique site number and determined through the function $f(R)$ as described in the main text. The additional prefactors in $(Q + T)$ (α_0 and α_{+1}, respectively) is accounted for when $\bar{n}(R)$ is included in H.

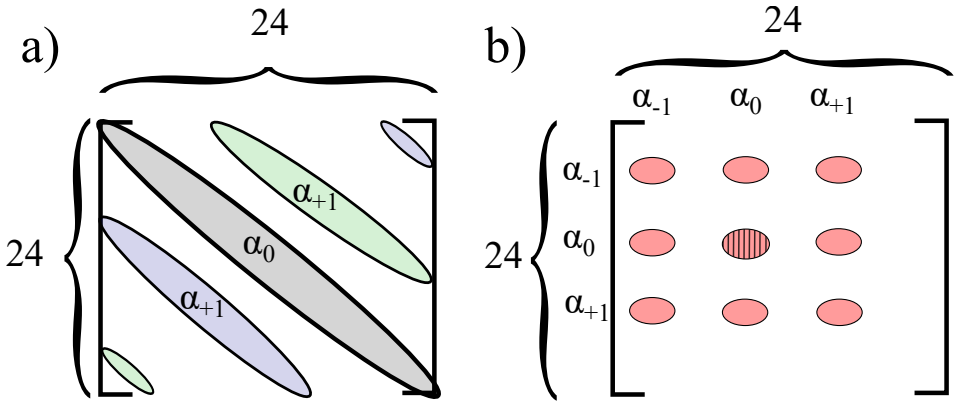

Figure F.1: **Visualization of Hartree and Fock terms**. The encapsulated areas represent the $\overline{MF}(R)$ matrix with 24×24 inputs. **a)** All mean fields included in $\bar{n}(R)$. Grey area is $\langle d^\dagger_{\tau',\sigma',p'} d_{\tau',\sigma',p'} \rangle$, green areas are $\langle d^\dagger_{\tau',\sigma',p'} d_{\tau',\sigma',p'+1} \rangle$ and blue areas are $\langle d^\dagger_{\tau',\sigma',p'+1} d_{\tau',\sigma',p'} \rangle$. $\alpha_{0,+1}$ indicate the relevant prefactor for terms in the given area. **b)** The nine terms included in a single Fock term. Centered, striped area marks the $\langle d^\dagger_{\tau'\sigma'p'} d_{\tau\sigma p} \rangle$ mean field. Remaining eight areas are the assisted hopping exchange terms, when $(n, m) \neq (0, 0)$. Each mean field is related to a prefactor combination indicated by $\alpha_{\pm 1,0}$ marking the prefactor for the given row/column.

In the Fock terms, the sums over primed and unprimed indicies cannot be separated. Thus we must compute an individual input for each $d^\dagger_{\tau,\sigma,p} d_{\tau',\sigma',p'}$ in the hexagon. A visualization of one of these inputs is depicted in Fig. F.1b. Each input is a sum of nine mean fields with nine different prefactor combinations. In Fig. F.1b the centered area marked with stripes illustrates the particular operator combination in question. Here we take the combination $d^\dagger_{+,\downarrow,4} d_{-,\uparrow,1}$ as an example. As the Fock terms are exchange terms, the centered area marked with stripes corresponds to $\langle d^\dagger_{-,\uparrow,1} d_{+,\downarrow,4} \rangle$. The value of this mean field is weighted by $\alpha_0(1)\alpha_0(4) = 1/9$ in accordance with Eq. (F.1). On top of this value, the input at $d^\dagger_{\tau,\sigma,p} d_{\tau',\sigma',p'}$ contains eight assisted hopping exchange terms depicted by the eight adjacent filled, red areas. These mean fields are $\langle d^\dagger_{-,\uparrow,0} d_{+,\downarrow,3} \rangle$, $\langle d^\dagger_{-,\uparrow,0} d_{+,\downarrow,4} \rangle$, $\langle d^\dagger_{-,\uparrow,0} d_{+,\downarrow,5} \rangle$, $\langle d^\dagger_{-,\uparrow,1} d_{+,\downarrow,3} \rangle$, $\langle d^\dagger_{-,\uparrow,1} d_{+,\downarrow,5} \rangle$, $\langle d^\dagger_{-,\uparrow,2} d_{+,\downarrow,3} \rangle$, $\langle d^\dagger_{-,\uparrow,2} d_{+,\downarrow,4} \rangle$ and $\langle d^\dagger_{-,\uparrow,2} d_{+,\downarrow,5} \rangle$. In our convention, the summation over said mean fields with the appropriate prefactors can be written as $\sum_{n,m} \alpha_n(p' = 1)\alpha_m(p = 4)\overline{MF}(R, i' + n, j' + m)$, where $n, m = \{-1, 0, 1\}$, $i' = 5$ and $j' = 18$. This summation is carried out for all 24×24 operator combinations of each hexagon and inserted at the uniquely defined positions in H by use of the function $f(R)$ as described in the main text.

Appendix G

Preprint: Correlation-induced insulating phases at charge neutrality in twisted bilayer graphene

Correlation-induced insulating topological phases at charge neutrality in twisted bilayer graphene

Yuan Da Liao,[1,2] Jian Kang,[3] Clara N. Breiø,[4] Xiao Yan Xu,[5] Han-Qing Wu,[6]
Brian M. Andersen,[4] Rafael M. Fernandes,[7] and Zi Yang Meng[8,1,9]

[1]*Beijing National Laboratory for Condensed Matter Physics and Institute of Physics, Chinese Academy of Sciences, Beijing 100190, China*
[2]*School of Physical Sciences, University of Chinese Academy of Sciences, Beijing 100190, China*
[3]*School of Physical Science and Technology & Institute for Advanced Study, Soochow University, Suzhou, 215006, China*
[4]*Niels Bohr Institute, University of Copenhagen, Lyngbyvej 2, 2100 Copenhagen, Denmark*
[5]*Department of Physics, University of California at San Diego, La Jolla, California 92093, USA*
[6]*School of Physics, Sun Yat-Sen University, Guangzhou, 510275, China*
[7]*School of Physics and Astronomy, University of Minnesota, Minneapolis, MN 55455, USA*
[8]*Department of Physics and HKU-UCAS Joint Institute of Theoretical and Computational Physics, The University of Hong Kong, Pokfulam Road, Hong Kong SAR, China*
[9]*Songshan Lake Materials Laboratory, Dongguan, Guangdong 523808, China*

(Dated: June 16, 2020)

Twisted bilayer graphene (TBG) provides a unique framework to elucidate the interplay between strong correlations and topological phenomena in two-dimensional systems. The existence of multiple electronic degrees of freedom – charge, spin, and valley – gives rise to a plethora of possible ordered states and instabilities. Identifying which of them are realized in the regime of strong correlations is fundamental to shed light on the nature of the superconducting and correlated insulating states observed in the TBG experiments. Here, we use unbiased, sign-problem-free quantum Monte Carlo simulations to solve an effective interacting lattice model for TBG at charge neutrality. Besides the usual cluster Hubbard-like repulsion, this model also contains an assisted hopping interaction that emerges due to the non-trivial topological properties of TBG. Such a non-local interaction fundamentally alters the phase diagram at charge neutrality, gapping the Dirac cones even for small values of the interaction. As the interaction strength increases, a sequence of different correlated insulating phases emerge, including a quantum valley Hall state with topological edge states, an intervalley-coherent insulator, and a valence bond solid. The charge-neutrality correlated insulating phases discovered here provide the sought-after reference states needed for a comprehensive understanding of the insulating states at integer fillings and the proximate superconducting states of TBG.

I. INTRODUCTION

The recent discovery of correlated insulating and superconducting phases in twisted bilayer graphene (TBG) [1–3] and other moiré systems [4–7] sparked a flurry of activity to elucidate and predict the electronic quantum phases realized in their phase diagrams [8–51]. Because the low-energy bands of TBG have a very small bandwidth, of about 10meV at the magic twist angle, the Coulomb interaction, which is of the order of 25meV, is expected to play a fundamental role in shaping the phase diagram [1, 13, 20, 22]. Indeed, insulating states have been reported at all commensurate fillings of the moiré superlattice [10], signaling to the importance of strong correlations. Besides correlations, topological phenomena have also been reported, including a quantum anomalous Hall (QAH) phase [52, 53].

An important issue is the nature of the quantum ground state at charge neutrality, characterized in real space by 4 electrons per moiré unit cell, and in momentum space by Dirac points at the Fermi level. Experimentally, a large charge gap characteristic of an insulating state was reported in transport measurements in Ref. [10] and in STM measurements in Ref. [11], despite no obvious alignment with the underlying hBN layer. The fact that this gap is not observed in all devices has been attributed to inhomogeneity [10]. Theoretically, because the electronic states in TBG have several degrees of freedom – spin, valley, and sublattice – various possible ground states can emerge. Indeed, Hartree-Fock calculations of the continuum model at charge neutrality found various possible phases, such as orbital-magnetization density-waves, valley polarized states, and states that spontaneously break the three-fold rotational symmetry of the moiré lattice [39, 43, 44, 54, 55]. To distinguish among these different possibilities, it is desirable to employ a method that is not only unbiased, but that can also handle strong correlations.

Large-scale quantum Monte Carlo (QMC) simulations provide an optimal tool, limited only by the finite lattice sizes. Although such a limitation makes it impossible to simulate a model with thousands of carbon atoms per moiré unit cell, it is very well suited to solve lattice models on the moiré length scale. At charge neutrality, the non-interacting part of the model has only Dirac points at the Fermi level. The crucial part of the model, however, is the interacting part, which governs the system's behavior in the strong coupling regime. At first sight, based on the analogy with other strongly-correlated models, it would seem enough to consider a cluster Hubbard-like repulsion as the main interaction of the problem. Previously, some of us used QMC to simulate this model, which does not suffer from the infamous fermionic sign-problem [56, 57]. The result was a variety of valence-bond insulating states, which however only onset at relatively large values of the interaction U, of the order of several times the bandwidth W. Below these large values, the system remained in the Dirac semi-metal phase.

However, microscopically, the full interaction of the lattice

model can be derived from projecting the screened Coulomb repulsion on the Wannier states of TBG. The latter turn out to be quite different than in other correlated materials, as they have nodes on the sites of the moiré honeycomb superlattice and a three-peak structure that overlaps with Wannier functions centered at other sites [20–22]. Recent work has shown that this leads to the emergence of an additional and sizable non-local interaction, of the form of an assisted-hopping term [32, 48]. This new interaction ultimately arises from the fact that, in a lattice model, the symmetries of the continuum model cannot all be implemented locally, a phenomenon dubbed Wannier obstruction [22]. Therefore, the assisted-hopping interaction is not a simple perturbation, but a direct and unavoidable manifestation of the non-trivial topological properties of TBG.

In this paper, we study the impact of the assisted-hopping interaction on the ground state of TBG at charge neutrality via sign-problem-free QMC simulations. We find that such a term qualitatively changes the phase diagram, as compared to the case where only the Hubbard interaction is included. In particular, the Dirac semi-metal phase is no longer stable, but is gapped already at weak-coupling. We show that this gap is a manifestation of a quantum valley Hall (QVH) state, characterized by topological edge states. We confirm this weak-coupling result by unrestricted Hartree-Fock (HF) calculations of the same model simulated by QMC. The HF calculations, well suited for weak interactions, also show that the QVH state is a robust property of the weak-coupling regime, and is directly connected to the assisted-hopping term. As the interaction strength increases, a different type of insulating phase arises, displaying intra-valley coherence (IVC) order. This onsite IVC order breaks the spin-valley SU(4) symmetry of the interacting part of the model, resembling recently proposed ferromagnetic-like SU(4) states proposed to emerge in TBG at charge neutrality and other integer fillings [32, 43]. Upon further increasing the interaction, a columnar valence bond solid (cVBS) insulator state appears, favored by the Hubbard-like interaction [56, 57]. Importantly, the presence of the assisted-hopping term makes the QVH and IVC states accessible already for substantially smaller values of U/W, as compared to the case where there is only Hubbard repulsion. Therefore, the experimental observation of such quantum states in TBG at charge neutrality would provide strong evidence for the importance of non-local, topologically-driven interactions in this system.

II. MODEL, SYMMETRY ANALYSIS AND METHOD

As shown in Fig. 1 (a), our model describes two valleys (orbitals) of spinful fermions on the honeycomb lattice that is dual to the triangular moiré superlattice. The Hamiltonian is given by $H = H_0 + H_{\hexagon}$, with the non-interacting tight-binding term:

$$H_0 = -t \sum_{\langle ij\rangle l\sigma} \left(c^\dagger_{il\sigma} c_{jl\sigma} + \text{h.c.} \right), \tag{1}$$

where $c^\dagger_{il\sigma}$ ($c_{il\sigma}$) denotes creation (annihilation) operators of electrons at site i, valley $l = 1, 2$ with spin $\sigma = \uparrow, \downarrow$. The nearest neighbor hopping $t = 1$ and we use the bare bandwidth $W = 6t$ as the energy unit in the remainder of the paper. While this simple band dispersion displays Dirac points at charge neutrality, it does not faithfully reflect the detailed band dispersion obtained by DFT calculations and the topological features of the bands. However, the precise form of H_0 is not expected to play a dominant role in the strong-coupling regime [32], which is our focus here. For this same reason, it is fundamental to correctly capture the effective interaction of this lattice model. Here, we consider an interaction term $H_{\hexagon}$ that contains two contributions:

$$H_{\hexagon} = U \sum_{\hexagon} (Q_{\hexagon} + \alpha T_{\hexagon} - 4)^2, \tag{2}$$

where U sets the overall strength of the Coulomb interaction. The two contributions in Eq. (2) consist of the cluster charge $Q_{\hexagon} \equiv \sum_{j\in\hexagon} \frac{n_j}{3}$, with $n_j = \sum_{l\sigma} c^\dagger_{jl\sigma} c_{jl\sigma}$, and the cluster assisted hopping $T_{\hexagon} \equiv \sum_{j,\sigma} \left(i c^\dagger_{j+1,1\sigma} c_{j,1\sigma} - i c^\dagger_{j+1,2\sigma} c_{j,2\sigma} + h.c. \right)$. Here, the index $j = 1, \ldots, 6$ sums over all six sites of the elemental hexagon in the honeycomb lattice. The pre-factor α controls the relative strength of the two interactions. Hereafter, we fix the electronic filling strictly at the charge neutrality point, where there are four electrons per hexagon once averaging over the lattice.

This form of $H_{\hexagon}$, introduced in Ref. [32], follows from projecting the screened Coulomb interaction on the Wannier states of TBG. The cluster charge term $Q_{\hexagon}$ is analogous to the Hubbard onsite repulsion in the standard Hubbard model; the reason why it extends over the entire hexagon is because of the screening length set by the separation between the gates in a TBG device and because of the overlap between Wannier states of neighboring sites. In TBG, the Wannier wave-functions are not peaked at the honeycomb sites, but instead are extended and peaked at the centers of the three neighboring hexagons. Therefore, one single Wannier state overlaps spatially with other Wannier states on neighboring sites, leading to the cluster charging term $Q_{\hexagon}$. On the other hand, the origin of the assisted hopping term $T_{\hexagon}$ is topological. As explained in Refs. [22, 58], there is an obstruction to construct fully symmetric Wannier states for the isolated nearly-flat bands if one attempts to extend the symmetries of the continuum model of TBG to a lattice model. However, it is still possible to construct Wannier states by implementing the valley-related symmetry $C_2\mathcal{T}$ non-locally [20, 21]. Here, C_2 refers to two-fold rotations with respect to the z-axis and $\mathcal{T}$, to time-reversal. As a consequence, the spatial integral of two neighboring Wannier states inside a single hexagon becomes nonzero, giving rise to the crucial $T_{\hexagon}$ term. The coefficient α is of order unity, and depends on the details of the Wannier states [32].

An interesting feature of $H_{\hexagon}$ is its emergent SU(4) symmetry. To illustrate this, we introduce the spinor $\psi_i = \left(c_{i1\uparrow}, c_{i1\downarrow}, c_{i2\uparrow}, c_{i2\downarrow}\right)^T$ and rewrite the interactions as:

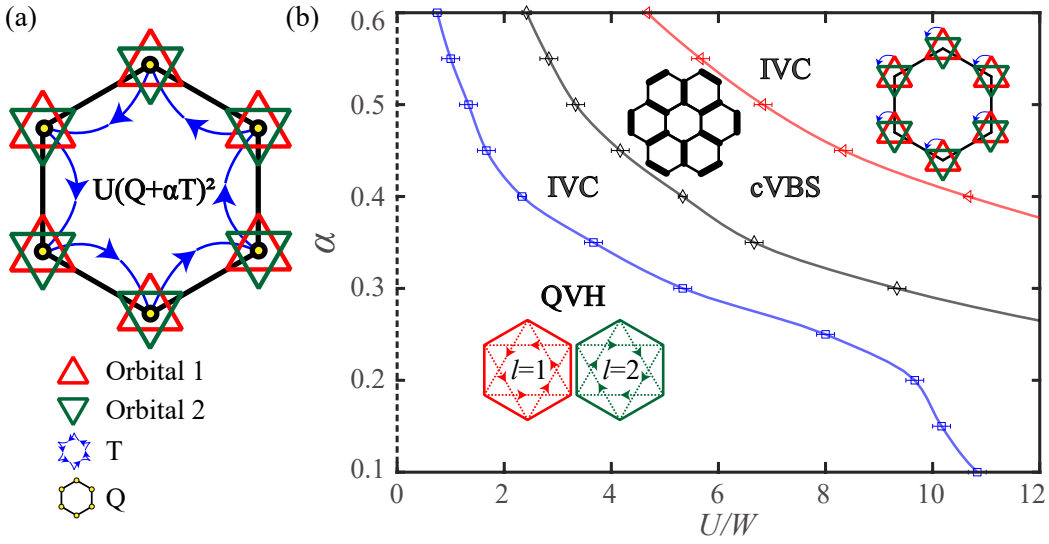

FIG. 1. **Ground state phase diagram at charge neutrality obtained via QMC simulations.** (a) Schematics of the model: each lattice site on the dual moiré honeycomb lattice contains two valleys $l = 1, 2$ (red and green triangles) and spins $\sigma = \uparrow, \downarrow$ (not shown), with spin-valley SU(4) symmetry. The interactions act on every hexagon and consist of the cluster charge term $Q_{\hexagon}$ (yellow dots) and the assisted-hopping interaction term $T_{\hexagon}$ (blue arrows). (b) Ground state phase diagram, spanned by the U/W and α axes, obtained from QMC simulations. The y-axis at $U = 0$ (dash line) stands for the Dirac semi-metal phase. At very small U, the ground state is a quantum valley Hall (QVH) phase characterized by emergent imaginary next-nearest-neighbor hopping with complex conjugation at the valley index, as illustrated by the red and green dashed hoppings with opposite directions. The system has an insulating bulk but acquires topological edge states. Upon further increasing U, an intervalley-coherent (IVC) insulating state is found, which breaks the SU(4) symmetry at every lattice site by removing the valley symmetry. Because it preserves the lattice translational symmetry, it is ferromagnetic-like. The columnar valence bond solid (cVBS) insulator, which appears after the IVC phase, breaks the lattice translational symmetry and preserves the onsite SU(4) symmetry. Note that there is a re-emergence of the IVC phase for the largest interactions probed. The phase transitions between QVH and IVC (blue line), between the IVC and cVBS (black line), and between the cVBS and IVC (red line) are all first order.

$$Q_{\hexagon} = \frac{1}{3}\sum_{i\in\hexagon} \psi_i^\dagger \psi_i \tag{3}$$

$$T_{\hexagon} = i\sum_{i\in\hexagon} \psi_{i+1}^\dagger T_0 \psi_i + \text{h.c.} \tag{4}$$

with $T_0 = \text{diag}(1, 1, -1, -1)$ denoting a diagonal matrix. Consider the unitary transformation $\psi_{i\in\mathcal{A}} \to U\psi_i$ and $\psi_{i\in\mathcal{B}} \to T_0 U T_0 \psi_i$, where U is an arbitrary 4×4 unitary matrix and $\mathcal{A}(\mathcal{B})$ are the two sublattices of the honeycomb lattice. It is clear that both $Q_{\hexagon}$ and $T_{\hexagon}$ are invariant under this transformation. On the other hand, the kinetic term H_0 is not SU(4) symmetric, but invariant only under $\text{U}(1) \times \text{SU}(2) \times \text{SU}(2)$, i.e. the valley U(1) symmetry and the two independent spin SU(2) rotations for the two valleys [22, 38]. Thus, strictly speaking, the SU(4) symmetry is exact for $H_{\hexagon}$ but only approximate for H_0.

To solve the model $H = H_0 + H_{\hexagon}$ non-perturbatively, we employ large-scale projection QMC simulations [56, 57]. This QMC approach, employed in several previous studies [56, 57, 59–62], provides results about the $T = 0$ ground state, the correlation functions (which are used to determine broken symmetries), and the electronic spectra (both single-particle and collective excitations). Despite the presence of the assisted hopping interaction, the model at charge-neutrality does not suffer from the sign-problem (see Appendix B). Thus, it can be efficiently simulated by introducing an extended auxiliary bosonic field that dynamically couples to the electrons on a hexagon – in contrast to the standard Hubbard model, where the auxiliary field is local. Details about the QMC implementation, as well as comparison with results from exact diagonalization, are discussed in the Appendix A and Appendix C.

We also complemented the unbiased QMC simulations with self-consistent HF calculations, which are well-suited for the weak-coupling regime, and can be employed even when additional terms are included in H that introduce a sign-problem for QMC. The HF approach is fully unrestricted in the sense that $H_0 + H_{\hexagon}$ is mean-field decoupled in all channels, and free to acquire any value in site-, spin-, and valley-space. Further technical details, including the resulting coupled set of (real-space) self-consistency equations, can be found in the Appendix E. In the regime of weak interactions, we find excellent agreement between the results obtained from HF and QMC, as shown below.

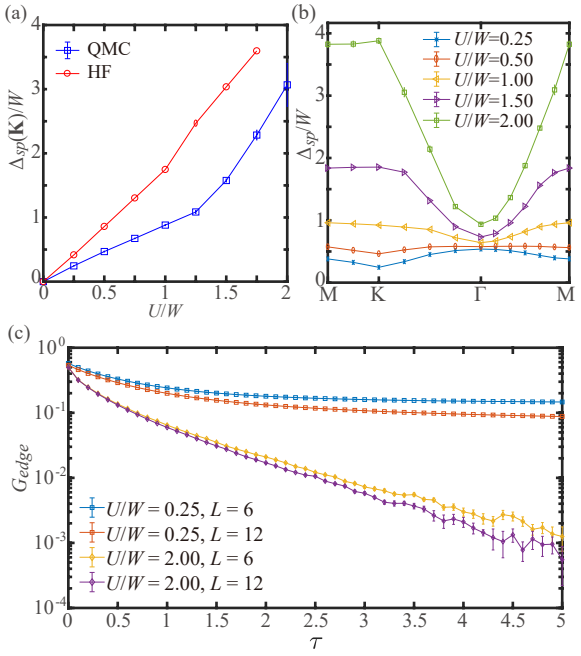

FIG. 2. **Quantum valley Hall insulator (QVH) and gapless edge states.** (a) The single-particle gap $\Delta_{\rm sp}(K)/W$ at the K point as a function of U/W for $\alpha = 0.45$, extracted from both QMC (blue points) and HF calculations (red points). For QMC, the spatial system size is $L = 12$. The Dirac semi-metal is gapped out at the smallest small U values probed. (b) Single-particle gap extracted from QMC with $L = 12$ along a high-symmetry path of the Brillouin zone. (c) The topological nature of the QVH phase is manifested by valley-polarized edge states. Here we compare the edge Green's function for valley $l = 1$ and spin $\uparrow$ at $U/W = 0.25$ (inside the QVH phase) and $U/W = 2.0$ (inside the IVC phase). It is clear that gapless edge modes only appear in the former case, highlighting the topological nature of the QVH phase.

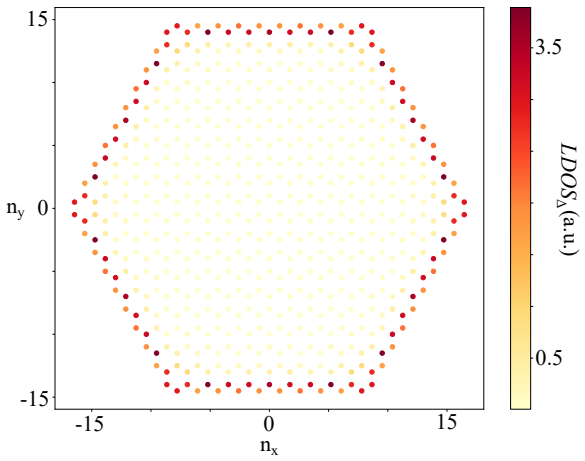

FIG. 3. **In-gap local density of states in the QVH phase.** Real space plot of the local density of states integrated over $1.66 < E/W < 2.00$ with $U/W = 0.5$. The result is computed with parameters as in Table I and open boundary conditions.

III. QUANTUM VALLEY HALL PHASE, INTERVALLEY-COHERENT INSULATOR, AND VALENCE-BOND SOLID

The QMC-derived phase diagram for the ground states at charge neutrality is shown in Fig. 1 (b) as a function of U/W and α. We emphasize that while U gives the overall magnitude of the total interaction term, α is proportional to the relative strength between the assisted-hopping and cluster-charge terms. We find that three types of correlated insulating phases emerge in the phase diagram: the quantum valley Hall (QVH) phase, the intervalley-coherent (IVC) phase, and the columnar valence bond solid (cVBS).

The QVH phase is the ground state for small U values and is characterized by a gap in the single-particle spectrum. This gap can be extracted from the imaginary-time decay of the Green's function along a high-symmetry path of the Brillouin zone (BZ), $G(\mathbf{k}, \tau) \sim e^{-\Delta_{\rm sp}(\mathbf{k})\tau}$. Fig. 2(a) shows the enhancement of the single-particle gap at the K point of the BZ as a function of U for a fixed $\alpha = 0.45$ (blue points). Together with Fig. 2(b), one sees the gap opens at the entire BZ at infinitesimally small U. In many honeycomb lattice models, the Dirac cone at the K point is protected by a symmetry, and the semi-metal phase is robust against weak interactions [56, 57, 59, 66]. In TBG, however, the relevant symmetry, $C_2\mathcal{T}$, cannot be implemented locally due to the topological Wannier obstruction. This opens up the possibility of very weak interactions gapping out the Dirac cone.

In our QMC simulations, for any non-zero α that we investigated, a gap appeared even for the smallest values of U probed. This suggests a weak-coupling origin of this phase. To verify it, we performed HF calculations on the same lattice model. The results, shown by the red points in Fig. 2(a), are in very good agreement with the QMC results. We also used HF to investigate the stability of the gap against changing the phase that appears in the assisted-hopping term $T_{\hexagon}$ [32]. This phase can be gauged away, at the expense of introducing complex hopping terms in H_0, which introduce a sign-problem to the QMC simulations. However, they do not affect the efficiency of the HF algorithm. As discussed in the Appendix E, our analysis confirm that the onset of the QVH phase is robust and appears regardless of the phase of $T_{\hexagon}$.

Importantly, we find that the gap completely disappears when $\alpha = 0$, in agreement with Ref. [57]. Combined with the fact that the gap onsets for small interaction values when $\alpha \neq 0$, this suggests that the origin of the gap can be understood from a mean-field decoupling of the cross-term $\sum_{\hexagon} Q_{\hexagon} T_{\hexagon}$ of the interaction in Eq. 2. This cross-term can be rewritten as:

$$\sum_{\hexagon} Q_{\hexagon} T_{\hexagon} = i \sum_{\hexagon} \sum_{i,j=1}^{6} \sum_{l,m=1}^{2} (-1)^m \left(c^{\dagger}_{i,l} c^{\dagger}_{j+1,m} c_{j,m} c_{i,l} - h.c. \right) \tag{5}$$

where l and m are valley indices and the spin index is omitted for simplicity. The terms with $j = i - 1$ and $j = i$ vanish after summing over different hexagons. In the weak-coupling limit, we can do a mean-field decoupling and use $\langle c^{\dagger}_{i,l} c_{i+1,m} \rangle \propto \delta_{lm}$, due to the nearest-neighbor hopping term present in H_0. The

cross-term then becomes:

$$\sum_{\hexagon} Q_{\hexagon} T_{\hexagon} \propto -i \sum_{\hexagon} \sum_{i=1}^{6} \sum_{l=1}^{2} (-1)^l \left(c^{\dagger}_{i,l} c_{i+2,l} + c^{\dagger}_{i-2,l} c_{i,l} - h.c. \right) \tag{6}$$

Thus, the cross-term of the interaction naturally induces an imaginary hopping between next-nearest-neighbors in the weak-coupling limit. As a consequence, the mean-field Hamiltonian becomes two copies (four, if we consider the spin degeneracy) of the Haldane model [64], leading to a Chern number of ± 1 for the two different valleys. For this reason, we call this state a QVH phase; it is illustrated in the corresponding inset in Fig. 1 (b). We verified that our self-consistent HF calculation generates the same pattern of imaginary NNN hopping.

One of the hallmarks of the Haldane model is the existence of gapless edge modes, despite the bulk being gapped. In the QVH phase, these edge states should be valley-polarized. To probe them, we performed QMC simulations with open boundary conditions and extracted the imaginary-time Green's functions on the edge, $G_{\text{edge}}(\tau) \sim e^{-\Delta_{\text{sp}}\tau}$. As shown in Fig. 2 (c), in the regime of small U ($U/W = 0.25$), the Green's function on the edge decays to a constant in the long imaginary-time limit, demonstrating the existence of a gapless edge mode in the QVH phase. To verify the existence of edge states, we also use HF to capture the topological nature of the QVH phase. In practice, we open the boundaries in the system and compute a self-consistent result with parameters as in Table I ($t = 1$,$\alpha = 0.45$, $U/W = 0.5$, $T = 2.5 \cdot 10^{-5}$ and $N = 4 \times 600$). We find clear evidence of edge states as seen in Fig. 3. Note that a Chern number can be defined separately for each valley $l = 1$ and $l = 2$ (with spin degeneracy). Because the valley $U(1)$ symmetry guarantees that these two Chern numbers must be equal, the whole system is characterized by one Chern number that takes integer values, i.e. it belongs to a $\mathcal{Z}$ classification [65].

Fig. 2(c) also shows that, as U increases ($U/W = 2$), the gapless edge mode disappears, signalling a departure from the topological QVH phase. Clearly, the bulk remains gapped, as shown in Fig. 2(a). The new insulating phase is an intervalley coherent (IVC) state, which spontaneously breaks the onsite spin-valley SU(4) symmetry. In the QMC simulations, IVC order is signalled by an enhancement of the correlation function $C_I(\mathbf{k}) = \frac{1}{L^4} \sum_{i,j \in \mathcal{A}(\mathcal{B})} e^{i\mathbf{k}\cdot(\mathbf{r}_i - \mathbf{r}_j)} \left\langle I_i I_j \right\rangle$, here, the operator $I_i = \sum_{\sigma} (c^{\dagger}_{i,l,\sigma} c_{i,l',\sigma} + h.c.)$, $l \neq l'$, represents an "onsite hopping" between the two different valleys. Thus, the correlation function is a 2×2 matrix in sublattice space, i.e. $\begin{pmatrix} C_I^{\mathcal{A}\mathcal{A}} & C_I^{\mathcal{A}\mathcal{B}} \\ C_I^{\mathcal{B}\mathcal{A}} & C_I^{\mathcal{B}\mathcal{B}} \end{pmatrix}$, which has the relation $C_I^{\mathcal{A}\mathcal{A}} = C_I^{\mathcal{B}\mathcal{B}} = -C_I^{\mathcal{A}\mathcal{B}} = -C_I^{\mathcal{B}\mathcal{A}}$. In the upper panels of Figs. 4(a) and 4(b), we show one of diagonal compent $C_I^{\mathcal{A}\mathcal{A}}(\mathbf{k})$. The fact that the correlation function is peaked at $\mathbf{k} = \mathbf{\Gamma}$ implies that the IVC order is ferromagnetic-like, i.e. it does not break translational symmetry. Such an onsite coupling between opposite valleys (see the corresponding inset in the phase diagram in Fig. 1 (b)) breaks the valley $U(1)$ symmetry, and hence the SU(4) symmetry of the model. The fact that the SU(4) symmetry-breaking pattern is ferromagnetic-like is similar to recent analytical results [32, 33], which focused, however, at integer fillings away from charge neutrality.

For larger values of U/W, as shown in Fig. 4, the IVC order fades away, but the system remains insulating. The new state that emerges is the columnar valence-bond solid (cVBS) insulator, characterized by the appearance of strong nearest-neighbor bonds forming the pattern illustrated in the corresponding inset of Fig. 1 (b). The onset of cVBS order is signalled by an enhancement of the bond-bond correlation function [56, 57], $C_B(\mathbf{k}) = \frac{1}{L^4} \sum_{i,j} e^{i\mathbf{k}\cdot(\mathbf{r}_i - \mathbf{r}_j)} \left\langle B_{i,\delta} B_{j,\delta} \right\rangle$, with bond operator $B_{i,\delta} = \sum_{l,\sigma} (c^{\dagger}_{i,l,\sigma} c_{i+\delta,l,\sigma} + h.c.)$ and δ denoting one of the three nearest-neighbor bond directions of the honeycomb lattice ($\hat{e_1}$, $\hat{e_2}$ and $\hat{e_3}$). For this particular calculation, $\hat{e}_1$ was chosen.

As shown in the lower panels of Figs. 4(a) and 4(b), we find an enhanced $C_B(\mathbf{k})$ at momenta $\mathbf{K}$ and $\mathbf{K}'$, demonstrating that the bond-order pattern breaks translational symmetry. However, a peak of $C_B(\mathbf{k})$ at these momenta does not allow us to unambiguously identify the cVBS state, as the plaquette valence-bond solid (pVBS) also displays peaks at the same momenta [56, 57, 66, 67]. To further distinguish the two types of VBS phases, we construct the complex order parameter $D_{\mathbf{K}} = \frac{1}{L^2} \sum_i \left(B_{i,\hat{e}_1} + \omega B_{i,\hat{e}_2} + \omega^2 B_{i,\hat{e}_3} \right) e^{i\mathbf{K}\cdot\mathbf{r}_i}$ with $\omega = e^{i\frac{2\pi}{3}}$. The Monte Carlo histogram of $D_{\mathbf{K}}$ is different for the two VBS phases [66, 67]: for the pVBS state, the angular distribution of $D_{\mathbf{K}}$ is peaked at $\arg(D_{\mathbf{K}}) = \frac{\pi}{3}, \pi, \frac{5\pi}{3}$, whereas for the cVBS state, it is peaked at $\arg(D_{\mathbf{K}}) = 0, \frac{2\pi}{3}, \frac{4\pi}{3}$. Our results, shown in the inset of Fig. 4(a), clearly demonstrate that the cVBS order is realized in our phase diagram.

The phase boundaries in Fig. 1(b) are obtained by scanning the correlation functions $C_I(\mathbf{\Gamma})$ and $C_B(\mathbf{K})$ as a function of U/W for fixed values of α. Two of these scans are shown in Fig. 4, for $\alpha = 0.4$ (panel (a)) and $\alpha = 0.6$ (panel (b)). It is clear that, as U/W increases, in both cases the ground state evolves from QVH to IVC to cVBS and then back to IVC. Furthermore, in the strong coupling limit $U/W \to \infty$, the IVC order $C_I(\mathbf{k} = 0)$ is independent of α and saturates at 0.5, consistent with our analytical calculation at the charge neutrality point, see Appendix D. The transitions between IVC to cVBS are first order, as signaled by the fact that as the system size L increases, the suppression of the IVC order becomes sharper (see for instance the region around $U/W \sim 5$ and $U/W \sim 11$ in panel (a)). A similar sharp drop is also featured at the QVH-IVC transition (region around $U/W \sim 2.5$ in panel (a)), indicating that the QVH-IVC and IVC-cVBS transitions are all first-order. It is interesting to note that, as α increases, the values of U/W for which the IVC and cVBS phases emerge are strongly reduced.

IV. DISCUSSION

In this paper, we employed QMC simulations, which are exact and unbiased, to obtain the phase diagram of a lattice model of TBG at charge neutrality. Our main result is that even very small interaction values trigger a transition from the non-interacting Dirac semi-metal phase to an insulating

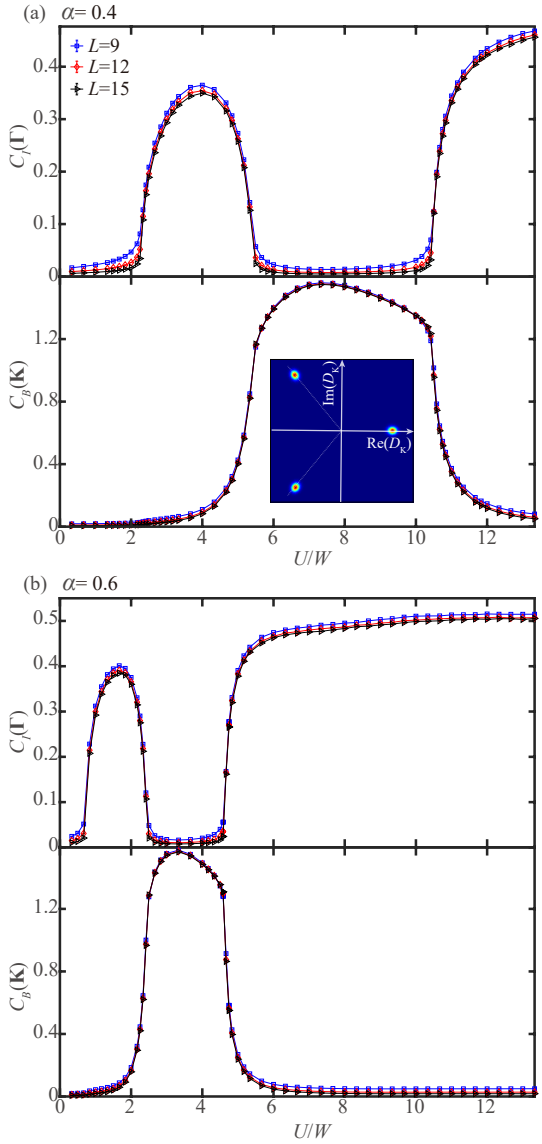

FIG. 4. **Intervalley coherent (IVC) and columnar valence bond solid (cVBS) insulating states.** Correlation functions $C_I(\mathbf{\Gamma})$ and $C_B(\mathbf{K})$, indicative of IVC and cVBS orders, respectively, as a function of U/W for (a) $\alpha = 0.4$ and (b) $\alpha = 0.6$. Linear system sizes are indicated in the legend. In both panels, the QVH-IVC transition, the IVC-cVBS transition, and the cVBS-IVC transition are all first-order. The inset in panel (a) presents the histogram of the complex bond order parameter $D_{\mathbf{K}}$ at $U/W \sim 5.3$. The positions of the three peaks are those expected for a cVBS phase, instead of a pVBS state.

state. Upon increasing U, the nature of the insulator changes from a non-symmetry-breaking topological QVH phase, to an onsite SU(4) symmetry-breaking IVC state, to a translational symmetry-breaking cVBS phase, and then finally back to a reentrant IVC state. This rich phase diagram is a consequence of the interplay between two different types of interaction terms: a cluster-charge repulsion $Q_{\hexagon}$ and a non-local assisted-hopping interaction $T_{\hexagon}$. The former is analogous to the standard Hubbard repulsion and, as such, is expected to promote either SU(4) antiferromagnetic order or valence-bond order in the strong-coupling regime. The latter, on the other hand, arises from the topological properties of the flat bands in TBG. When combined with $Q_{\hexagon}$, it gives rise not only to SU(4) ferromagnetic-like order, but also to correlated insulating phases with topological properties, such as the QVH phase.

While the precise value of U/W in TBG is not known, a widely used estimate is that this ratio is of order 1 [32]. Referring to our phase diagram in Fig. 1(b), this means that certainly the QVH phase and possibly the IVC phase can be realized at charge neutrality, provided that α is not too small. While some experimental probes do report a gap at charge neutrality Ref. [10, 11], additional experiments are needed to establish its ubiquity among different devices and the nature of the insulating state. The main manifestation of the QVH phase would be the appearance of gapless edge states, whereas in the case of the IVC state, it would be the emergence of a $\mathbf{k} = 0$ order with onsite coupling between the two different valleys.

In a more general context beyond TBG, our work offers a promising route to realize correlation-driven topological phases. As explained above, the topological QVH insulating state appears due to the cross-term in the interaction Hamiltonian that contains both $Q_{\hexagon}$ and $T_{\hexagon}$. While repulsive interactions similar to the charge-cluster one are generally expected to appear in any correlated electronic system, an interesting question is about the necessary conditions for the emergence of an interaction similar to the assisted-hopping. In our case, it arises from the projection of the standard Coulomb repulsion on Wannier states that suffer from topological obstruction. The latter, in turn, is a manifestation of the phenomenon of fragile topology [68]. Thus, interacting systems with fragile topology may offer an appealing route to search for interaction-driven topological states.

ACKNOWLEDGEMENTS

We thank Eslam Khalaf, Ashvin Vishwanath, Yi Zhang for insightful conversations on the subject, especially on the nature of the IVC phase. We also thank Oskar Vafek for valuable suggestions and pointing out a missing factor in the IVC correlation function. YDL and ZYM acknowledge support from the National Key Research and Development Program of China (Grant No. 2016YFA0300502), NSFC (Grant Nos. 11574359, 11674370), and Research Grants Council of Hong Kong SAR China (Grant No. 17303019). HQW is supported by NSFC through Grant No. 11804401 and the Fundamental Research Funds for the Central Universities. JK is supported by Priority Academic Program Development (PAPD) of Jiangsu Higher Education Institutions. RMF is supported by the U. S. Department of Energy, Office of Science, Basic Energy Sciences, Materials Sciences and Engineering Division, under Award No. DE-SC0020045. YDL and ZYM thank the Center for Quantum Simulation Sciences in the Institute of Physics, Chinese Academy of Sciences, the Computational Initiative at the Faculty of Science at the University of Hong Kong, the

Platform for Data-Driven Computational Materials Discovery at the Songshan Lake Materials Laboratory and the National Supercomputer Centers in Tianjin and Guangzhou for their technical support and generous allocation of CPU time. JK thanks the Kavli Institute for Theoretical Sciences for hospitality during the completion of this work. ZYM, JK, and RMF thank the hospitality of the Aspen Center for Physics, where part of this work was developed. The Aspen Center for Physics is supported by National Science Foundation grant PHY-1607611.

Appendix A: Projection QMC method

Since we are interested in the ground state properties of the system, the projection QMC is the method of choice [59, 62, 69]. In PQMC, one can obtain a ground state wave function $|\Psi_0\rangle$ from projecting a trial wave function $|\Psi_T\rangle$ along the imaginary axis $|\Psi_0\rangle = \lim_{\Theta\to\infty} e^{-\frac{\Theta}{2}\mathbf{H}}|\Psi_T\rangle$, then observable can be calculated as

$$\langle\hat{O}\rangle = \frac{\langle\Psi_0|\hat{O}|\Psi_0\rangle}{\langle\Psi_0|\Psi_0\rangle} = \lim_{\Theta\to\infty}\frac{\langle\Psi_T|e^{-\frac{\Theta}{2}\mathbf{H}}\hat{O}e^{-\frac{\Theta}{2}\mathbf{H}}|\Psi_T\rangle}{\langle\Psi_T|e^{-\Theta\mathbf{H}}|\Psi_T\rangle}. \quad \text{(A1)}$$

To evaluate overlaps in the above equation, we performed Trotter decomposition to discretize Θ into L_τ slices ($\Theta = L_\tau\Delta\tau$). Each slices $\Delta\tau$ is small and the systematic error is $O(\Delta\tau^2)$. After the Trotter decomposition, we have

$$\langle\Psi_T|e^{-\Theta H}|\Psi_T\rangle = \langle\Psi_T|\left(e^{-\Delta\tau H_U}e^{-\Delta\tau H_0}\right)^{L_\tau}|\Psi_T\rangle + O(\Delta\tau^2) \quad \text{(A2)}$$

where the non-interacting and interacting parts of the Hamiltonian is separated. To treat the interacting part, one usually employ a Hubbard Stratonovich (HS) transformation to decouple the interacting quartic fermion term to fermion bilinears coupled to auxiliary fields.

For the cluster interaction in Eq. (2) of the main text, we make use of a fourth order $SU(2)$ symmetric decoupling

$$e^{-\Delta\tau U(Q_{\hexagon}+\alpha T_{\hexagon}-4)^2} = \frac{1}{4}\sum_{\{s_{\hexagon}\}}\gamma(s_{\hexagon})e^{i\alpha\eta(s_{\hexagon})\left(Q_{\hexagon}+\alpha T_{\hexagon}-4\right)} \quad \text{(A3)}$$

with $\alpha = \sqrt{\Delta\tau U}$, $\gamma(\pm1) = 1+\sqrt{6}/3$, $\gamma(\pm2) = 1-\sqrt{6}/3$, $\eta(\pm1) = \pm\sqrt{2(3-\sqrt{6})}$, $\eta(\pm2) = \pm\sqrt{2(3+\sqrt{6})}$ and the sum is taken over the auxiliary fields $s_{\hexagon}$ on each hexagon which can take four values ±2 and ±1. After tracing out the free fermionic degrees of freedom, we obtain the following formula with a constant factor omitted

$$\langle\Psi_T|e^{-\Theta H}|\Psi_T\rangle = \sum_{\{s_{\hexagon,\tau}\}}\left[\left(\prod_\tau\prod_{\hexagon}\gamma(s_{\hexagon,\tau})e^{-4\alpha\eta(s_{\hexagon,\tau})}\right)\det\left[P^\dagger B(\Theta,0)P\right]\right] \quad \text{(A4)}$$

where P is the coefficient matrix of trial wave function $|\Psi_T\rangle$. In the simulation, we choose the ground state wavefunction of the half-filled non-interacting system (described by H_0) as the trial wave function. In the above formula, the B matrix is defined as

$$B(\tau+1,\tau) = e^{V[\{s_{\hexagon,\tau}\}]}e^{-\Delta_\tau K} \quad \text{(A5)}$$

and has properties $B(\tau_3,\tau_1) = B(\tau_3,\tau_2)B(\tau_2,\tau_1)$, i.e. the B matrix is an imaginary time propagator, where we have written the coefficient matrix of interaction part as $V[\{s_{\hexagon,\tau}\}]$ and K is the hopping matrix from the H_0.

The configurational space $\{s_{\hexagon}(i,\tau)\}$ with size $L\times L\times\Theta$ is the space in which the physical observables in Eq. (A1) are computed with ensemble average. We choose the projection length $\Theta = 2L/t$ and discretize it with a step $\Delta\tau = 0.1/t$. The spatial system sizes are $L = 6, 9, 12, 15$.

Every hexagon contains six sites, as shown in the figure below, so our $V[\{s_{\hexagon,\tau}\}]$ matrix is a block matrix, every block contributes a 6×6 matrix,

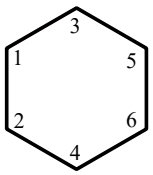

$$\begin{pmatrix} \frac{1}{3} & i\alpha & -i\alpha & 0 & 0 & 0 \\ -i\alpha & \frac{1}{3} & 0 & i\alpha & 0 & 0 \\ i\alpha & 0 & \frac{1}{3} & 0 & -i\alpha & 0 \\ 0 & -i\alpha & 0 & \frac{1}{3} & 0 & i\alpha \\ 0 & 0 & i\alpha & 0 & \frac{1}{3} & -i\alpha \\ 0 & 0 & 0 & -i\alpha & i\alpha & \frac{1}{3} \end{pmatrix}$$

The Monte Carlo sampling of auxiliary fields are further performed based on the weight defined in the sum of Eq. (A4). The measurements are performed near $\tau = \Theta/2$. Single particle observables are measured by Green's function directly and many body correlation functions are measured from the products of single-particle Green's function based on their corresponding form after Wick-decomposition. The equal time Green's function are calculated as

$$G(\tau,\tau) = 1 - R(\tau)\left(L(\tau)R(\tau)\right)^{-1}L(\tau) \quad \text{(A6)}$$

with $R(\tau) = B(\tau,0)P$, $L(\tau) = P^\dagger B(\Theta,\tau)$.

Appendix B: Absence of sign-problem

At the charge neutrality point, the model is sign-problem-free, as can be seen from the following analysis. Define W_{σ,l,S_i} as the update weight of one fixed auxiliary field at the i-th hexagon, where $l = 1, 2$ is a valley/orbital index and

$\sigma = \uparrow, \downarrow$ is a spin index. From the symmetry of the Hamiltonian, $W_{\uparrow,l,S_i} = W_{\downarrow,l,S_i}$. Since the model is particle-hole symmetric at charge neutrality, one can perform a particle-hole transformation (PHS) only for the valley $l = 2$. Then one can focus on a fixed auxiliary field, and focus only on one spin flavor, such as spin up. Eq. (A3) in the main text can then be abbreviated as Eq. (B1) and Eq. (B2). Applying PHS for valley 2 and using the relation Eq. (B3), we find that Eq. (B2) becomes Eq. (B4).

$$For\ l = 1,\ \exp\left(i\alpha\eta(S_i)\left[\sum_{p=1}^{6}\left(ic^{\dagger}_{p+1,1,\uparrow}c_{p,1,\uparrow} - ic^{\dagger}_{p,1,\uparrow}c_{p+1,1,\uparrow}\right) + \frac{1}{3}\sum_{p=1}^{6}\left(c^{\dagger}_{p,1,\uparrow}c_{p,1,\uparrow} - \frac{1}{2}\right)\right]\right) \tag{B1}$$

$$For\ l = 2,\ \exp\left(i\alpha\eta(S_i)\left[\sum_{p=1}^{6}\left(-ic^{\dagger}_{p+1,2,\uparrow}c_{p,2,\uparrow} + ic^{\dagger}_{p,2,\uparrow}c_{p+1,2,\uparrow}\right) + \frac{1}{3}\sum_{p=1}^{6}\left(c^{\dagger}_{p,2,\uparrow}c_{p,2,\uparrow} - \frac{1}{2}\right)\right]\right) \tag{B2}$$

$$\begin{gathered} -ic^{\dagger}_{p+1,2,\uparrow}c_{p,2,\uparrow} + ic^{\dagger}_{p,2,\uparrow}c_{p+1,2,\uparrow} \overset{PHS}{\longrightarrow} ic^{\dagger}_{p+1,2,\uparrow}c_{p,2,\uparrow} - ic^{\dagger}_{p,2,\uparrow}c_{p+1,2,\uparrow} \\ c^{\dagger}_{p,2,\uparrow}c_{p,2,\uparrow} - \frac{1}{2} \overset{PHS}{\longrightarrow} \frac{1}{2} - c^{\dagger}_{p,2,\uparrow}c_{p,2,\uparrow} \end{gathered} \tag{B3}$$

$$For\ l = 2\ PHS,\ \exp\left(i\alpha\eta(S_i)\left[\sum_{p=1}^{6}\left(ic^{\dagger}_{p+1,2,\uparrow}c_{p,2,\uparrow} - ic^{\dagger}_{p,2,\uparrow}c_{p+1,2,\uparrow}\right) + \frac{1}{3}\sum_{p=1}^{6}\left(\frac{1}{2} - c^{\dagger}_{p,2,\uparrow}c_{p,2,\uparrow}\right)\right]\right) \tag{B4}$$

$$\begin{gathered} For\ l = 1,\ e^{-\alpha\eta(S_i)\mathbf{B}+i\alpha\eta(s_{\hexagon})\mathbf{A}} \rightarrow e^{-\alpha\eta(s_{\hexagon})\mathbf{B}}e^{i\alpha\eta(s_{\hexagon})\mathbf{A}} \\ For\ l = 2\ PHS,\ e^{-\alpha\eta(S_i)\mathbf{B}+i\alpha\eta(s_{\hexagon})\mathbf{A}} \rightarrow e^{-\alpha\eta(s_{\hexagon})\mathbf{B}}e^{-i\alpha\eta(s_{\hexagon})\mathbf{A}} \end{gathered} \tag{B5}$$

Let us define the matrices $\mathbf{A} = \frac{1}{3}\sum_{p=1}^{6}\left(c^{\dagger}_{p,2,\uparrow}c_{p,2,\uparrow} - \frac{1}{2}\right)$ and $i\mathbf{B} = \sum_{p=1}^{6}\left(ic^{\dagger}_{p+1,1,\uparrow}c_{p,1,\uparrow} - ic^{\dagger}_{p,1,\uparrow}c_{p+1,1,\uparrow}\right)$ – or, equivalenty, $\mathbf{B} = \sum_{p=1}^{6}\left(c^{\dagger}_{p+1,1,\uparrow}c_{p,1,\uparrow} - c^{\dagger}_{p,1,\uparrow}c_{p+1,1,\uparrow}\right)$. The matrices $\mathbf{A}$ and $\mathbf{B}$ are real matrices. Then, due to the fact that the matrix $\mathbf{A}$ is a diagonal matrix and $\mathbf{A}_{ii} = \mathbf{A}_{jj}$, Eqs. (B1) and (B4) can be writen as Eq. (B5).

Because of the relations above, the total weight of the model is $\sum_{S_i} W_{\uparrow,1,S_i} * W_{\uparrow,2,S_i} * W_{\downarrow,1,S_i} * W_{\downarrow,1,S_i} = \sum_{S_i}\left(W_{\uparrow,1,S_i}W^{*}_{\uparrow,1,S_i}\right)^2$, which is a real positive number. This implies that the QMC simulations are sign-problem-free.

Appendix C: Benchmark with Exact Diagonalization

We employ Lanczos exact diagonalization (ED) to benchmark the PQMC results. The system contains 2×2 unit cells of the honeycomb lattice with periodic boundary condition (16 electrons in total). We make use of symmetries, such as the valley $U(1)$ symmetry and the total S_z conservation for each valley, to reduce the computational cost of the ED. The ground state lays in the subspace with $N_{\uparrow} = 4$, $N_{\downarrow} = 4$ in both valleys, where $N_{\uparrow}(N_{\downarrow})$ is the number of electrons with spin up (down) in each valley. The dimension of the ground-state subspace is about 24 million. In the PQMC simulations, we choose the linear system size $L = 2$ and the projection length $\Theta = 100/t$ with Trotter slice $\Delta\tau = 0.0005/t$. We compared the ground-state expectation values of $\langle H_0\rangle$ and of the double occupation as a function of U/t at $\alpha = 0.3$, which are shown below. The results of both methods agree very well.

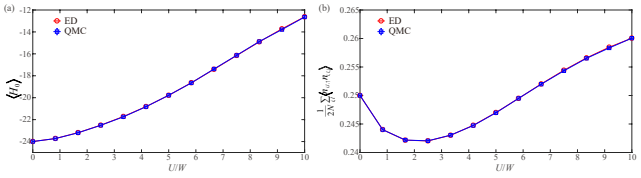

FIG. 5. (a) Kinetic energy and (b) Double occupancy as a function of U/W for $\alpha = 0.3$. Red circles and blue squares with error bars are obtained from ED and QMC, respectively.

Appendix D: Strong Coupling Limit at the charge neutrality point

For the system at the charge neutrality point, each unit cell contains four fermions in average. Following the method applied in Ref. [32], the ground state $|\Psi_{gr}\rangle$ of the interaction $H_{\hexagon}$

should be annihilated by the assisted hopping operator $T_{\hexagon}$ for any hexagon. The general form of the wavefunction is

$$|\Psi_{gr}\rangle = \prod_i \left(\alpha_1 c^\dagger_{i,1,\hat{n}} + (-)^{s(i)}\alpha_2 c^\dagger_{i,2,\hat{m}}\right)\left(\gamma\left(\alpha_2^* c^\dagger_{i,1,\hat{n}} - (-)^{s(i)}\alpha_1^* c^\dagger_{i,2,\hat{m}}\right) + \beta_1 c^\dagger_{i,1,-\hat{n}} + (-)^{s(i)}\beta_2 c^\dagger_{i,2,-\hat{m}}\right)|\emptyset\rangle \tag{D1}$$

where $s(i) = 0$ and 1 if the site i is on sublattice $\mathcal{A}$ and $\mathcal{B}$ respectively. $\hat{n}$ and $\hat{m}$ are two arbitrary spin quantization directions. α_1, α_2, β_1, and β_2 are four complex variables that satisfy $|\alpha_1|^2 + |\alpha_2|^2 = |\gamma|^2 + |\beta_1|^2 + |\beta_2|^2 = 1$.

Furthermore, consider the hopping between two sites. Applying the second order perturbation theory, the energy is minimized when $|\alpha_1| = |\alpha_2| = 1/\sqrt{2}$, $\gamma = 0$, and $|\beta_1| = |\beta_2| = 1/\sqrt{2}$. So the ground state is an equal mixture of two valleys.

It is easy to obtain that

$$\begin{aligned}
\langle c^\dagger_{i,1,\hat{n}} c_{i,2,\hat{m}}\rangle &= (-)^{s(i)}\alpha_1^*\alpha_2 \\
\langle c^\dagger_{i,1,\hat{n}} c_{i,2,-\hat{m}}\rangle &= \langle c^\dagger_{i,1,-\hat{n}} c_{i,2,\hat{m}}\rangle = 0 \\
\langle c^\dagger_{i,1,-\hat{n}} c_{i,2,-\hat{m}}\rangle &= (-)^{s(i)}\beta_1^*\beta_2
\end{aligned} \tag{D2}$$

Suppose that $\hat{n} = (\sin\theta\cos\phi, \sin\theta\sin\phi, \cos\theta)$ and $\hat{m} = (\sin\theta'\cos\phi', \sin\theta'\sin\phi', \cos\theta')$. We obtain that the operator

$$I_{i,\uparrow} = \langle c^\dagger_{i,1,\uparrow} c_{i,2,\uparrow} + h.c.\rangle = (-)^{s(i)}\left(\cos\frac{\theta}{2}\cos\frac{\theta'}{2}\alpha_1^*\alpha_2 + \sin\frac{\theta}{2}\sin\frac{\theta'}{2}e^{i(\phi-\phi')}\beta_1^*\beta_2 + c.c\right) \tag{D3}$$

$$I_{i,\downarrow} = \langle c^\dagger_{i,1,\downarrow} c_{i,2,\downarrow} + h.c.\rangle = (-)^{s(i)}\left(\cos\frac{\theta}{2}\cos\frac{\theta'}{2}\beta_1^*\beta_2 - \sin\frac{\theta}{2}\sin\frac{\theta'}{2}e^{i(\phi-\phi')}\alpha_1^*\alpha_2 + c.c\right) \tag{D4}$$

As a consequence, when average over all the possible configurations of the ground states, we obtain

$$\begin{aligned}
C_I^{\mathcal{A}\mathcal{A}} &= \frac{1}{L^4}\sum_{i,j\in\mathcal{A}} \langle\langle \left(I_{i,\uparrow} + I_{i,\downarrow}\right)\left(I_{j,\uparrow} + I_{j,\downarrow}\right)\rangle\rangle = \frac{1}{L^4}\sum_{i,j\in\mathcal{A}}\left(\langle\langle I_{i,\uparrow} I_{j,\uparrow}\rangle\rangle + \langle\langle I_{i,\downarrow} I_{j,\downarrow}\rangle\rangle\right) \\
&= 2\times\left(\langle\langle\cos^2\frac{\theta}{2}\cos^2\frac{\theta'}{2}\rangle\rangle\left(|\alpha_1|^2|\alpha_2|^2 + |\beta_1|^2|\beta_2|^2\right) + \langle\langle\sin^2\frac{\theta}{2}\sin^2\frac{\theta'}{2}\rangle\rangle\left(|\alpha_1|^2|\alpha_2|^2 + |\beta_1|^2|\beta_2|^2\right)\right)
\end{aligned} \tag{D5}$$

where $\langle\langle\cdots\rangle\rangle$ refers to the average over the direction $\hat{n}$ and $\hat{m}$, as well as the phases of α_1, α_2, β_1, and β_2. Averaging over $\hat{n}$ and $\hat{m}$ on the sphere, we obtain $\langle\langle\cos^2\frac{\theta}{2}\rangle\rangle = \langle\langle\cos^2\frac{\theta'}{2}\rangle\rangle = \langle\langle\sin^2\frac{\theta}{2}\rangle\rangle = \langle\langle\sin^2\frac{\theta'}{2}\rangle\rangle = \frac{1}{2}$. Thus, $C_I^{\mathcal{A}\mathcal{A}} = \frac{1}{2}$. Similarly, we can obtain $C_I^{\mathcal{B}\mathcal{B}} = -C_I^{\mathcal{A}\mathcal{B}} = -C_I^{\mathcal{B}\mathcal{A}} = \frac{1}{2}$. This is consistent with the QMC result in the limit $U/W \to \infty$.

Appendix E: Hartree-Fock method

To solve the TBG model within the Hartree-Fock approach, we write the Hamiltonian in Eq. (2) of the main text as

$$H_{\hexagon} = U\sum_{\hexagon}(Q'_{\hexagon} + \alpha T'_{\hexagon})(Q_{\hexagon} + \alpha T_{\hexagon}), \tag{E1}$$

where primes indicate independent index summations. The direct terms immediately give

$$H^H_{\hexagon} = 2U\sum_{\hexagon}\langle Q'_{\hexagon} + \alpha T'_{\hexagon}\rangle(Q_{\hexagon} + \alpha T_{\hexagon}). \tag{E2}$$

The exchange terms are Eq. (E3), where $\sum_{\text{all}} = \left(\sum_{l,l'=1,2}\sum_{\sigma\sigma'}\sum_{i,i'=1}^{6}\right)$. Manipulating and collecting terms in (E2) and (E3) yields the Hartree-Fock Hamiltonian Eq. (E3).

$$\begin{aligned}
H^F_{\hexagon} =& -U\sum_{\hexagon}\sum_{\text{all}}\Big[\frac{1}{9}[\langle c^\dagger_{i'l'\sigma'} c_{il\sigma}\rangle c^\dagger_{il\sigma} c_{i'l'\sigma'} + h.c.] \\
&+ \frac{\alpha i}{3}\left\{[(-)^{l'+1}\langle c^\dagger_{i'+1l'\sigma'} c_{il\sigma}\rangle c^\dagger_{il\sigma} c_{i'l'\sigma'} + h.c.] + [(-)^{l'}\langle c^\dagger_{i'l'\sigma'} c_{il\sigma}\rangle c^\dagger_{il\sigma} c_{i'+1l'\sigma'} + h.c.]\right\} \\
&+ \alpha^2 i^2\left\{[(-)^{l'+l}\langle c^\dagger_{i'+1l'\sigma'} c_{il\sigma}\rangle c^\dagger_{i+1l\sigma} c_{i'l'\sigma'} + h.c.] - [(-1)^{l'+l}\langle c^\dagger_{i'+1l'\sigma'} c_{i+1l\sigma}\rangle c^\dagger_{il\sigma} c_{i'l'\sigma'} + h.c.]\right. \\
&\left. - [(-1)^{l'+l}\langle c^\dagger_{i'l'\sigma'} c_{il\sigma}\rangle c^\dagger_{i+1l\sigma} c_{i'+1l'\sigma'} + h.c.] + [(-)^{l'+l}\langle c^\dagger_{i'l'\sigma'} c_{i+1l\sigma}\rangle c^\dagger_{il\sigma} c_{i'+1l'\sigma'} + h.c.]\right\}\Big],
\end{aligned}$$

$$H^{HF}_{\hexagon} = 2U \sum_{\hexagon} \Big\{ \bar{n}_{\hexagon}(Q_{\hexagon} + \alpha T_{\hexagon}) - \sum_{\text{all}} \Big[\sum_{n,m} \alpha_n(l')\alpha_m(l+1)\langle c^\dagger_{i'+nl'\sigma'} c_{i+ml\sigma} \rangle \Big] c^\dagger_{il\sigma} c_{i'l'\sigma'} \Big\}. \tag{E3}$$

Here $n, m = \{-1, 0, 1\}$ and we have defined

$$\bar{n}_{\hexagon} = \langle Q_{\hexagon} + \alpha T_{\hexagon} \rangle,$$
$$\alpha(l) = \begin{pmatrix} \alpha_{-1} \\ \alpha_0 \\ \alpha_1 \end{pmatrix} = \begin{pmatrix} (-1)^l\, i\, \alpha \\ 1/3 \\ (-1)^{l+1}\, i\, \alpha \end{pmatrix}.$$

We solve the full Hartree-Fock Hamiltonian ($H = H_0 + H^{HF}_{\hexagon}$) self-consistently using that

$$\langle c^\dagger_\kappa c_\lambda \rangle = \sum_{\epsilon,\eta=1}^{N} U^\dagger_{\epsilon\kappa} U_{\lambda\eta} \langle \gamma^\dagger_\epsilon \gamma_\eta \rangle = \sum_{\epsilon} U^\dagger_{\epsilon\kappa} U_{\lambda\epsilon} f(E_\epsilon, \mu), \tag{E4}$$

where $\kappa, \lambda = \{il\sigma\}$, U is the unitary tranformation diagonalizing H, γ's are the eigenvectors and $f(E_\epsilon, \mu)$ is the Fermi-Dirac distribution of the excitation energies, E_ϵ. We explicitly write the dependence on the chemical potential, μ, as we iterate this value to fulfil $N^{-1}\sum_\epsilon f(E_\epsilon, \mu) = \nu$, where ν is the filling.

We compute results at charge neutrality ($\nu = 0.5$) with a total of 600 lattice sites and periodic boundary conditions. The calculations are fully unrestricted; thus we iterate all $(4 \times 600)^2$ mean-fields, and define convergence by the condition that $\sum |\Delta E_\epsilon| < N \times 10^{-10}$, where ΔE_ϵ is the change of the excitation energies from one iteration to the next, and N is the total number of states (4×600). In Table I we present an example of the HF calculations, displaying results for $t = 1$,$\alpha = 0.45$ and $U/W = 0.5$. We set the temperature $T = 2.5 \cdot 10^{-5}$ in all computations. The values in the table are the renormalized mean-fields. It is evident that all hoppings within each hexagon are renormalized due to the interactions. The simple hopping renormalizations, however, do not open a gap in the Dirac cones. The gap is generated directly by the mean-fields $\langle c^\dagger_{i,1,\sigma} c_{i\pm2,1,\sigma} \rangle = -\langle c^\dagger_{i,2,\sigma} c_{i\pm2,2,\sigma} \rangle = \pm 0.0914i$, which explicitly display a spin degenerate quantum valley Hall (QVH) phase, as illustrated in Fig. 1(b) of the main text.

In Fig. 6(a) we show the single-particle gap in the QVH phase with $\alpha = 0.45$ for several interaction strengths. Fig. 6(b) displays the corresponding band structures. The Dirac cone at K in the bare bands is immediately gapped out when including interactions. The renormalization initially flattens the bands with a significant gap at all high-symmetry points. As U increases the valence band gradually develops a peak at Γ while it is pushed down correspondingly at K. This behavior results in a gradual shift of the maximal gap value from Γ to K.

Finally we present results obtained by implementing the interaction terms found in Ref. [32]. As mentioned in the discussion section of the main text, we are able to solve this model within the HF approach as it does not suffer from sign problems. The assisted hopping reads

$$T_{\hexagon} = \sum_{i=1}^{6} \sum_{l,\sigma} (-)^{i-1} \big(c^\dagger_{il\sigma} c_{i+1l\sigma} + \text{h.c.} \big). \tag{E5}$$

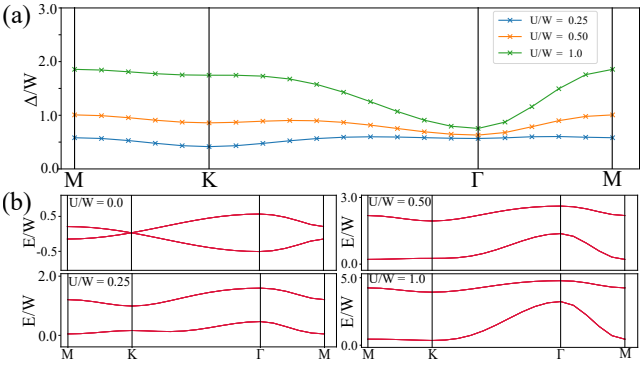

FIG. 6. **QVH insulator and band strutures (a)** The single-particle gap Δ/W along the high-symmetry path of the BZ with $\alpha = 0.45$ and various interaction strengths. The Dirac cones are gapped at infinitely small U and the system enters the QVH state. The maximal gap value gradually shifts from Γ to the K. **(b)** Band structures at various interaction strengths with $\alpha = 0.45$. Top left plot displays the bare kinetic bands in the absence of any interactions. The Dirac cone at K is evident and confirms the semi-metallic phase of the bare bands. The remaining three plots of **(b)** present the renormalized band structures with increasing U. The two bands flattens for small U and gradually develops a peak at Γ. All bands are fourfold degenerate, as the QVH phase does not break the approximate $SU(4)$ symmetry.

The other terms, $Q_{\hexagon}$ and H_0, remain unchanged. To reach this expression for $T_{\hexagon}$, we have performed the following gauge transformation,

$$c_{il\sigma} \longrightarrow e^{i\theta_l/2} c_{il\sigma}, \quad i \text{ odd}$$
$$c_{il\sigma} \longrightarrow e^{-i\theta_l/2} c_{il\sigma}. \quad i \text{ even} \tag{E6}$$

The transformation introduces phases in H_0 effectively causing t to become complex. We set the phases according to Ref. [32], that is $\theta_1 = -\theta_2 = 0.743\pi$. The renormalized mean-fields are presented in Table II, where we have performed the inverse gauge transformation for direct comparison with Table I. Input parameters are the same as those used to generate Table I. The result is consistent with the values presented in Table I and clearly also features a QVH phase.

	U/W = 0.50							
	$c_{i,1,\sigma}$	$c_{i,2,\sigma}$	$c_{i\pm1,1,\sigma}$	$c_{i\pm1,2,\sigma}$	$c_{i\pm2,1,\sigma}$	$c_{i\pm2,2,\sigma}$	$c_{i+3,1,\sigma}$	$c_{i+3,2,\sigma}$
$c^\dagger_{i,1,\sigma}$	-	-	-0.0209	-	$\pm0.0914i$	-	0.0024	-
$c^\dagger_{i,2,\sigma}$	-	-	-	-0.0209	-	$\mp0.0914i$	-	0.0024

TABLE I. **Mean-field renormalization with $U/W = 0.50$ and $\alpha = 0.45$.** The input on $[c^\dagger_{il\sigma}, c_{jl'\sigma}]$ represents the renormalized mean-field parameter $\langle c^\dagger_{il\sigma} c_{jl'\sigma}\rangle$. The result is homogenous and spin degenerate, hence the listed values contain information about all sites and flavours. Note that interactions have generated neither spin- nor valley-mixing. We have subtracted the bare band contributions evaluated at $\nu = 0.5$ and ignored all mean-fields with $\frac{|MF|_{max}}{|MF|} > 100$.

	U/W = 0.50							
	$c_{i,1,\sigma}$	$c_{i,2,\sigma}$	$c_{i\pm1,1,\sigma}$	$c_{i\pm1,2,\sigma}$	$c_{i\pm2,1,\sigma}$	$c_{i\pm2,2,\sigma}$	$c_{i+3,1,\sigma}$	$c_{i+3,2,\sigma}$
$c^\dagger_{i,1,\sigma}$	-	-	$-0.1015 - (-)^i 0.0555i$	-	$\mp0.0945i$	-	$-0.0806 + (-)^i 0.0300i$	-
$c^\dagger_{i,2,\sigma}$	-	-	-	$-0.1015 + (-)^i 0.0555i$	-	$\pm0.0945i$	-	$-0.0806 - (-)^i 0.0300i$

TABLE II. **Mean-field renormalization with $U/W = 0.50$ and $\alpha = 0.45$ using model from Ref. [32].** The input on $[c^\dagger_{il\sigma}, c_{jl'\sigma}]$ represents the renormalized mean-field parameter $\langle c^\dagger_{il\sigma} c_{jl'\sigma}\rangle$. The result is homogenous and spin degenerate, hence the listed values contain information about all sites and flavours. We have subtracted the bare band contributions evaluated at $\nu = 0.5$ and ignored all mean-fields with $\frac{|MF|_{max}}{|MF|} > 100$.

[1] R. Bistritzer and A. H. MacDonald, Proceedings of the National Academy of Sciences **108**, 12233 (2011).

[2] Y. Cao, V. Fatemi, A. Demir, S. Fang, S. L. Tomarken, J. Y. Luo, J. D. Sanchez-Yamagishi, K. Watanabe, T. Taniguchi, E. Kaxiras, R. C. Ashoori, and P. Jarillo-Herrero, Nature **556**, 80 (2018).

[3] Y. Cao, V. Fatemi, S. Fang, K. Watanabe, T. Taniguchi, E. Kaxiras, and P. Jarillo-Herrero, Nature **556**, 43 (2018).

[4] C. Shen, Y. Chu, Q. Wu, N. Li, S. Wang, Y. Zhao, J. Tang, J. Liu, J. Tian, K. Watanabe, T. Taniguchi, R. Yang, Z. Y. Meng, D. Shi, O. V. Yazyev, and G. Zhang, Nature Physics (2020), 10.1038/s41567-020-0825-9.

[5] X. Liu, Z. Hao, E. Khalaf, J. Y. Lee, K. Watanabe, T. Taniguchi, A. Vishwanath, and P. Kim, arXiv preprint arXiv:1903.08130 (2019).

[6] Y. Cao, D. Rodan-Legrain, O. Rubies-Bigorda, J. M. Park, K. Watanabe, T. Taniguchi, and P. Jarillo-Herrero, arXiv preprint arXiv:1903.08596 (2019).

[7] G. Chen, A. L. Sharpe, E. J. Fox, Y.-H. Zhang, S. Wang, L. Jiang, B. Lyu, H. Li, K. Watanabe, T. Taniguchi, *et al.*, Nature **579**, 56 (2020).

[8] A. Kerelsky, L. J. McGilly, D. M. Kennes, L. Xian, M. Yankowitz, S. Chen, K. Watanabe, T. Taniguchi, J. Hone, C. Dean, *et al.*, Nature **572**, 95 (2019).

[9] S. Tomarken, Y. Cao, A. Demir, K. Watanabe, T. Taniguchi, P. Jarillo-Herrero, and R. Ashoori, Physical review letters **123**, 046601 (2019).

[10] X. Lu, P. Stepanov, W. Yang, M. Xie, M. A. Aamir, I. Das, C. Urgell, K. Watanabe, T. Taniguchi, G. Zhang, *et al.*, Nature **574**, 653 (2019).

[11] Y. Xie, B. Lian, B. Jäck, X. Liu, C.-L. Chiu, K. Watanabe, T. Taniguchi, B. A. Bernevig, and A. Yazdani, Nature **572**, 101 (2019).

[12] Y. Jiang, X. Lai, K. Watanabe, T. Taniguchi, K. Haule, J. Mao, and E. Y. Andrei, Nature **573**, 91 (2019).

[13] D. Wong, K. P. Nuckolls, M. Oh, B. Lian, Y. Xie, S. Jeon, K. Watanabe, T. Taniguchi, B. A. Bernevig, and A. Yazdani, arXiv preprint arXiv:1912.06145 (2019).

[14] U. Zondiner, A. Rozen, D. Rodan-Legrain, Y. Cao, R. Queiroz, T. Taniguchi, K. Watanabe, Y. Oreg, F. von Oppen, A. Stern, *et al.*, arXiv preprint arXiv:1912.06150 (2019).

[15] Y. Saito, J. Ge, K. Watanabe, T. Taniguchi, and A. F. Young, arXiv preprint arXiv:1911.13302 (2019).

[16] P. Stepanov, I. Das, X. Lu, A. Fahimniya, K. Watanabe, T. Taniguchi, F. H. Koppens, J. Lischner, L. Levitov, and D. K. Efetov, arXiv preprint arXiv:1911.09198 (2019).

[17] G. Chen, L. Jiang, S. Wu, B. Lyu, H. Li, B. L. Chittari, K. Watanabe, T. Taniguchi, Z. Shi, J. Jung, *et al.*, Nature Physics **15**, 237 (2019).

[18] G. Chen, A. L. Sharpe, P. Gallagher, I. T. Rosen, E. J. Fox, L. Jiang, B. Lyu, H. Li, K. Watanabe, T. Taniguchi, *et al.*, Nature **572**, 215 (2019).

[19] C. Xu and L. Balents, Physical review letters **121**, 087001 (2018).

[20] J. Kang and O. Vafek, Phys. Rev. X **8**, 031088 (2018).

[21] M. Koshino, N. F. Q. Yuan, T. Koretsune, M. Ochi, K. Kuroki, and L. Fu, Phys. Rev. X **8**, 031087 (2018).

[22] H. C. Po, L. Zou, A. Vishwanath, and T. Senthil, Phys. Rev. X **8**, 031089 (2018).

[23] C.-C. Liu, L.-D. Zhang, W.-Q. Chen, and F. Yang, Physical review letters **121**, 217001 (2018).

[24] M. Ochi, M. Koshino, and K. Kuroki, Physical Review B **98**, 081102 (2018).

[25] J. F. Dodaro, S. A. Kivelson, Y. Schattner, X.-Q. Sun, and C. Wang, Physical Review B **98**, 075154 (2018).

[26] H. Guo, X. Zhu, S. Feng, and R. T. Scalettar, Physical Review B **97**, 235453 (2018).

[27] H. Isobe, N. F. Yuan, and L. Fu, Physical Review X **8**, 041041 (2018).

[28] J. W. Venderbos and R. M. Fernandes, Physical Review B **98**, 245103 (2018).

[29] F. Guinea and N. R. Walet, Proceedings of the National Academy of Sciences **115**, 13174 (2018).

[30] Q.-K. Tang, L. Yang, D. Wang, F.-C. Zhang, and Q.-H. Wang, Physical Review B **99**, 094521 (2019).

[31] J. Gonzalez and T. Stauber, Physical review letters **122**, 026801 (2019).

[32] J. Kang and O. Vafek, Phys. Rev. Lett. **122**, 246401 (2019).

[33] K. Seo, V. N. Kotov, and B. Uchoa, Physical review letters **122**, 246402 (2019).

[34] Y.-H. Zhang, D. Mao, Y. Cao, P. Jarillo-Herrero, and T. Senthil, Physical Review B **99**, 075127 (2019).

[35] J. Y. Lee, E. Khalaf, S. Liu, X. Liu, Z. Hao, P. Kim, and A. Vishwanath, Nature communications **10**, 1 (2019).

[36] F. Wu and S. Das Sarma, Phys. Rev. Lett. **124**, 046403 (2020).

[37] X.-C. Wu, A. Keselman, C.-M. Jian, K. A. Pawlak, and C. Xu, Physical Review B **100**, 024421 (2019).

[38] N. Bultinck, S. Chatterjee, and M. P. Zaletel, arXiv e-prints , arXiv:1901.08110 (2019), arXiv:1901.08110 [cond-mat.str-el].

[39] S. Liu, E. Khalaf, J. Y. Lee, and A. Vishwanath, arXiv preprint arXiv:1905.07409 (2019).

[40] Y. Alavirad and J. D. Sau, arXiv preprint arXiv:1907.13633 (2019).

[41] S. Chatterjee, N. Bultinck, and M. P. Zaletel, arXiv preprint arXiv:1908.00986 (2019).

[42] D. V. Chichinadze, L. Classen, and A. V. Chubukov, arXiv preprint arXiv:1910.07379 (2019).

[43] N. Bultinck, E. Khalaf, S. Liu, S. Chatterjee, A. Vishwanath, and M. P. Zaletel, arXiv e-prints , arXiv:1911.02045 (2019), arXiv:1911.02045 [cond-mat.str-el].

[44] J. Liu and X. Dai, arXiv preprint arXiv:1911.03760 (2019).

[45] R. M. Fernandes and J. W. Venderbos, arXiv preprint arXiv:1911.11367 (2019).

[46] Y. Zhang, K. Jiang, Z. Wang, and F. Zhang, arXiv preprint arXiv:2001.02476 (2020).

[47] C. Repellin, Z. Dong, Y.-H. Zhang, and T. Senthil, arXiv preprint arXiv:1907.11723 (2019).

[48] J. Kang and O. Vafek, arXiv preprint arXiv:2002.10360 (2020).

[49] S.-M. Huang, Y.-P. Huang, and T.-K. Lee, "Slave-rotor theory on magic-angle twisted bilayer graphene," (2020).

[50] C. Lu, Y. Zhang, Y. Zhang, M. Zhang, C.-C. Liu, Z.-C. Gu, W.-Q. Chen, and F. Yang, (2020), arXiv:2003.09513 [cond-mat.str-el].

[51] S.-Y. Li, Y. Zhang, Y.-N. Ren, J. Liu, X. Dai, and L. He, "Experimental evidence for orbital magnetic moments generated by moiré-scale current loops in twisted bilayer graphene," (2019), arXiv:1912.13133 [cond-mat.mtrl-sci].

[52] A. L. Sharpe, E. J. Fox, A. W. Barnard, J. Finney, K. Watanabe, T. Taniguchi, M. Kastner, and D. Goldhaber-Gordon, Science **365**, 605 (2019).

[53] M. Serlin, C. Tschirhart, H. Polshyn, Y. Zhang, J. Zhu, K. Watanabe, T. Taniguchi, L. Balents, and A. Young, Science **367**, 900 (2020).

[54] M. Xie and A. H. MacDonald, Phys. Rev. Lett. **124**, 097601 (2020).
[55] T. Cea and F. Guinea, arXiv:2004.01577 (2020).
[56] X. Y. Xu, K. T. Law, and P. A. Lee, Phys. Rev. B **98**, 121406 (2018).
[57] Y. Da Liao, Z. Y. Meng, and X. Y. Xu, Phys. Rev. Lett. **123**, 157601 (2019).
[58] L. Zou, H. C. Po, A. Vishwanath, and T. Senthil, Phys. Rev. B **98**, 085435 (2018).
[59] Z. Y. Meng, T. C. Lang, S. Wessel, F. F. Assaad, and A. Muramatsu, Nature **464**, 847 (2010).
[60] X. Y. Xu, K. S. D. Beach, K. Sun, F. F. Assaad, and Z. Y. Meng, Phys. Rev. B **95**, 085110 (2017).
[61] Y.-Y. He, X. Y. Xu, K. Sun, F. F. Assaad, Z. Y. Meng, and Z.-Y. Lu, Phys. Rev. B **97**, 081110 (2018).
[62] Y. Liu, W. Wang, K. Sun, and Z. Y. Meng, Phys. Rev. B **101**, 064308 (2020).
[63] The projection QMC method, the symmetry analysis of the model and absence of sign-problem and its PQMC implementations and benchmark results with the exact diagonalization..
[64] F. D. M. Haldane, Phys. Rev. Lett. **61**, 2015 (1988).
[65] Y.-Y. He, H.-Q. Wu, Y.-Z. You, C. Xu, Z. Y. Meng, and Z.-Y. Lu, Phys. Rev. B **93**, 115150 (2016).
[66] T. C. Lang, Z. Y. Meng, A. Muramatsu, S. Wessel, and F. F. Assaad, Phys. Rev. Lett. **111**, 066401 (2013).
[67] Z. Zhou, D. Wang, Z. Y. Meng, Y. Wang, and C. Wu, Phys. Rev. B **93**, 245157 (2016).
[68] H. C. Po, H. Watanabe, and A. Vishwanath, Phys. Rev. Lett. **121**, 126402 (2018).
[69] F. Assaad and H. Evertz, "World-line and determinantal quantum monte carlo methods for spins, phonons and electrons," in *Computational Many-Particle Physics*, edited by H. Fehske, R. Schneider, and A. Weiße (Springer Berlin Heidelberg, Berlin, Heidelberg, 2008) pp. 277–356.